Stability, Transport and Modification of Zeolitic Imidazolate Framework-8 Membranes for Light Hydrocarbon Separations

By

Joshua B. James

A Dissertation Presented in Partial Fulfillment
of the Requirements for the Degree
Doctor of Philosophy

Approved October 2017 by the
Graduate Supervisory Committee:

Jerry Lin, Chair
Heather Emady
Bin Mu
Mary Lind
Dong Seo

ARIZONA STATE UNIVERSITY

December 2017

ABSTRACT

Membrane technology is a viable option to debottleneck distillation processes and minimize the energy burden associated with light hydrocarbon mixture separations. Zeolitic imidazolate frameworks (ZIFs) are a new class of microporous metal-organic frameworks with highly tailorable zeolitic pores and unprecedented separation characteristics. ZIF-8 membranes demonstrate superior separation performance for propylene/propane (C_3) and hydrogen/hydrocarbon mixtures at room temperature. However, to date, little is known about the static thermal stability and ethylene/ethane (C_2) separation characteristics of ZIF-8. This dissertation presents a set of fundamental studies to investigate the thermal stability, transport and modification of ZIF-8 membranes for light hydrocarbon separations.

Static TGA decomposition kinetics studies show that ZIF-8 nanocrystals maintain their crystallinity up to 200°C in inert, oxidizing and reducing atmospheres. At temperatures of 250°C and higher, the findings herein support the postulation that ZIF-8 nanocrystals undergo temperature induced decomposition via thermolytic bond cleaving reactions to form an imidazole-Zn-azirine structure. The crystallinity/bond integrity of ZIF-8 membrane thin films is maintained at temperatures below 150°C.

Ethane and ethylene transport was studied in single and binary gas mixtures. Thermodynamic parameters derived from membrane permeation and crystal adsorption experiments show that the C_2 transport mechanism is controlled by adsorption rather than diffusion. Low activation energy of diffusion values for both C_2 molecules and limited

energetic/entropic diffusive selectivity are observed for C_2 molecules despite being larger than the nominal ZIF-8 pore aperture and is due to pore flexibility.

Finally, ZIF-8 membranes were modified with 5,6 dimethylbenzimidazole through solvent assisted membrane surface ligand exchange to narrow the pore aperture for enhanced molecular sieving. Results show that relatively fast exchange kinetics occur at the mainly at the outer ZIF-8 membrane surface between 0-30 minutes of exchange. Short-time exchange enables C_3 selectivity increases with minimal olefin permeance losses. As the reaction proceeds, the ligand exchange rate slows as the 5,6 DMBIm linker proceeds into the ZIF-8 inner surface, exchanges with the original linker and first disrupts the original framework's crystallinity, then increases order as the reaction proceeds. The ligand exchange rate increases with temperature and the H_2/C_2 separation factor increases with increases in ligand exchange time and temperature.

DEDICATION

To My Parents
Willard & Sharon James

ACKNOWLEDGMENTS

I first want to thank my parents. Ever since I can remember, both my father and mother have displayed a relentless work ethic and a strong emphasis on continuous improvement in both education and personal growth. You taught me to do the right things, the right way, the first time which has definitely helped me throughout this experience. I thank you for your enduring love and support throughout my graduate education. Without you, my pursuit of the PhD degree would not have been possible.

To my older brothers, you each have had a large influence on my life. You both looked after me when I was young and I can remember wanting to do everything you did, from chores to playing sports, and you each took the time to help me learn many things both practical and academic to made me very responsible at young age. You pushed me in sports, helped me relate the lessons learned on the field to experiences throughout my education and were a large source of encouragement for me to attend graduate school. To my little sister, I admire your diligence, intelligence, maturity and desire to learn. Thank you for always being a source of encouragement. I cannot wait to see what awaits you after college. To each of you, my parents and siblings, thank you and I love you.

I would also like to give an enormous thank you to my advisor, Dr. Jerry Lin for his support and guidance throughout my graduate study. You are an excellent mentor. It has been an honor and a pleasure to work with an advisor who is an eminent researcher in his field. I first met Dr. Lin as an undergraduate student of chemical engineering and finance and was uncertain of which path I fit most during that time. Since then, Dr. Lin has helped mold me into an avid researcher, challenging me every day to become a better

engineer and scientist. I greatly admire his passion for research, developing students and his approach to managing research projects. I have noticed not only his technical acumen but also the many other skills and talents needed to lead a research lab. I thank Dr. Lin very much for this opportunity to work on novel research, it has been a true blessing.

I am also grateful to Dr. Heather Emady, Dr. Mary Laura Lind, Dr. Bin Mu and Dr. Don Seo for serving on my dissertation committee and providing invaluable input. I have been privileged to take courses with Drs. Lind and Seo and interact with Drs. Emady and Mu and their dedication to teaching, research and development of graduate students is well noted. I aspire to connect with and cultivate new scientists just as they have done for me. I would also like to thank Dr. Jonathan Posner, he gave me my first opportunity to conduct research as an undergrad and sparked my initial interest in research. A special thank you to Mr. Fred Peña whose work is invaluable to our research. His constant insight and technical advice enhanced my mechanical and electric aptitude during this journey and has made me a better engineer and helped me conduct successful experiments.

I have had the opportunity to learn from and work with many fellow graduate students, post-docs and visiting scholars during my tenure in graduate school. Thank you to each of the current and former lab members of the Membrane and Energy Laboratory for their kindness, friendship and input during my PhD studies.

I greatly appreciate the financial support of the National Science Foundation during my research.

TABLE OF CONTENTS

Page

LIST OF TABLES

Table Page

LIST OF FIGURES

Figure Page

Figure Page

Figure Page

Figure Page

Figure Page

Figure Page

Figure Page

Figure Page

CHAPTER 1

INTRODUCTION & BACKGROUND

1.1 General Background

Sustainable separation of light hydrocarbons and substituent gasses formed during light hydrocarbon processing is emerging as an increasingly important topic. Expanding middle class economies and economic growth in both developing and developed world markets have increased the demand for polymer purity (99.5%) olefins ethylene ($C_{2=}$) and propylene ($C_{3=}$). As shown in Figure 1.1, the demand for both chemicals has shown stable growth since 1990 and total demand for ethylene and propylene is expected to grow by 100 billion pounds between 2016 and 2020 (Cooms, 2016).

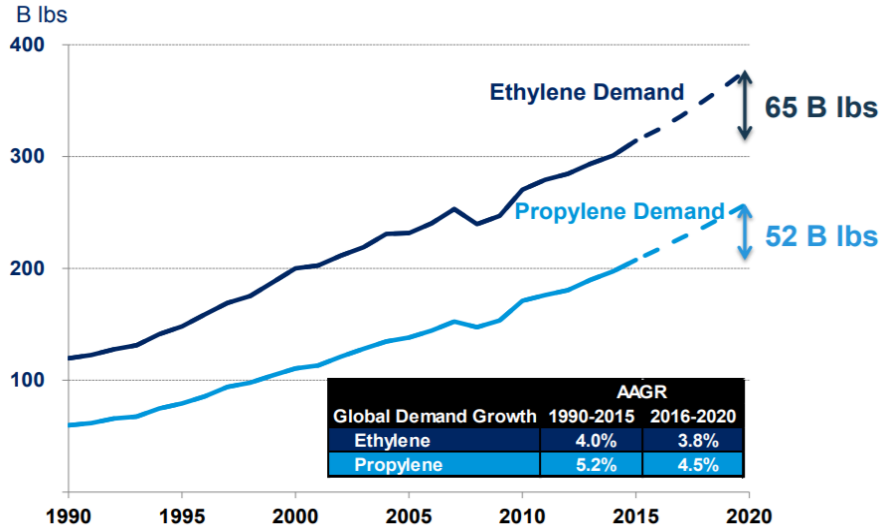

Figure 1.1 World ethylene and propylene demand between 1990 and 2016 with projection to 2020 (Cooms, 2016)

Ethylene and propylene are essential polymerization precursors used to form polyethylene and polypropylene plastic products and numerous derivatives which are ubiquitously essential for many uses each day.

In 2015 world scale consumption of polyethylene and polypropylene reached approximately 150 million tons with the majority of the annual consumption growth rates in each region greatly exceeding world GDP growth. Accelerated world plastic consumption with respect to GDP growth shown in Figure 1.2 is a result of significant growth in the industrial, retail and automotive sectors in each of the world markets. As emerging economies specifically in China, India and Africa continue to grow, demand for each product is projected to increase (Galiè, 2016). Meeting demand is quite feasible due to the development of hydraulic fracking which has made it possible and more economically viable to access petroleum and natural gas resources once deemed inaccessible. In 2015, the U.S. alone produced approximately 20 million metric tons of polyethylene and by 2018 it is estimated that U.S. polyethylene capacity will increase to 24.5 million metric tons (Petrochemical Update, 2017) and is projected to be 6 million metric tons in excess of total demand by 2020 (Galiè, 2016). In terms of polypropylene supply, Middle Eastern dominated exports and significant investments in on-purpose technologies will each serve to meet global polypropylene market needs in the future (Galiè, 2016).

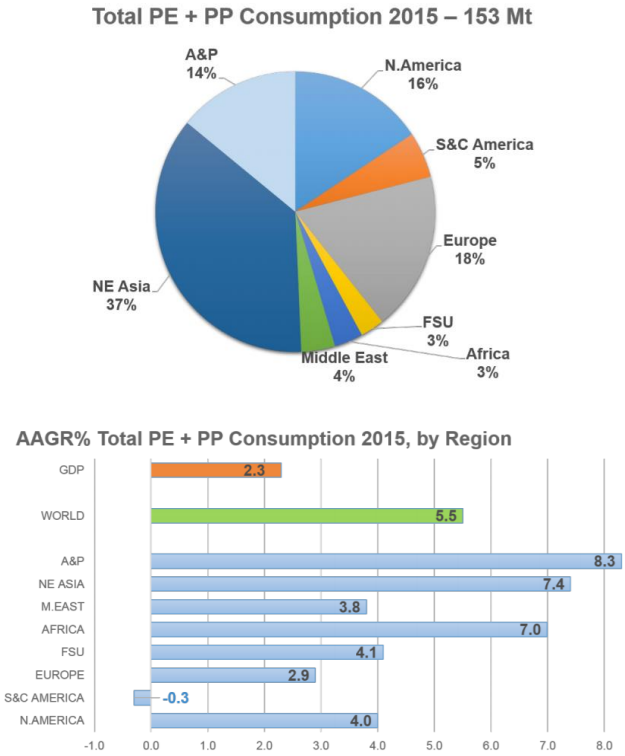

Figure 1.2 Total consumption of polyethylene (PE) and polypropylene (PP) and average annual growth rate (AAGR) of total PE and PP consumption by world region (Galiè, 2016)

Traditionally, most of the world's ethylene and propylene were produced as by-products of heavy oil feedstock/naphtha thermal and catalytic cracking processes. More recently, the advent of hydraulic fracking has significantly increased the supply of once inaccessible light hydrocarbon liquid petroleum gas (LPG) components such as ethane, propane and butane and has made light hydrocarbons more profitable cracking feedstocks for light olefin production and propane a valuable source for on-purpose production of propylene through propane dehydrogenation.

Depending upon the feedstock and process utilized, considerable amounts of high-value co-products such as hydrogen (H_2), methane (C_1), ethane (C_{2-}), propane (C_{3-}) and potentially higher hydrocarbons are produced in mixture with light olefins after cracking.

Each of the gasses are important products in their own right when separated/purified. High purity hydrogen is a valuable feedstock for numerous chemical processes, is essential in hydroprocessing (cracking and treating) and is an important and emerging source of energy. Methane and propane are widely used as sources of relatively clean industrial and residential fuels, and ethane, in addition to its use as a cracking feedstock is an important refrigerant for the cryogenic separation of post-cracking products.

Modern facilities employ cryogenic distillation processes to separate H_2, C_1, LPGs and $C_{2=}/C_{2-}$ and $C_{3-}/C_{3=}$ post cracking. The method is effective in producing high purity product streams but the method is highly energy intensive. The United States Department of Energy (DOE) estimates that approximately 0.34 quads or 3.4×10^{14} BTUs (3.6 kilojoules) per year are dedicated to separating LPGs and C_2/C_3 olefin/paraffin mixtures (Ozokwelu, 2005). To place this number in a broader context, approximately 98 quads of energy were consumed in the U.S. in 2015, therefore 0.3% of U.S. energy use was allocated to separating just 5 molecules.

Although light olefin precursors are now produced more efficiently, the separation of light olefins from their reaction co-products continues to induce large energy costs which will only increase as growing international middle class economies demand more plastic and energy products. To this accord, both academia and industry have placed great focus on designing effective, yet more sustainable separation techniques aimed at purifying olefins and valuable substituent gasses produced from cracking and dehydrogenation.

1.1.1 Alternative Separation Processes

To better understand the potential and efficacy of alternative separation processes for purification olefins and high-value cracking/dehydrogenation products the current process should first be briefly detailed. Cracked naphtha produces a mixture of H_2 and C_1-C_{4+} olefin/paraffins. The relative amount of each component depends upon the feedstock and process used. Figure 1.3 shows a simplified schematic of a fractionation train utilized for separation of gasses post hydrocarbon cracking. Post cracking, the hydrocarbon stream is first stripped of sour gasses and dehydrated. In the subsequent fractionation units, CH_4/H_2, C_2 and C_3 are produced in the overhead streams of the demethanizer (DM), deethanizer (DE) and depropanizer (DP) respectively.

The C_2 and C_3 splitters are largest fractionation columns (>120 trays) and perform the more intensive ethylene/ethane and propylene/propane separations. If it is necessary to produce more propylene, propane from the C_3 splitter is fed to the high temperature a propane dehydrogenation reactor which forms propylene and hydrogen. Hydrogen produced from the demethanizer and dehydrogenation processes are typically recovered through pressure-swing adsorption or cryogenic separations. The process detailed in Figure 1.3 is just one of many possible configurations, but what is inherent in all configurations are the expensive and energy intensive compression, heat exchange and refrigeration steps required to attain the extreme tower/feed conditions shown and the high reflux ratios necessary to obtain high purities.

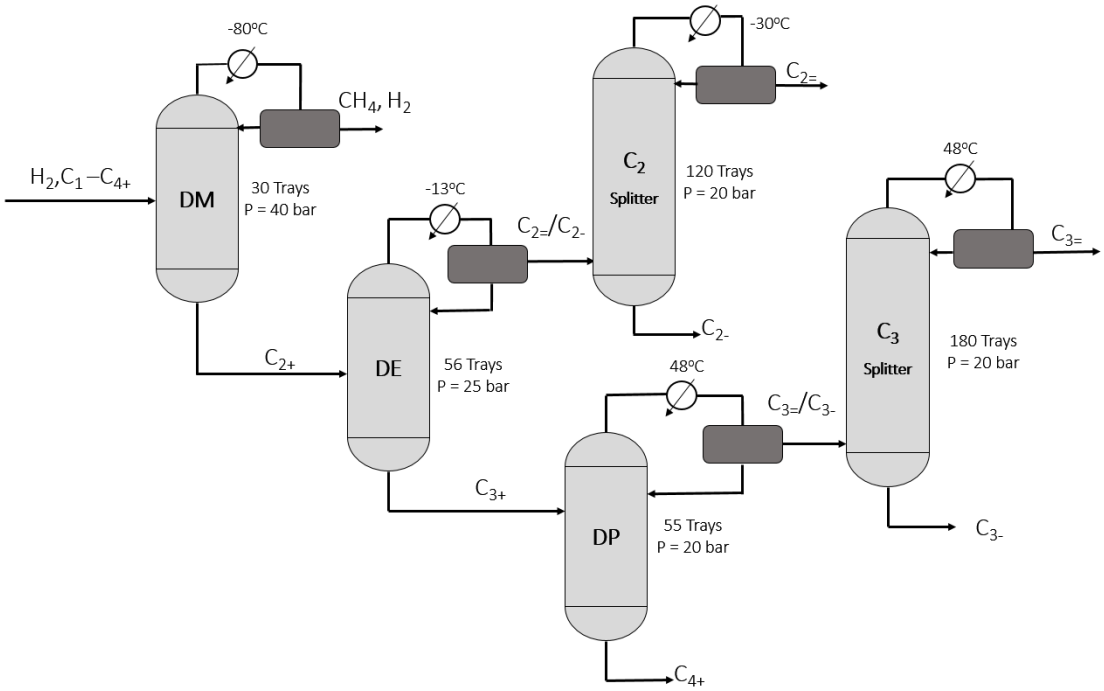

Figure 1.3 Simplified schematic of light hydrocarbon fractionation train post cracking. Process conditions adapted from Eldridge, 1993

Absorption, adsorption and membranes are the most researched alternative or augmentative technologies suggested to replace or debottleneck the unit operations outlined in Figure 1.3 (Angelini et al., 2005; Eldridge, 1993; W. J. Koros & Fleming, 1993). In contrast to distillation, the alternative processes do not require thermodynamic phase change of the mixture components to attain separation. Separation of products can commence in the gas phase at moderate temperatures without the need for extensive compression and refrigeration. As debottlenecking steps, the alternative units can provide pre or post purification steps that decrease the number of equilibrium stages, condenser/reboiler heat duties and reflux ratios required for distillation units to produce high-purity product streams. Alternative separation technologies should perform high throughput separations, be resilient in the presence of feed impurities and not significantly disrupt the intricate heat integration schemes and upstream/downstream process

parameters already present within the olefin production plant in addition to alleviating energy consumption (Eldridge, 1993).

In absorptive processes olefins are separated from paraffins by contacting the gas mixture with an aqueous amine, nitrile, ionic liquid or aromatic solvent containing a copper or silver metal salt. The olefin remains dissolved in the liquid phase through cation-π complexation with metal ions (Moura, Darwich, Santini, & Costa Gomes, 2015; Safarik & Eldridge, 1998). The absorption process suffers a trade-off between loading and absorptive separation ability (Safarik & Eldridge, 1998) (Reine & Eldridge, 2005) and deactivation of the cation's complexing ability occurs in the presence of CO and H_2S. Less expensive lean oil is the solvent phase for H_2 purification from hydrocarbon streams, but identical to the olefin/paraffin process, still requires large amounts of energy to heat/cool non-active liquid/solvent.

Adsorptive olefin/paraffin and H_2/hydrocarbon separation is a major area of study and is a technique currently performed in industry. Adsorptive processes are generally utilized when low-to medium contents of a desired component exist in a feed. In practice, solid zeolite materials packed in fixed bed vessels selectively separate gas phase adsorbate molecules based upon their size and chemical affinity. In academia, porous carbons, metal-organic frameworks, and zeolites have been investigated as sorbent materials for adsorptive separations (Bao et al., 2011; Da Silva & Rodrigues, 1999). Much work has been dedicated to tuning the pore aperture for molecular exclusion, pore size for maximum uptake/capacity and surface chemistry to enhance the adsorption affinity of one substituent over the other (Lin, 2016).

Membranes of thin polymer or polycrystalline film material formed from the sorbent precursors mentioned above and are generally utilized when medium-to-high content of a desired component exists in a feed. The pore aperture, pore size and surface characteristics of the membrane thin film are important in determining the permeability and selectivity of each permeating gas. In both material forms (membrane or adsorbent) there often exists a trade-off between permeability (adsorption capacity) and selectivity (Beyond, Rungta, Zhang, Koros, & Liren, 2013). However a large advantage of thin film membranes is the ability to conduct separation processes under steady-state conditions as compared to adsorbent technology which is operated under transient conditions requiring an energy intensive regeneration step.

An intrinsically stable membrane with exceptional permeance, able to obtain 99% olefin purity and high recovery has yet to be realized, however, technoeconomic analyses estimate that current state of the art olefin/paraffin membrane separation technology implemented optimally within current distillation infrastructure (Figure 1.4) could potentially alleviate energy consumption by 90% as compared to current processes (Sholl & Lively, 2016) and makes membrane separation the most compelling process among alternatives for debottlenecking or possible replacement of current separation technologies.

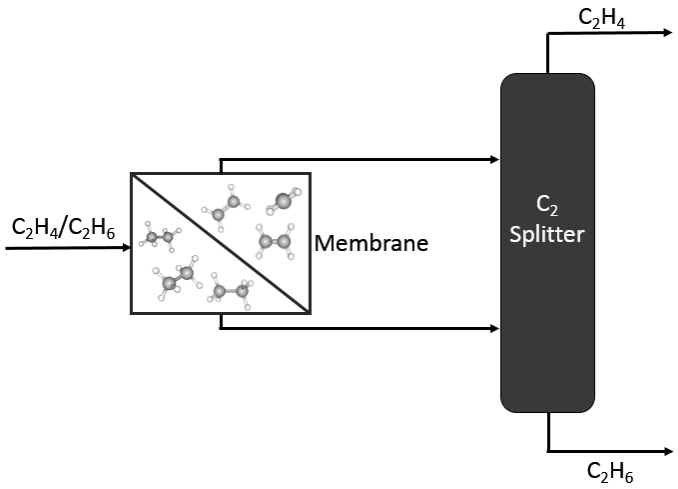

Figure 1.4 Membrane-distillation process for ethene/ethane debottlenecking process

1.2 Membranes for Light Hydrocarbon Separations

The energy savings potential associated with membranes over distillation is an effect of the disparate thermodynamics which control each process. Distillation relies on thermodynamic phase change to achieve separation of higher volatility mixture components from lower volatility components through contact of vapor and liquid phases within equilibrium stages. Table 1.1 shows the physiochemical properties of hydrogen and light hydrocarbons.

Table 1.1 Selected Physiochemical Properties of Hydrogen and Light Hydrocarbons

Molecule	van der Waals Diameter (Å)	Molecular Weight (g/mol)	Boiling Point (^oC)
H_2	2.76	2.02	-252.9
C_2H_4	3.59	28.05	-103.7
C_2H_6	3.72	30.07	-89.0
C_3H_6	4.03	42.08	-47.6
C_3H_8	4.16	44.10	-42.0

Due to their similar relative volatilities, the separation of C_2 olefin/paraffin and C_3 olefin/paraffin mixtures requires a large number of equilibrium stages (100+), high reflux ratios and thus energy (Comyns, 2001). Additionally, high pressures and/or cryogenics are necessary to obtain liquid phases for low boiling point hydrocarbons and hydrogen. In the case of membrane separations, phase change is not required. Mechanical energy normally already present from an upstream process is sufficient to drive membrane separation processes which approach the much less energy intensive thermodynamic limit of demixing (William J. Koros & Lively, 2012; Pimentel, Parulkar, Zhou, Brunelli, & Lively, 2014). Figure 1.5 provides an illustrative graphic of a basic membrane separation process in which molecules A and B enter the feed side of the membrane, the molecule with greater permeability across the membrane (A) will be enriched on the permeate side, while the pressurized retentate will be enriched with molecule B.

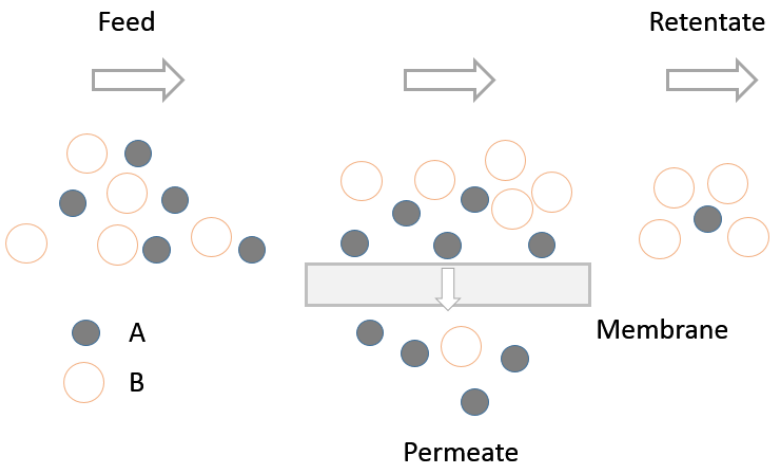

Figure 1.5 Membrane-based gas separation

Membranes with high permeability (productivity):

$$P = \frac{J * l}{P_h - P_L} \tag{1.1}$$

or flux (J) normalized by membrane thickness (l) and transmembrane pressure difference, [upstream pressure (P_h) - downstream pressure (P_L)] for the selective component and selectivity:

$$\alpha = \frac{P_A}{P_B} \tag{1.2}$$

in addition to stability, have potential to intensify the separation and reaction processes purvey energy savings in multiple areas in accordance with Figure 1.2 Hydrogen separation membranes implemented prior to the demethanizer will increase the dew point or condensability of the hydrocarbon mixture thus decrease the amount of cooling/refrigeration required by the demethanizer unit (Baker, 2002). Membranes which can perform C_2 and C_3 olefin/paraffin pre-purification to a reasonable extent prior to the C_2 and C_3 splitters can reduce the necessary reflux and boilup ratios required by the condenser and reboilers respectively. The heat duties (energy) of the reboiler and condenser are a function of the reflux and boilup ratios respectively (Seader & Henley, 2006):

$$Q_C = DR\Delta H^{vap} \tag{1.3}$$

$$Q_R = BV_B\Delta H^{vap} \tag{1.4}$$

Where Q_c and Q_R are the condenser and reboiler heat duties for a partial condenser and partial reboiler respectively. D, R and H^{vap} are the distillate rate, reflux ratio and heat of vaporization. B and V_B are the bottoms flow rate and boilup ratio respectively. Membranes also present an opportunity to intensify dehydrogenation processes. Propane dehydrogenation is thermodynamically limited and highly endothermic. Membranes offer a method to shift reaction equilibrium when implemented as membrane reactor systems through simultaneous reaction and removal/separation of reaction products during the dehydrogenation process to produce enriched olefin and hydrogen streams (Choi et al., 2015). Membranes with attractive productivity, selectivity and stability present an opportunity to enhance hydrocarbon separations while providing energy/cost savings.

1.3 Membrane Materials, Transport and Stability for Light Hydrocarbon Separations: A Literature Review

Figure 1.6 illustrates the major modes of molecule transport through membrane substructures. Permeability (productivity) and selectivity (efficiency) are of the utmost importance in addition to stability when initially evaluating membranes for specific applications. Membranes are generally classified according to their pore size. The IUPAC designations pore classifications and expected light hydrocarbon transport mechanisms are highlighted in Table 1.2. Membranes exploit size or chemical differences between permeating molecules to facilitate separations. Depending upon the permeating molecule's size and chemical affinity relative to the membrane substructure, its mode of transport varies. While macropores and mesopores offer high permeances, they are not efficient in separating small molecules comparable to the sizes shown in Table 1.1. Small molecules

(< 0.5 Å) permeating in macro or mesopores experience viscous or Knudsen diffusion respectively and selectivities approach that of Knudsen. Knudsen diffusion is based upon the relationship between a molecule's mean free path (λ) and pore diameter (d_p) as shown in Equation 1.6:

$$Kn = \frac{\lambda}{d_p} \tag{1.6}$$

$$\lambda = \frac{1.15\mu T^{\frac{1}{2}}}{PM_w^{1/2}} \tag{1.7}$$

where Kn is the Knudsen number, μ and M_w are the viscosity and molecular weight of the permeating gas, P and T are the system pressure and temperature respectively. If the Knudsen number is greater than 10, gas transport is in the Knudsen regime; that is, gas molecules have more pore wall collisions than intermolecular collisions. This diffusion mechanism is predominant in smaller mesopores and large micropores depending upon the molecule's size. When Knudsen diffusion is the dominating transport mechanism, the Knudsen diffusion coefficient (D_k) is modeled by Equation 1.8:

$$D_k = \frac{d_p}{3}\sqrt{\frac{8RT}{\pi M_w}} \tag{1.8}$$

At low pressures and high temperatures in the absence of adsorption effects, Knudsen selectivity (α_{ij}) is inversely proportional to the square root of molecular weights of the permeating gasses:

$$\alpha_{ij} = \sqrt{\frac{M_j}{M_i}} \tag{1.9}$$

The highest achievable Knudsen separation factor corresponding to the molecular weights for the molecules in Table 1.1 is 4.7 for H_2/C_3H_8 which is quite low in comparison to microporous and dense membranes which employ much disparate transport mechanisms that take advantage of size and physiochemical differences between hydrogen and light hydrocarbons in order to perform high resolution separations (William J. Koros & Mahajan, 2001).

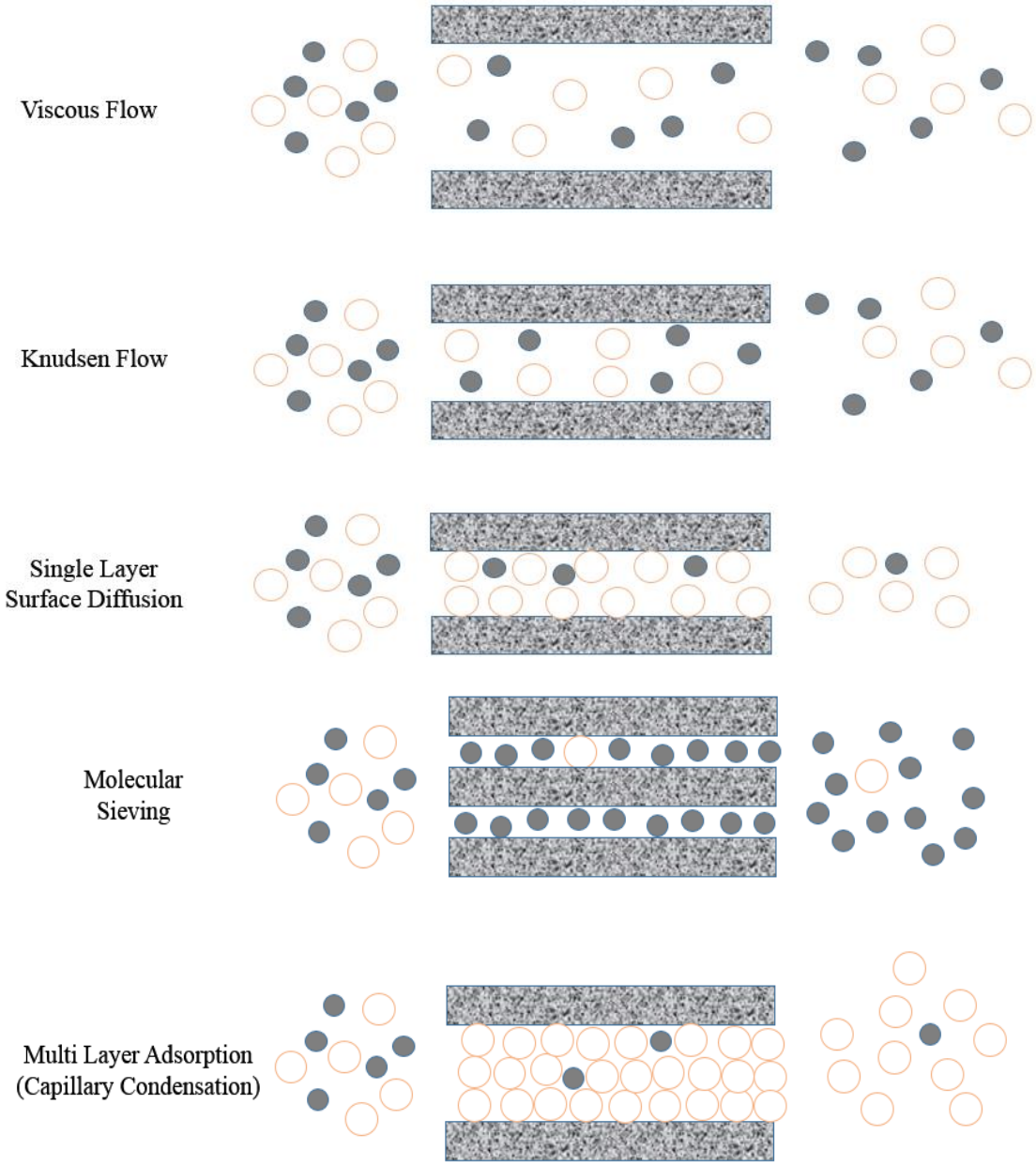

Figure 1.6 Transport mechanisms through porous membranes

Table 1.2 IUPAC Membrane Pore Size Classifications and Expected Transport Mechanisms for Light Hydrocarbons and Hydrogen

Membrane Pore Classification	Pore Diameter	Expected Transport Mechanism for Light Hydrocarbons and Hydrogen
Macroporous	> 50 nm	Viscous
Mesoporous	2-50 nm	Viscous, Knudsen, Capillary Condensation
Microporous	< 2 nm	Knudsen, Molecular Sieving, Solution-Diffusion
Dense	≈ 0 nm	Solution Diffusion, Facilitated Transport

1.3.1 Polymeric Membranes

In this review of membrane materials, transport and stability for olefin/paraffin and hydrogen/hydrocarbon separations it is fitting to begin with a discussion of polymeric materials which have a long history in membrane-based gas separation research and industrialization. Polymeric (natural rubber) membranes first demonstrated gas separation potential in the 1830's and subsequently during the first half of the 20th century, the majority of gas phase membrane separation work was applied to isotope separations (Ockwig & Nenoff, 2007). It was not until the 1950's that membranes garnered attention beyond isotope separation and were considered for helium/methane separations, oxygen removal from air and hydrogen recovery from hydrocarbon streams (Perry, Nagai, & Koros, 2006). Further industrialization of gas separation membranes remained mostly dormant until 1977 upon introduction of DuPont's melt spun polyester hollow fiber membranes for hydrogen recovery (Gardner, Crane, & Hannan, 1977). Polymeric materials have since continued to hold a monopoly for industrial gas separation applications such as

H_2 and CO_2/CH_4 separations due to their efficiency, ease of manufacturability, comparatively low cost and high modular scalability in high surface area-to-volume spiral-wound or hollow fiber modules (Baker, 2002).

Gas transport in polymeric membranes can be described using the solution-diffusion model (William J. Koros & Mahajan, 2001):

$$P = D * S \tag{1.10}$$

in which permeability (P) is a function of a gas's diffusivity and solubility (S) within the membrane. Specifically in polymers, gas molecules sorb on the upstream surface of the membrane, diffuse through the polymer matrix and desorb on the permeate side (W. J. Koros & Fleming, 1993). Dense polymeric membranes typically fall into two broad categories: glassy (high T_g) and rubbery (low T_g). Glassy polymers possess rigid molecular chains with limited segmental motion that typically enable sized-based separation of gas mixtures but exhibit low permeance while rubbery polymers contain mobile chains that enhance the diffusivity of all gasses from which larger penetrates benefit the greatest and facilitate sorption-reliant selectivity for the larger more condensable permeating gas. For olefin/paraffin separation glassy polymers present the greatest performance due to the similar size and solubility of the gasses, while for H_2 separations, both glassy H_2 selective and rubbery hydrocarbon selective membranes have been studied.

The limitation of the absolute and relative single gas permeabilities (permselectivity) for each separation mentioned above are well predicted for polymeric membranes. In 1991 Robeson analyzed the permeability and selectivity of CO_2 and several

permanent gas pairs in high performing glassy polymers in literature and a clear, inversely proportional relationship between selectivity (α) and permeability (P) was identified (Robeson, 1991):

$$\alpha_{A/B} = \frac{\beta_{A/B}}{P_A^{\lambda_{A/B}}} \tag{1.11}$$

The relationship now referred to as the Robeson upper bound is usually presented as a log-log plot of α vs P and applies to most gasses in polymers including olefin, paraffin and hydrogen molecules. It is the standard with which polymeric and all other membrane materials are compared and thus is of great importance.

In 1999, Freeman presented a model to predict the upper bound slope ($\lambda_{A/B}$) (Freeman, 1999) which is proportional to the ratio of the slow gas (B) to the fast gas (A) Lennard-Jones diameters:

$$\lambda_{A/B} = \left(\frac{d_B}{d_A}\right)^2 - 1 \tag{1.12}$$

and the front factor ($\beta_{A/B}$):

$$\beta_{A/B} = \frac{S_A}{S_B} {S_A}^{\lambda_{A/B}} exp\left\{-\lambda_{A/B}\left[b - f\left(\frac{1-a}{RT}\right)\right]\right\} \tag{1.13}$$

controls the intercept. The front factor is a function of: S_A and S_B which are the solubilities of gasses A and B within the polymer matrix, the parameter f which considers polymer interchain spacing and ranges from 0 for low performance rubbery polymers to 14,000 kcal/mol for high performance rigid polyamides (Freeman, 1999; Haraya et al., 1989) and a and b are linear free energy coefficients which relate the diffusion front factor (D_{0A}) to the activation energy of diffusion E_d (Barrer & Rideal, 1939; Van Amerongen, 1946):

$$lnD_{0A} = a\,\frac{E_{dA}}{RT} - b \tag{1.14}$$

The value of (a) has a generally accepted value of 0.64 (Barrer & Skirrow, 1948) independent of gas and polymer type and b also independent of gas type is equal to $-\ln(10^{-4}\ cm^2/s)$ for rubbery polymers and $-\ln(10^{-5}\ cm^2/s)$ for glassy polymers (Rungta et al., 2013; van Krevelen, 1997).

The major significance of the combined efforts of Robeson (Robeson, 1991) and Freeman (Freeman, 1999) was that the upper bound trade-off between ideal permeability and selectivity of gas pairs within polymers could be rationally predicted based upon the relative gas sizes, gas solubilities within the polymer matrix in addition to the intrinsic properties of the polymer studied. The upper bound is the standard at which all new membrane materials, polymeric and non-polymeric are evaluated against. Specific to olefin/paraffin separation, Koros and co-workers presented the experimental upper bound lines for $C_{2=}/C_{2-}$ (Rungta et al., 2013) and $C_{3=}/C_{3-}$ (Burns & Koros, 2003) using data points tabulated directly from studies which utilized only the highest performing polymers. This

method is in direct accord with the work of Robeson such that only a few exceptional polymer materials reside at the upper bound line (Robeson, 1991).

Koros and co-workers also predicted the upper bound upper bound slope and front factor for C_2 and C_3 molecules based upon the physical properties of 6FDA polyamides which are best in class for both separations (Burns & Koros, 2003; Rungta et al., 2013).

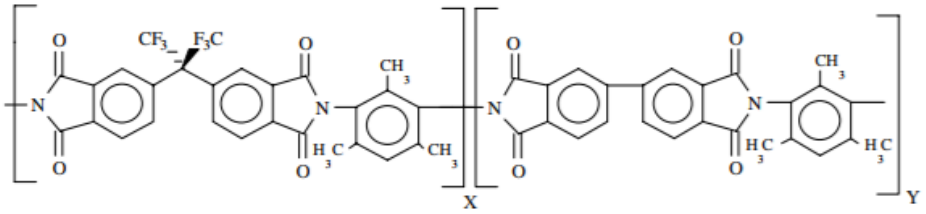

Figure 1.7 Structure of 6FDA/BPDA-DAM polymer precursor (Steel & Koros, 2005)

The upper bound slope is modeled well by the stiff polymer chains of 6FDA chemistries which enable size based exclusion of gasses. The upper bounds obtained from the experiments and modeling coincide well and predict for C_2 molecules, a selectivity of 10 can only be achieved at low permeability (< 0.5 Barrer) and for permeabilities greater than 10 Barrer, selectivity cannot exceed 6 (Figure 1.8) In the case of larger C_3 molecules, selectivity of 90 can be reached at 0.01 Barrer and for permeabilities of 1000 Barrer a selectivity of only 8 is achievable (Figure 1.9). The current upper bound limitations placed on even the highest performing stable, plasticization-resistant polyamides have limited their consideration for industrial use in olefin paraffin separations.

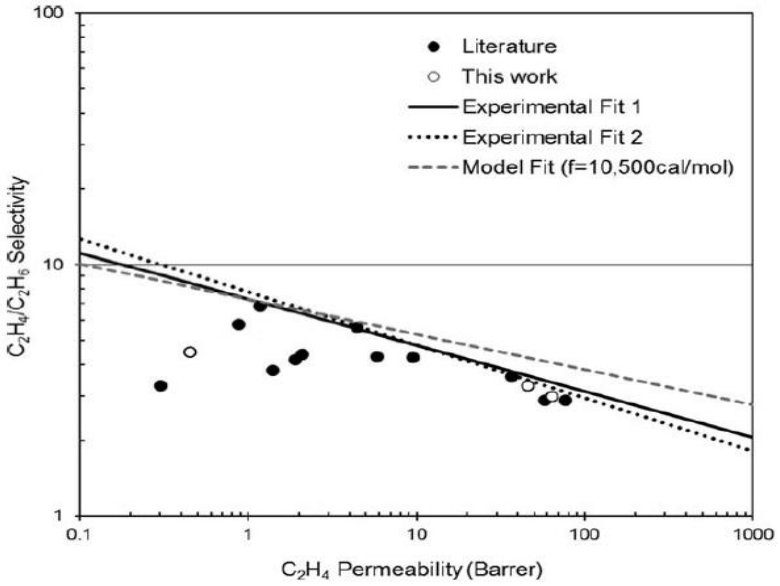

Figure 1.8 C_2H_4/C_2H_6 experimental data and upper bound prediction and experimental fits (Rungta et al., 2013)

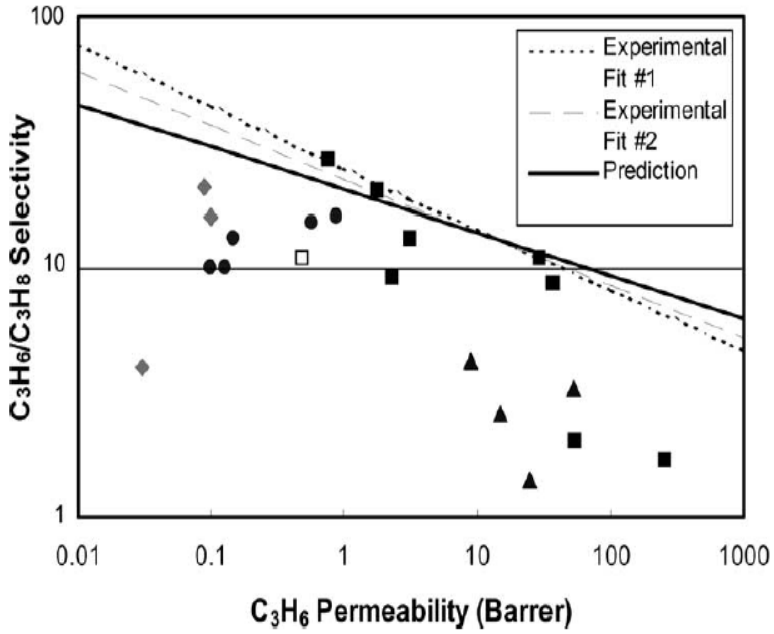

Figure 1.9 C_3H_6/C_3H_8 experimental data and upper bound prediction and experimental fits (Burns & Koros, 2003)

In terms of hydrogen separation, polymeric membranes have been used in industrial applications for H_2/CO ratio adjustment in syngas processes, removal of hydrogen from

ammonia purge gas and hydrogen recovery from petrochemical/refinery gas streams (Ockwig & Nenoff, 2007; Perry et al., 2006). Wide-scale, economical implementation of membranes was enabled by Monsanto, Separex, Air Products and Ube hydrogen selective membranes that give higher hydrogen productivity rates in comparison to the first generation DuPont hollow fibers (Perry et al., 2006). Table 1.3 shows H_2/CH_4 separation factors for top commercial membrane materials. Solely separation factor data is presented because limited transport data is provided for the commercial membranes.

Table 1.3 Hydrogen/Methane Separation Factors of First Generation Commercial Gas Separation Membranes Adapted from Perry et al., 2006

Membrane Material	Developer	H_2/CH_4
Cellulose Acetate	Separex	26
Polyamide	Ube	-
Polysulfone Silicone Rubber	Monsanto	24

In academia both hydrogen selective and hydrogen rejective membranes have been studied for hydrogen/hydrocarbon separations. Figure 1.10 shows the H_2/CH_4 upper bound for newest state-of-the-art hydrogen selective polymeric materials for comparison to the commercial materials in Table 1.3. Currently Triptycene-based polymer of intrinsic microporosity (PIM) polyamide (KAUST-PI) membranes and other PIM based membranes transcend the upper bound defined by earlier generation 6FDA-based polyamide membranes (Ghanem, Swaidan, Litwiller, & Pinnau, 2014). As compared to low-free volume 6FDA polyamides, PIMs contain relatively high free volume, yet tightly packed highly interconnected microstructures. High free volume along with the ability to tune the

rigidity of microstructure endows PIMs with both enhanced permeabilities and selectivties over all known polymers used in industrial gas separations.

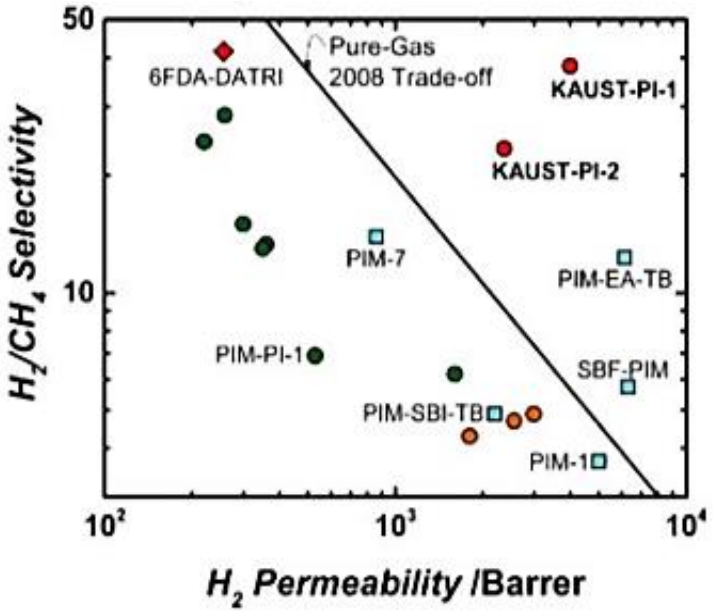

Figure 1.10 H_2/CH_4 2008 upper bound trade-off line with notable PIM membranes highlighted (Ghanem et al., 2014)

Hydrocarbon selective membranes offer an attractive method for recovering high pressure hydrogen from the retentate stream. Although the separation factors for hydrogen rejective membranes are often lower than the H_2 selective membranes mentioned above, hydrogen recompression is avoided and offsets the cost of hydrogen losses (Baker, 2002). Hydrocarbon selective PTMSP (I. Pinnau, Casillas, Morisato, & Freeman, 1996) and PMP (Morisato & Pinnau, 1996) membranes are the most highly cited of their type and especially interesting because they are glassy polymers which would typically lead to H_2 selectivity, but due to the extremely high excess free volume in PTMSP (20-25%) and PMP (28%) which is ~18-20% greater than conventional glassy polymers (Morisato & Pinnau, 1996; I. Pinnau et al., 1996).

It is postulated that the free-volume elements are interconnected and allow transport of larger condensable gasses by a sorption/surface diffusion mechanism favorable for large molecule permeability. Sorption of condensable hydrocarbons in the intersegmental free space allows efficient blocking of smaller molecules such as hydrogen for sizeable propane/H_2 and butane/H_2 selectivities of 13 and 39 respectively with high permeabilities of 28,000 (propane) and 85,300 (butane) Barrer respectively.

Polymer stability especially in the presence of highly condensable hydrocarbons (C_{3+}) is of great concern. At high feed pressures in the presence of condensable gasses, polymer chains experience swelling/dilation and drop in glass transition temperature while this can be advantageous for sorption based separations, this is detrimental for glassy polymers which exclude molecules based upon size. This phenomena termed plasticization leads to a drop in selectivity and membrane performance. Crosslinking is a method utilized to circumvent plasticization in membranes, however this process can be complex and will add complexity to the manufacturing process (Baker & Lokhandwala, 2008). Pretreatment to remove C_{3+} molecules prior to membrane separation has also been proposed.

In terms of thermal stability, polymeric membranes are suitable for low temperature and near-ambient olefin/paraffin and hydrogen/hydrocarbon separations, however, due to their low T_g most polymers suitable for membrane reactor applications which are typically operated at temperatures above 300°C. In an effort to provide a shift in reaction equilibrium, 6FDA-IPA with a T_g of 310°C was studied in a butane to butene membrane-assisted reactor configuration by Koros and co-workers (Rezac, Koros, & Miller, 1994). The membrane was continuously operated at 180°C for inter-stage production and removal

of hydrogen between two catalytic reactors enable a conversion 33% which is 12% greater than normal equilibrium conversion.

As advanced polymeric membranes are further developed, potential improvements in paraffin/olefin and hydrogen/hydrocarbon separations may enable further implementation in industrial applications. However, the current upper bound limitations and plasticization increase the pursuit of other membrane materials in both academic and industrial research.

1.3.2 Facilitated Transport & Dense Metallic Membranes

Facilitated transport membranes boast extremely high C_2 and C_3 olefin/paraffin selectivity and permeability. Virtually absolute olefin selectivity is enabled through olefin-metal complexation which was originally discovered in the early 19th century by Ziese who discovered platinum-ethylene complexes upon boiling a metal salts in ethanol (Zeise, 1831). Metal-olefin complexes are formed by two chemical bonds which include a σ-bond formed from the overlap of the vacant outermost s orbital of the metal with the full, electron dense π molecular orbital of the olefin, and a π-bond is formed from the donation of outer 4d atomic electrons of the olefin to the vacant π^* (antibonding) orbital of the olefin.

Dense or porous membranes containing an aqueous liquid or solid electrolyte composed of a metal (Cu or Ag) salt solution take advantage of olefin-cation complexations which facilitate the still debated transport mechanism of activated jumping of olefins across metal sites of the membrane or passive transport enabled by the carrying of olefin molecules across the membrane by metal cations. In liquid-based systems, a porous support is impregnated with an immobilized liquid or a support (SLM) saturated with flowing

solution; both configurations containing metal facilitators. Teramoto et al. were the first to investigate ethylene/ethane transport in supported liquid membranes containing aqueous silver nitrate solutions impregnated within porous supports. An ethylene/ethane selectivity of 1000 was reported, but after continuous membrane operation it was noted that ethylene selectivity was depleted due to solvent evaporation (Teramoto, et al., 1986).

Subsequent studies proposed using ion-exchanged polymeric membranes (IEM) which originally are in proton form, then upon pretreatment swelling occurs and subsequently enhances metal-salt solution absorption not only in the pores but also at electrostatic exchange sites within the polymer matrix. IEMs more stable than their SLM counterparts, however the swelling effect is not permanent and the only method for maintaining high olefin permeability (1000 Barrer) and selectivity (470) over long periods is to saturate feeds with steam to prevent solution dehydration (Eriksen, Aksnes, & Dahl, 1993). This method is highly impractical for real-world applications.

Flowing liquid membranes (FLM) have been studied to overcome the shortcomings of immobilized liquid membranes by providing a continuous flow of the liquid carrier solution. HFMCs utilize bore/shell configurations in which the olefin/paraffin mixture flows through the bore side of the hollow fiber and the solvent phase is pumped either counter-currently on the shell side or co-currently through the bore side of the membrane along with the gas mixture. During HFMC operation with carrier solution flowing counter-currently, researchers have cited significant olefin mass transfer resistance due to solvent penetrating the pores (Faiz & Li, 2012). Sulfonated poly(ether ketone) hollow fiber membrane contactors have shown high olefin selectivity (> 2700) and permeability (10,000 Barrer) (Nymeijer, Visser, Assen, & Wessling, 2004) . The HFMC process has been

validated as technically sound, but presented limited long-term chemical and thermal stability due to continuous contact with silver nitrate (Narasimhan Calamur, Mark P. Kaminsky, Vincent J. Kwasniewski, John A. Mahoney, Charles G. Scouten, 1999). Another possible issue not significantly highlighted in literature is that the olefin must be removed from the solvent and which necessitates a thermal regeneration step.

Membrane electrolytes are a novel class of facilitated transport membranes. Metal facilitators are dissolved within polymer matrices which enables the facilitated transport process to occur entirely in the solid phase. Both the cations and anions of the metal salt are sufficiently mobile without a liquid solvent. In contrast to liquid based facilitation systems, the membrane electrolyte process can operate at higher transmembrane pressure drops without physical loss of the complexing agent, can be operated with dry feeds and don't call for olefin separation from solvents (Ingo Pinnau & Toy, 2001).

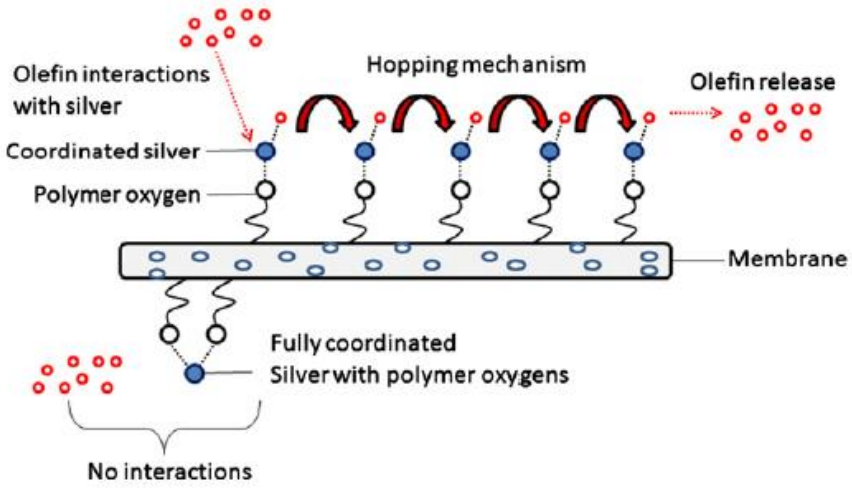

Figure 1.11 Olefin transport mechanism in solid electrolyte membrane (Faiz & Li, 2012)

Ethylene selectivities of 280 have been achieved (Ryu, Lee, Kim, Kang, & Kim, 2001), however, metal ions can be reduced in the presence of light, and the presence of trace impurities such as H_2, H_2S, and acetylene in the feed can poison the metal carriers. Overall, facilitated transport membranes maintain allure because they are not subjected to the permeability/selectivity tradeoff exhibited by most membranes, however their stability is a major contention for future industrial implementation (Faiz & Li, 2012).

Similar to olefin facilitated transport membranes, dense metallic membranes allow highly selective permeation of a single molecule: hydrogen. Hydrogen permeation proceeds via 7 intricate steps but can be elucidated down to H_2 chemisorption/oxidation at the catalytic metal surface of the membrane to form H^+ ions, H^+ diffusion through the metallic lattice interstitial vacancies, dislocations/grain boundaries, H^+ reduction/re-association and diffusion of H_2 gas away from the permeate interface (Ward & Dao, 1999). Hydrogen permeability in dense membranes is generally governed by the solution diffusion model as presented in the previous section. Dense metallic membranes are operated at high temperatures for high hydrogen flux and have shown potential for high temperature separation of hydrogen from hydrocarbons. At high temperatures when the bulk diffusion of H^+ ions is non rate limiting, the bulk concentration of H^+ is low and metal-hydrogen interactions are negligible, Sievert's law can be used to model H_2 flux as a function of the upstream/downstream H_2 partial pressure difference (Ward & Dao, 1999):

$$J = \frac{D_{H_2}}{l} * S * (P_{H_2}^{feed})^{0.5} - (P_{H_2}^{perm})^{0.5} \tag{1.16}$$

Pure, crystalline palladium membranes with body-centered cubic (BCC) microstructure typically out-perform most other metallic materials in terms of H_2 permeability, however Pd-H phase transition at ~ 300°C causes membrane degradation due to significant lattice strain caused by hydrogen embrittlement and pure palladium membranes are highly susceptible to deactivation by CO and H_2S impurities (Ockwig & Nenoff, 2007). Palladium membranes are intricately alloyed with group IV, group V or other metals such Ag, Al, Co, Cr, Cu, Fe, and Ni among others to avoid Pd-H formation and/or reduce surface deactivation by H_2S/CO while maintaining the BCC microstructure for high hydrogen permeability (Ockwig & Nenoff, 2007).

Pd-Ag membranes have shown good performance in ethane and propane dehydrogenation membrane reactor studies for in situ production and separation of ethylene or propylene from hydrogen. Gobina and Hughes performed ethane dehydrogenation experiments using a Pd-Ag membrane reactor and observed a conversion of 18% at 387°C which is 7 times greater than equilibrium conversions achievable in conventional fixed-bed reactor systems (Gobina & Hughes, 1994). Using the same membrane material, Yildirium et al. were able to obtain a 21% propane conversion at 400°C which is 4 times greater than typical fixed-bed equilibrium (Yildirim, Gobina, & Hughes, 1997).

In each of the above studies stability issues were not cited, but in the very specific case of long-term $H_2/C_{3=}$ separations, metallic membranes have shown performance instability. At high temperatures (> 400°C) propylene dissociatively chemisorbs on palladium forming a coking layer at the membrane surface, the resulting carbon atoms dissolve in the palladium lattice forming Pd-C which significantly deactivates sites for

hydrogen dissociation and permeation (Jung, 2000). Formation of carbonaceous matter on the membrane surface can be avoided by performing H_2/hydrocarbon separations at lower temperature, however, H_2 permeability is greatly reduced at lower temperatures, which decreases hydrogen recovery and if running as a membrane reactor, paraffin conversion would decrease. In order to remove carbonaceous matter and recover H_2 permeability, the palladium membrane can be reactivated in air at 600°C.

Further research on doping, grain size manipulation and amorphous microstructures is in progress to enhance the mechanical strength, eliminate stability issues and augment the manufacturability of metal membranes (Bryden, 2002; Lai, Yin, & Lind, 2015; McCool & Lin, 2001), but even with the above alleviated, the cost of such membranes and dopants may be prohibitively expensive for industrial realization and may limit metallic membranes to niche applications where ultra-high purity hydrogen is necessary.

1.3.3 Microporous Membranes

1.3.3.1 Transport in Microporous Membranes

Molecular sieving of light olefin/paraffin and hydrogen/hydrocarbon mixtures based on molecular size exclusion is a viable technique that has already surpassed the upper bound set by advanced polymeric materials (Burns & Koros, 2003). Microporous membranes such as zeolites, silica and metal organic framework (MOF) membranes can be selected or tailored to contain pore diameters/apertures that are just between the larger and smaller component molecular sizes for effective molecular sieving. The remainder of this work seeks to highlight the potential of microporous molecular sieving membranes for

light hydrocarbon separations and therefore transport in such membranes will be developed in more detail than in the previous sections.

Considering the application of light hydrocarbon and hydrogen separations, defect-free small micropore (< 8Å) membranes should be utilized. Inorganic/metal organic membranes are typically grown on mechanically/thermally stable ceramic supports or on polymeric supports depending upon the application. Growth of a continuous, thin film layer free of grain boundary defects is often times challenging. Smaller gas (< 5Å) transport through membranes containing moderate defects or larger micropores can present similar transport behavior to that of mesoporous membranes. Small gas permeance in defect containing or large micropores membranes can be modeled by a simplification of the Dusty-Gas model (Lin & Burggraaf, 1993):

$$F = \alpha + \beta\left(\frac{P_f + P_p}{2}\right) \tag{1.17}$$

where F is permeance P_f is the feed pressure and P_p is permeate pressure. The Dusty-Gas model considers the contribution of both Knudsen flow (α) through relatively larger pores and viscous flow (β) through macroporous defects. As mentioned earlier, Knudsen and viscous transport are not sufficient to separate light hydrocarbon mixtures. In relatively defect free microporous membranes the transport mechanism highly dependent on both the kinetic factor (diffusivity) and the thermodynamic factor solubility (adsorption) and is macroscopically described using 5 steps (Bakker, Kapteijn, Poppe, & Moulijn, 1996): adsorption from the gas phase to the feed side membrane surface, mass transport from the

external surface to the membrane pore, intracrystalline diffusion, transport from the pore to the external surface and finally, desorption from the external surface to the gas phase. Steady-state single gas hydrocarbon flux through microporous membranes is best modeled microscopically by the Maxwell-Stefan (M-S) treatment as described by Krishna with modifications (Krishna & Paschek, 2000):

$$J = -\phi q_{sat} D_c \left(\frac{\theta_i}{RT} \nabla \mu\right) \tag{1.18}$$

where Φ is a geometric correction factor which accounts for membrane physical properties density (ρ) and porosity (ε) and tortuosity (τ): ($\Phi = \rho \cdot \varepsilon / \tau$). θ is fractional surface occupancy of adsorption sites within the microporous material. The transport of gas phase molecules in microporous materials involves the activated movement of sorbed gas molecules from open sorption sites on the porous surface. μ is the chemical potential of the adsorbed species or the driving force required to make a diffusive jump from one adsorption site to the next which is directly proportional to the gradient of the fractional surface occupancies:

$$\frac{1}{RT} \nabla \mu = \frac{1}{\theta} \Gamma \nabla \theta \tag{1.19}$$

$$\Gamma = \theta \frac{\partial ln P}{\partial \theta} \tag{1.20}$$

D_c is the Maxwell-Stefan (M-S) thermodynamically corrected diffusivity Fickian diffusivity is highly loading dependent whereas, the Maxwell-Stefan treatment decouples drag effects (M-S diffusivity can be physically interpreted as inverse drag) from thermodynamic (sorption) effects and assumes that the mechanism of transport of molecules inside the micropores is by activated movement of adsorbed species along sorption sites (Krishna & van den Broeke, 1995). Γ is the Darken thermodynamic correlation factor which decouples typical Fickian diffusivity (D) from D_c:

$$D = D_c\Gamma \tag{1.21}$$

The thermodynamic factor is inversely proportional to the density of un-occupied adsorption sites:

$$\Gamma = \frac{1}{1-\theta} \tag{1.22}$$

Light hydrocarbons often show Langmuir-type isotherm behavior when adsorbing on microporous materials such as zeolites (Duong D Do, 1998). Other isotherm types may more appropriate but the proceeding analysis will assume the Langmuir relationship exists. Langmuir theory assumes localized (one adsorbate per adsorption site) monolayer surface adsorption and is modeled by:

$$\theta = \frac{q}{q_{sat}} = \frac{bP}{1+bP} \tag{1.23}$$

where q is the quantity adsorbed (mmol/g), q_{sat} is the total saturation of the adsorbed species, b is the affinity constant and P is system pressure.

Steady-state single gas flux can be presented in terms of experimentally, readily measurable variables from the following model (Nikolakis et al., 2001):

$$J = \frac{\rho}{L} * \frac{\varepsilon}{\tau} \int_{q_{feed}}^{q_{perm.}} D_c \frac{dlnP}{dlnq} dP \tag{1.24}$$

where q is quantity adsorbed (mmol/g) derived from the Langmuir equation, the term after D_c corresponds to the thermodynamic driving force. After integration an expression explicit in terms of the feed and permeate (perm) pressures can be obtained:

$$J = \frac{\rho}{L} \frac{\varepsilon}{\tau} q_{sat} D_c \ln\left(\frac{1 + bP^{feed}}{1 + bP^{perm}}\right) \tag{1.25}$$

The diffusion of hydrocarbons in microporous membranes, specifically zeolites was studied extensively by Xiao and Wei (Xiao & Wei, 1992). In microporous membranes, if the permeating molecule size is comparable to the pore channel diameter, diffusion is said to reside within the configurational regime. As the molecule size approaches the pore size, the potential field of the solid surface effects the molecule to a greater extent than that which occurs during Knudsen diffusion and must be modeled accordingly (Xiao & Wei, 1992):

$$D = g\gamma u e^{-\frac{E_d}{RT}} \tag{1.26}$$

where g is a geometrical factor, u is velocity of the permeating molecule, γ is the diffusive jump length and $E_{a.}$ is energy barrier that must be overcome for a molecule to make a diffusive jump between adjacent adsorption sites. In the case of no specific adsorbate-adsorbent interactions with the pore wall surface Xiao and Wei purposed the gas translational (GT) model (Xiao & Wei, 1992):

$$D_{GT} = \frac{\alpha}{z} d_p \sqrt{\frac{8RT}{\pi M_W}}\, e^{-\frac{E_d}{RT}} \tag{1.27}$$

where α replaces L as the diffusion length and 1/z is the diffusion coordination number. This model is most often utilized for high temperature permeation where adsorption is minimal (Masakoto Kanezashi, O'Brien-Abraham, Lin, & Suzuki, 2008). In the case of strong gas molecule/solid lattice interaction, the solid vibration model is used:

$$D_{SV} = \frac{\alpha^2}{z} v_e e^{-\frac{E_d}{k}} \tag{1.28}$$

where v_e is the effective vibrational frequency of the molecule inside the solid and k is Boltzmann's constant. In the aforementioned diffusivity models it is assumed that diffusion takes place via activation diffusion across adsorption sizes within the pore channel. In

certain cases the pore cage and/or the pore aperture separating cages is small enough to limit the rotational, translational and/or vibrational degrees of freedom of the diffusing molecule which must orient itself such that it can pass through the channel/aperture to the adjacent cage. This is typically the case for diffusion of larger non-permanent molecules in ultramicropores (< 5Å pore diameter) and the effects of intracrystalline partitioning (entropy) must be considered (D. M. Ruthven, Derrah, & Loughlin, 1973; Xiao & Wei, 1992). Diffusivity is then expressed in terms of a pre exponential factor (D_0) and activation energy:

$$D_c = D_0 e^{-\frac{E_d}{RT}} \tag{1.29}$$

Intracrystalline partitioning is modeled in the pre-exponential term:

$$D_0 = e\gamma^2 \frac{kT}{h} e^{\frac{S_D}{R}} \tag{1.30}$$

where S_D is the activation entropy of diffusion, k is Boltzmann's constant and h is Plank's constant. From transition state theory, S_D can be described in terms of partition coefficients and Equation 1.30 can be re-written as:

$$D_c = \gamma^2 \frac{kT}{h} \frac{F^{\neq}}{F} e^{\frac{-E_d}{RT}} \tag{1.31}$$

where F is the product of the translational, rotational and vibrational partition functions: $F = F_{trans} \cdot F_{rot} \cdot F_{vib}$ in the normal state (within the pore cage) and $F^{\neq}$ is the partition function in the transition state (at the ultramicropore window): $F^{\neq} = F_{trans}^{\neq} \cdot F_{rot}^{\neq} \cdot F_{vib}^{\neq}$.

$$F_{trans} = \left(\frac{2\pi mkT}{h^2}\right)^{\frac{n}{2}} \cdot a^n \tag{1.32}$$

where m is the mass of the molecule and n is the number of degrees of freedom

$$F_{rot} = \frac{\pi^{n/6}}{\sigma^{n/3}} \cdot \left(\frac{T^3}{\Theta_{rA}\Theta_{rB}\Theta_{rC}}\right)^{\frac{n}{6}} \tag{1.33}$$

$$\Theta_r = \frac{h^2}{8\pi Ik} \tag{1.34}$$

$$F_{vib} = \left(\frac{e^{-\frac{h\nu}{2kT}}}{1 - e^{-\frac{h\nu}{kT}}}\right)^n \tag{1.35}$$

where Θ_r is the characteristic rotational temperature which is expressed in terms of moment of inertia I. The diffusion coefficient utilized should be selected based upon the specific regime of gas transport occurring during permeation. Ideal permselectivity can be calculated from the ratio of the individual component fluxes.

It is also important to model binary gas mixtures in order in order to observe how the diffusivity and solubility of one component in the mixture affects other permeating

components. In multicomponent mixtures, adsorbate-adsorbate interactions affect both the diffusivity and solubility of the mobile components as outlined by Krishna (Krishna & Paschek, 2000):

$$J = -\phi[B]^{-1}[\Gamma]\nabla\theta \tag{1.36}$$

$$B_{ii} = \frac{1}{D_i} + \sum_{\substack{j=1 \\ j\neq i}}^{n} \frac{\theta_j}{D_{ij}}; B_{ij} = -\frac{\theta_i}{D_{ij}} \; for \; i,j = 1,2,\dots n \tag{1.37}$$

Equation 1.37 is the multicomponent flux equation explicit in terms of the n-dimensional rectangular matrix B which accounts for single component diffusivities D_i and interchange diffusivities D_{ij}. Interchange diffusivities represent the counter exchange of gas j and i at a sorption site where i is replaced by j. During counter exchange the faster molecule is slowed by the species with lower mobility and the slower molecule is accelerated by the faster component. The extent of slowing down or speeding up can be expressed by the exchange coefficients which adhere to the Onsager reciprocal relationship (Krishna, Li, van Baten, Falconer, & Noble, 2008):

$$D_{ij}q_{sat,j} = D_{ji}q_{sat,i} \tag{1.38}$$

The elements of matrix Γ are often determined by ideal adsorbed solution theory (IAST) as outlined by Myers and Prausnitz (Myers & Prausnitz, 1965) or a simplified treatment of

mixed gas adsorption using the extended Langmuir model (van de Graaf, Kapteijn, & Moulijn, 1999):

$$\theta_i = \frac{q_i}{q_{i,sat}} = \frac{b_i P_i}{1 + \sum_{i=1}^{n} b_j P_j} \; i, j = 1,2, \ldots n \tag{1.39}$$

If intermolecular interactions are negligible binary permeance can be modeled using the following equation (Nikolakis et al., 2001):

$$J_i = \frac{\rho}{L}\frac{\varepsilon}{\tau} D_{c,i} q_{sat,i} \frac{b_i (P_i^{feed} - P_i^{perm})}{b_i \left(P_i^{feed} - P_i^{perm}\right) + b_j (P_i^{feed} - P_i^{perm})} \ln\left(\frac{1 + b_i P_i^{feed} + b_j P_j^{feed}}{1 + b_i P_i^{perm} + b_j P_j^{perm}}\right) \tag{1.40}$$

1.3.3.2 Zeolite Membranes

Aluminosilicate zeolites are highly diverse group ordered structures composed of SiO_4 and AlO_4 building blocks with O-M-O (O = oxygen, M = metal) bonds of 145° with a diverse array of cell configurations that have resulted in more than 200 different types of zeolites being discovered or synthesized. In terms of light hydrocarbon separations, small-pore molecular sieving zeolite crystals such as FAU (0.7 nm), MFI (0.55 nm), LTA (0.3-0.5 nm), DDR (0.4 nm) SAPOs - CHA type (0.38 nm) have been evaluated in kinetic gas uptake and equilibrium sorption experiments and present promising diffusive molecular sieving of ethane/ethylene and propylene/propane mixtures (Agarwal et al., 2010; Douglas

M. Ruthven & Reyes, 2007) but comparatively less work has been reported for thin film membranes.

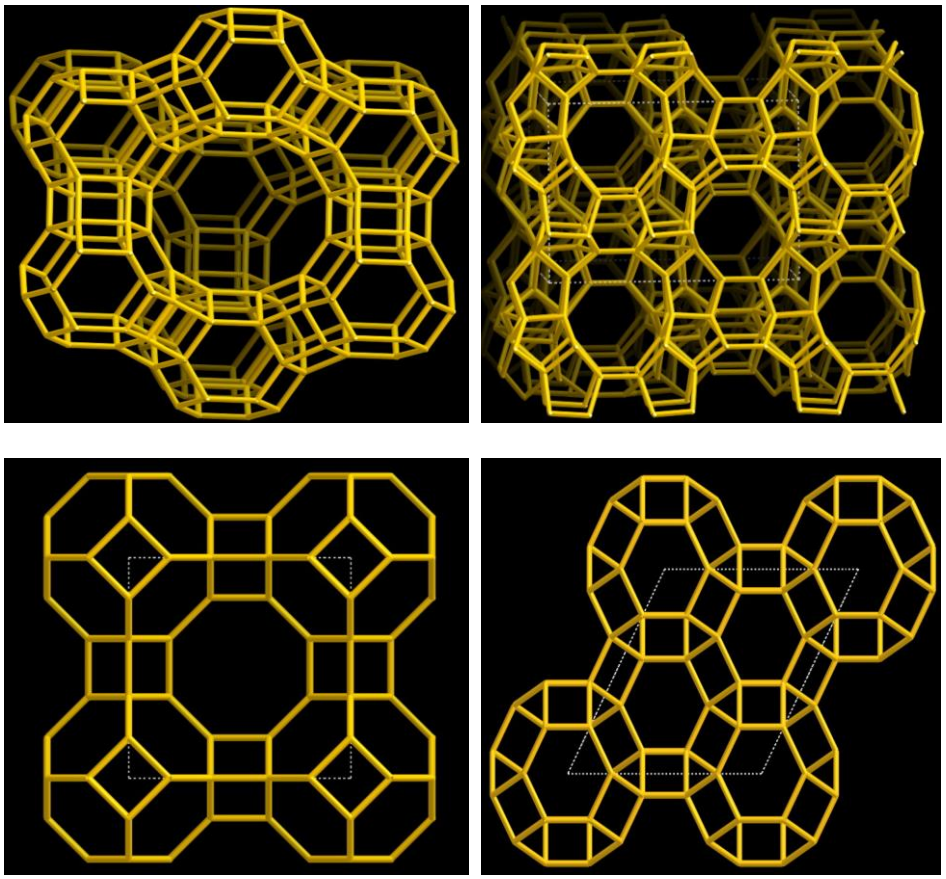

Figure 1.12 From left to right: FAU, MFI, LTA and CHA type zeolite crystallographic structures from IZA database

Fajusite-type (FAU) membranes have shown ideal C_3 selectivities of 28, however in the binary mixture, the propylene/propane selectivity is reduced to 13.7 (Ioannis G. Giannakopoulos & Vladimiros Nikolakis, 2004) due to the enhancement of propane diffusivity in the presence of propylene (Y. H. Huang, Liapis, Xu, Crosser, & Johnson, 1995). ETS-10 membranes have shown good propylene permeability ($C_{3=}$ permeance = 7.9 x 10^{-8}, thickness = ~ 8 μm) and a separation factor of 5.5 however this value was diminished

by 19% over time due to hydrocarbon decomposition/carbonaceous residue formation caused by interaction with the highly basic sites located on ETS-10 surface (Tiscornia, Irusta, Téllez, Coronas, & Santamaría, 2008).

Strong molecular sieving of C_2 molecules in zeolite membranes has yet to be reported. C_2 molecules are smaller and closer in size as compared to C_3 molecules, zeolite molecular sieves haven't produced separation factors much beyond 3 for C_2H_4/C_2H_6 mixtures (Rungta et al., 2013). Metal-cation doped zeolites such as Ag-Zeolite A (Aguado et al., 2012) have shown excellent C_2H_4/C_2H_6 sorption selectivity through strong electrostatic interactions between the π-bond of C_2H_4 and the adsorbent surface, but selectivity is quickly diminished as atmospheric/saturation pressures are approached and are a manifestation of the capacity/selectivity trade-off often experienced by many adsorbent materials at higher pressures. C_2H_4/C_2H_6 permselectivities are predicted to be less than 5 in most cases (Rungta et al., 2013).

Similar to polymeric materials, depending upon the structure zeolites can present either hydrogen selective or hydrogen rejective behavior. Silicoaluminophosphate SAPO-34 which crystallizes in the CHA zeolite topology has been the most prominently cited hydrogen/hydrocarbon selective molecular sieving zeolite material. Nair and co-workers synthesized thin (~1 μm thick) SAPO-34 membranes and showed H_2/C_3H_8 binary selectivities ranging from ~7 at room temperature up to 27 at 650°C with a permeance increase from ~3 x 10^{-8} to 2.3 x 10^{-7} mol/m^{2}sPa over the temperature interval and showed good stability at high temperature (S.J. Kim et al., 2016). The membranes from the same study were evaluated as packed bed membrane reactors and presented propane conversions (65-75%) that were 10-15% greater than that of conventional packed bed reactors under

similar conditions (S.-J. Kim et al., 2016). SAPO-34 membranes have also shown promising H_2/CH_4 separation characteristics. Selectivties >20 have been achieved with hydrogen permeabilities greater than commercial polymeric membranes (M. Hong, Li, Falconer, & Noble, 2008).

LTA-type membranes also contain small pores but have typically have not shown sharp molecular sieving for gas phase separations. The high hydrophilicity, cation content and often reported hard to control intercrystalline defects have limited its use as a gas separation membrane (Aoki, Kusakabe, & Morooka, 1998; A. Huang, Liang, Steinbach, Gesing, & Caro, 2010) however neutral, cation-free LTA-type aluminophosphate membranes with low hydrophilicity fabricated by Caro and co-workers has shown long-term permeation stability and an H_2/C_3H_8 separation factor of 146 (A. Huang, Liang, et al., 2010).

MFI (silicalite) zeolite membranes were studied in extensive detail by Dong and Lin (J. Dong, Lin, & Liu, 2000) for hydrogen separation from refinery gas (85% H_2, balance C_1-C_4 molecules). In isobaric, temperature dependent experiments the membrane showed excellent hydrogen rejection at temperatures below 100°C due to competitive adsorption effects. At room temperature, no hydrogen or iso-butane permeance was detected; the efficient blocking of the zeolite pores inhibits non-adsorbing hydrogen flow and the shape selectivity of the MFI membrane hinders iso-butane flow. As temperature increased beyond 200°C the permeation selectivity became diffusion controlled due to low adsorption of all components and hydrogen flux reached one to two orders of magnitude greater than that of the hydrocarbons as temperature increased to 500°C. The work clarified that for hydrocarbons, the major driving force for flux is the concentration in zeolite pores,

while for non-adsorbing hydrogen, the fraction of free pores/H_2 partial pressure gradient across the membrane is the major driving force for flux. Furthermore the MFI zeolite membrane showed good thermal and permeation stability with no negative permeation, selectivity or structural effects after repeated heating to 500°C (J. Dong et al., 2000).

Zeolites are deemed as chemically and thermally stable materials due to strong O-Si-O bonds. The degree of stability depends on the silica to aluminum ratio. High silica content zeolites are considered the most stable and hydrophobic and less susceptible to water vapor effects. However, it been noted that at high temperatures after long periods, aluminum content from ceramic aluminum oxide supports can migrate from the support layer to the zeolite layer and decrease performance stability of even high silica content membranes. Lin and co-workers proposed usage of a thermally stable yttria stabilized zirconia interlayer between the support and the membrane layer to avoid aluminum migration and demonstrated stable separation performance with a simulated syngas feed containing 500 ppm H_2S at 500°C (Wang & Lin, 2012).

1.3.3.3 Carbon Molecular Sieves

Carbon Molecular Sieves (CMS) are a formidable contender amongst membrane materials for C_2 and C_3 paraffin/olefin separations. CMS membranes are formed from temperature programmed pyrolysis of polymer precursors. Through careful polymer selection, tuning of pyrolysis temperature programming and pyrolysis O_2 partial pressure, the CMS pore structure and thus permeability/selectivity can be modulated (Kiyono, Williams, & Koros, 2010; R. Singh & Koros, 2013). CMS membranes contain a bimodal pore distribution, a majority of the structure containing ultramicropores $\leq$ 0.6 nm and the

remainder of pores ranging between 0.6-2 nm. CMS are visualized as condensed sp^2 hybridized, hexagonal graphite-like sheets with slit-like pores formed from ordering imperfections. CMS 1-D slit-shaped pores offer an advantage over highly ordered 3-D pore structures of crystalline materials though size/shape exclusion; the CMS pore can discriminate between the planar ethylene molecule versus the bulkier ethane configuration which is a difficult task.

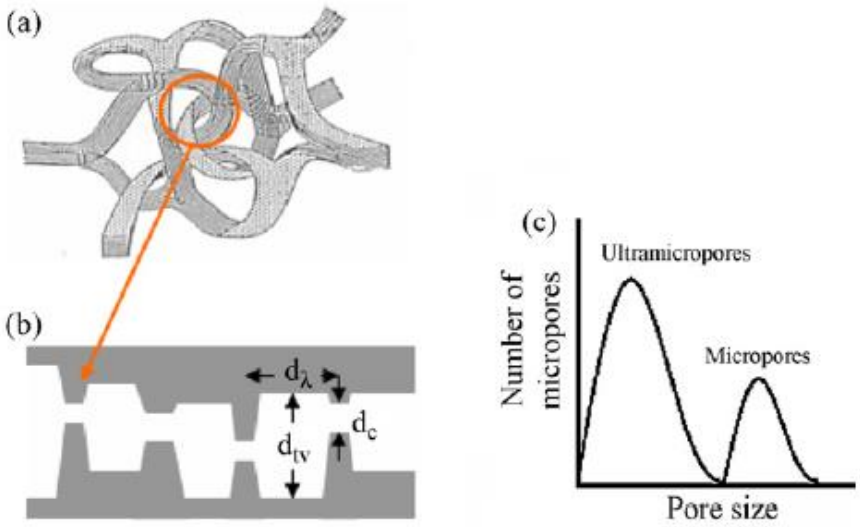

Figure 1.13 Carbon molecular sieve sheets (a), pore structure (b) and bimodal pore size distribution (c) (Kiyono et al., 2010)

CMS membranes formed from Matrimid and high performance polyimides have overcome both the C_3 and C_2 the upper bound. Suda and Haraya formed a pyrolized Kapton polyamide CMS membrane after pyrolysis at 1000°C under vacuum, then activated the membrane in water vapor for pore volume enlargement from < 4.0 Å to 80% of pores with size < 4 Å and 20% between 4.0-4.3 Å (Suda & Haraya, 1997). The resulting membrane

displayed pure gas ideal C_2 and C_3 selectivities of 6 and 20 respectively and permeabilities for both olefins around 10 Barrer.

Steel and Koros investigated the effects of various polymer precursors and pyrolysis conditions on the gas separation properties of flat CMS membranes using 6FDA and Matrimid polymer precursors (Steel & Koros, 2005). The 6FDA/BPDA-DAM derived CMS membrane presented the best performance when pyrolized at 550°C for 2 hours showed a C_3 selectivity of 100 with a propylene permeability around 200 Barrers, while the best performing Matrimid derived CMS membrane exhibited slightly lower performance; propylene permeability 20 Barrer and C_3 selectivity ~40. Their findings showed that lower temperature pyrolysis conditions < 550°C enabled an open pore structure and avoided closure of main selective ultramicropores to maintain high selectivity and permeability. Ma et al. (Ma, Lin, Wei, & Kniep, 2016) formed extremely thin (520 nm) CMS membranes derived from a proprietary 6FDA-based polyamide by coating the polymeric layer on gamma alumina supported by a mechanically stable alpha alumina support. Their membrane showed low C_3 permeability (10 Barrer) but achieved competitively high permeance (1×10^{-8} mol/m^{2}sPa) and separation factor (31) due to the high integrity thin membrane layer.

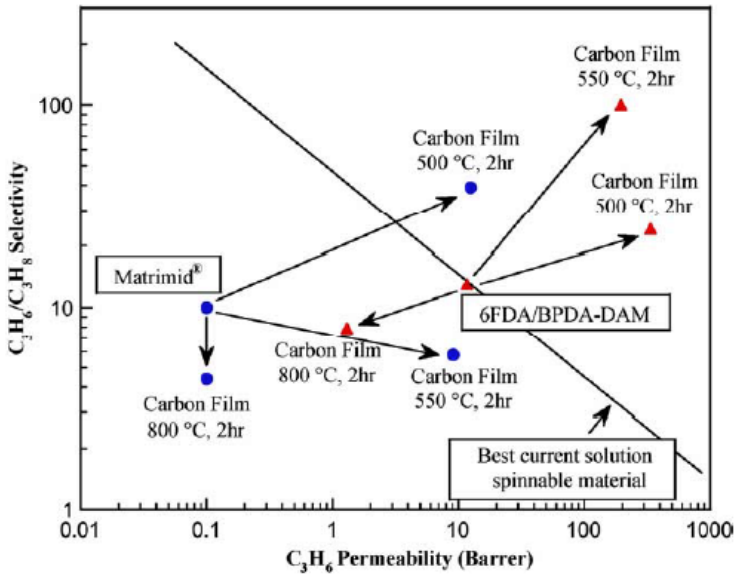

Figure 1.14 C_3H_6/C_3H_8 selectivity and propylene permeability in relation to polymer precursor type and pyrolysis time/temperature (Steel & Koros, 2005)

For C_2 separations, Matrimid derived CMS membranes have been the most studied in literature. Koros and co-workers have demonstrated C_2 selectivities up to 12, however the membranes produce low ethylene permeabilities (15-20 Barrer) which is attributable to the collapse of the dense Matrimid substructure (L. Xu, Rungta, & Koros, 2011). CMS membranes based on intrinsically microporous polymers such as carbonized PIM-1 have reached ethylene/ethane ideal selectivities of 17.5 at a C_2 olefin permeability of 10 Barrer and a selectivity of ~6.5 at 70 Barrer (Salinas, Ma, Litwiller, & Pinnau, 2016). Higher permeabilities at selectivities comparable to Matrimid were attributed to the higher free volume PIM-6FDA-OH polymer which did not fully collapse during pyrolysis.

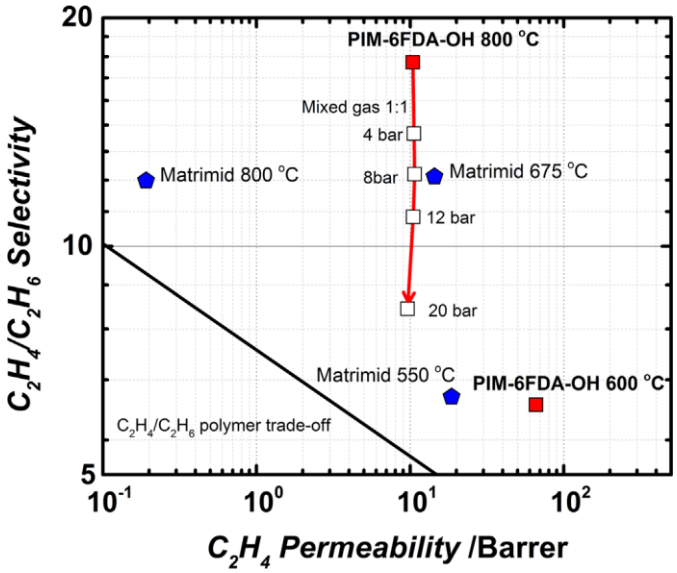

Figure 1.15 Plot of ethylene/ethane selectivity as a function of ethylene permeability for highest performing carbon molecular sieves with polymer membrane Robeson upper bound depicted (Salinas et al., 2016)

In terms of stability, CMS have been cites as thermally stable up to ~500°C in most gasses but < 200°C in O_2. A major concern associated with carbon molecular sieves is physical aging as a result of the presence of highly reactive sites within the ultramicropores. Oxygen chemisorption and physical adsorption of organics and water can occur at structural microvoids causing a decrease in long-term membrane performance (L. Xu et al., 2014). Membranes must often times must be aged for long periods (5-12 months) (L. Xu et al., 2014), consistently activated (Jones & Koros, 1994) or undergo pyrolysis in low partial pressure O_2 to stabilize reactive sites during synthesis (Kiyono et al., 2010) in order to observe consistent results.

1.3.3.4 Metal Organic Frameworks

Metal-organic frameworks are a set of highly studied hybrid materials containing micropores with high surface area that have been studied for light olefin/paraffin

separations. Metal-organic frameworks consist of metal cations (Al, Cu, Co, Mg, Mn, Zn) (non-exhaustive), coordinated to the oxygen a vast array of organic ligands including benzene tri or di carboxylates and imidazoles in a large number of coordination geometries. Due to the diversity of metal/organic chemistries and coordination, an unprecedented number of MOFs of varying pore shapes for molecular exclusion and pore functionality for selective adsorption affinity been created and have yet to be synthesized.

As in zeolites, a majority of the light hydrocarbon separation MOF studies have focused on adsorptive separations in crystals. Early investigations of light olefin/paraffin in MOFs were conducted with $Cu_3(BTC)_2$ which showed sorptive selectivity for olefins enabled by cation-π interactions between the π electrons of ethylene/propylene and the open metal Cu sites of the MOF (Wang et al., 2002). Further studies showed limited C_2 and C_3 olefin selectivities (~2) in $Cu_2(BTC)_3$ (Wang et al., 2002; Plaza et al., 2012), but sparked further studies in MOFs with open metal sites for olefin/paraffin separations. The heavily cited M_2(dobdc), (M = metal, $dobdc^{4-}$ = 2,5-dioxido-1,4-benzenedicarboxylate) or MOF-74 which gives C_2 and C_3 sorptive selectivities between 4-18 at low loadings (~1 atm), with the highest selectivity presented in the Fe-based isostructure (Fe-MOF-74) (Bloch et al., 2012).

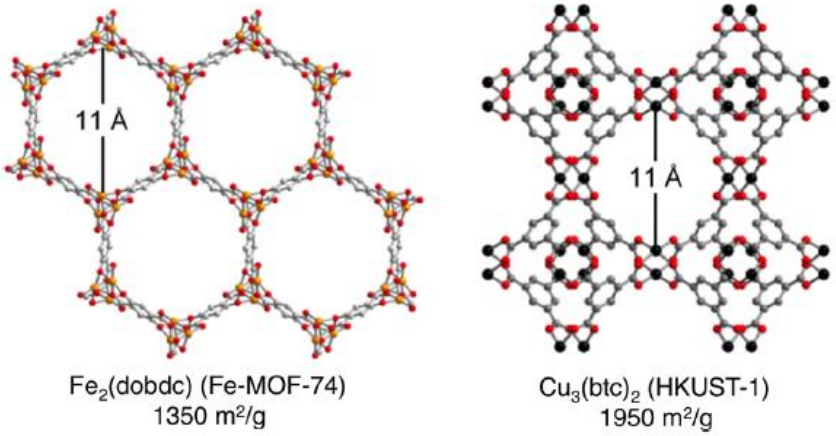

Figure 1.16 Crystallographic Structures of Mg-MOF-74 and $Cu_3(BTC)_2$ (Herm, Bloch, & Long, 2014)

At higher feed pressures (> 1 atm) olefin sorption selectivity in MOF-74 diminishes due to the capacity/selectivity trade-off. While the high adsorption selectivity may be advantageous for a possible for low olefin partial pressure feeds, however the capacity/selectivity trade-off in addition to low diffusive selectivity hinders further development of MOF crystallites into polycrystalline membranes because significant feed pressures are needed to drive membrane separation processes, therefore binary permeation selectivties are expected to be less than 5 in most applicable process conditions (Rungta et al., 2013).

The rationally designed NbOFFIVE-1-Ni or KAUST-7 may offer an exception as a MOF with a potential for future membrane development (Cadiau et al., 2016). KAUST-7 features Ni(II) square grid layers with $NbOF_5^{2-}$ pillars connecting pyrazine ligands. The Nb cation was specifically selected to impede rotation of the pyrazine ligand and create a small 3.05Å aperture that facilitates excellent molecular sieving of propylene and propane mixtures. Propane sorption was negligible up to 1.2 bar while propylene showed

considerable uptake which is indicative of strong molecular sieving. Further work with uptake kinetics will further prove the feasibility of KAUST-7 as a potential membrane material for C_3 olefin/paraffin separations.

A. B.

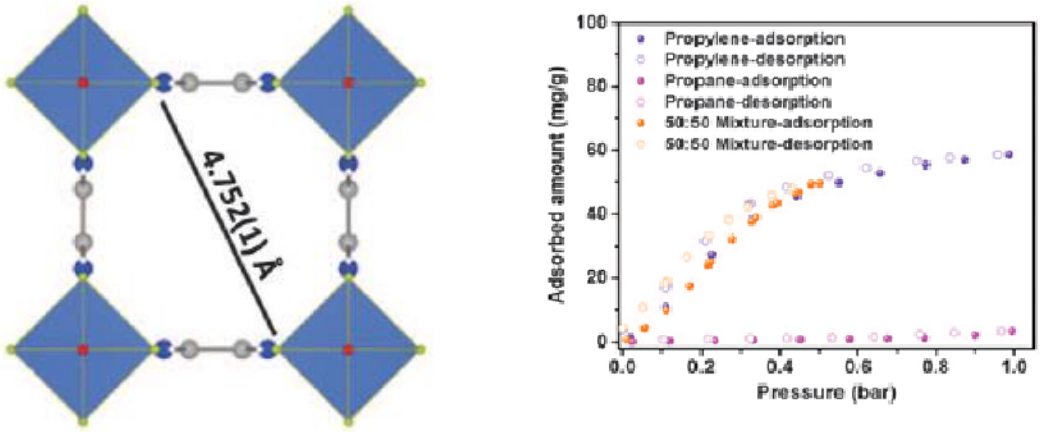

Figure 1.17 Crystallographic structure of NbOFFive-1-Ni (A) and pure/equimolar C_3H_6 and C_3H_8 adsorption isotherms 298 K (B) (Cadiau et al., 2016)

Zeolitic Imidazolate Frameworks (ZIFs) are a relatively new subclass of metal-organic frameworks which contain zeolitic topologies in which the Si-O-Si bond is replaced with a M-Im-M bond (M = metal, Im = Imidazole) just slightly perturbed from 145°. Like traditional MOFs, the basic building unit of a ZIF consists of a metal cation coordinated to an organic linker but instead of metal-oxygen bonds, the metal is coordinated to 4 nitrogen atoms from 4 different imidazole ligands. Each ligand coordinates two metal centers. The functionality of the imidazole linker and the coordination enables tuning of the ZIF structure for a specific steric or adsorptive based separation. ZIF-8 membranes surpass the polymer upper bound and outperform most carbon membranes in the areas of $C_{3=}$ permeability and $C_{3=}/C_{3-}$ selectivity through

molecular sieving (Pan, Li, Lestari, & Lai, 2012). Table 1.4 shows the light hydrocarbon selectivities in ZIF-8:

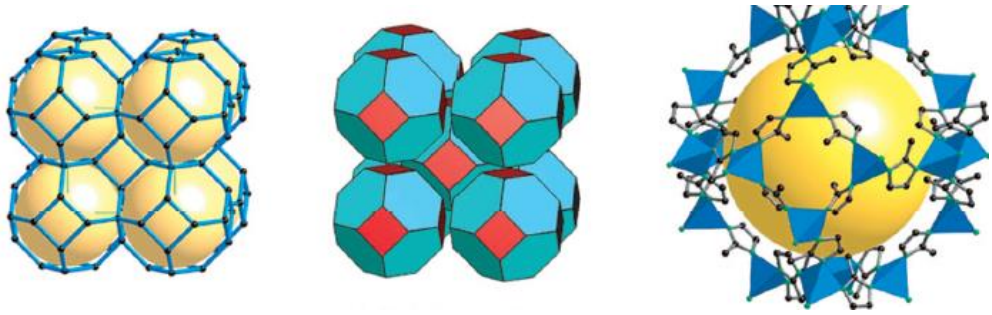

Figure 1.18 Illustrative graphic of Zeolitic Imidazolate Framework-8 (ZIF-8): sodalite cage (left & center) and cage showing Zn-imidazole coordination bonding (right) (Park et al., 2006)

Table 1.4 Light Hydrocarbon Separation Characteristics of ZIF-8 Membranes Reported in Literature

Light Hydrocarbon Mixture	Light Gas Permeance (mol/m^{2}sPa)	Binary Separation Factor
$H_2/C_{3=}$	3.0-3.8- x 10^{-7} mol/m^{2}sPa	23
H_2/C_{3-}	3.0-4.4- x 10^{-7} mol/m^{2}sPa	545-2700
$C_{2=}/C_{2-}$	1.8-14 x 10^{-8} mol/m^{2}sPa	2.1-2.8
$C_{3=}/C_{3-}$	0.1-3 x 10^{-8} mol/m^{2}sPa	20-180

In terms of C_3 separation, the lowest propylene permeability represented in Table 1.4 is 98 Barrer confirming separation and permeability performance which exceeds reported CMS membranes.

The exceptional C_3 performance is due to the sodalite (SOD) topology of ZIF-8 along with bonding coordination and crystal dimensions that enable a structure with a 6-member ring sieving-active pore aperture of 3.4 Å and a pore cage size of 11.6 Å. Framework flexibility and the swinging motion of the 2-methylimidazole (2-MIm) ligands enables an effective pore aperture of 4.2 Å (C. Zhang et al., 2012). The ZIF-8 effective

pore aperture diameter is just a perturbation larger or statistically identical to the van der Waals diameter of propane (4.16 Å) and larger than propylene (4.03 Å) and hydrogen (2.76 Å) which facilitates exceptional molecular sieving of C_3 substituents and hydrogen while maintaining industrially attractive light gas permeability. ZIF-67 is an isostructural Co analogue to ZIF-8 and also shows promise for C_3 sieving. The shorter/stronger Co-N bond limits liker motion to attain propylene/propane selectivties of 200 while still maintaining permeances comparable to those shown in Table 1.4.

Results of C_2 separations are also shown for ZIF-8 in Table 1.4. There has yet to be a ZIF membrane realized or precisely tuned for exceptional C_2 paraffin exclusion that compares to CMS membranes in terms of separation factor. The similar sizes of ethylene (3.59 Å) and ethylene (3.72 Å) which are both smaller than the effective ZIF-8 pore aperture limit binary selectivities to just below 3. Smaller pore ZIFs such as ZIF-7 (3.0 Å) which contains a larger benzimidazole ligand has been studied for adsorptive separation of alkanes from alkenes but there are no studies specifically focused on the diffusive behavior of C_2 molecules in ZIF-7.

The stability of traditional MOFs is often of concern. Open metal site MOFs experience instability in the presence of water vapor and other nucleophiles, water molecules coordinate at the unsaturated metal sites and are susceptible to protonation/bond breaking through hydrolysis reactions (DeCoste et al., 2013). Although hydrocarbon feeds are dehydrated prior to downstream separation, long term stability even with small magnitudes of water impurity should be studied.

ZIFs are regarded as the most stable in the MOF family materials. ZIF particles have shown resilience in the presence of boiling water and organic solvents in addition to

thermal stability up to 550°C in dynamic TGA experiments (Park et al., 2006). The exceptional chemical and thermal stability of ZIFs is linked to strong metal-nitrogen bonds and hydrophobic pores. Researchers have reported stable separation for both on-stream and off-stream propylene/propane experiments for durations longer than 1 month. The exceptional H_2/C_3 selectivities in ZIF-8 and perceived thermal stability may present a new application for ZIFs as membrane reactors for propane dehydrogenation. However little is known about the static thermal stability of zeolitic imidazolate frameworks and thus should be studied in detail.

1.3.4 Concluding Remarks on Membrane Materials, Transport and Stability for Light Hydrocarbon Separations

As previously discussed, the permeability and selectivity and stability of a membrane material are immensely important for its consideration as a viable replacement or debottlenecking step for light hydrocarbon separation. Productivity and efficiency are governed by the intrinsic properties of the material and the transport properties which facilitate separation of the permeating mixture. Without exceptional stability, the separation properties of a membrane cannot be maintained for long periods. Although not discussed in high detail, the cost/processability of a membrane is of immense importance for further industrial consideration.

In the above review, a number of membranes were discussed for light hydrocarbon separations, however most do not currently present all four requisites: productivity, selectivity, stability and processability/cost that are necessary for large-scale implementation. Polymeric membranes are attractive and currently utilized in industry due

to low cost, ease of fabrication and decent separation performance for hydrogen separations. However these membranes often show instability in the presence of C_3 hydrocarbons and are subject to the upper-bound tradeoff in olefin/paraffin separations.

Dense metallic and facilitated transport membranes offer a distinct opportunity to produce ultrapure hydrogen from hydrogen/hydrocarbon or olefins from olefin/paraffin mixtures respectively. However, propylene deterioration in the presence of metallic membranes and instability of facilitators dampen the prospects of using these membranes for light hydrocarbon separations. Additionally, the cost of such membranes may not be attractive for industrial implementation for the specific application.

The microporous membranes discussed offer an interesting characteristic of tuneability to select or design a membrane material which can fit a specific light hydrocarbon separation application. Zeolites show exceptional stability and have potential for sieving hydrogen/hydrocarbon mixtures at high temperatures and low temperatures for basic separations or membrane reactor configurations. Zeolites do not however show as strong of potential for sieving olefin/paraffin mixtures as CMS and MOF/ZIF membranes. CMS membranes set themselves apart from the other microporous materials in that they can be easily produced from polymeric hollow fibers and directly implemented into easily manufacturable modules. Zeolites and MOFs must be grown on supports and often the reproducibility of high-quality thin films is of concern. CMS membranes also offer an advantage thus far for C_2 separations due to their 1-D slit pore geometry. Ageing and brittleness of CMS membranes are of concern for future implementation.

Zeolitic imidazolate frameworks, specifically ZIF-8, has proven the ability to sieve hydrogen and C_3 mixtures and outperforms most other microporous materials in terms of

productivity and selectivity. The reported chemical and thermal stability of ZIFs material make them a promising prospect for further study. Exceptional thermal properties could present an opportunity for high temperature membrane reactor applications. Furthermore, the countless number of linkers, cations and coordination geometries that can be realized for ZIFs broaden the possibility of rationally designing new ZIF structures which can sieve other light hydrocarbon mixtures such as C_2 molecules.

1.4 Zeolitic Imidazolate Frameworks (ZIFs) for Light Hydrocarbon Separations

1.4.1 ZIF Chemistry: Bonding and Crystal Formation

Zeolitic imidazolate frameworks are an emerging class of metal-organic frameworks (MOFs) that embrace both the hybrid metal-organic nature of MOFs and the topologies zeolites. Since their inception over a decade ago, discovery of their exceptional chemical/thermal stability in addition to their permanent, high porosity/surface area and the ability to tune the framework both electronically and sterically for a specific separation has generated an abundance of studies on ZIF materials. ZIFs and zeolites diverge largely due to organic nature of the ZIF framework. ZIFs show interesting framework flexibility (rotational displacement of the imidazole ligand), framework tuneability through facile de novo syntheses or post synthetic modification. The wide array of imidazole functionalities at specific positions of imidazole linker and the ability to mix linkers provides routes not only to tune the electronic/chemical properties of the ZIF, but also the type of zeolitic topology (Pimentel et al., 2014). The first step to taking advantage of the of the highly customizable ZIF framework for the study and enhancement of light hydrocarbon

separation applications is to gain a better understanding of the basic processes which form the fundamental building units.

In comparing zeolites to ZIFs, Yaghi and co-workers described the structural building unit of a zeolite as a four coordinated net of metal vertices in which tetrahedrally coordinated metals (Si, Al, P) are covalently bonded to -O- links whereas ZIFs are composed of metals (Zn or Co) tetrahedrally coordinated to the nitrogen of an imidazole ligand which is an unsaturated, 5 member ring containing two nonequivalent amides (Tranchemontagne, Mendoza-Cortés, O'Keeffe, & Yaghi, 2009). As previously described, the zeolitic topologies of ZIFs are derived from M-Im-M bond angles that are similar to that of zeolite Si-O-Si as shown in Figure 1.19:

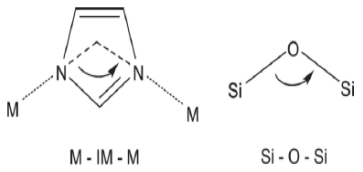

Figure 1.19 Comparison of M-Im-M and Si-O-Si bond angle in ZIFs and zeolites respectively (Park et al., 2006)

The bonding in ZIFs is slightly different than that for the covalently bonded zeolite. In a normal covalent bond each atom contributes one electron and shares the pair between the two nuclei. In ZIFs the coordination bond is such that the nitrogen solely contributes electrons to a metal cation when mixed in solution. As shown in Figure 1.19, the formal bond valence between zinc and nitrogen is 1/2 thus the tetrahedrally coordinated zinc effectively shares ½ an electron with 4 nitrogen atoms from four different imidazole ligand and this sum (2) corresponds to the oxidation number of zinc (+2). The normal covalent

zeolite bonds are stronger than the coordination bonds of ZIFs, however the non-zero valence of the Zn-N tetrahedral coordination bonds enable strong bond energy (~360 kJ/mol) similar to that of a C-C bond (Tranchemontagne et al., 2009). The Lewis basicities of imidazole ligands are typically higher than that of benzene carboxylate molecules of MOFs and leads to stronger metal-organic bonds and greater chemical/thermal stability for ZIFs (Karagiaridi, Bury, Mondloch, Hupp, & Farha, 2014).

The formation of M-N bonds in ZIFs are facilitated through the deprotonation of imidazole ligands which form bidentate coordination with solvated metal nodes to yield structural building units. Continuous coordination of the building units enables the formation of 3-dimensional supermolecular structure. Below, we specifically outline the most robust procedure of ZIF-8 crystal formation in methanol as it is the most the most studied and gives insight into the general processes that occur during the formation of all ZIFs.

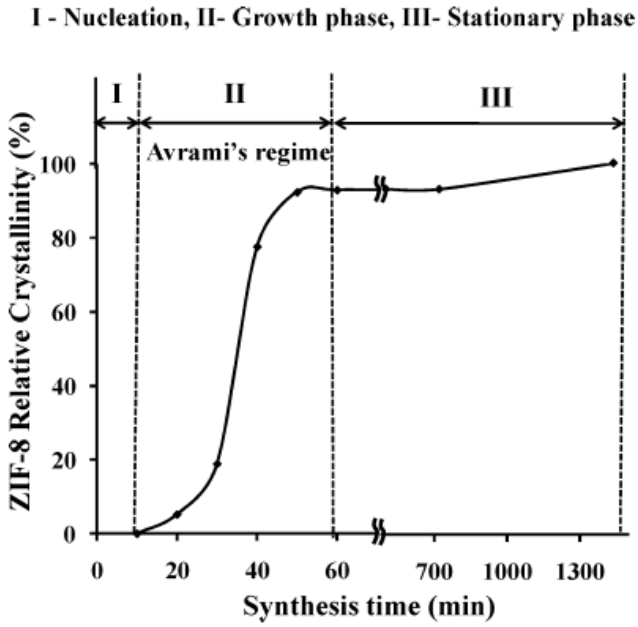

Figure 1.20 Kinetics of transformation of ZIF-8 as a function of time (Venna, Jasinski, & Carreon, 2010)

Table 1.5 ZIF-8 Formation Solution pH and Crystal Size as a Function of Growth Time Adapted from Reference X

Reaction Time	pH	Crystal Size
0	7.8	Nuclei Formation
10 min	7.5	50
1 hr	7.2	230 ± 20
12 hrs	7.2	500 ± 40
24 hrs	7.2	500

The structural evolution of ZIFs (specifically ZIF-8) was deconvoluted in the work of Venna et al. using time-resolved XRD and pH analyses during ZIF-8 crystal formation in methanol (Venna et al., 2010). Figure 1.20 shows ZIF-8 crystallinity and Table 1.5 shows the ZIF-8 solution pH and crystal size as a function of time from their experiments. In a typical ZIF synthesis imidazole and a zinc salt are separately dissolved in an organic solvent. At equilibrium, in a protic solvent the imidazole, 2-methylimidazole exists in its neutral (HMIm) and protonated H_2MIm^+ forms (Cravillon, Münzer, Lohmeier, Feldhoff, & Huber, 2009).

As shown in Table 1.5 and Figure 1.20, it can be deduced that the initial stage of ZIF formation (< 10 minutes) is dominated by nuclei evolution which corresponds to the initial deprotonation of HMim ligands caused by the driving force for crystallization (pH decrease between 0-10 mins) enabling coordination with zinc to form primary ZIF-8 building units. At the onset of stage 2 (10 mins), crystal growth begins as evidenced by formation of 50 nm ZIF-8 particles evolved from the solution. Crystallinity measurement is not possible due to a low yield of metastable crystals.

Further reaction time (10 min – 1 hour) presents significant crystallinity/crystal size increases and corresponds to further deprotonation of imidazole ligands (pH decrease) and coordination to form larger likely more stable crystals. The sigmoidal increase in crystallinity/crystal size corresponds to Avrami's classical model for crystal growth and is further correlated to the Ostwald ripening effect where smaller higher energy crystals dissolve/re-precipitate onto larger crystals.

Beyond 1 hour of growth signifies stage 3; the stationary phase, upon which crystallinity, crystal size and pH stabilize. As more HMIm deprotonate, the driving force for further linker deprotonation decreases causing a stabilization in the solution pH. The neutral imidazole ligands can then form monodentate coordination at positively charged portions of ZIF crystals and terminate growth (Cravillon et al., 2009) while the imidazole solution comes into new equilibrium with stable ZIF-8 crystals formed. The detailed process above is specifically relevant for the case of ZIF-8 crystal formation in methanol solution but is broadly relevant to the formation of most ZIFs which undergo nucleation, growth, Ostwald ripening and stabilization processes upon formation.

A deeper understanding of ZIF bonding, formation processes and methods to alter nucleation and growth provide a basic background to further understand topology control. Topology control allows for effective tuning of the overall physical properties of the framework such as pore/pore aperture size, pore aperture shape, surface area and volume which each have an effect on the transport and separation of molecules throughout the framework. The effects of ligand substitution and solvent on topological control are detailed below.

1.4.2 Topology Control

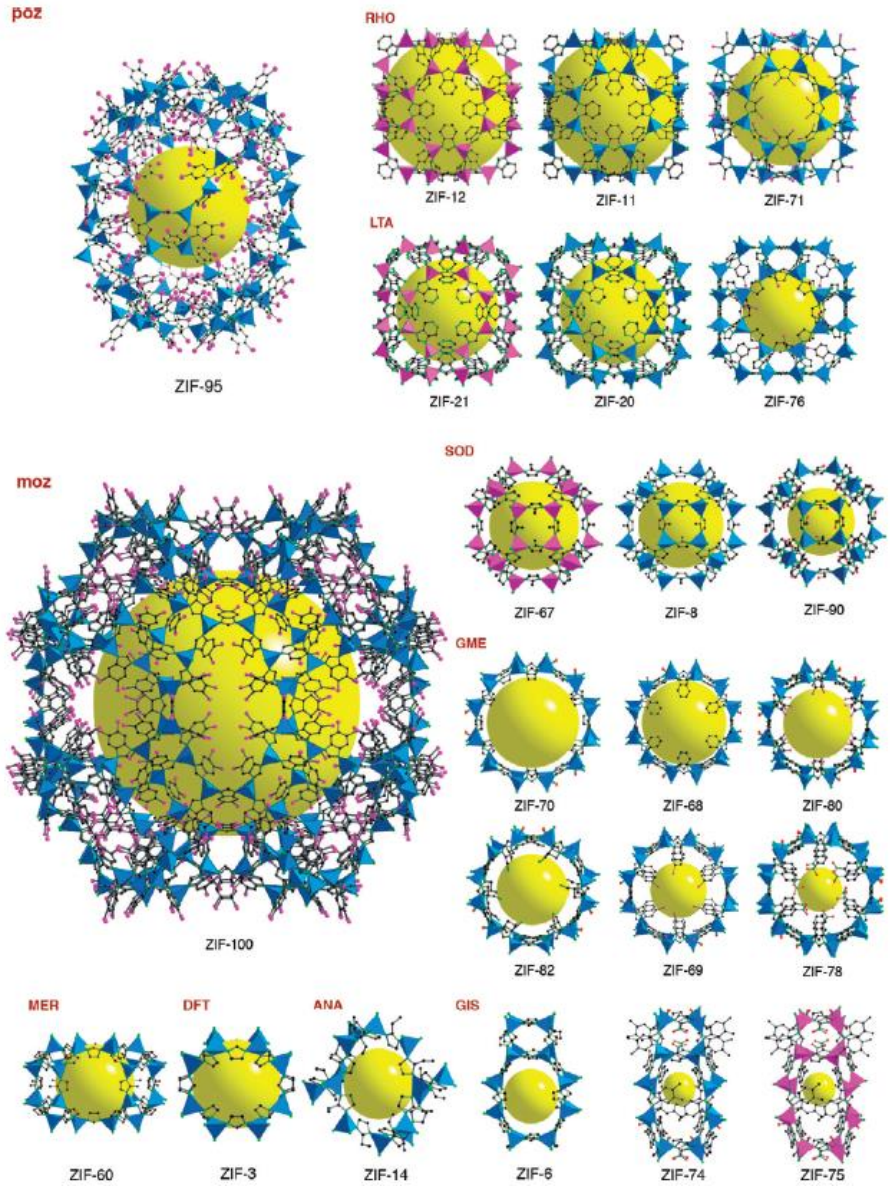

Figure 1.21 ZIF crystal structures organized by topology. Reproduced with permission (Phan et al., 2010). Copyright American Chemical Society 2010.

The steric and chemical functionality of the imidazole ligand play a crucial role in the coordination and substitution equilibria which direct ZIF crystallization. Imidazole ligands present functionality at the 2, 4 and 5 positions of the 5-member ring, without

ligand functionalization, dense and/or low symmetry structures are formed (Park et al., 2006; Tian et al., 2007). Under similar reaction conditions, substitution at the 2 position with a methyl (electron donating) or carboxaldehyde (electron withdrawing) enables the SOD topology with a apertures of ~ 3.3 Å (Huang, Lin, Zhang, & Chen, 2006) and 5.0 Å (Eum et al., 2015) respectively while substitution at the same position with an ethyl group (electron donating) formed the ANA topology and a smaller aperture size (~2.2 Å) due to the bulkier ligand at the pore aperture window (X. C. Huang et al., 2006). In this specific case of substitution at the 2 position, steric effects likely lead to the differences in topologies rather than the chemical composition of the substituent.

The effect of ligand substitution in single linker ZIFs was further demonstrated in the work of Yaghi et al (Hayashi, O E, Furukawa, & Yaghi, 2007) who showed using similar synthesis conditions that benzimidazole could form the SOD structure ZIF-7, however N substitution on the benzene substituent (purinate/5-azabenzimidazole) at the 5 position was necessary for crystallization of LTA type zeolitic imidazolate frameworks. In their work it was postulated that electrostatic and dipole-dipole interactions between CH-N···N-CH of two adjacent imidazole ligands, (N is at position 5 and C is at position 6) show significant interactions that produce the LTA topology.

The complexity of ligand substitution and number of realizable topologies was exponentially expanded when 2-linker ZIFs were introduced. ZIFs with the GME topology were obtained by mixing functionalized imidazole and benzimidazole linkers (Banerjee et al., 2009b). It was also determined that ZIFs could present a single topology in both a single linker and 2 linker system. For example, a ZIF material was crystallized into the RHO structure by mixing 2-methylimidazole and 2-ethylimidazole in DMF (X. C. Huang et al.,

2006) whereas, single linker (benzimidazole) ZIF-11 formed in N, N diethylformamide contains the same topology.

In addition to ligand substitution, solvents play crucial roles as both a structural template for overall pore formation and can alter ligand-ligand interactions during the crystallization process to form different topologies. The effects of solvent as a template for pore formation in ZIFs formation is well exhibited in the case of ZIF-11 and ZIF-7 which both contain benzimidazole as a single linker. ZIF-7 is formed in DMF and crystallizes into the SOD structure while ZIF-11 is synthesized in the larger DEF and crystallized into the more open RHO structure. A similar example is exhibited for ZIF-7/ZIF-9 (SOD) and ZIF-11/ZIF-12 (RHO) using methanol as the main solvent. When solely ethanol is utilized the SOD structures are formed, however addition of toluene alters ligand-ligand interactions and spacing by forming π-π T-stacking of toluene with the benzene substituent of the imidazole ligand to once again produce the higher pore volume RHO topology (He et al., 2013).

An underlying set of guidelines to specifically design or obtain specific topology has not yet been fully elucidated. As further knowledge is developed using high through-put methods to obtain more ZIFs and correlate imidazole chemical and structural functionalization to the intricate interplay of solvent selection as well as time/temperature effects, guiding principles will be developed to precisely control ZIF topology.

1.4.3 Composition Control

Composition control of imidazolate frameworks is the practice of modulating the chemical composition of identical frameworks within a fixed topological group.

Composition control is exercised by alternating the ligand and/or cation of physically similar or isoreticular frameworks. This method has been performed to tune the chemical and physical properties of ZIF structures for enhanced attributes to fit specific applications (Kaneti et al., 2017). Composition control can be achieved through multiple routes in ZIFs which is another property which makes them attractive candidates for gas separations.

1.4.3.1 Mixed Linker and Hybrid ZIFs

The advent of mixed linker/hybrid ZIFs opens a plethora of additional degrees of freedom in rational design that may be advantageous for light olefin/paraffin separations in ZIFs. Mixed linker ZIFs are prototypical ZIF structural materials often cited in literature such as ZIF-68 (nitroimidazole/benzimidazole) or ZIF-69 (nitroimidazole/chlorobenzimidazole) (Hou & Li, 2010) among others. The synthesis of ZIFs containing multiple linkers can enable increased functionality and tunablility over single linker ZIF materials.

A representative example of mixed linker synthesis with composition control was performed in the work of Yaghi and co-workers (Banerjee et al., 2009a). Isostructural mixed linker ZIFs with GME topology were prepared by mixing equimolar amounts of nitroimidazole and a second linker (imidazole or benzimidazole) to vary pore diameter (7.1-15.9 Å) and functionality was introduced to each linker type to vary polarity across the pore sizes. Their study determined that pore polarity rather than pore size presented the largest effect on CO_2 uptake in the set of isoreticular ZIFs studied. Mixed linker materials are known to form specific porous structures over a specific imidazole linker concentration range. Outside of this concentration range, the structure will crystallize into unwanted

topologies or non-porous structures (Pimentel et al., 2014) and thus considerable time and effort are necessary to tune the synthesis parameters for enhanced structure-property relationships as compared to single linker ZIFs.

Hybrid ZIFs can be crystallized into a porous structure that includes two different linkers and present linker mixtures over a wider range of relative concentrations. The properties of the hybrid ZIFs (adsorption, sieving properties etc.) are usually concomitant with the relative linker concentration. The first reported hybrid ZIFs were ZIF-8-90 and ZIF-7-8 crystals synthesized de novo by Thompson et al. (J. A. Thompson et al., 2012). The size similarity between 2-methylimidazole (2-MIm) (ZIF-8 linker) and 2-imidazolecarboxaldehyde (Imca) (ZIF-90 linker) allowed synthesis across the large range of compositions without crystal structure alteration. For ZIF-8-90, as the fraction of hydrophilic carbonyl groups from the Imca linkers was increased in the de novo synthesis procedure, the pore aperture size increased from 3.4 Å (pure ZIF-8) to 5.0 Å (pure ZIF-90) and correspondingly, the hybrid crystals' hydrophilicity increased as observed from water vapor uptake measurements performed by Eum et al. (Figure 1.22) (Eum et al., 2015).

A. B.

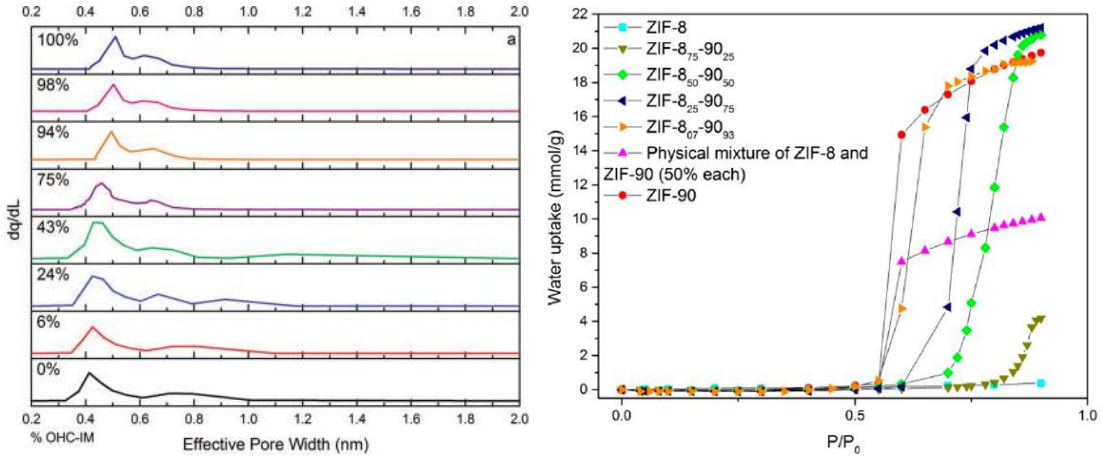

Figure 1.22 Pore size distributions of ZIF-8-90 hybrids (A) (J. A. Thompson et al., 2012) and water adsorption isotherms in ZIF-8-90 hybrid crystals 308 K (B) (Eum et al., 2015).

Upon incremental incorporation of BzIm into the ZIF-7-8 hybrid framework, the pore size distribution became bimodal and presented a smaller pore size (0.32 nm) closer to that of ZIF-7 (3.0 Å) (Figure 1.23) (Thompson et al., 2012). However, after reaching a 35 mol% composition of BzIm in the hybrid framework (ZIF-7_{35}-8_{65}), steric hindrance of the bulkier benzimidazole (BzIm ZIF-7 linker) caused crystal structure change which was evident from XRD spectra. The structural change was a result of transition from the ZIF-8 cubic I43 space group to the ZIF-7 R3 rhombohedral space group.

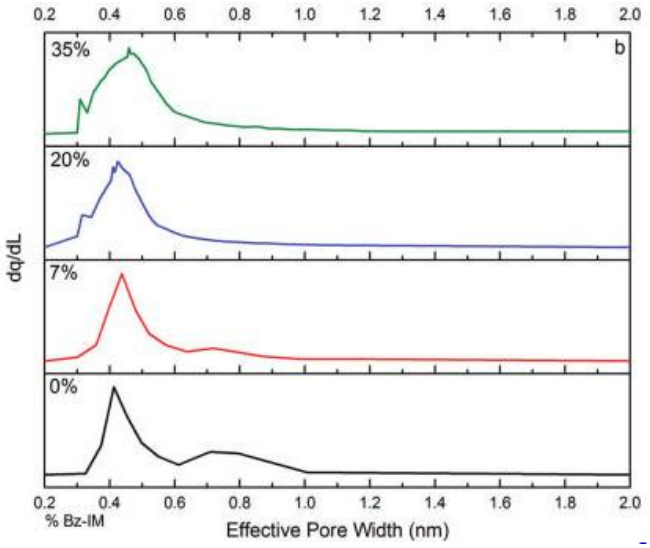

Figure 1.23 Pore size distributions of ZIF-7-8 hybrids (J. A. Thompson et al., 2012)

The works by Thompson (J. A. Thompson et al., 2012) and Eum proved (Eum et al., 2015) that both the chemical and steric properties of hybrid ZIFs can be effectively tuned over a comparatively wide range of linker concentrations.

Hybrid ZIF synthesis may present an effective solution for enhancement of light hydrocarbon separations. A ZIF membrane incorporating both ZIF-8 and ZIF-7 functionality could potentially enhance light hydrocarbon separations. ZIF-7 contains the bulkier aromatic benzene ring connected to the imidazole substituent thus producing a smaller (3Å) aperture. Thin (2μm thickness) ZIF-7 membranes have been synthesized, but have low hydrogen permeance of ($4.5x10^{-8}$ mol/m^2sPa) (Y. Li, Liang, Bux, Yang, & Caro, 2010) indicative of low intrinsic permeability, and it can be assumed that ethylene permeability in a pure ZIF-7 membrane would be far too low for industrial use. However, ZIF-7 membranes have demonstrated enhanced H_2 sieving ability over ZIF-8 (Y. Li et al., 2010) and could potentially enhance C_2 and C_3 olefin paraffin separation. A hybrid

membrane incorporating a finely tuned composition of both ZIF-7 and ZIF-8 functionality could possibly exhibit increases in light hydrocarbon separation factors while maintaining attractive hydrogen/olefin permeability.

A slight challenge associated with hybrid ZIFs is quantitative control. Although linker ratios within the framework can be varied over a wide range of compositions, synthesis of specific compositions is difficult because linker solubility differences and metal site competition is a factor. Quantitative compositional control is feasible after experimental trials in free crystals, but would become extremely difficult in membrane fabrication.

Although ZIF membranes are usually synthesized through well established in-situ, counter-diffusion, or seeded secondary growth methods, the synthesis of new hybrid polycrystalline membranes would two eminent challenges: (1) many of the hybrid MOFs (ZIFs) have only been obtained on the scale of a few crystals. Synthesis of a large quantity is often difficult or costly and thus limits the amount of information necessary to decide whether further fabrication into a polycrystalline membrane is advantageous. (2) Conversion of new MOF materials to membrane thin films requires cumbersome trial-and-error fine tuning of synthesis parameters which may or may not yield success. For this reason, of the thousands of MOFs synthesized, only twenty to thirty thin film membranes have been prepared. While formulating hybrid ZIF membranes through de novo synthesis would enable unparalleled diffusion and adsorbent-adsorbate control for separation purposes, the fabrication process would become even more arduous.

1.4.3.2 Solvent Assisted Ligand Exchange

Further development of new single linker, mixed linker/hybrid ZIFs into polycrystalline membranes is needed and necessary, however there already exists large number of prototypical ZIFs (ZIF-7, ZIF-8, ZIF-67, ZIF-68, ZIF-69) that have well established crystal and membrane syntheses protocols that contain attractive but imperfect physical and chemical properties which poise them for small to moderate composition changes to enhance their separation performance.

A facile route for modifying prototypical ZIF crystals to obtain mixed linkage over of varying concentrations for framework tuning is through solvent assisted ligand exchange (SALE) (Karagiaridi et al., 2014). SALE is a novel postsynthetic modification (PSM) method in which a parent MOF particle is placed in solution with a linker other than that already within the framework. Ligand exchange between linkers of the parent MOF and free linkers in solution occurs to form an isostructural, topologically identical daughter ZIF structure with new functionality. In order to be considered a true post synthetic modification, the reaction must proceed in a single-crystal to single crystal fashion, thus dissolution/recrystallization to form new crystals does not fit the definition a PSM (Cohen, 2017). Reactions can proceed via solution-to-particle ligand exchange (Figure 1.23 A) or particle-to-particle ligand exchange (Figure 1.23 B). Each type of exchange has been reported, even in very stable MOFs such as UIO-66 (M. Kim, Cahill, Fei, Prather, & Cohen, 2012)

A.

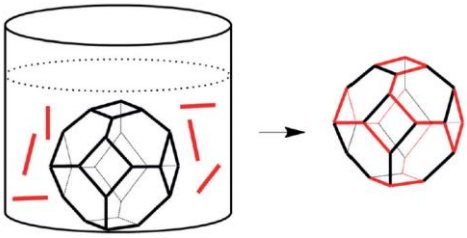

B.

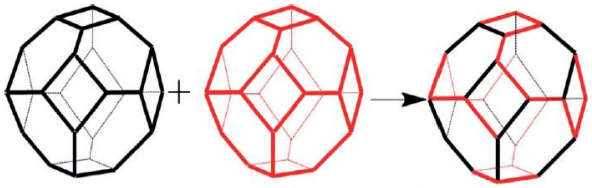

Figure 1.24 Illustrative graphics showing (A) solution-to-particle and (B) particle-to-particle ligand exchange (Pimentel et al., 2014)

Since SALE places parent MOF linkers in a concentrated solution with new linkers. The linker solubility differen4e/metal competition hurdle experienced in hybrid/mixed linker synthesis is alleviated because the concentration of linker present in the MOF prior to exchange is fixed. The driving force for linker exchange can be explained by the following (Gross, Sherman, Mahoney, & Vajo, 2013):

$$\Delta G = \Delta G^0 + RT \cdot ln \frac{[L_o]}{[L_i]} \cdot \frac{X_i}{X_o} \tag{1.41}$$

where L_o is the concentration of original framework linker exchanged out from the framework into the exchanging solution after reaction, L_i is the concentration of the exchanging linker in the original solution, X_i is the concentration of the new ligand in the framework after reaction, and X_o is the concentration of the original linker remaining in

the framework after reaction. Explained in more general terms, the driving force for ligand exchange is determined by the free energy difference between the original and modified structures. This this driving force is partially a result of relative coordination bond strength between the original/substituting ligand with the metal site of the ZIF framework.

A direct example is evidenced in the work of Hupp and co-workers (Karagiaridi, Bury, Sarjeant, Stern, Farha, Hupp, et al., 2012). In the Cd-based MOF CdIF-4 (RHO topology) 2-ethylimidazole was successfully exchanged (100%) with 2-methylimidazole to form a new MOF (SALEM-1) and the RHO topology was successfully maintained, however, when attempting to exchange either ligand with nitroimidazole which contains lower basicity nitrogens, framework dissolution occurred due to the weaker Cd-nitroimidazole bond; the alkyl-substituted linkers extracted the Cd ions from the framework (Karagiaridi et al., 2012).

Thus, in the specific system studied, it is likely that the most favorable exchange reaction was one in which stronger coordinating ligands are replaced with weaker coordinating ligands. However, this is not to say that the converse is not true, stronger coordinating ligands have been exchanged with weaker coordinating ligands already in the framework. Other variables/reaction conditions must be considered such as solvent, temperature, steric/kinetic factors and relative concentration of exchanging ligand and amount of ZIF material in solution must be considered in order to predict the most favorable products to be formed upon exchange (Karagiaridi et al., 2012; Lalonde et al., 2015).

Although further understanding of the SALE processes is needed, the method provides an exceptionally facile route for framework property tuning for specific

applications. In conceptual studies, ligand exchange has been carried out in a number of MOFs including: MOF-5 (Gross et al., 2013), MIL-53, MIL-68, UIO-66 (M. Kim, Cahill, Fei, et al., 2012), ZIF-7 (Jiang, Yang, & Yan, 2015) ZIF-8 (Karagiaridi et al., 2012) and ZIF-71 (Fei, Cahill, Prather, & Cohen, 2013) to add new functionality to each framework while maintaining their original crystallinity and topological features. For application, ZIF-8 crystals have been exchanged with the more hydrophobic 5,6 dimethylbenzimidazole to enhance framework hydrophobicity for stability in the presence of high water activity (H. Zhang et al., 2017) and for enhancement of butanol uptake (X. Liu et al., 2013). ZIF-8 crystals have also been exchanged with the more hydrophilic ZIF-90 2-imidazolecarboxaldehyde linker to increase water uptake (Jayachandrababu, Sholl, & Nair, 2017). Considerable CO_2 adsorption enhancement was achieved in UIO-66 through exchange of the original terephthalic acid linker with alkanedioic acid.

To date, only Lin and co-workers have utilized ligand exchange for direct postsynthetic modification of a supported polycrystalline membrane (H. Zhang et al., 2017). In their work ZIF-8 membranes exhibited decomposition by hydrolysis during static immersion and pure water pervaporation experiments. A single solvothermal reaction was performed by placing a pristine, as-synthesized ZIF-8 membrane in solution of 5,6 dimethylbenzimidazole for 15 hours. After treatment, membrane surface ligand exchange was successfully exhibited by characterization tests and enhanced water stability during pure water flux experiments conducted for 24 hours. This study fully exhibited the effective and facile nature of solvent assisted ligand exchange for membranes and may prove to be effective for new applications including light hydrocarbon separations.

1.5 Problem Statement, Research Objectives and Structure of the Dissertation

1.5.1 Problem Statement

ZIF-8 is particularly compelling for light hydrocarbon separation study because it contains a large pore (11.6 Å) for high olefin/hydrogen permeability and small pore aperture (3.4 Å) for large molecule exclusion and greatly exceeds the propylene/propane separation performance of most of the previously reviewed membrane materials. Further analyses are needed to evaluate ZIF-8 for applications beyond the highly studied C_3 olefin/paraffin separation.

There are few fundamental studies assessing the static thermal properties of ZIF-8 crystals and membranes to determine their suitability for high temperature separation applications. An assessment ZIF-8 thermal stability will dictate the range of applications in which the framework can be applied. If thermally stable at high temperatures (> 300°C), ZIF-8 would be an exceptional membrane reactor material for light hydrocarbon dehydrogenation processes.

Additionally, ZIF-8 literature lacks a fundamental description of the thermodynamic and kinetic properties that govern C_2 molecule transport in single gas and binary mixtures. Further understanding of the transport characteristics of C_2 molecules in the prototypical ZIF-8 membrane will offer insight into the factors which affect C_2 permeability/selectivity and enable development new or modification of prototypical ZIF membranes for enhanced C_2 separations.

Finally, ZIF-8 is a prototypical membrane material which can be facilely modified through solvent assisted ligand exchange to enhance its properties. To date, most studies have focused on hydrostability improvement, but the technique has yet to be explored for

gas separation enhancement; specifically light hydrocarbons. A systematic study of ZIF-8 membrane postsynthetic modification will provide new insight into the mechanism of solvent-assisted ligand exchange in ZIF membranes how it can be utilized to exploit and enhance the steric properties of ZIF-8 for light hydrocarbon separations.

1.5.2 Objectives

This dissertation will present findings from fundamental studies of the stability, transport and modification of zeolitic imidazolate framework-8 for light hydrocarbon separations. Objective 1 of this research is to assess the static thermal stability and changes in physical properties of ZIF-8 crystals and membranes in various environments and temperatures. Membrane studies will also characterize the transport properties of gas mixtures as a function of temperature/time and correlate the changes in transport to changes in the physical structure of the membrane. The overall purpose of objective 1 is to determine the suitability of ZIF-8 for high temperature applications.

The results of thermal stability tests will guide and place a temperature limitation on subsequent analyses of the temperature dependency of C_2 permeation in single gas and binary mixtures to partially fulfill objective 2 of this research which is to provide fundamental knowledge of both the thermodynamic and kinetic properties which control C_2 transport in ZIF-8 membranes. Temperature dependent permeation and adsorption tests in ZIF-8 membranes and crystals will enable thermodynamic properties such as activation energy of diffusion, entropy of diffusion and heat of adsorption to be derived to understand the contribution of each factor to the diffusive/adsorptive selectivity and permeation behavior of C_2 molecules in ZIF-8. A deeper understanding of C_2 transport will aid in

characterizing H_2/C_2 separation performance of ZIF-8 membranes as a function of temperature which is relevant for post ethane cracking applications. Additionally, the pressure dependency of C_2 transport will be evaluated for further understanding of the C_2 transport mechanism in ZIF-8.

Finally, objective 3 of this research is to utilize the facile process of solvent assisted ligand exchange to enhance the gas separation properties of ZIF-8 membranes. A time and temperature dependent study of membrane surface ligand exchange with the bulkier 5,6 dimethylbenzimidazole ligand will be performed with the goal of tuning the steric properties of ZIF-8 to obtain higher resolution C_2, C_3 and hydrogen separation performance. Characterization of both the physical and permeation properties of the framework during the exchange process will provide a deeper understanding of the membrane ligand exchange mechanism and how to control the chemistry for light hydrocarbon separation enhancement.

1.5.3 Structure of Dissertation

The following chapters in this dissertation will accomplish the objectives set forth in the preceding section. Chapter 2 is a detailed study of the static thermal stability of ZIF-8 nanocrystals in inert, oxidizing and reducing environments. Chapter 3 characterizes the stability of ZIF-8 thin film membranes through analyses of changes in the physical material properties and transport characteristics of the membrane as a function of temperature and time. Chapter 4 details the transport characteristics of C_2 molecules in ZIF-8 in single gas and binary mixtures. Chapter 5 will provide a fundamental study of the solvent assisted ligand exchange reaction using ZIF-8 membranes and will describe the effects of

postsynthetic modification time and temperature on light hydrocarbon gas permeation and separations.

CHAPTER 2

KINETICS OF ZIF-8 THERMAL DECOMPOSITION IN INERT, OXIDIZING AND REDUCING ENVIRONMENTS

2.1 Introduction

As outlined in Chapter 1, the steric properties of ZIF-8 enable its 0.34 nm diameter pore aperture which facilitates exceptional performance in C_3 paraffin/olefin, C_4 isomer separations and hydrogen/light hydrocarbon separations (C. Zhang & Koros, 2015). In addition, the coexistence of both Lewis acid (Zn) and Lewis base (imidazole nitrogen) sites makes ZIF-8 a promising material for catalysis applications (Bhattacharjee, Jang, Kwon, & Ahn, 2014). Many of the aforementioned separation and some catalytic applications involving ZIF-8 can be carried out at temperatures below 100°C. However, ZIF-8 is a promising membrane for kinetic separation of H_2 from propylene, ethylene and isobutene (Bux, Feldhoff, et al., 2011; Pan & Lai, 2011). A ZIF-8 dehydrogenation membrane reactor could potentially be utilized for the on-purpose production and in situ removal of H_2 from C_2-C_{3+} olefins. A ZIF-8 catalytic membrane reactor for paraffin dehydrogenation would need to be operated continuously at temperatures greater than 300°C (Champagnie et al., 1992; Ziaka, Minet, & Tsotsis, 1993).

Although ZIF-8 is often highlighted for its potential as high performance membrane material in terms of its intrinsic permeability and selectivity properties, the stability of ZIF-8 has yet to be measured using realistic experimental conditions. Upon its inception, ZIF-8 along with many other ZIFs first reported, were originally lauded for their exceptional chemical and thermal stability. It was reported that ZIF powders could

maintain their chemical and structural integrity in boiling water and alkaline environments for durations up to 24 hours (Park et al., 2006). The thermal robustness of ZIFs and MOFs such as ZIF-8 and MOF-5 are attributable to strong Zn-N and Zn-O bonds with non-zero formal bond valences (Tranchemontagne et al., 2009).

However, recent studies showed that ZIF-8 was not as stable as originally reported. It was recently determined that when in dilute concentrations as a powder or in membrane form, less hydrophobic ZIFs such as ZIF-8, undergo hydrolysis in the presence of water and other organic solvents (X. Liu et al., 2013; H. Zhang, Liu, Yao, Zhang, & Lin, 2015). Gas phase thermal stability studies conducted in inert and oxidizing atmospheric conditions report that dramatic ZIF-8 decomposition is not incurred until reaching temperatures between 400-550^{o}C when utilizing dynamic temperature thermal gravimetric analyses depending upon TGA conditions and particle sizes utilized (Chen, Yang, Zhu, & Xia, 2014; Pimentel et al., 2014). Increasing temperature analyses such as these only capture the instantaneous temperature at which MOFs or ZIFs decompose under fast temperature ramping rate conditions. For industrial applications, isothermal TGA tests under static temperature conditions are more relevant for material valuation.

Various studies have performed isothermal heat treatments at temperatures between 300-1000°C to directly carbonize ZIF-8 and enhance its structure for CO_2 adsorption (Bai, Xia, Chen, Su, & Zhu, 2014; Gadipelli & Guo, 2015), C_4 transport (C. Zhang & Koros, 2015), supercapacitor electrode (Chaikittisilp et al., 2012; Gao et al., 2014), and electrocatalyst (Li, Zhu, & Xu, 2015; Linjie Zhang et al., 2014) applications, but few studies have methodically examined ZIF-8 with the purpose of understanding its kinetic isothermal stability to determine its limitations. Lai and co-workers conducted isothermal

stability TGA tests with ZIF-8 nanocrystals in air atmosphere and observed no changes in XRD spectra in comparison to as-synthesized crystals after being subjected to thermal treatment at 200°C for 24 hours. However, XRD analyses illustrated a slight elimination of ZIF-8 crystallinity when holding fresh ZIF-8 nanocrystals at 300°C in air atmosphere for only 10 hours and significant crystallinity depletion during 300°C isothermal treatment for 24 hours (Pan, Liu, Zeng, Zhao, & Lai, 2011). Yin et al. recently examined ZIF-8 thermal decomposition under isothermal temperature conditions for long periods (24 hours) in both inert, steam and oxidative environments to evaluate Au/ZIF-8 as a possible catalyst for CO oxidation (Yin, Kim, Choi, & Yip, 2014). Significant degradation was observed when holding ZIF-8 in the presence of air or steam environments at temperatures greater than 300ºC for 24 hours. ZIF-8 was also extensively depleted when held in inert environments at temperatures above 400ºC (Yin et al., 2014).

The works by Lai (Pan et al., 2011) and Yin (Yin et al., 2014) provided a greater understanding of the thermal limitations of ZIF-8, but there has not yet been a rigorous study on understanding ZIF-8 thermal decomposition (carbonization) kinetics, an analysis of how environment affects decomposition kinetics and a postulation of the mechanism/chemical composition of the carbonized structure after thermal decomposition. This work will assess the rate of weight change in ZIF-8 crystals under inert, oxidizing and reducing atmospheres at isothermal conditions between 200-300°C to develop ZIF-8 thermal decomposition kinetics and deduce the resulting structure after decomposition.

2.2 Experimental

2.2.1 Preparation of ZIF-8 Crystals

ZIF-8 crystals were prepared by the method reported by Cravillion et al. (Cravillon et al., 2011). 734.4 mg of zinc nitrate hexahydrate [$Zn(NO_3)_2 \bullet 6H_2O$] (99.0% Sigma Aldrich) and 810.6 mg of 2-methylimidazole (99% Sigma Aldrich) were each dissolved separately in 50 mL of methanol and stirred for 30 minutes. The 2-methylimidazole solution was then added slowly to the zinc nitrate solution under stirring and mixed for 6 hours. After mixing, the ZIF-8 crystals were aged in solution for 24 hours without stirring. The resulting supernatant was poured off, and white precipitate crystals were collected after 3 cycles of centrifugation and washing with fresh methanol (99% BDH). After washing, the ZIF-8 crystals were placed under vacuum (60 kPa) for 12 hours at room temperature. After drying the ZIF-8 crystals, the resulting white powder was placed in a tightly sealed container and stored in a desiccator.

2.2.2 ZIF-8 Characterization

ZIF-8 crystallinity analysis for each experimental trial was conducted utilizing a Panalytical X'Pert Pro X-Ray Diffractometer at 45 kV and 40 mA with a scan speed of 2.99^o/min about 2θ using CuKα radiation ($\lambda = 0.1543$ nm). An XL30 Environmental FEG (FEI) scanning electron microscope (SEM) equipped with EDAX software for EDS measurement implementing an accelerating voltage between 20-30 kV was used for a comparative analysis of ZIF-8 morphology and atomic composition change between fresh ZIF-8 samples versus crystals remaining after heat treatment at 300^oC for 20 hours. Prior to SEM/EDS characterization, ZIF-8 powder samples were coated with Au-Pd prior to

imaging, to prevent surface charging. Fourier Transform Infrared (FTIR) spectra of as-synthesized ZIF-8 and ZIF-8 samples thermally treated at 300°C for 20 hours were analyzed with a Thermo Scientific Nicolet iS50 Fourier Transform Infrared (FTIR) equipped with a deuterated triglycine sulfate (DTGS) potassium bromide (KBr) detector element and potassium bromide (KBr) window. Spectra were compared utilizing 5 mg of as-synthesized or thermally treated sample which was then mixed with 90 mg of KBr powder to prevent IR detector saturation. Measurements were performed after collecting a pure KBr background spectra.

2.2.3 Thermal Gravimetric Stability Tests

Thermal gravimetric tests were conducted utilizing a TA Instruments SDT Q600 Thermal Gravimetric Analyzer. Approximately 15 mg of ZIF-8 sample was loaded into an alumina sample pan which was placed on a sample beam for each experimental trial. Isothermal stability tests utilized either air, argon, a 50:50 (mol) mixture of hydrogen/carbon dioxide (H_2/CO_2) or nitrogen at a temperature of 200, 250, or 300°C for each trial. The respective gas or gas mixture flow rates were set to a total of 50 mL/min (1 atm, 25°C) using a mass flow controller (MFC). Hydrogen and carbon dioxide gasses were set at flow rate of 25 mL/min each at their respective MFCs, then mixed and fed to the auxiliary reactive gas line on the TGA. After closing the TGA, each respective gas or gas mixture was used to purge the system before commencing the temperature program. The temperature ramping rate was set to 5°C/min for all isothermal experimental runs. After reaching either 200, 250 or 300°C, the TGA furnace temperature was held isothermal for 20 hours. In addition to isothermal stability analyses, two dynamic temperature tests were

conducted in air and nitrogen atmosphere for comparison to literature. The TGA temperature was increased from room temperature to 1000^{o}C at a temperature ramping rate of 10 ^{o}C/min with gas flowing at 50 mL/min.

2.3 Results and Discussion

2.3.1 Results of Thermal Stability Tests

Highly crystalline, rhombic dodecahedral ZIF-8 crystals of approximately 100 nm in diameter were formed utilizing the room temperature methanol synthesis method (Cravillon et al., 2011). The size and crystallinity of the ZIF-8 particles formed were verified through SEM micrographs and the XRD spectra included in Figure 2.1 (A&B). The combination of both figures corroborate existence of the highly reported ZIF-8 geometric morphology (Pan et al., 2011) and sharp, characteristic peaks around 7.3° (011), 10.2° (002) and 12.7° (112) indicating ZIF-8 of high integrity was synthesized.

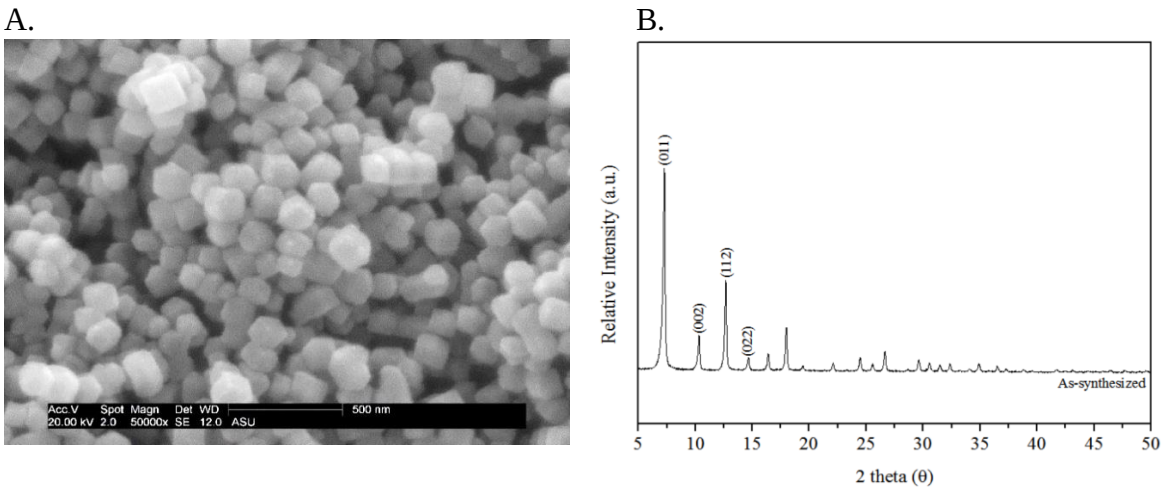

Figure 2.1 SEM micrograph (A) and XRD spectra (B) of as-synthesized ZIF-8 crystals

Figure 2.2 shows results of the dynamic temperature TGA thermal stability tests of ZIF-8 powder under air or nitrogen implementing the increasing temperature method. The weight change profile with respect to temperature shown in Figure 2.2 remains constant until reaching 100°C at which point weight reduction increases in relation to temperature up to 200°C. Between 100 and 200°C a 10% weight reduction is incurred and corresponds to the removal of guest molecules occluded within and adsorbed on the ZIF-8 surface. After reaching 200°C, a constant weight profile up to temperatures of 425°C in air and 500°C in nitrogen, upon which significant weight loss with respect to temperature occurs and suggests the onset of instability temperature of the ZIF-8 nanocrystals. After reaching either decomposition temperature, the TGA weight curve indicated a steep reduction in weight corresponding to a collapse of the ZIF-8 structure and carbonization under extreme thermal stress. In both experiments a final equilibrium of 33 weight% composition was reached. The results obtained verify the findings in previous literature which indicate that ZIF-8 is more stable in inert versus oxidative air environments (Yin et al., 2014). However, dynamic TGA temperature tests do not give an accurate indication of how the ZIF-8 structure changes as a result of sustained thermal loads for extended periods of time.

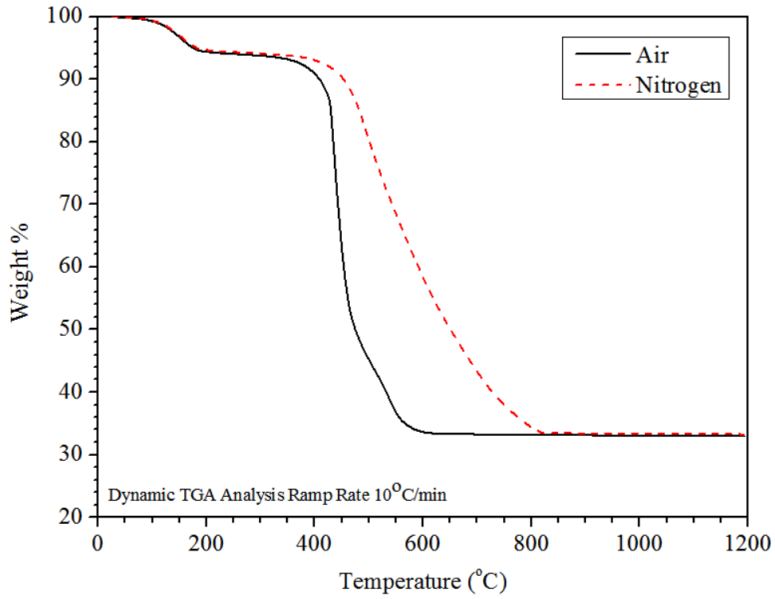

Figure 2.2 Temperature dependent TGA weight decomposition traces of as-synthesized ZIF-8 in air (black) and nitrogen (red) environments

Figure 2.3 illustrates weight decomposition and temperature ramping profiles for ZIF-8 while held under isothermal stress during experimental treatments in H_2/CO_2 environment. As shown in Figure 3, the ZIF-8 sample exhibited an initial steep decrease in weight (5-11%) which is attributed to evaporation of solvent and vaporization of excess, unreacted imidazole ligands adsorbed on the surface and within the ZIF-8 framework (Yin et al., 2014). The initial weight loss profiles representing the release of volatile components from the ZIF-8 framework were almost identical irrespective of decomposition environment and are well represented by the initial weight decreases shown in Figure 2.3. Differences in initial weight loss are due to heating time which is proportional to the final isothermal temperature. After volatilization of adsorbed components, the isothermal weight change profiles depict a small amount of further guest volatilization but mainly structural decomposition especially in the case of 300°C decomposition.

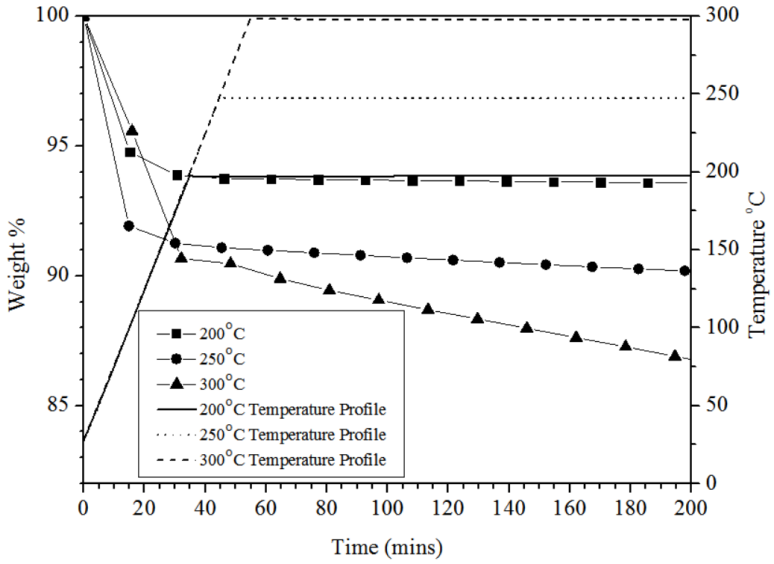

Figure 2.3 Representative ZIF-8 weight decomposition and temperature ramping (5°C/min) profiles to 200, 250 and 300°C depicting initial weight loss dependence on final isothermal temperature (H_2/CO_2 atmosphere profile shown)

Plots of weight at time t (W_t) normalized by weight after reaching each respective isothermal temperature (W_o) with respect to time are displayed in Figures 2.4-2.6 and graphically describe ZIF-8 structural decomposition in each isothermal decomposition environment. It is expected that after an extended time beyond 20 hours, a steady-state, equilibrium weight greater than that found in the dynamic TGA experiment should be reached during the decomposition process, but the experimental conditions employed in this study suggest an approximately statistically linear relationship between ZIF-8 decomposition and time over the 20 hour experimental duration. The approximately linear relationship between ZIF-8 weight decomposition and time is corroborated by R^2 values all greater than 0.97 for the regression lines overlaying the transient weight change profiles in Figures 2.4-2.6.

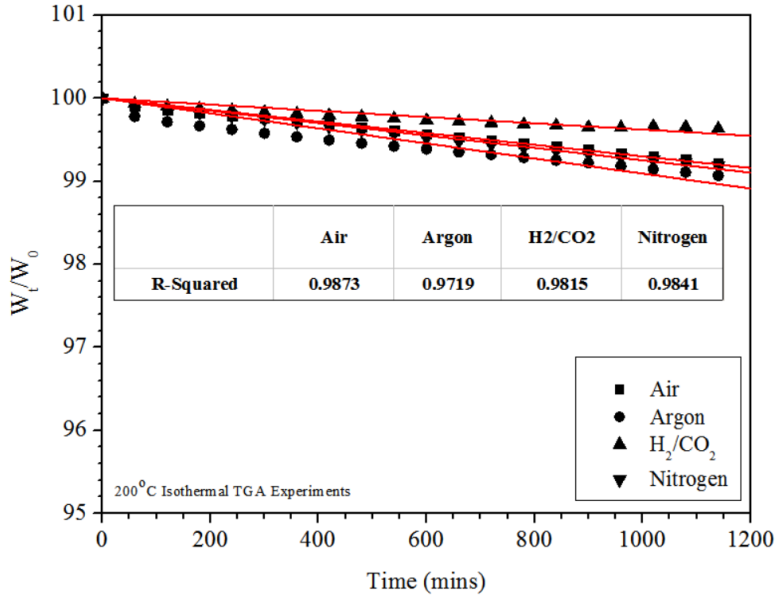

Figure 2.4 Isothermal transient profiles of ZIF-8 weight decomposition at time t (W_t) normalized by weight after reaching isothermal state (W_0) at 200°C in air, argon, H_2/CO_2 and nitrogen atmospheres

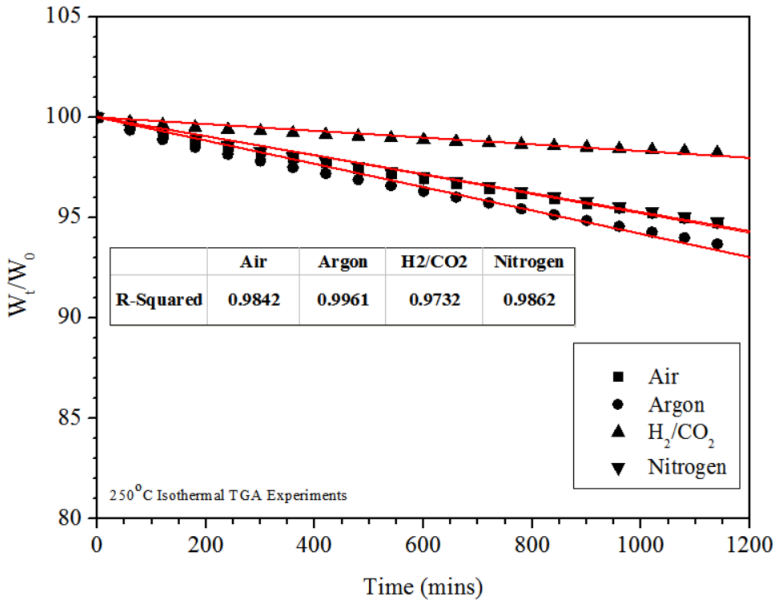

Figure 2.5 Isothermal Transient profiles of ZIF-8 weight decomposition at time t (W_t) normalized by weight after reaching isothermal state (W_0) at 250°C in air, argon, H_2/CO_2 and nitrogen atmospheres

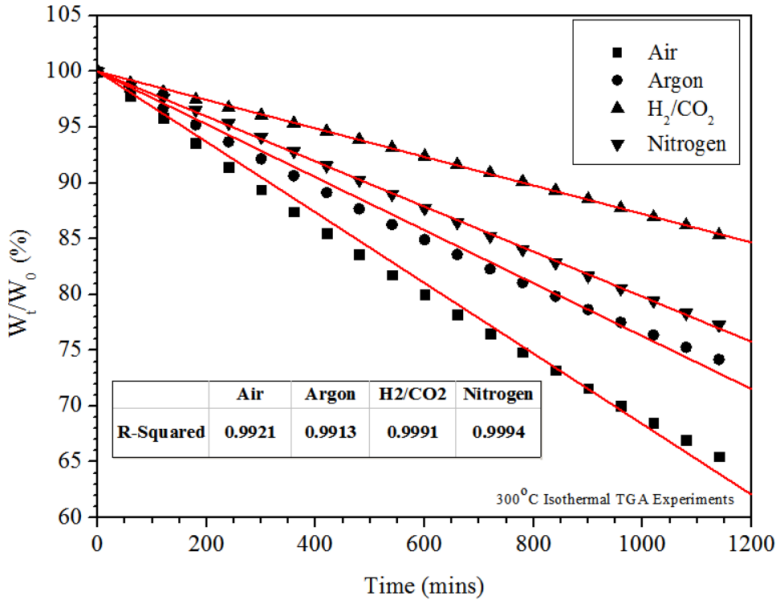

Figure 2.6 Isothermal Transient profiles of ZIF-8 weight decomposition at time t (W_t) normalized by weight after reaching isothermal state (W_0) at 300°C in air, argon, H_2/CO_2 and nitrogen atmospheres

Qualitative analysis of the transient profiles in Figures 2.4-2.6 suggests that the rate of weight decomposition increases upon intensification of the isothermal temperature irrespective of environment. Evaluation of ZIF-8 decomposition with respect to environment shows that the deviation between decomposition rates increases as isothermal temperature increases, suggesting a temperature-environment interaction especially in the case of decomposition in air. At 300°C ZIF-8 decomposition in air is greatest, but at lower isothermal temperatures, the rate of ZIF-8 thermal decomposition is closer to that of argon, H_2/CO_2 and nitrogen. At 200ºC, the rates of ZIF-8 thermal decomposition in all environments nearly converge to a minimum value. From these observations we postulate that the mechanism for ZIF-8 thermal decomposition in air especially at high temperatures is most distinctly different than thermal decomposition in inert and reducing environments,

and low temperature (200°C) transient data suggests that the ZIF-8 framework experiences minimal change irrespective of environment.

The transient weight decrease curves, like those shown in Figures 2.4-2.6, can be quantitatively analyzed by the following kinetic equation (Jasinki, 1964):

$$\frac{d\alpha}{dt} = k(T) * (1-\alpha)^n \tag{2.1}$$

where α is the fraction of reactant decomposed or fractional conversion at time t, k(T) is the kinetic fractional decomposition rate constant as a function of temperature T, and n is the reaction rate order.

$$\alpha = \frac{m_0 - m_t}{m_0 - m_f} \tag{2.2}$$

m_o, m_t and m_f are the mass of the sample at the isothermal state, sample mass at time t and final mass of the sample respectively. As observed earlier, weight loss versus time follows an approximately linear trend after vaporization of volatile components. Thus $\frac{d\alpha}{dt}$ is constant and it corresponds to pseudo 0-order fractional decomposition kinetics over the fractional conversion range.

With the Arrhenius rate law:

$$k(T) = Ae^{\frac{-E_a}{RT}} \tag{2.3}$$

Equation (2.1) can be written as:

$$\frac{d\alpha}{dt} = Ae^{\frac{-E_a}{RT}} \tag{2.4}$$

where A is the pre-exponential frequency factor, E_a is activation energy associated with thermal decomposition. The parameters A and E_a were determined by regressing $\ln\left(\frac{d\alpha}{dt}\right)$ with respect to 1000/T for ZIF-8 decomposition in each gas environment.

Table 2.1 presents ZIF-8 thermal fractional decomposition rate constants at each experimental temperature and Arrhenius parameters collected during ZIF-8 decomposition experiments. A gas environment-temperature interaction is quantitatively confirmed in the case of ZIF-8 decomposition in air. At 300°C, the ZIF-8 fractional decomposition in rate air is 33%, 147% and 57% greater than the decomposition rates measured in argon, H_2/CO_2 and nitrogen atmospheres respectively. However, as the isothermal temperature decreases, the ZIF-8 fractional decomposition rate in air converges closer to that of argon and nitrogen. The preceding analysis suggests that oxygen interactions or oxidative effects enhance ZIF-8 decomposition in air at temperatures greater than 250°C, but once ZIF-8 decomposition commences at temperatures below 250°C, the decomposition process/rate in air becomes identical to that of nitrogen and oxidative effects are less apparent.

Table 2.1 ZIF-8 Thermal Fractional Decomposition Rate Constants k(T) & Arrhenius Parameters in Inert, Oxidizing and Reducing Atmospheres

Gas Atmosphere	k(T) [0.01/min]			Arrhenius Parameters	
	200°C	250°C	300°C	E_a (kJ/mol)	A [0.01/min]
Air	7.00×10^{-6}	4.81×10^{-5}	3.16×10^{-4}	85.69 ± 4.16	1.93×10^{4} ± 1.65
Ar	9.07×10^{-6}	5.81×10^{-5}	2.37×10^{-4}	73.71 ± 1.80	1.27×10^{3} ± 1.52
H_2/CO_2	3.77×10^{-6}	1.68×10^{-5}	1.28×10^{-4}	78.83 ± 11.22	1.27×10^{3} ± 13.60
N_2	7.47×10^{-6}	4.73×10^{-5}	2.02×10^{-4}	74.40 ± 1.03	1.24×10^{3} ± 1.13

It can also be noted that ZIF-8 decomposition in argon atmosphere is consistently greater than nitrogen irrespective of temperature and greater than that of air at 200°C. In addition, ZIF-8 decomposition in H_2/CO_2 environment is consistently the slowest irrespective of isothermal temperature. Using thermodynamic intuition, at 300°C the greater extent of ZIF-8 decomposition in argon as compared to decomposition in nitrogen is plausible because ZIF-8 decomposition takes place in an environment devoid of a nitrogen partial pressure. Under the absence of an N_2 partial pressure, nitrogen molecules from the imidazole ligand more are more readily released from the framework as equilibrium is further shifted towards a nitrogen-deficient structure as compared to the case when decomposition occurs in an N_2 rich atmosphere. This explanation in conjunction with air temperature-dependent oxidative effects explains why at 300°C the ZIF-8 decomposition rate with respect to environment trend is as follows: air > Ar > N_2 > H_2/CO_2, but at 200°C the trend is Ar > N_2/air > H_2/CO_2.

The Arrhenius parameters found in Table 2.1 are representative of macroscopic mechanistic models which include multiple reaction steps, diffusion of gasses, evaporation of structural components and gas-solid interfacial interactions specific to the current system being studied and TGA parameters utilized (M. E. Brown, 1997). The activation energy

and pre-exponential values derived from TGA analyses are not necessarily indicators of energy barriers and molecular collision probabilities respectively. However, in this study, comparison of activation energy values with respect to gas environment can give qualitative insight into similarities/disparities between the temperature dependencies governing the reactions which induce framework decomposition (Fox, Gilman, De Long, & Trulove, 2005). The activation energy of ZIF-8 decomposition in air (85.69 ± 4.16) is the most statistically distinct as compared to the values obtained in Ar (73.71 ± 1.80) and N_2 (74.40 ± 1.03) environments when considering mean and standard deviation. The activation energy of ZIF-8 decomposition in H_2/CO_2 atmosphere (78.83 ± 11.22) is most similar to Ar and N_2 on a mean basis, but not as conclusive when considering standard deviation as well. The pre-exponential factors present an identical trend. Observation of the mean Arrhenius parameters enables deduction that the temperature dependency of ZIF-8 thermal decomposition is most unique in air, and the activation energy of ZIF-8 decomposition is more comparable in inert and reducing environments.

Comparative XRD spectra in Figures 2.7-2.10 illustrate ZIF-8 decomposition with respect to temperature in each gas environment and corresponds well with the transient trends from Figures 4-6 as well as the kinetic data from Table 2.1. After subjecting ZIF-8 crystals to thermal stress in each gas at 200°C for 20 hours all XRD spectral peaks and intensities corresponding to ZIF-8 remained. ZIF-8 crystallinity was preserved irrespective of gas environment. This aligns well with the transient curves in Figure 2.4 which indicate extremely slow decomposition under isothermal conditions at 200°C. XRD spectral analysis indicated significant structural decomposition of ZIF-8 at temperatures above 200°C irrespective of gas environment, but the least amount of crystallinity loss is evident

in the case of decomposition in H_2/CO_2 and confirms TGA weight loss data. As seen from the 250 and 300ºC spectra in Figures 2.7-2.10 there is a significant decrease in overall XRD spectral intensity corresponding to ZIF-8 partial framework carbonization/elimination of crystallinity and incremental loss of long range order at miller indices corresponding to 2θ> 19 with respect to increasing isothermal temperature.

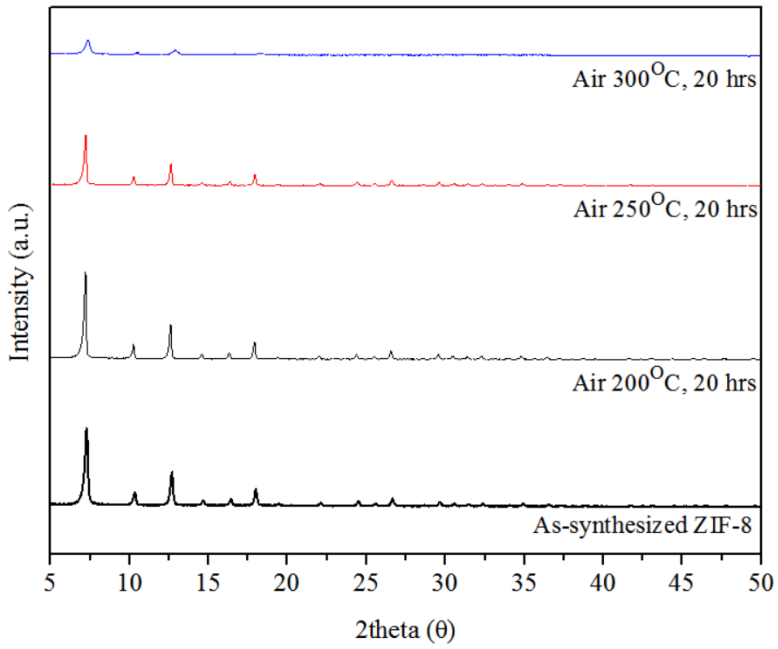

Figure 2.7 XRD spectra after isothermal heat treatment at 200, 250 and 300°C for 20 hours in air

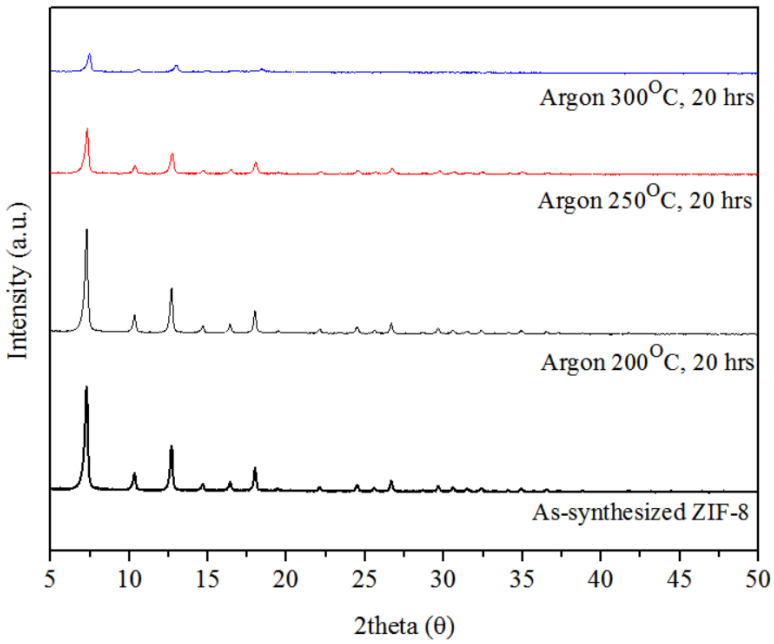

Figure 2.8 XRD spectra after isothermal heat treatment at 200, 250 and 300°C for 20 hours in argon

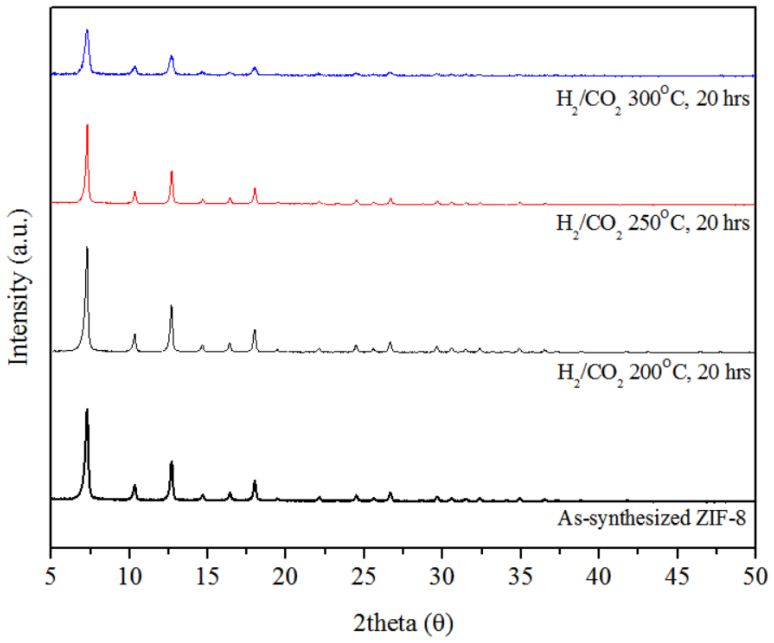

Figure 2.9 XRD spectra after isothermal heat treatment at 200, 250 and 300°C for 20 hours in H_2/CO_2

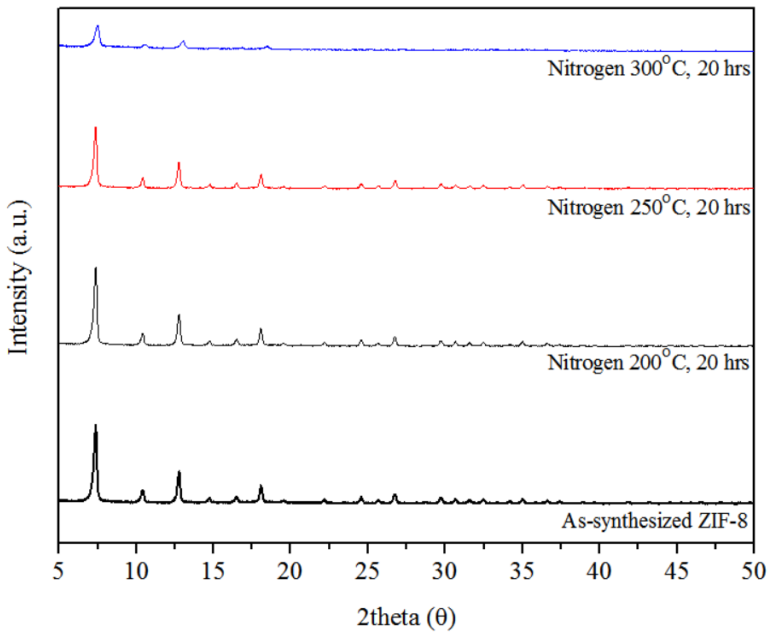

Figure 2.10 XRD spectra comparison to as-synthesized sample after isothermal heat treatment at 200, 250 and 300°C for 20 hours in nitrogen

In experiments conducted by Yin et al. (Yin et al., 2014), after exposing ZIF-8 to temperatures of 300ºC for 24 hours and 400ºC for 10 hours in air, a complete disappearance of characteristic ZIF-8 XRD spectral peaks and emergence of zinc oxide peaks was observed, but when holding ZIF-8 at 300°C in inert argon atmosphere for 24 hours, all peaks were preserved (Yin et al., 2014). In this work, significant decreases in XRD intensity were observed when holding ZIF crystals at 300°C for 20 hours irrespective of environment. In addition, the ZIF-8 sample synthesized by Yin and co-workers decomposed at a rate of ~ 1 wt%/hr in air at 300 ºC (Yin et al., 2014). In this work under similar conditions, the as-synthesized ZIF-8 sample decomposed at a rate of 1.89 wt%/hr. The TGA purge flow rate in this study (50 mL/min) versus that utilized in the work of Yin and co-workers (25 mL/min) is the most identifiable and possibly significant difference

between decomposition protocols. The greater purge flow rate utilized in this work promotes faster removal of decomposition products, increasing the driving force for thermal decomposition which can shift the reaction equilibrium and increase decomposition kinetics and may explain some of the differences in results.

In the work of Pan et al. (Pan et al., 2011), XRD spectra showed slight crystallinity elimination when holding ZIF-8 crystals in air atmosphere at 300^{o}C for 10 hours and similar to this work, significant degradation was shown when holding crystals at 300^{o}C for 24 hours in air. Complete loss of ZIF peaks and emergence of ZnO peaks were not observed until ZIF-8 nanocrystals were held under air atmosphere at 400^{o}C for 5 hours. The absence of ZnO XRD peaks and significant oxygen signals in EDS characterization (Tables 2-4) during the experiments conducted in this study most likely indicates that measurable amounts of crystalline/amorphous ZnO were not formed during ZIF-8 decomposition in air at 300 ^{o}C. Lai and co-workers concluded that ZIF-8 particles present kinetic thermal stability at temperatures of 200^{o}C and below which is similar to the results found herein.

Figure 2.11 (A-D) shows SEM micrographs of ZIF-8 crystals exposed to each gas environment at 300^{o}C for 20 hours. A common, moderate morphology change is evident amongst the samples thermally annealed in air, argon, and nitrogen atmospheres. The carbonized ZIF-8 crystal aggregates show a less uniform rhombic-dodecahedral morphology, with reduced grain boundaries that present larger, rounded aggregates with significant crystal size inhomogeneity as compared to the small, individual crystals shown in Figure 1. The change in remaining particle size and shape is attributable to thermally induced particle coarsening/Ostwald ripening (Wakai, Yoshida, Shinoda, & Akatsu, 2005), previously observed during ZIF thermal decomposition studies (Hongyu Wu et al., 2016).

The crystals thermally treated under H_2/CO_2 conditions show the greatest structural morphology change despite kinetics results indicating that decomposition is slowest in the presence of hydrogen and carbon dioxide. The remaining structure completely transformed from a network of smooth dodecahedra to bud-shaped structures patterned with a striated texture.

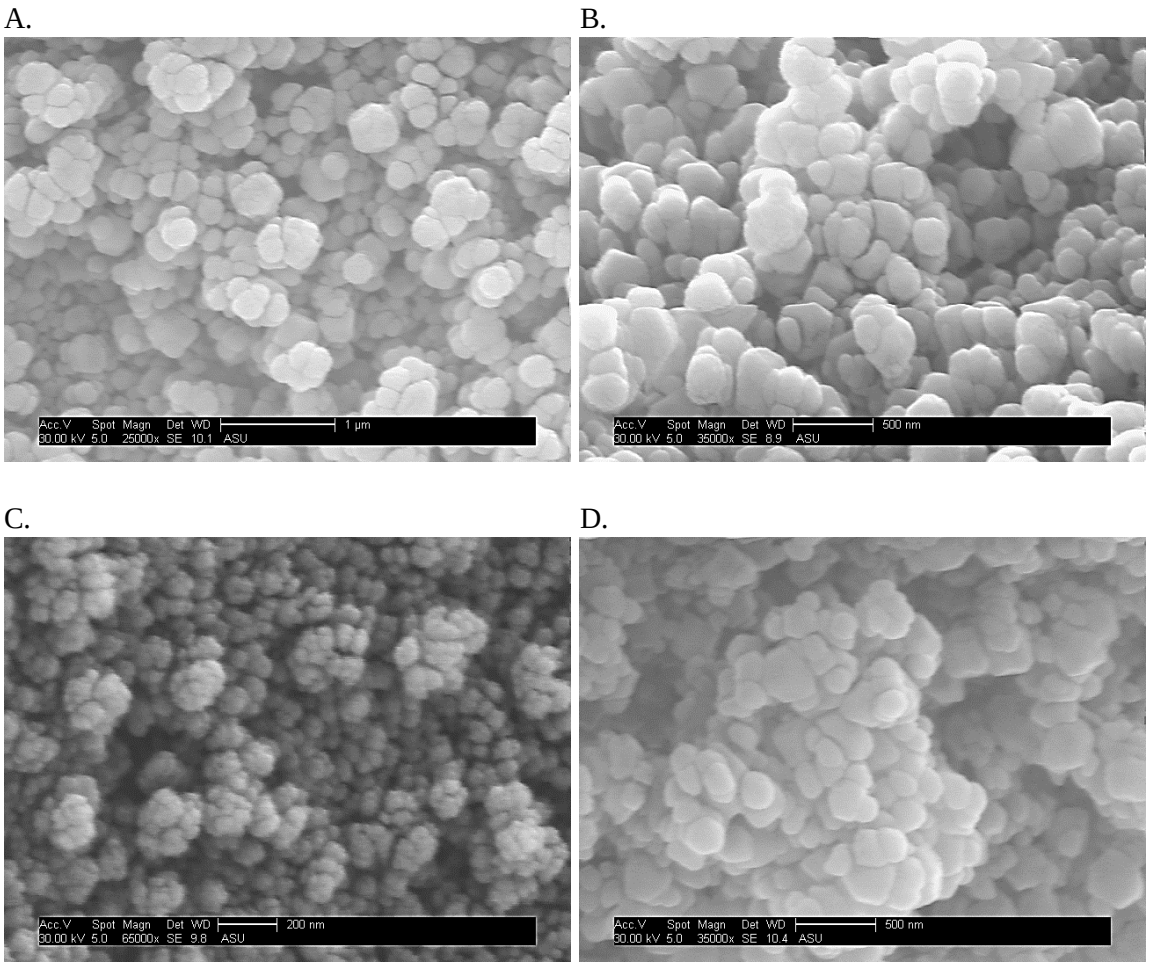

Figure 2.11 (A-D) SEM micrographs of carbonized ZIF-8 after decompositon at 300°C for 20 hours in (A) air, (B), argon, (C) H_2/CO_2, (D) nitrogen

2.3.2 Thermal Decomposition Residual Structure Analysis

Tables 2.2 & 2.3 present comparative weight and atomic percentage and proportion data capturing C, N and Zn energy dispersive x-ray spectroscopy (EDS) elemental quantification of fresh ZIF-8 crystals and samples treated at 300^{o}C for 20 hours in each atmospheric environment. The weight of zinc is expected to remain unchanged since all experiments were carried out at temperatures below its melting point, thus proportion tables were normalized with respect to zinc composition. The "Ideal ZIF-8" column tabulates C, N and Zn quantification data based on the work by Park et al. which presented the ZIF-8 chemical Equation $C_{24}H_{30}N_{12}O_{10}Zn_3$ (Park et al., 2006). Please note that oxygen was added to the chemical formula for ZIF-8 as a means of reconciling x-ray crystallography data due to unidentified electron density (guest molecules) within expected void spaces of the framework. The following analysis uses $C_{24}H_{30}N_{12}Zn_3$ as the theoretical basis.

EDS quantification data in Table 2.2 of the as-synthesized ZIF-8 sample gives a C:N:Zn atomic ratio of 10.51:4.32:1 which is proximate the theoretical value of 8:4:1. Hence, EDS quantification analysis can provide a reliable, preliminary, semi-quantitative relative order of magnitude atomic comparison between fresh and thermally treated samples. Upon observation of as-synthesized ZIF-8 and thermally treated ZIF-8 samples, quantification data indicates a significant decrease in the carbon and nitrogen content of the remaining carbonized ZIF-8 residual structure. After being exposed to air atmosphere at 300°C for 20 hours EDS quantification suggested the residual carbonized ZIF structure contained a C:N:Zn atomic ratio of 2.70:0.52:1. ZIF-8 decomposition in the inert and H_2/CO_2 mixture environments, yielded statistically comparable deviations in C, N and Zn composition with respect to the ideal ZIF-8 structure (Table 2.2). Averaging the C, N and

Zn content of the residual framework after decomposition in argon, nitrogen and reducing environments produces a postulated carbonized ZIF structure with a C:N:Zn atomic ratio of 5.64:1.61:1.

Table 2.2 Weight%/Atomic% Composition and Proportion EDS Quantification Data for Ideal, As-synthesized and Heat Treated ZIF-8 Samples

	Weight %/Atomic % Composition			Weight %/Atomic % Proportion Normalized by Zinc	
State	C (Wt/At)	N (Wt/At)	Zn (Wt/At)	C/Zn (Wt/At)	N/Zn (Wt/At)
Ideal ZIF-8	44.18/61.54	25.76/30.77	30.06/7.69	1.47/8.00	0.86/4.00
As-synthesized ZIF-8	50.07/66.39	24.00/27.29	25.93/6.32	1.93/10.51	0.93/4.32
ZIF-8 (Air, 300^{o}C, 20 hrs)	30.86/63.98	6.93/12.32	62.21/23.70	0.50/2.70	0.11/0.52
ZIF-8 (Ar, 300^{o}C, 20 hrs)	42.84/67.48	15.06/20.34	42.10/12.18	1.02/5.54	0.36/1.67
ZIF-8 (H_2/CO_2, 300^{o}C, 20 hrs)	44.25/69.55	13.56/18.27	42.19/12.18	1.05/5.71	0.32/1.50
ZIF-8 (N_2, 300^{o}C, 20 hrs)	43.49/68.15	14.76/19.83	41.75/12.02	1.04/5.67	0.35/1.65

EDS quantification data was utilized to derive a preliminary chemical composition of the residual carbonized ZIF structure after carbonization in air atmosphere and a single structure after carbonization in inert/reducing environments. Table 2.3 summarizes the C and N atomic composition ratios of carbonized ZIF-8 with respect to the ideal ZIF-8 chemical composition. EDS quantification shows that the residual carbonized ZIF structure exposed to air contained approximately 34% of the C atomic content and just over 10% of the N atomic content of an ideal ZIF-8 sample. After carbonization of ZIF-8 in inert and reducing environments EDS quantification suggests that approximately 71% of the C

content and roughly 40% of N remained in the residual structure. Referring back to the theoretical ZIF-8 basis: $C_{24}H_{30}N_{12}Zn_3$, two carbonized ZIF-8 chemical equations can be postulated.

For ZIF-8 decomposition in air at 300°C for 20 hours:

$$C_{24}H_{30}N_{12}Zn_3 + Air + Heat \rightarrow C_8H_{10}N_2Zn_3 + Gaseous\ Products \quad (2.A)$$

ZIF-8 decomposition in inert/reducing environments at 300°C for 20 hours:

$$C_{24}H_{30}N_{12}Zn_3 + Heat \rightarrow C_{17}H_{21}N_5Zn_3 + Gaseous\ Products \quad (2.B)$$

Table 2.3 ZIF-8 C, N Atomic Composition Ratios of Heat Treated Samples to Ideal ZIF-8 Structure

	Ideal ZIF-8 Atomic Composition/Experimental Atomic ZIF-8 Composition Ratio	
State	$C_{Experimental}/C_{Ideal}$	$N_{Experimental}/N_{Ideal}$
ZIF-8 (Air, 300ºC, 20 hrs)	0.34	0.13
ZIF-8 (Ar, 300ºC, 20 hrs)	0.69	0.42
ZIF-8 (H_2/CO_2, 300ºC, 20 hrs)	0.71	0.38
ZIF-8 (N_2, 300ºC, 20 hrs)	0.71	0.41

The focus of the preceding analysis was to postulate the residual carbonized structure remaining after decomposition at 300°C for 20 hours in inert, oxidizing and reducing atmospheres. The off-gasses in the products for each reaction could not be measured by thermal gravimetric-mass spectra (TG-MS) analysis because the decomposition reaction is a slow (0.77-1.89 wt%/hr), constant process upon reaching 300°C and forms diluted decomposition products over the 20 hour decomposition duration

at concentration levels below MS detection limits. In comparison, Gadipelli and co-workers performed isothermal TG-MS measurements of ZIF-8 crystals under argon atmosphere at temperatures ranging from 600-1000°C (Gadipelli & Guo, 2015). MS detection was possible for their work because after reaching isothermal temperatures of 600°C or greater, a significantly larger (~32 wt%/hr) ZIF-8 decomposition rate was observed (Gadipelli & Guo, 2015). To account for hydrogen evolution during this work, it was assumed that the ratio of hydrogen loss was identical to that of carbon. For approximation, atomic stoichiometry values were rounded to the nearest whole number after comparison to the ideal structure. The molar mass of the proposed air carbonized ZIF-8 structure is 330.32 g/mol and 491.53 g/mol for the samples decomposed in inert/reducing environments which represents a 51.61% and 28.01% mass loss with respect to the ideal ZIF-8 structure containing a molar mass of 682.73 g/mol.

The preceding model can be refined to postulate a decomposition mechanism through examination of comparative FTIR spectra of as-synthesized ZIF-8 and ZIF-8 samples decomposed at 300°C for 20 hours presented in Figure 2.12. The spectral bands of the as-synthesized sample are in good agreement with those presented by Ordonez et al. (Ordoñez, Balkus, Ferraris, & Musselman, 2010). The overall weakening/broadening of the convoluted bands between 1350-1500 cm^{-1}, 900-1350 cm^{-1} and below 800 cm^{-1} corresponding to entire ring stretching, in-plane bending and out-of-plane bending of the imidazole ring respectively and macroscopically indicates overall carbonization/disordering of the ring-ring interactions between imidazole substituents of the ZIF-8 framework in each of the decomposed samples (Y. Hu, Kazemian, Rohani, Huang, & Song, 2011). The specific breaking of Zn-N, C=N and aliphatic/aromatic C-H

bonds of the imidazole ring is realized by the loss/broadening in spectral intensity at stretching bands located at: 421 cm^{-1}, 1584 cm^{-1}, and 2929/3135 cm^{-1} respectively. Complete loss of spectral bands at 1668 and 1731 cm^{-1} further confirm significant cleavage or disruption at the C=N bond for the air, Ar and N_2 decomposed samples and noticeable weakening at each band is confirmed in the case of the sample thermally annealed in H_2/CO_2 atmosphere.

Methyl group dissociation from the 2 position of the imidazole ring is confirmed through weakening of the δ CH_3 IR mode at 1384 cm^{-1}. Note for the case of air decomposition, the δ CH_3 IR absorbance signal is almost depleted and is noticeably less intense than when ZIF-8 was decomposed in inert and reducing environments. The emergence of IR modes at 904, 1041, 1251 and 2200 cm^{-1} are associated with disordering-induced bond structures formed between C and N (Gadipelli, Travis, Zhou, & Guo, 2014) and the specific IR mode at 1041 cm^{-1} most likely can be assigned to formation of an aliphatic amine within the solid phase linked to zinc after ring pyrolization. Isothermal TG-MS ZIF-8 carbonization studies in argon determined that carbon and nitrogen containing molecules are not released from the framework until reaching temperatures of at least 600-700^{o}C (Gadipelli & Guo, 2015). However, in this work, a steady decomposition rate similar to that experienced in the work of Yin and co-workers (Yin et al., 2014) is shown, and we conclude that under the specific TGA protocol utilized herein, C and N molecules are released from the framework.

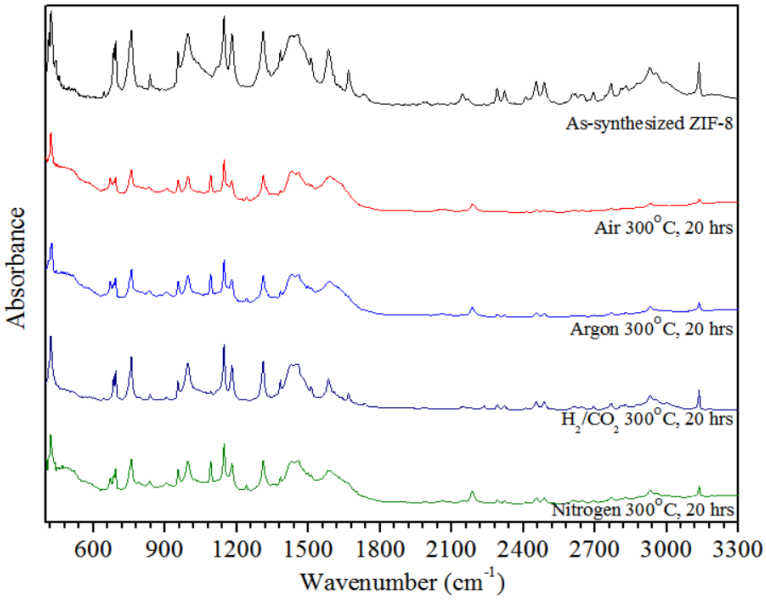

Figure 2.12 FTIR Spectra of As-synthesized ZIF-8 and carbonized ZIF-8 after decomposition at 300°C for 20 hours in air, argon, H_2/CO_2 or nitrogen atmosphere

The magnitude of IR mode weakening and to some extent, IR mode emergence for each sample is concomitant with decomposition atmosphere and agrees well with earlier data suggesting that the decomposition rate follows the trend: air > Ar > N_2 > H_2/CO_2, which affirms a significant difference between ZIF-8 samples decomposed in oxidative atmosphere versus inert and reducing environments. Time-resolved FTIR studies of a 150μm thick undecylimidazole film adhered to a copper slide annealed isothermally at 150°C in air atmosphere showed the rapid increase of carbonyl IR bands at 1580 and 1640 cm^{-1} and complete destruction of imidazole IR modes after 2 hours, indicating a fast rate of imidazole cleavage and incorporation of oxygen within the decomposed imidazole structure during thermal decomposition/oxidation at moderate temperatures (Yoshida & Ishida, 1995). Ishida and co-workers noted that the cleavage rate of the both the imidazole ring and elimination of substituted alkyl groups are enhanced during thermal oxidation,

however a significant metal source/surface area is needed to catalyze a reaction which forms carbonyl (Yoshida & Ishida, 1995).

Although the isothermal temperature and time were both greater in this work, IR modes corresponding to the formation of carbonyl were not observed after thermal decomposition, we suspect that a majority of the oxidative interactions occurred directly at the methyl substituent of the imidazole ligand which may explain why measurable amounts of Zn-O were not observed. The oxidized methyl group would form CO_2 and other gas phase products. In the case of decomposition in H_2/CO_2 environment, peaks corresponding to the formation of a carbonyl group, indicative of CO_2 chemisorption to form an imidazole-carbamate or imidazole-carbonate structure were not observed. Formation of such a structure is sterically unfavorable. This enables deduction that the presence of reducing hydrogen molecules may slow the driving force for hydrogen evolution from the framework and the formation of N atoms to be oxidized and released from the imidazole ligand as compared to decomposition in inert and oxidizing environments. Although hydrogenation reactions typically occur at much greater temperatures than those utilized in this study, it is possible that hydrogen interactions at the decomposing imidazole ring slow framework decomposition but cause morphological changes of ZIF-8 crystals and could be a point for future study.

2.3.3 Proposed ZIF-8 Thermal Decomposition Mechanism

A concrete understanding of specific bond cleavage reactions during the ZIF-8 decomposition process under the conditions imposed during this study enables formation of a possible chemical structure after decomposition and refinement of thermal

decomposition reaction Equations 2.A & 2.B. TGA decomposition studies have confirmed onset decomposition temperatures of approximately 200-300°C for un-substituted and substituted imidazole and triazole molecules (Anniyappan, Sonawane, Pawar, & Sikder, 2015; Fox et al., 2005; Hadjiantoniou-Maroulis, Charalambopoulos, & Maroulis, 1998; Venkatesh, Ravi, & Tewari, 2013). Detailed analyses of single methyl substituted imidazole decomposition reaction mechanisms were not found. However, previous work on the thermal decomposition of imidazole suggests the formation of vinylcarbene through a reaction pathway involving competitive reactions of imidazole cyclization to 3H-imidazole and nitrogen extrusion/elimination to form vinylcarbene, which then rearranges into more stable propyne (Venkatesh et al., 2013). 2-nitroimidazole thermal decomposition studies confirm the cleavage of C-NO_2 bonds and after which, the imidazole ring is attacked in an autocatalytic decomposition reaction in which dissociated gas-phase oxidative NO_2 radicals decompose the remaining destabilized imidazole molecule (J. Li et al., 2008). In the ZIF-8 structure, steric hindrance of zinc-nitrogen coordination bonds greatly negates the possibility of formation of a zinc substituted propyne structure.

Recent studies have shown that the decomposed methyl radicals from ZIF form gas phase products and/or recombine with other methyl radicals to form C_2H_6 (Gadipelli & Guo, 2015) and thus, attack by the methyl substituent is not as likely as in the case of highly oxidative NO_2. Quaternary amines such as tetrapropylammonium hydroxide or tetrapropylammonium bromide decompose into lower amines and olefin products in the presence of their strong basic substituents (OH^- and Br^-) at temperatures greater than 400°C through a Hofmann/E2 elimination mechanism (Bhange, Pandya, Jha, & Ramaswamy, 2008; Cope & Mehta, 1963; Karwacki & Weckhuysen, 2011). During ZIF-8 carbonization

an olefin gaseous product and a solid residual lower amine containing structure are formed without significant presence of a strong base and occurs at lower temperatures as compared to quaternary amine decomposition, which possibly precludes a Hofmann/E2 elimination mechanism as the major decomposition reaction. The works by Aniyappan and Maroulis involving the pyrolysis of imidazole and triazole ligands suggest thermolytic bond cleavage as a main mechanism for imidazole thermal decomposition (Anniyappan et al., 2015; Hadjiantoniou-Maroulis et al., 1998). Both authors concluded that azirine molecules were formed after thermal decomposition.

Based upon known azirine formation upon imidazole decomposition and FTIR spectra in Figure 2.12, we propose a two refined decomposition reaction equations.

For ZIF-8 decomposition in air at 300°C for 20 hours:

$$Zn(C_4H_5N_2)_2 + Air + Heat \rightarrow C_3H_3N_2 - Zn - C_2H_2N + Gaseous\ Products \qquad (2.C)$$

For ZIF-8 decomposition in inert/reducing environments for 20 hours:

$$Zn(C_4H_5N_2)_2 + Heat \rightarrow C_4H_5N_2 - Zn - C_2H_2N + Gaseous\ Products \qquad (2.D)$$

where the ZIF-8 chemical composition on the reactants side of Equations 2.C & 2.D represent a single building block of ZIF-8 (227.58 g/mol) consisting of a zinc cation coordinating two imidazole ligands. $[Zn(C_4H_5N_2)_2]_3$ (682.73 g/mol) yields the original $C_{24}H_{30}N_{12}Zn_3$ basis found in Equations 2.A & 2.B. We propose that the average remaining structural unit within the ZIF-8 framework after 20 hours of decomposition in air at 300°C

consists of a zinc cation coordinated with an N atom of a mostly intact de-methylated imidazole ligand and the N of an azirine substituent that was formed upon decomposition of the corresponding imidazole ligand. The corresponding average carbonized ZIF-8 structure after decomposition in inert/reducing environments at 300°C for 20 hours consists of a zinc cation coordinated with an N atom of a fully intact 2-methylimidazole ligand and the N atom of an azirine substituent decomposed from imidazole. With respect to weight, the remaining carbonized ZIF-8 structures derived based on Equations 2.C & 2.D represent building units with molecular masses of 172.50/186.52 g/mol or 517.48/559.75 g/mol respectively when utilizing the basis presented for Equations 2.A & 2.B. The derived decarbonized structures present a 24.2% mass loss in air and an 18.0% mass loss in inert/reducing environments with respect to as-synthesized ZIF-8.

We propose an intermediate product formed from a series of thermolytic cleavage reactions over the 20 hour decomposition duration that is illustrated in Figures 2.13 & 2.14. TGA weight change data does not indicate finite step changes for a sequence of bond breaking reactions, however we outline the steps to obtain the proposed intermediate and final products. It has been noted that in the ZIF-8 crystal, the relatively weak bonds are the Zn-N coordination bond and the C-C bond bridging the imidazole ring to the methyl substituent (Gadipelli et al., 2014). It is likely that dissociation of the methyl group occurs through homolytic cleavage at the C-CH_3 bond of the imidazole ring. The methyl radical formed can further decompose to form hydrogen radicals which interact at the decomposing imidazole ring or recombine with other methyl radicals to form C_2H_6.

To further proceed with ring decomposition, Zn-N heterolytic cleavage in which the nitrogen bond inherits both electrons would be a logical step in the decomposition

process. The same N which underwent heterolytic cleavage with Zn would also undergo heterolytic cleavage at the C-N bond of the decomposing ring, forming a positively charged carbon atom at one end of the structure. Heterolytic cleavage must also occur at the opposite N atom (still connected to Zn) in which the N-C bond is broken and the N atom inherits both electrons forming a highly negatively charged N atom one end of the decomposed structure. As a result of the series of thermolytic reactions it is proposed that an azirine ring forms after electron donation from the negatively charged N atom to the positively charged carbocation. We propose that the main difference between ZIF-8 samples carbonized in air versus inert/reducing environments, is the cleavage of a second methyl group upon decomposition in air.

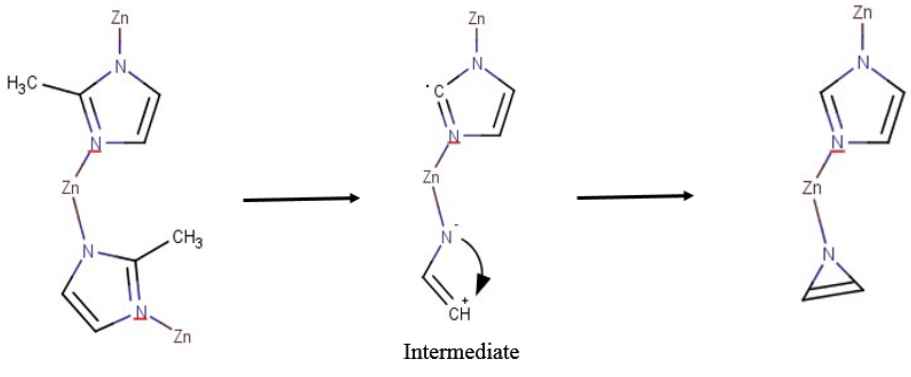

Figure 2.13 FTIR-azirine derived proposed thermolysis decomposition mechanism depicting the average ZIF-8 building unit after thermal treatment at 300°C for 20 hours in air atmosphere

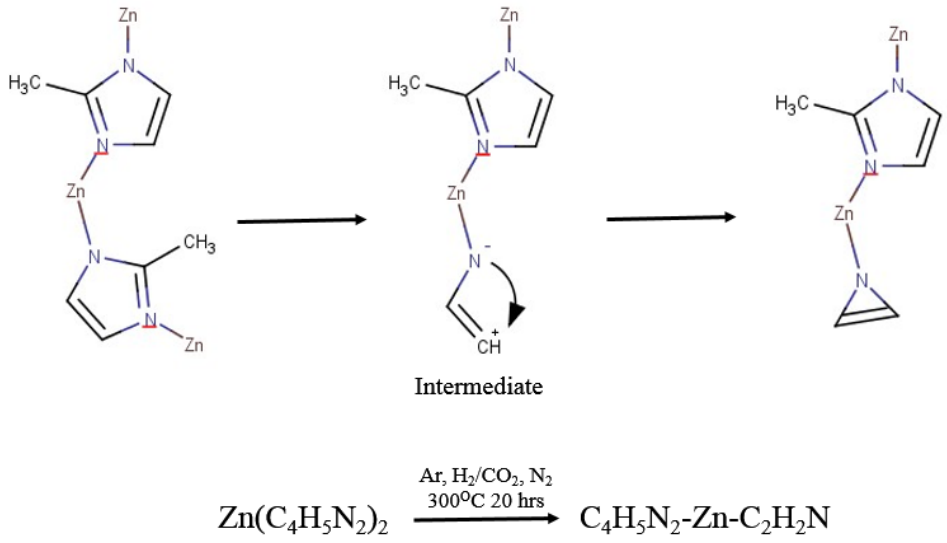

Figure 2.14 FTIR-azirine derived decomposition thermolysis mechanism depicting the average ZIF-8 building unit after thermal treatment at 300°C for 20 hours in argon, H_2/CO_2 or nitrogen atmosphere

Table 2.4 ZIF-8 Decomposition Reaction Equation Validation with Respect to Actual TGA Weight Loss for 300°C Isothermal Experiments

Gas Environment 300°C, 20 hrs	ZIF-8 Decomposition Reaction Equation	ZIF-8 Remaining Weight % After Decomposition at 300°C	ZIF-8 Weight % Change Including Solvent Removal	Initial Solvent Loss (Weight %)	ZIF-8 Weight % Decomposition after Initial Solvent Loss	Theoretical ZIF-8 Weight % Decomposition from Reaction Equation	Difference in Theoretical vs Actual Weight % of Remaining ZIF-8 Sample
Air	(A)	54.01	45.99	10.00	35.99	51.61	15.62
Ar	(B)	63.28	36.72	9.83	26.89	28.01	1.12
H_2/CO_2		75.55	24.45	9.00	15.45		12.56
N_2		65.24	34.76	11.00	23.76		4.25
Air	(C)	54.01	45.99	10.00	35.99	24.2	-11.79
Ar	(D)	63.28	36.72	9.83	26.89	18.04	-8.85
H_2/CO_2		75.55	24.45	9.00	15.45		2.59
N_2		65.24	34.76	11.00	23.76		-5.72

Table 2.4. compares theoretical percentage mass losses derived from EDS quantification and the FTIR/azirine derived mechanism of the carbonized ZIF structures with the actual mass losses observed in the TGA experiments to validate Reactions 2.A-2.D. Reaction 2.A moderately overestimated ZIF-8 weight loss by 15.62% for ZIF-8 decomposition in air. However, Reaction 2.B was significantly more accurate in predicting ZIF-8 percentage weight loss for decomposition in inert environments and slightly better for prediction in the reducing mixture. On average, Equation 2.B overestimated weight loss by 5.98%. Equation 2.C underestimated air decomposition by 11.79%. Equation 2.D underestimated ZIF-8 decomposition in inert and reducing environments by an average of 3.99%. Overall, the EDS derived models overestimate ZIF-8 decomposition by 8.39% and the FTIR/azirine derived model underestimates ZIF-8 decomposition by 5.94%.

Differences in theoretical versus actual weight loss for Equations 2.A & 2.B can be attributed to error in EDS quantification and/or an incorrect assumption of hydrogen loss. In addition, the final remaining carbonized ZIF-8 weight/composition just after TGA analysis may be greater than the values measured by EDS because after placing samples under vacuum for EDS analysis, the content of the carbonized samples possibly changed. The underestimation of weight decomposition in Equations 2.C & 2.D for decomposition in air, Ar and N_2 may arise because an average structure was calculated, it is possible that a greater fraction of the intact imidazole ring or azirine further decomposed. It is also possible that during TGA tests, guest solvent molecules were still being removed after reaching isothermal temperatures and thus the weight change during ZIF-8 decomposition was actually slightly less than observed. We postulate that a heterogeneous carbonized ZIF

structure containing both 2-methylimidazole and azirine rings was formed. The theoretical equations developed from the methods described above can serve as a respectable starting point for future, refined prediction of the residual structures produced during ZIF-8 thermal decomposition.

2.4 Conclusions

ZIF-8 crystals thermally treated in inert, oxidizing and reducing environments isothermally at 200, 250 and 300°C for 20 hours exhibit increasing fractional decomposition rates with respect to temperature. At 200°C, ZIF-8 crystallinity was preserved irrespective of environment, but above 200°C the magnitude of crystallinity depletion increased with respect to isothermal decomposition temperature. At 300°C in air atmosphere, ZIF-8 carbonization is accelerated in comparison to decomposition in inert and reducing environments due to oxidative effects. At lower temperatures the decomposition rate in air behaves more similarly to that of nitrogen and argon indicative of a significant temperature-environment effect. The rate of ZIF-8 thermal decomposition is the lowest in the reducing H_2/CO_2 mixture atmosphere at all isothermal temperatures studied and may be attributable to ZIF-8 decomposition commencing in a hydrogen-rich environment which possibly lowers the driving force for hydrogen evolution and N oxidation to promote detachment from the framework and induces considerable morphology change.

FTIR spectra specifically confirm carbonization of the imidazole ring and Zn-N and C/N bond cleavage. Four chemical formulas postulating the chemical composition of the residual ZIF structures decomposed at 300°C were developed based on the results of

EDS, FTIR and XRD analyses of the crystals. The results cohesively suggest that an imidazole-azirine structure is produced upon carbonization of ZIF-8 crystals at 300°C in inert, oxidizing and reducing environments.

CHAPTER 3

THERMAL STABILITY OF ZIF-8 MEMBRANES FOR GAS SEPARATIONS

3.1 Introduction

The study of ZIF-8 thermal stability in Chapter 2 revealed that ZIF-8 crystals preserve their crystallinity in inert, oxidizing and reducing atmospheres at 200°C under isothermal conditions for 20 hours. However, a slight elimination of ZIF-8 crystallinity when subjecting crystals to isothermal temperatures of 250°C or greater for 20 hours in each environment (James & Lin, 2016). When held at 300°C for 20 hours, ZIF-8 crystals underwent partial carbonization in inert, oxidizing and reducing atmospheres to form an imidazole-Zn-azirine structure as postulated though evidence obtained from multiple characterization techniques (James & Lin, 2016). The finding likely precludes ZIF-8 as a potential light hydrocarbon dehydrogenation membrane reactor material.

Hydrogen selective membranes also have potential for use in moderate temperature applications such the low temperature water-gas shift and hydrocarbon dehydrogenation membrane-assisted reactor configurations which typically operate at temperatures of 180°C or greater (M.E. Rezac, Koros, & Miller, 1994; Y. Zhang, Wu, Hong, Gu, & Xu, 2012). Since ZIF-8 crystals have shown preliminary stability at 200°C. ZIF-8 membranes can potentially add value in each of the mentioned processes. A fundamental understanding of the thermal limitations of ZIF-8 membrane thin films is of great importance for valuation of future ZIF-8 applications. ZIF enabled membranes including ZIF-7, ZIF-8/PBI and ZIF-90 have each displayed promising thermal stability with stable hydrogen separation at temperatures of 200°C and greater (A. Huang, Dou, & Caro, 2010; Y. Li et al., 2010; Yang

& Chung, 2013). Specific to ZIF-8 enabled membranes, Caro and co-workers prepared ZIF-8 membranes using novel polydopamine functionalized supports and reported H_2/CO_2 separation factors of 8.1 and 8.9 respectively at temperatures of 100 and 150°C respectively (a. Huang, Liu, Wang, & Caro, 2014; Q. Liu, Wang, Caro, & Huang, 2013), however the single data points collected at each temperature do not give indication of thermal stability.

Zhang et al. performed successive single gas permeation experiments with ZnO nanorod supported ZIF-8 membranes from 25-200°C in H_2, CO_2, N_2 and CH_4 atmospheres and noted that the membrane remained defect free after repeated heating and cooling for each single gas test (X. Zhang et al., 2014). Drobek and co-workers formed ZIF-8 membranes through a novel ZnO atomic layer deposition (ALD) conversion method and performed binary H_2/CO_2 separation from 25-100°C and observed an increasing separation factor from ~3.2-7.8 with respect to temperature (Drobek et al., 2015). The studies by Zhang and Drobek stressed the use of ZnO interlayers between the ZIF-8 thin film and α-alumina supports to compensate for the thermal expansion coefficient mismatch between α-alumina and ZIF-8 to decrease the likelihood of thin film cracking upon successive heating and cooling between experiments.

The aforementioned works provided insight to solve a specific dynamic, thermomechanical stability issue for ZIF-8 membranes, however there has yet to be a static or isothermal stability study which simultaneously observes changes in the physical characteristics and separation performance of ZIF-8 membrane thin films as a result of sustained thermal stress. The present work and experiments within are designed to obtain a fundamental understanding of ZIF-8 membrane thermal stability using H_2 and CO_2 as a sample gas mixture.

3.2 Experimental

3.2.1 ZIF-8 Membrane Synthesis and Characterization

ZIF-8 membranes were prepared according to our previously reported method with a few modifications (D. Liu, Ma, Xi, & Lin, 2014). α-alumina membrane supports 22 mm in diameter and 2 mm thick (average pore diameter: 120 nm, porosity: 45% were custom prepared using A-16 calcinated alumina powder (Almantis). After sintering at 1150^{o}C for 30 hours, α-alumina disks were polished to form a smooth membrane substrate using 500, 800, 1200, and 2000 silicon carbide (SiC) polishing paper (Struers). The supports were then washed under sonication for 10 minutes in 20 mL of pure deionized water, then for 10 minutes in pure methanol for removal of impurities. After 5 minutes in each solvent, full liquid exchange was performed to provide a fresh bath. The supports were subsequently dried at 250^{o}C for 4 hours after washing.

ZIF-8 crystals were prepared by the method reported by Cravillion et al. (Cravillon et al., 2011). 734.4 mg of zinc nitrate hexahydrate [$Zn(NO_3)_2 \bullet 6H_2O$] (99.0% Alpha Aesar) and 810.6 mg of 2-methylimidazole (99% Sigma Aldrich) were each dissolved separately in 250 mL beakers containing 25 mL of methanol and stirred for 30 minutes. The 2-methylimidazole solution was then added slowly to the zinc nitrate solution under stirring and mixed for 6 hours. After amalgamation, the mixture was aged for 24 hours without stirring. White precipitate crystals were collected after 3 cycles of centrifugation and washing with methanol (99% BDH). After washing, the ZIF-8 seeds were placed under vacuum (60 kPa) for 12 hours at room temperature. A stable, well dispersed colloidal solution of ZIF-8 nuclei was prepared by forming a 0.035 wt% ZIF-8 suspension in methanol.

An earlier prepared α-alumina disk support with polished side down was brought in contact with the ZIF-8 seed solution for 10 seconds followed by drying in air for 10 minutes, the preceding steps were then conducted a second time. Two dip-coatings were performed for short time intervals to decrease the probability of forming seed layer cracks while ensuring homogenous seed coverage across the entire substrate. The ZIF-8 seed coated disk was placed in an oven and ramped by 0.3°C/min to 95°C, held for 3 hours then ramped down to room temperature at the same rate.

A seeded secondary growth method adapted from Pan et al. (Pan et al., 2012) was utilized to promote growth of a thin, continuous, defect-free membrane layer across the α-alumina substrate. The secondary growth solution was prepared by dissolving 2.27 g of 2-methylimidazole and 0.12 g of $Zn(NO_3)_2 \bullet 6H_2O$ in 40 mL of deionized water. The seeded disk was placed vertically with the polished face tilted slightly up in a Teflon holder contained within a 45 mL Teflon lined stainless steel autoclave. The clear secondary growth solution was poured slowly into the Teflon container and immersed the seeded support. Secondary growth was carried out at 130°C for 6.5 hours. After membrane growth the stainless steel autoclave was removed from the oven and cooled to room temperature. The ZIF-8 membrane was removed from the secondary growth solution, washed briefly with deionized water then immersed in a methanol bath for 6.5 hours to exchange solvent within the membrane pores. After solvent exchange the membrane was placed under vacuum (60 kPa) for 12 hours at room temperature. The secondary growth synthesis was repeated again to seal defects and generate a highly crystalline ZIF-8 structure in a highly reproducible process.

Membrane surface morphology and cross section analyses were conducted using an XL30 Environmental FEG (FEI) scanning electron microscope (SEM) with an accelerating voltage of 20 kV. Samples underwent gold/palladium deposition prior to imaging to prevent surface charging. The ZIF-8 membrane crystal structure was examined using a Bruker D8 x-ray diffractometer at 20 kV, 5 mA with a scan speed of 2°/min about 2θ using Cu Kα radiation (λ = 0.1543 nm). ZIF-8 membrane functional group characterization was observed using a Thermo Nicolet 6700 Fourier transform infrared spectrometer equipped with a deuterated triglycine sulfate (DTGS) detector element and a diamond window. An α-alumina support was used as a zero background so that only ZIF-8 spectral peaks were displayed.

3.2.2 Gas Permeation/Separation Experiments and Thermal Gravimetric Analysis

Each as-synthesized α-alumina supported ZIF-8 membrane was sealed into a stainless steel permeation cell using VITON O-rings (O-rings West). The permeation area of each membrane was 2.27×10^{-4} m^2. All membranes were probed at room temperature using helium (He) and sulfur hexafluoride (SF_6) to evaluate their molecular sieving transport characteristics using a single gas steady-state permeation system (D. Liu et al., 2014). He or SF_6 was supplied to the permeation cell directly from tubing attached to each respective gas cylinder and maintained at 20 psig using a needle valve. The permeate side was connected to a bubble flow meter at atmospheric pressure without a sweep gas.

Membrane permeance F_i of component i is defined as:

$$F_i = \frac{Q_i}{\Delta P_i A} \tag{3.1}$$

where Q_i is the permeate molar flow rate of component i (mol/s), ΔP_i the transmembrane pressure drop of i (Pa) and A, is the effective permeation area (m^2). Ideal or permselectivity in molecular probing experiments is defined by the ratio of pure gas permeances:

$$Ideal\ Selectivity = \frac{F_i}{F_j} \tag{3.2}$$

where j denotes larger kinetic diameter component j.

Hydrogen/carbon dioxide single gas, binary temperature dependent and binary transient permeance experiments were performed using the Wicke-Kallenbach technique shown in Figure 3.1. For the single, binary temperature dependent and binary transient gas permeance experiments, H_2 and CO_2 feed gases were each maintained at 25 mL/min (50:50 mol ratio) and nitrogen sweep gas at 50 mL/min using mass flow controllers. Volumetric flow rates correspond to ambient temperatures ranging between 23.6-25.0°C and a pressure of 1 atmosphere. In each experiment, both the feed and sweep sides of the permeation cell were maintained at 1 atmosphere. The feed pressure was controlled by a needle valve on the retentate side (fully open) and the sweep side pressure was maintained using N_2 sweep gas. The composition of both the retentate and sweep gasses were analyzed by gas chromatography (GC) (Aligent 6890 N, Alltech Haysep DB 100/120 column with dimensions: 9.1 m x 3.2 mm O.D. x 2.2 mm I.D., argon carrier gas and TCD detector). The

single gas and binary temperature dependent permeance tests present H_2/CO_2 permeance behavior as a function of temperature. Temperatures were ramped by 1°C/min from 25°C to 300°C (25-250°C in single gas tests) and held for 1.5 hours at each successive 25°C increment to reach a steady state permeance before collecting permeate and retentate compositions. Permeate and retentate composition collection by GC lasted approximately 30 minutes in total, then the furnace was ramped to the next 25°C temperature interval. In the transient tests, H_2/CO_2 mixture permeance was studied as a function of time over a 24 hour period at 50, 100, 150 and 300°C respectively. A temperature ramping rate of 20°C/min was used to isolate temperature and time effects on the ZIF-8 membrane structure and transport properties during the 300°C test. A ramping rate of 1°C/min was utilized in subsequent transient tests.

The mixture gas separation factor (SF) calculated in both the temperature dependent and time dependent experiments is defined by:

$$\text{SF} = \frac{y_{H_2}/y_{CO_2}}{x_{H_2}/x_{CO_2}} \tag{3.3}$$

where y denotes permeate partial molar fraction and x denotes retentate partial molar fraction. Mixture permeance was calculated using the difference in retentate and permeate partial pressures as the driving force. Hydrogen permeance for example was calculated as follows during mixture gas tests

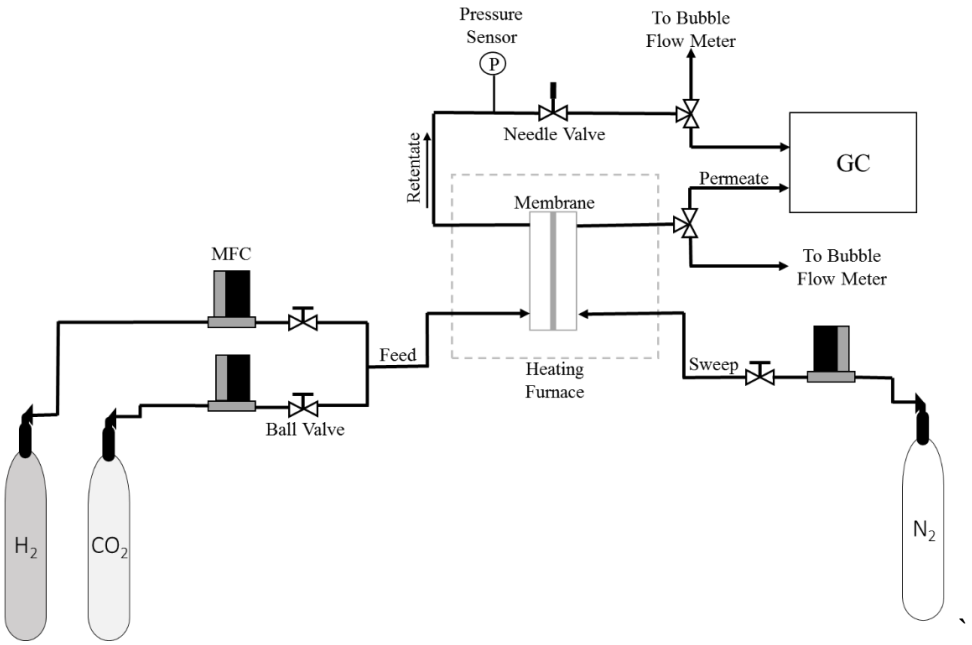

Figure 3.1 Binary gas permeance apparatus and configuration

$$F_{H_2} = \frac{Q_{H_2}}{\left(x_{H_2}P - y_{H_2}P\right) * A} \tag{3.4}$$

Carbon dioxide mixture permeance was calculated using the same method.

Thermal gravimetric analysis (TGA) measurements using ZIF-8 powders were utilized to help describe/prognosticate the underlying decomposition phenomena occurring during the ZIF-8 binary temperature dependent membrane test. TGA analyses were conducted under H_2/CO_2 atmosphere using mass flow controllers to achieve a 25 mL/min flow rate (50:50 mol) in each respective gas at 1 atmosphere. The TGA test utilized a time and temperature profile identical to the binary mixture temperature dependent membrane experiment (ramp rate 1°C/min, hold time 2 hours at each 25°C interval from 25-300°C).

The hold time of 2 hours corresponds to 1.5 hours to reach steady state followed by 30 minutes of GC sampling that occurred during membrane testing.

3.3 Results and Discussion

3.3.1 Membrane Characteristics and Temperature Dependent Binary Separation Properties

Figures 3.2 and 3.3 show cross-sectional, top surface view and XRD patterns representative of the as-synthesized ZIF-8 membranes obtained using the above synthesis procedure. SEM micrographs and sharp XRD pattern intensities at the corresponding 2θ values cohesively indicate the formation of 2.5-3.0μm thick, highly crystalline, continuous ZIF-8 films formed after membrane fabrication. Prior to H_2/CO_2 permeation tests, membranes underwent molecular probing with He/SF_6 to verify the presence of high integrity, molecular sieving ZIF-8 thin films present on the α-alumina surface. The presence of large defects can significantly affect permeance behavior and molecular sieving properties.

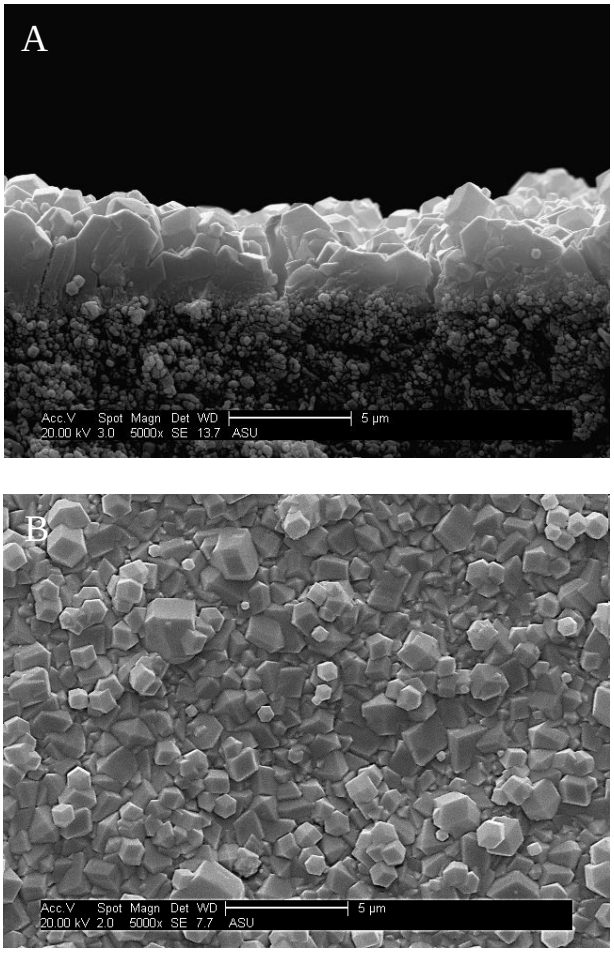

Figure 3.2 SEM micrograph of as-synthesized ZIF-8 membrane: cross section (A) and top view at 5000x magnification (B)

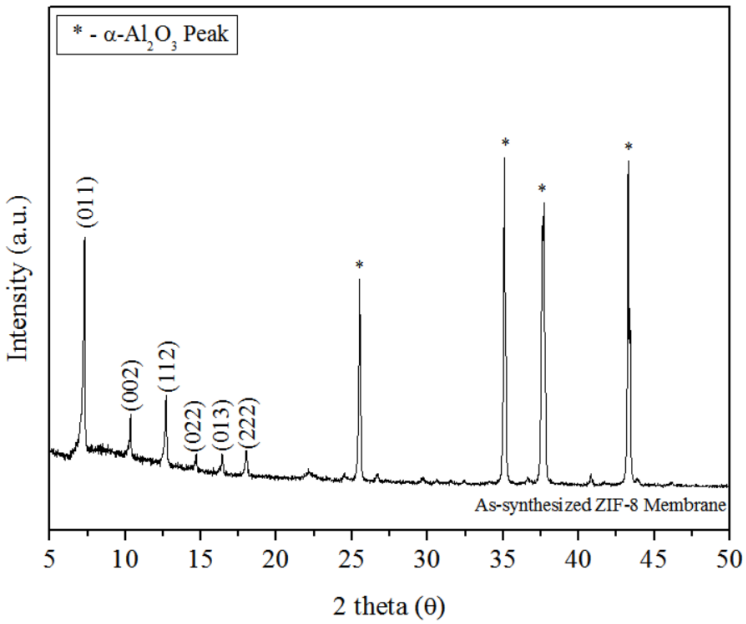

Figure 3.3 XRD pattern of as-synthesized ZIF-8 membrane on alumina support

Table 3.1 presents the single gas He and SF_6 permeances and ideal separation factors for the membranes used in each permeation experiment. All membranes exhibit separation factors at least 60 times greater than the ideal Knudsen He/SF_6 separation factor of 6.0, which verifies synthesis of molecular sieving membranes.

Table 3.1 Permeance (mol/m^{2}sPa) and ideal He/SF_6 Separation Factor Values for Membranes used in Thermal Stability Studies

Membrane	He Permeance	SF_6 Permeance	Ideal SF	Test Conducted
M1	4.6×10^{-7}	1.1×10^{-9}	402	H_2 Single Gas
M2	6.7×10^{-7}	1.7×10^{-9}	390	CO_2 Single Gas
M3	9.1×10^{-7}	2.3×10^{-9}	395	Binary H_2/CO_2
M4	6.5×10^{-7}	8.4×10^{-10}	775	Transient H_2/CO_2 at 300°C
M5	4.4×10^{-7}	1.1×10^{-9}	405	Transient H_2/CO_2 at 150°C
M6	4.4×10^{-7}	1.1×10^{-9}	395	Transient H_2/CO_2 at 100°C
M7	2.7×10^{-7}	5.1×10^{-10}	541	Transient H_2/CO_2 at 50°C

Figure 3.4 shows CO_2 and H_2 single gas permeances as a function of temperature. The permeance of both H_2 and CO_2 decrease with respect to increasing temperature. Since diffusivity and solubility are directly and inversely proportional to temperature respectively, the results suggest that the activation energy for diffusion is smaller than the heat of adsorption in ZIF-8 for both H_2 and CO_2. Molecular simulations incorporating specific force-field parameters to account for ZIF-8 framework flexibility indicate that the free energy of CO_2 migration through the ZIF-8 crystalline network (9.9 kJ/mol) is lower than the isoteric heat of adsorption (14.19 kJ/mol) (Liling Zhang, Wu, & Jiang, 2014). The CO_2 adsorptive affinity for the ZIF-8 framework is enabled by strong quadrupole-π electrostatic interactions between the π electrons of the imidazole ring and the partial positive charge of the carbon on CO_2 (Amrouche et al., 2011; D. Liu, Wu, Xia, Li, & Xi, 2013). In addition to electrostatic affinity for CO_2, the large cage diameter (1.16 nm) of the ZIF-8 structure enables significant equilibrium uptake of carbon dioxide (kinetic diameter = 0.33 nm) (Pérez-Pellitero et al., 2010).

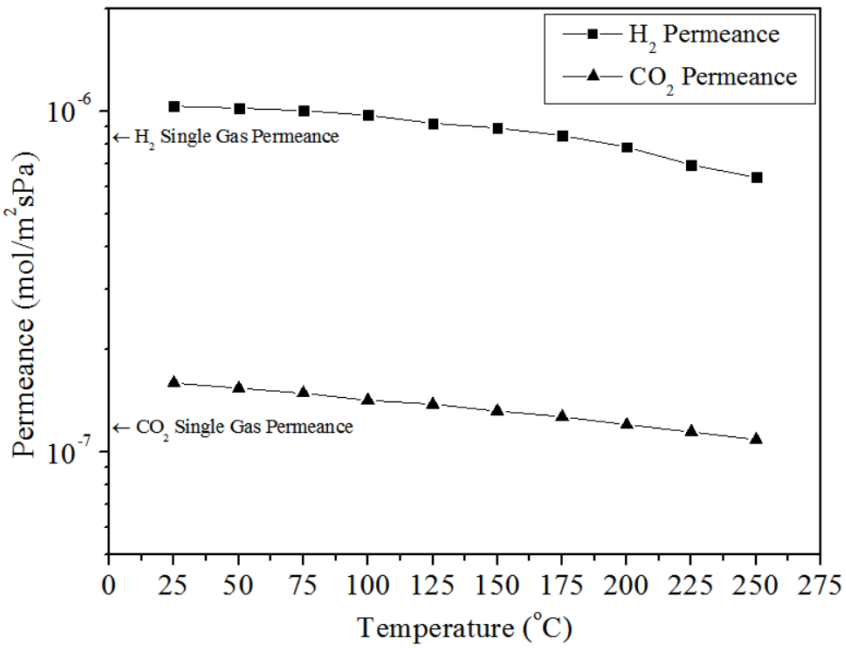

Figure 3.4 ZIF-8 membrane H_2 and CO_2 single gas permeance as a function of temperature from 25-250°C

The temperature dependent H_2 permeance plot in Figure 3.4 indicates a 38.2% decrease in H_2 permeance over the 25-250°C temperature range. This trend was also observed by (X. Zhang et al., 2014) who conducted hydrogen permeance as a function of temperature from 30°C to 200°C and observed a 65% decrease in hydrogen permeance (15.9-5.6x10^{-8} mol/m^2sPa) with incresing temperature. Distinct hydrogen electrostatic binding sites at the C=C bond of the imidazole ligand and at the center channel of the six member ring contribute to H_2 adsorption in ZIF-8 (Assfour, Leoni, & Seifert, 2010; Hui Wu, Zhou, & Yildirim, 2007). The temperature dependent permeation data for H_2 confirm lower activation energy for diffusion than heat of adsorption for H_2 in ZIF-8.

Figure 3.5 graphically illustrates the ZIF-8 membrane permeance and separation factor for a binary 50:50 H_2/CO_2 feed as a function of temperature ranging from 25-300°C. Between 25-250°C, the permeance for both H_2 and CO_2 decreases as a function of

increasing temperature, which is similar to the temperature dependency of pure gas permeance. Gas permeation through ZIF-8 membranes follows the solution-diffusion mechanism (D. Liu et al., 2014); the permeability of a permeating gas is the product of the diffusivity and solubility (or adsorption constant). Due to the similarity in single and binary gas permeance behavior, we map the ideal solution-diffusion model to the binary mixture to describe the phenomena observed. The kinetic diameters of H_2 and CO_2 are 0.29 and 0.33 nm respectively, each just slightly smaller than the 0.34 nm crystallographic pore aperture of ZIF-8.

However, due to framework flexibility and imidazole substituent displacement, the ZIF-8 pore configuration inhibits strict molecular sieving cut offs before 0.42 nm (C. Zhang et al., 2012). Framework flexibility/displacement results in large intracrystalline diffusivities for H_2 ($9.4x10^{-5}$ cm^2/s) and CO_2 ($1.7x10^{-6}$ cm^2/s) in ZIF-8 (D. Liu et al., 2014). H_2/CO_2 diffusive selectivity in ZIF-8 is 55, however, the adsorption equilibrium constant for CO_2 in ZIF-8 (0.56 mmol/g.bar) is much larger than that for H_2 (0.039 mmol/g.bar) (C. Zhang et al., 2012) at room temperature. This gives an adsorptive selectivity of about 1/15 for H_2/CO_2. The product of the H_2/CO_2 adsorptive and diffusive selectivites determines the ideal H_2/CO_2 permselectivity which is 3.7 and consequently is the same value as the separation factor obtained at room temperature during the binary experiment. The binary H_2/CO_2 separation factor is diffusion controlled or increases with respect to temperature between 25-225°C because of the relatively weaker adsorptive/stronger diffusive dependence for H_2 permeance as compared to that for CO_2 permeance.

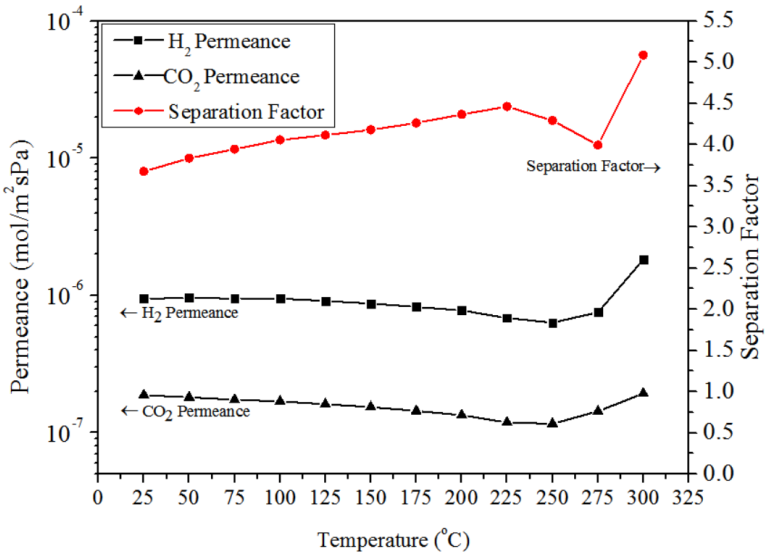

Figure 3.5 ZIF-8 membrane binary H_2/CO_2 permeance and separation factor as a function of temperature from 25-300°C

Figure 3.6 presents the transient weight change of ZIF-8 crystals under 50:50 H_2/CO_2 atmosphere using a temperature profile identical to the heating protocol utilized during the binary gas separation measurements shown in Figure 3.5. A dramatic rate of weight decrease at the onset of data collection, attributable to the loss of solvent molecules and unreacted organic moieties in trapped within ZIF-8 microcavities (Yin et al., 2014) is observed. Between 50-250°C the weight loss is extremely slow (0.04 wt %/hr) and small (less than 2%). This indicates that the large change observed for H_2 and CO_2 gas permeances (33-38%) in the membrane separation experiments between 50-250°C are not caused by membrane structural changes during the temperature dependent separation experiments, and confirms that the temperature dependence of gas permeance and separation factor shown in Figure 3.5 is determined by the temperature dependence of diffusivity and solubility of the mixture at temperatures between 25-250°C.

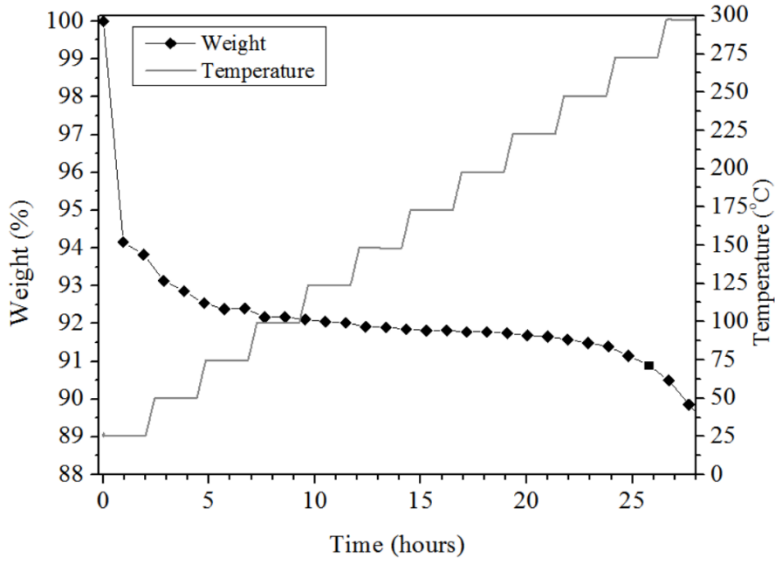

Figure 3.6 TGA weight decomposition profile of ZIF-8 crystals using a temperature profile and H_2/CO_2 atmosphere identical to temperature dependent permeation experiment

The mixture feed permeance temperature dependences for ZIF-8 membranes are quite different from the mixture permeation for microporous MFI zeolite membranes. MFI zeolite membranes have been substantially studied for H_2/CO_2 separations and provide an interesting comparison to ZIF-8 membranes. Both materials contain zeolitic structured micropores, yet present very disparate H_2/CO_2 separation characteristics as a function of temperature. During binary H_2/CO_2 permeation in MFI zeolite membranes, H_2 permeance increases while CO_2 permeance decreases as a function of increasing temperature, though pure gas permeance for both gasses decrease with increasing temperature (Bakker et al., 1996; M. Kanezashi & Lin, 2009).

It is known that diffusivity in micropores is mainly determined by the ratio of the permeating gas molecular diameter to the effective pore diameter, $\lambda=d_m/d_p$ (= 0.69 and 0.79 for H_2 and CO_2 in ZIF-8) and the activation energy for diffusion sharply increases or diffusivity decreases with increasing λ when it approaches 1 (permeating molecule size

close to the membrane pore size) (M. Kanezashi & Lin, 2009). The diffusivity for H_2 and CO_2 in MFI zeolite is respectively about $2x10^{-4}$ and $3x10^{-5}$ cm^2/s, much larger that in ZIF-8 ($9.4x10^{-5}$ cm^2/s and $1.7x10^{-6}$ cm^2/s) due to larger pore size for MFI zeolite (about 0.55 nm). The ratio of the diffusivity for H_2 to CO_2 for MFI zeolite (about 6) is also much smaller than that for ZIF-8 (about 55). Due to smaller differences in diffusivities for these two gases in MFI zeolite membranes, the presence of the strongly adsorbed CO_2 in the mixture feed has a larger effect on the diffusivity of lightly adsorbed H_2, reducing its permeance at low temperatures while CO_2 adsorption is enhanced. This explains the opposite temperature dependence of H_2 permeance within the mixture feed as compared to the pure H_2 permeance in MFI zeolite membranes (M. Kanezashi & Lin, 2009). For ZIF-8 membranes, such an adsorption induced effect in the mixture feed is insufficient to reverse the diffusion controlled selectivity that would give an opposite permeance temperature dependence for H_2 as compared to the single gas feed.

From 250-275°C, the permeance behavior for both H_2 and CO_2 inverts or increases as a function of increasing temperature, as shown in Figure 3.5. At such high temperatures, adsorption becomes negligible thus permeance is essentially controlled by diffusivity, which increases with temperature. The permeance selectivity decreases with temperature between 225-275°C because the change in diffusivity for CO_2 with a larger activation energy, increases more with temperature as compared to H_2. Beyond 275°C the H_2/CO_2 separation factor displays a step change from 4.0 to 5.1. TGA data in Figure 3.6 shows with a temperature increase from 275 to 300°C the membrane experiences a greater magnitude weight loss (2%) than previously experienced due to a faster decomposition rate (0.1-0.3 wt%/hr). As will be discussed later, this indicates a structural change in ZIF-8

material which is most likely responsible for altering the transport mechanism previously governing H_2/CO_2 permeability and selectivity.

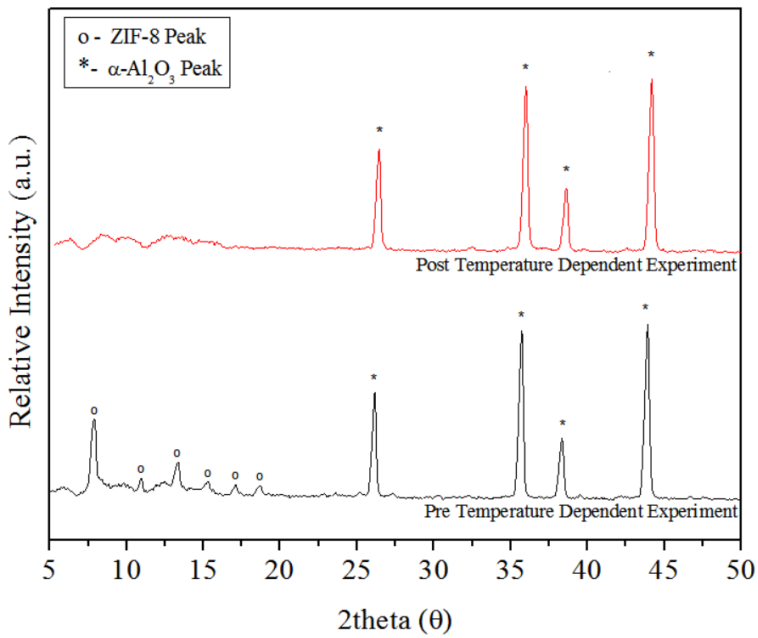

Figure 3.7 ZIF-8 membrane XRD patterns before and after binary H_2/CO_2 temperature dependent (25-300°C) permeance study

Figure 3.7 shows XRD patterns of the ZIF-8 membrane before and after the temperature dependent membrane experiment shown in Figure 3.5. Structural changes in the ZIF-8 membrane thin film are evidenced through the disappearance of all peaks associated with the ZIF-8 morphology. This finding is corroborated by corresponding SEM images of the ZIF-8 membrane after the temperature dependent experiment shown in Figure 3.8. The micrographs present a new structure bearing an amorphous topology similar to that of a polymeric or carbon molecular sieve membrane upon analysis at low magnification (Ma, Lin, Wei, Kniep, & Lin, 2013). Greater magnification shows evidence

of a transformed, lacerated surface with slightly raised portions resembling extremely faint, flattened/decomposed ZIF-8 rhombic dodecahedral crystals.

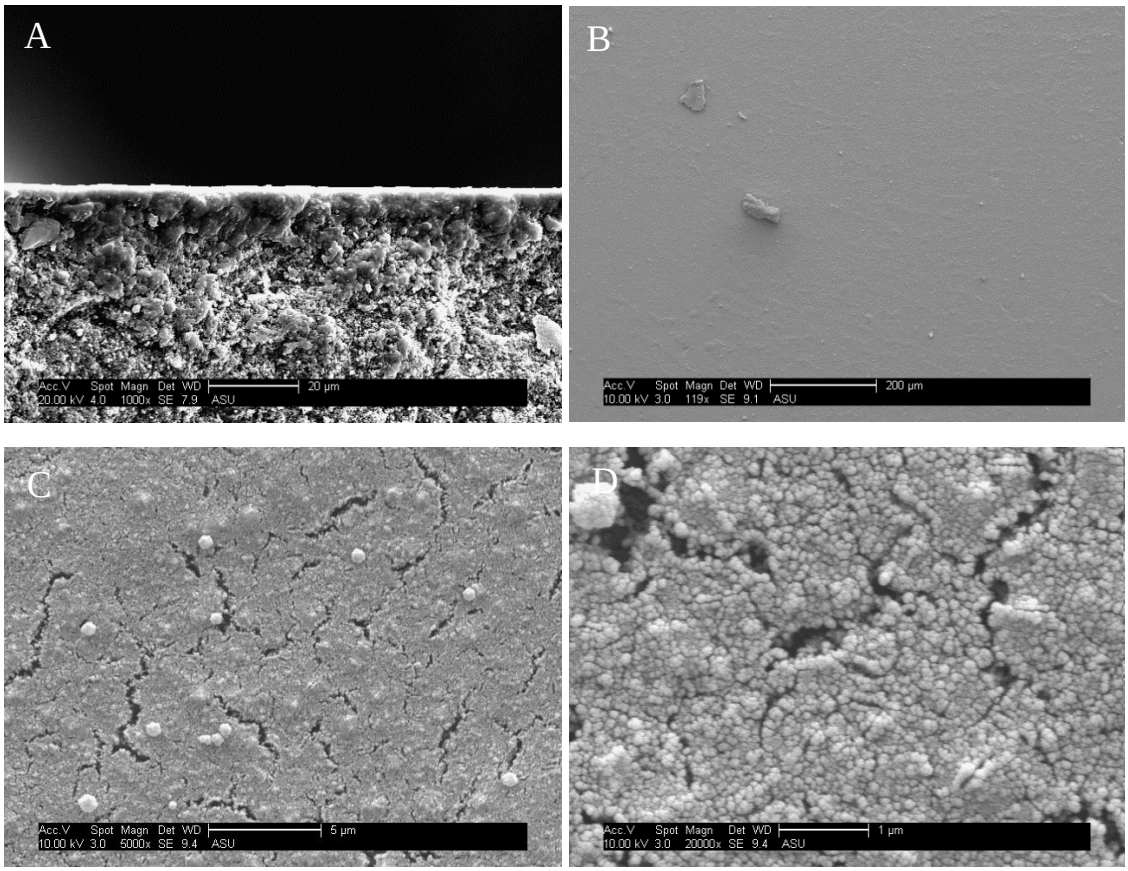

Figure 3.8 ZIF-8 membrane SEM micrographs after temperature dependent (25-300°C) binary H_2/CO_2 experiment: cross-section (A), top views (B-D)

ZIF-8 crystal decomposition from the analogous TGA experiment is also corroborated by pre and post experimental XRD patterns in *Figure 3.9* which show a decrease in peak intensities at the characteristic ZIF-8 2θ values. It is duly noted that only a partial decrease in XRD pattern intensity (56% decrease in (011) peak intensity) was experienced after the ZIF-8 powder temperature programmed TGA study. In contrast, the analogous membrane permeance test showed complete elimination of all peaks associated

with ZIF-8. A significantly larger amount of material must be consumed before crystallinity is eliminated in a 15 mg ZIF-8 powder sample as compared to a ZIF-8 film 2.5μm in thickness and 22 mm in diameter which weighs around 1.08 mg and can explain the differences in x-ray diffraction patterns.

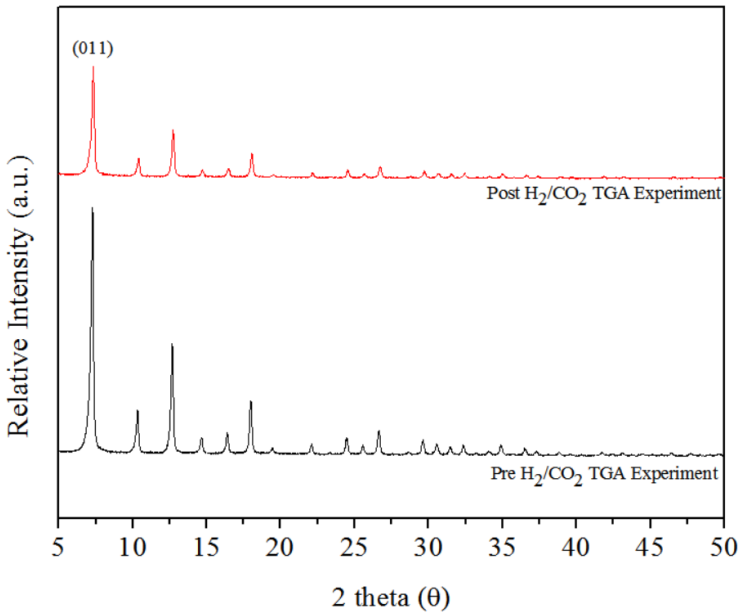

Figure 3.9 ZIF-8 powder XRD patterns before and after H_2/CO_2 atmosphere temperature dependent (25-300°C) TGA experiment

3.3.2 Transient Separation Properties and ZIF-8 Membrane Structural Changes

In the previously performed binary experiments the ZIF-8 membrane was subjected to each temperature for only 2.5 hours in a dynamic experiment over a 30 hour duration. To better understand and more carefully analyze the thermal stability of ZIF-8 membrane thin films, isothermal, transient, 50:50 H_2/CO_2 permeation experiments were conducted at temperatures of 50, 100 and 150°C for 24 hours enabling adequate bounds to be placed on ZIF-8 membrane static thermal stability. The permeation results of each isothermal test are shown in Figure 3.10.

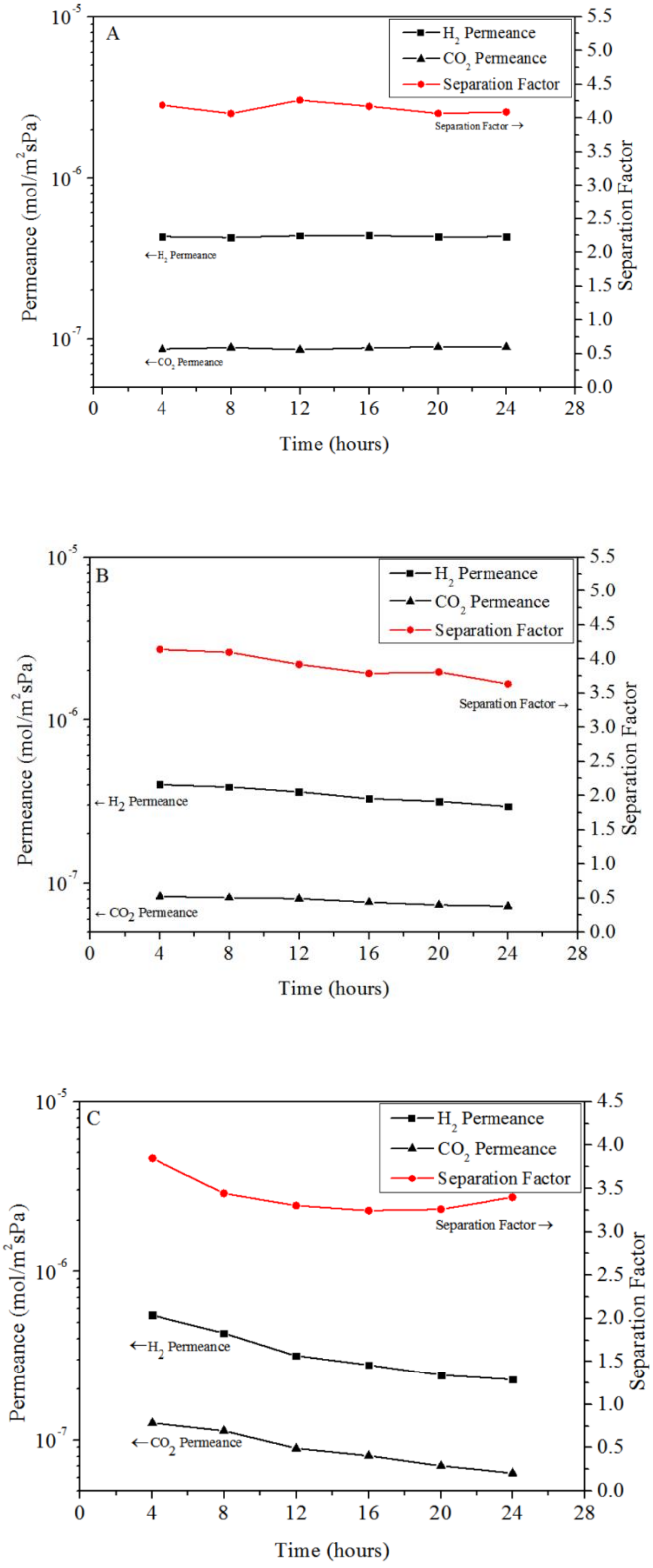

Figure 3.10 Transient profiles of ZIF-8 membrane H_2/CO_2 mixture permeance and separation factor with respect to time at isothermal temperatures of (A) 50°C, (B) 100°C and (C) 150°C (24 hours)

Table 3.2 ZIF-8 Membrane Percentage Change in H_2/CO_2 Separation Performance and XRD/FTIR Peak Intensity Ratios before and after Low Temperature Transient Tests

Transient Experiment	% Decrease in H_2 Permeance	% Decrease in CO_2 Permeance	% Decrease in CO_2 Separation Factor	ZIF-8 (011) Peak to α-Al_2O_3 (012) Peak XRD Intensity Ratio Before/After Transient Experiment	Experimental ZIF-8 Membrane/As-synthesized ZIF-8 Membrane δCH_3 FTIR Band Intensity	Experimental ZIF-8 Membrane/As-synthesized ZIF-8 Membrane C=N FTIR Band Intensity
50°C	0.2	0.0	2.5	1.20/1.26	1.06	1.00
100°C	26.5	12.2	12.9	1.20/1.23	1.04	1.25
150°C	58.6	49.6	11.6	1.69/0.95	0.67	0.68

Qualitative analysis of the transient profiles suggest that the extent of decline in both H_2 and CO_2 permeances is intensified with respect to increasing isothermal temperature. Table 3.2 tabulates and quantifies the percentage decreases in H_2/CO_2 permeances and separation factors during the isothermal transient experiments. At 50°C both H_2 and CO_2 permeances and separation factor remain essentially constant over the 24 hour duration. However, at 100°C 26.5% and 12.2% decreases in H_2 and CO_2 permeances are observed. The greater extent of decline in H_2 permeance as compared to that of CO_2 causes the separation factor to decrease by 12.9% over the 24 hour period. At an isothermal temperature of 150°C, more dramatic decreases in H_2 and CO_2 permeances are incurred. The transient permeance profiles obtained during the 150°C experiment indicate that the percentage declines in H_2 and CO_2 permeances were 2 and 4 times greater than those observed during the 100°C test respectively.

It is possible that local defects at un-saturated Zn sites of the ZIF-8 secondary building units might have been created during permeance tests and caused performance instability (Kwon, Jeong, Lee, An, & Lee, 2015b). It is also possible that the CO_2 chemisorption phenomena previously observed by Xu et al. (G. Xu et al., 2011) during transient H_2/CO_2 tests occurred, however it would seem that the temperature dependency of the CO_2/imidazole reaction is greater in this study and may be due to differences in membrane crystallinity. Xu et al. observed the postulated chemisorption phenomena at room temperature (G. Xu et al., 2011), whereas in this study, comparable H_2/CO_2 decreases were not observed until performing isothermal tests at 150°C.

Membrane characterization can enable further insight into the physical changes of the membrane structure and further explain the permeation phenomena observed**.** Figure

3.11 presents comparative pre and post transient experiment XRD patterns and changes in XRD relative pattern intensity are quantitatively described in Table 3.2 which tabulates ZIF-8 membrane (011) plane intensity with respect to α – alumina (012) plane intensity before and after the 24 hour isothermal transient experiments studied at 50, 100 and 150°C respectively. XRD patterns corroborate preservation of the ZIF-8 phase after each isothermal experiment. After isothermal 50 and 100°C experiments, ZIF-8 to α-alumina peak intensity is essentially comparable or even slightly increased due to slight changes in ZIF-8 crystal dimensions through removal of guest solvent molecules during permeation. However, decreases in the relative peak intensity are significant for the sample tested at 150°C and indicates that ZIF-8 degradation or crystallinity elimination occurred over the 24 hour isothermal experiment.

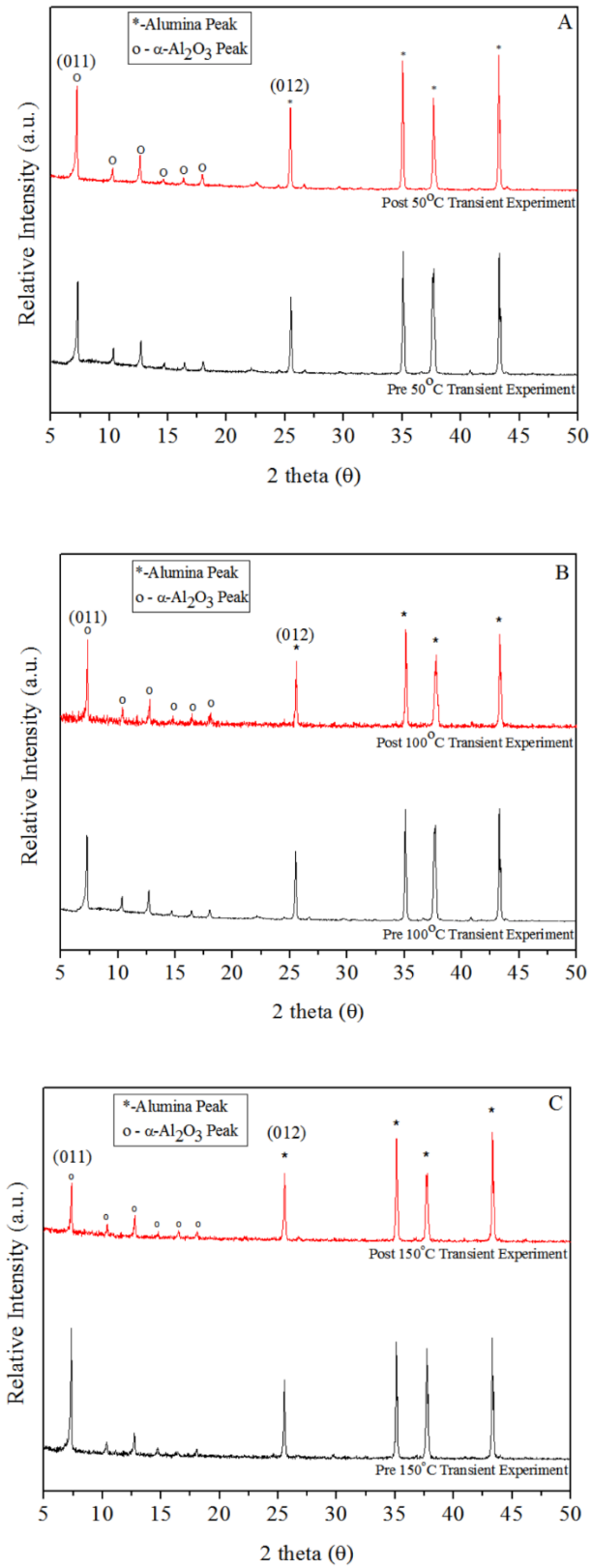

Figure 3.11 ZIF-8 membrane XRD patterns before and after 24 hour binary H_2/CO_2 separation isothermal study at (A) 50°C, (B) 100°C and (D) 150°C

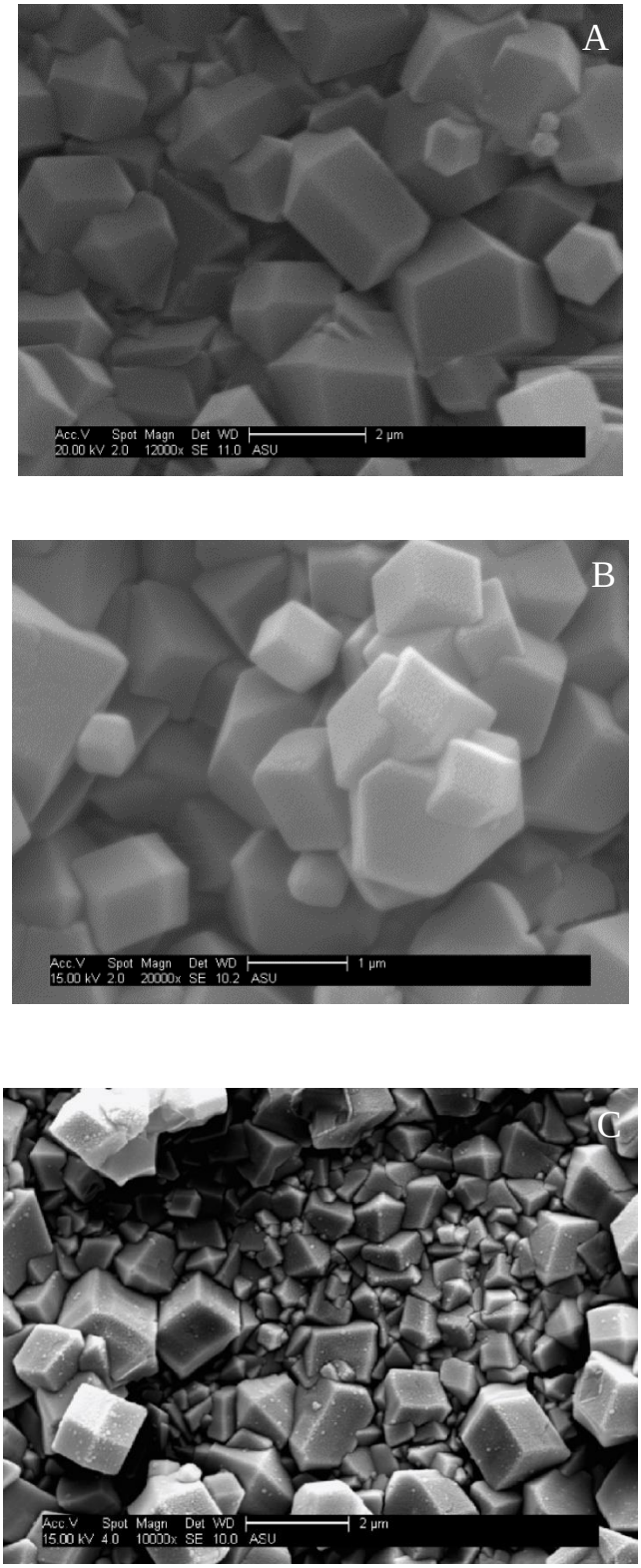

Figure 3.12 SEM micrographs of ZIF-8 membranes post binary H_2/CO_2 24 hour transient separation studies at isothermal temperatures of (A) 50°C, (B) 100°C and (C) 150°C

Upon analysis of SEM micrographs, the crystal morphology and textural features of the membranes held at 100 and 50°C remain intact (Figures 3.12 A&B). However, intermittent defects are expressed along the faces and edges of the rhombic dodecahedral crystals composing the ZIF-8 membrane held at 150°C *(Figure 3.12 C)* and may illustrate ZIF material precipitating out from the ZIF-8 polycrystalline network crystals. The results found in SEM micrographs and XRD analysis complement each other and the permeance data well. The greatest amount of crystal destruction and permeance performance decreases were observed during the 150°C isothermal transient experiment, but at lower temperatures, comparatively little to no changes in crystallinity, external crystal morphology and performance were observed.

The data shown in Figures 3.7 and 3.8 suggest more prominent changes in the ZIF-8 thin film structure occur at higher temperatures. To further understand structural changes in the ZIF-8 framework at high temperature, a transient separation test was conducted on a separate ZIF-8 membrane at 300°C for 24 hours. Figure 3.13 graphically depicts H_2/CO_2 permeance and separation factor during the high temperature isothermal transient experiment. Between 0-4 hours, a sharp decrease in H_2 and CO_2 permeances with a resulting increase in H_2/CO_2 separation factor is observed. After 4 hours, the H_2 and CO_2 permeances both increase and reach steady-state values after 12 total hours of permeation time and a separation factor of ~3.7 is sustained for the duration of the study. After 12 hours, we prognosticate that a stable permeance and separation factor is indicative of forming a structure that is kinetically or possibly thermodynamically stable at 300°C.

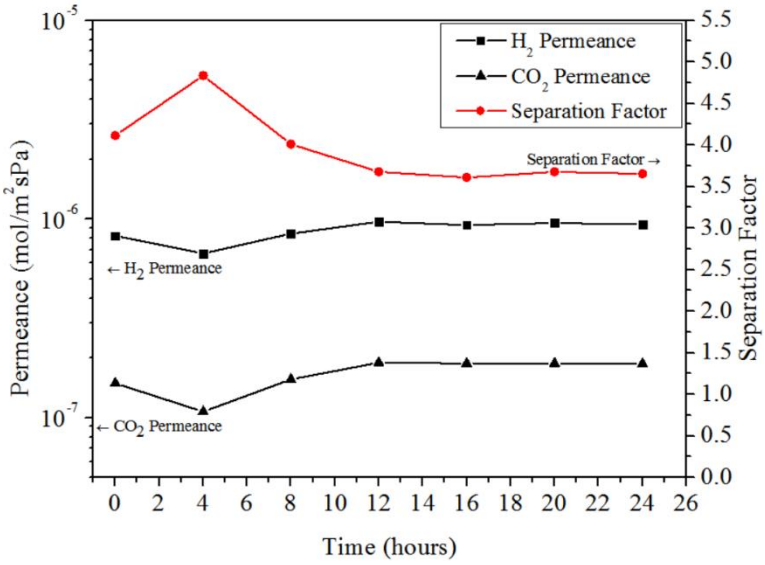

Figure 3.13 ZIF-8 membrane H_2/CO_2 mixture permeance and separation factor with respect to time during 300°C isothermal transient experiment (24 hours)

Post experimental XRD patterns and SEM micrographs of the membrane utilized in the 300°C isothermal transient experiment are depicted in Figures 3.14 & 3.15. The disappearance XRD peaks associated with the ZIF-8 phase again indicates formation of an amorphous structure. SEM images show that the surface of the ZIF-8 membrane after subjection to thermal stress at 300°C still retains crystal facets but with less defined, eroded faces. As noted from Figure 3.13, the steady-state H_2 and CO_2 permeances are slightly greater than the initial rates observed at 0 hours and although the separation factor is lower than initially observed, the newly formed amorphous material is still able to separate H_2 from CO_2. It is likely that the new amorphous structure has a somewhat wider pore structure that decreases transport resistance enabling greater H_2 and CO_2 permeances. To maintain H_2/CO_2 selectivity, the new structure with comparatively less-order, likely bears new pore shape with a modified tortuosity that enables separation of H_2 and CO_2 more based upon

entropic selectivity rather than energetic/sorptive selectivity similar to that of carbon molecular sieve (CMS) membranes (Rungta, Xu, & Koros, 2012).

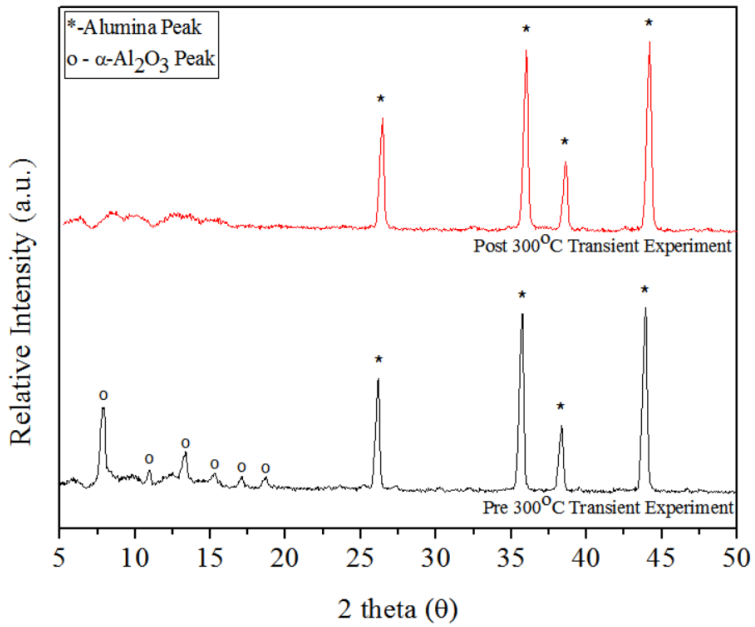

Figure 3.14 ZIF-8 membrane XRD pattern before and after 24 hour binary H_2/CO_2 separation isothermal study at 300°C

Figure 3.16 illustrates comparative IR spectral bands of experimental membranes. The fresh, as-synthesized ZIF-8 membrane transmittance bands are in good agreement with those reported by Ordonez et al. (Ordoñez et al., 2010) and Hu et al. (Y. Hu et al., 2011). IR bands between 900-1350 cm^{-1} are associated with in-plane bending modes of the imidazole ring. The intense bands between 1350-1500 cm^{-1} are concomitant with entire imidazole ring stretching and the small peaks indicated at 1384 cm^{-1} and 1584 cm^{-1} correspond to $–CH_3$ bending and C=N stretching modes respectively. Due to spectral saturation, Zn-N modes usually present at 421 cm^{-1} are not shown. Table 3.2 additionally highlights relative IR spectral intensities of the $–CH_3$ and C=N bonds of isothermally tested

membrane thin film surfaces with respect to an as-synthesized membrane for semi-quantitative relative magnitude analysis.

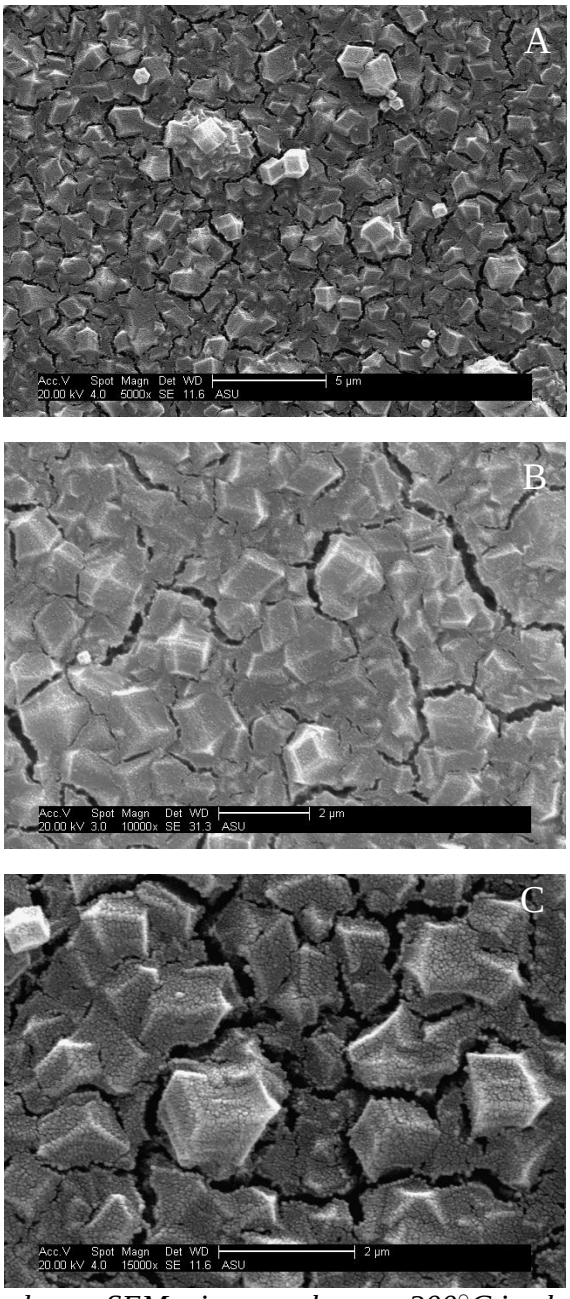

Figure 3.15 ZIF-8 membrane SEM micrographs post 300°C isothermal transient binary H_2/CO_2 experiment: 5,000X magnification (A), 10,000X magnification (B) and 15,000X magnification (C)

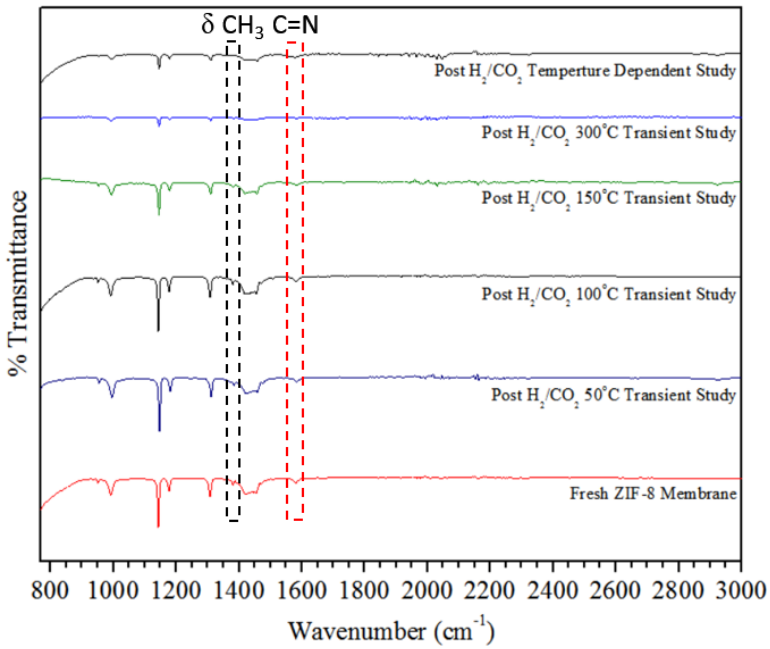

Figure 3.16 FTIR spectra of ZIF-8 membranes held in H_2/CO_2 atmosphere after 25-300°C temperature dependent experiment and 24 hour transient isothermal experiments at 50, 100, 150, and 300°C respectively all relative to as-synthesized (fresh) ZIF-8 membrane spectrum

Visual comparison of post experimental low temperature isothermal IR spectra to that of the as-synthesized spectra indicate preservation of imidazole ring physical properties after permeation at 50 and 100°C. Further detailed evidence of bond preservation is evidenced by the relative intensity data in Table 3.2 which show comparable spectral intensities before and after the 50 and 100°C experiments. In contrast, relative intensity values at the corresponding spectral bands for the membrane isothermally tested at 150°C indicate depletion of CH_3 and C=N bonds. The results found in the FTIR experiments complement the SEM/XRD data well and indicate that alumina supported ZIF-8 thin films preserve full crystallinity and structural integrity at temperatures below 150°C.

At greater temperatures, significant, definitive changes in C=N, methyl group and entire ring bonding occurred and is evidenced by considerable broadening of the corresponding spectral modes for the membranes isothermally tested at 300°C and utilized in the temperature dependent test. Specific evidence of C=N bond breaking and demethylation observed in the high temperature spectra agree with the results observed by Lin and James (James & Lin, 2016) who postulated that a heterogeneous imidazole-Zn-azirine partially carbonized ZIF-8 structure is formed through a sequence of thermolytic decomposition reactions after thermally annealing ZIF-8 crystals at 300°C for 20 hours in H_2/CO_2 atmosphere. For ZIF-8 crystal decomposition in H_2/CO_2 environment at 300°C for 20 hours the following decomposition reaction equation was proposed (James & Lin, 2016):

$$Zn(C_4H_5N_2)_2 + heat \rightarrow C_4H_5N_2 - Zn - C_2H_2N + Gaseous\ Products \quad (3.A)$$

where the Zn complex on the reactants side of Reaction 3.A represents a single building block of ZIF-8 consisting of a zinc cation coordinating two imidazole ligands. After sustained thermal stress at the corresponding temperature it is postulated that the average solid structure remaining (product) after ZIF-8 crystal decomposition is a Zn cation coordinated to the N atom of a fully intact 2-methylimidazole ligand and the N atom of an azirine molecule. Differences in ZIF-8 material concentration between a bulk sample of ZIF-8 crystals and an alumina supported ZIF-8 thin film invalidate a 1-to-1 comparison of FTIR spectra, however we postulate that a similar structure is formed upon decomposition of ZIF-8 membranes.

The morphology changes shown in the post experimental SEM images of Figures 3.8 and 3.15 can be explained in part by the partial carbonization process described in Reaction 3.A. Upon sustained thermal stress of ZIF-8 membrane crystals at 300°C, demethylation and release of framework N atoms from deteriorated C/N and Zn-N bond destruction each occur to form the postulated imidazole-Zn-azirine structure. Although Zn-N spectral bands are not shown, Zn must lose coordination with N in order to form the postulated imidazole-Zn-azirine structure. We deduce that if C=N and $–CH_3$ bonds are broken, Zn-N bonds must also break as they are comparatively the weakest bond in the ZIF-8 structure (Gadipelli et al., 2014). In the case of ZIF-8 membrane crystals, partial carbonization and loss of coordination at Zn-N nodes which act as major structural supports most likely induces framework collapse to form eroded crystals which eventually reduce to a partially carbonized membrane surface topology that is visibly flat or presents eroded crystal facets.

The structural collapse noted in this study somewhat contrasts the phenomena observed when thermally treating loosely packed ZIF-8 crystalline powders. In our previous work (James & Lin, 2016), ZIF-8 crystalline powders were treated isothermally at 300°C in H_2/CO_2 atmosphere for 20 hours in a TGA experiment analogous to the 300°C transient membrane experiment conducted in the current study. Comparative SEM characterization analyses before and after thermal treatment of ZIF-8 crystals illustrated particle growth through coarsening/Ostwald through ripening phenomena (James & Lin, 2016) and XRD pattern/FTIR spectral analyses from our previous work (James & Lin, 2016) show that ZIF-8 crystals retain a relatively greater amount of crystallinity/bond preservation as compared to membrane thin films decomposed under similar conditions. In

this study, particle collapse occurs rather than particle coarsening and may allude to slight differences in microstructural changes that occur upon thermal treatment of ZIF-8 powders which present kinetic thermal stability up to 200°C versus ZIF-8 membrane thin films which seem thermally stable below 150°C.

It has been noted in literature that the thermomechanical compatibility (Drobek et al., 2015; X. Zhang et al., 2014) and acidity (J. Kim & Lee, 2016) of the membrane support plays a significant role in membrane thermal and hydrothermal stability respectively. Under hydrothermal conditions in the presence of 10 mol% water vapor it was determined that the acidic nature of α-alumina supports catalyzes hydrolysis reactions which enable protonation and subsequent deterioration of ZIF-7 and ZIF-8 material adhered α-alumina supports (J. Kim & Lee, 2016), however, under dry (J. Kim & Lee, 2016) and more mild humidity conditions (3 mol% water vapor) (Y. Li et al., 2010), the support does not seem to initiate ZIF decomposition through protonating reactions. These findings enable deduction that support acidity does not play a significant role in ZIF stability under dry conditions.

During thermal annealing under dry conditions, ZIF-8 thin films are subjected to incongruent mechanical stresses as a result of differences in thermal expansion coefficients between the alumina support and the membrane structure (X. Zhang et al., 2014). The resulting thermomechanical stress possibly compromises the ZIF thin film bonds during thermal annealing. ZIF crystals do not experience the aforementioned thermomechanical stresses during TGA experiments. The additional stress mechanism induced during thermal annealing of alumina supported ZIF-8 membranes likely exacerbates framework instability upon static thermal treatment. High temperature static stability experiments directly

comparing α-alumina supported ZIF-8 membranes with and without thermomechanically stabilizing interlayers or supports with thermal expansion coefficients more similar to that of ZIF-8 may be a point for future study. Additionally, metal oxide supports of varying acidity that are thermomechanically compatible with ZIF-8 would enable an effective study on the influence of support acidity on ZIF-8 hydrothermal stability.

3.4 Conclusions

The thermal stability of high quality ZIF-8 membranes was systematically studied in terms of material structure and separation characteristics in H_2/CO_2 atmosphere at high temperatures. Dynamic temperature dependent permeation experiments show that H_2/CO_2 permeance and selectivity adhere to the solution-diffusion model between 25-275°C, however beyond 275°C it is postulated that an amorphous carbonized imidazole-Zn-azirine structure is formed. Static isothermal permeation tests more adequate for static stability determination, show that ZIF-8 membrane thin films maintain crystallinity/bond integrity and sustain separation performance over a 24 hour experimental duration at temperatures below 150°C. However, at temperatures of 150°C and greater, ZIF-8 membrane thin films incur increased amounts of thermally induced carbonization of the imidazole ligand with respect to increasing temperature. The extent of carbonization changes the pore structure of the ZIF-8 membrane, and hence H_2/CO_2 permeance and selectivity. Thermomechanically induced stresses are caused by differences in thermal expansion coefficients of ZIF-8 membrane thin films and α-alumina supports which likely compromise ZIF-8 membrane structural bonds and may account for differences in static

thermal stability observed when comparing ZIF-8 thin films and ZIF-8 crystals which do not incur identical thermomechanical stresses upon thermal annealing.

CHAPTER 4

ZIF-8 MEMBRANE ETHYLENE/ETHANE TRANSPORT CHARACTERISTICS IN SINGLE GAS AND BINARY MIXTURES

4.1 Introduction

According to the preceding thermal stability studies, ZIF-8 shows the most immediate promise for low to moderate temperature (< 150°C) separation applications which is not prohibitively limiting because the intricate Zn-N coordination in ZIF-8 enables a structural configuration which facilitates excellent kinetic-based separation of propylene (propene)/propane ($C_{3=}/C_{3-}$) (K. Li et al., 2009; Pimentel & Lively, 2016) which is conducted at near-ambient temperatures. The effective ZIF-8 pore aperture (0.42 nm) (C. Zhang et al., 2012) is just above that of $C_{3=}$ (0.402 nm) and comparable to C_{3-} (0.416 nm). In binary propylene/propane studies ZIF-8 membrane thin films have demonstrated high separation factors ranging between 30-180 (Eum, Ma, Rownaghi, Jones, & Nair, 2016; Kwon, Jeong, Lee, An, & Lee, 2015a), acceptable stability specific for light hydrocarbon separations (Eum et al., 2016; D. Liu et al., 2014), and promise of modular scale-up (A. J. Brown et al., 2014; Eum et al., 2016) to potentially debottleneck and alleviate energy consumption in highly intensive C_3 splitter processes (Alshehri & Lai, 2015).

While the C_3 separation prowess of ZIF-8 is largely known, ethylene (ethene)/ethane ($C_{2=}/C_{2-}$) separations which are currently conducted in highly energy intensive cryogenic distillation processes are less abundant in ZIF-8 literature. Most experimental works focus on equilibrium adsorption (Böhme et al., 2013; C. Zhang et al., 2012) and kinetic uptake (Chmelik, Freude, Bux, & Haase, 2012; Pimentel & Lively, 2016;

C. Zhang et al., 2012) of ethylene and ethane in ZIF-8 crystals. Consensus amongst studies show that ethane/ethylene adsorptive selectivity is close to 2 (Böhme et al., 2013; Bux, Chmelik, Krishna, & Caro, 2011; C. Zhang et al., 2012) and ethylene/ethane diffusive selectivity is approximately 5 (Bux, Chmelik, et al., 2011; Chmelik et al., 2012) in the linear adsorption isotherm pressure region.

In terms of membrane study, Caro and co-workers performed ethylene/ethane permeation experiments in ZIF-8 membranes as a function of pressure (Bux, Chmelik, et al., 2011) and utilized grand canonical monte Carlo (GCMC) simulations and infrared microscopy (IRM) equilibrium/transient uptake experiments in a single ZIF-8 crystal to describe phenomena observed in the membrane. A decrease in the C_2 separation factor (2.8-2.4) as a function of total feed pressure (1 to 6 atm) as a result of decreased ethylene diffusive selectivity with increasing adsorbate loading in the ZIF-8 pore was observed (Bux, Chmelik, et al., 2011). At a total feed pressure of 6 atm, it was noted that the ideal C_2 separation factor was above 4.2; approximately 75% greater than observed in binary experiments (Bux, Chmelik, et al., 2011). In subsequent ZIF-8 membrane studies, Lai and co-workers obtained thermodynamically corrected C_2 diffusivities calculated from pressure dependent permeation measurements correlated to previously collected isotherm data (Pan, Liu, Zhao, Wang, & Lai, 2015). Previous studies have also shown sharp molecular sieving of ethane/propane (Pan & Lai, 2011), ethylene/propane (Pan & Lai, 2011) and H_2/C_3 mixtures (Eum et al., 2016; Pan & Lai, 2011).

The previous studies on ZIF-8 membranes reported C_2 diffusivity/permselectivity data at room temperature (Bux, Chmelik, et al., 2011; Pan & Lai, 2011) and the pressure dependency of binary C_2 permeation (Bux, Chmelik, et al., 2011). However, the differences

between binary and single gas C_2 permeation/separation behavior as a function of pressure and an explanation of why binary C_2 selectivity is significantly lower than single component ideal selectivity has not been provided. Furthermore, there lacked C_2 permeation data for ZIF-8 membranes as a function of temperature, from which, parameters such as activation energy and entropy of diffusion can be derived to obtain a better understanding of the energetic and entropic contributions to C_2 transport and selectivity. Additionally, H_2/C_2 separations as a function of temperature, relevant to post ethane cracking applications have not been studied in ZIF-8 membranes.

A better understanding of C_2 transport properties in the well-understood ZIF-8 structure can enable the design/selection of new or existing ZIF materials with structures that can provide improved ethylene/ethane separation characteristics. In the present work, we studied single and binary gas permeation/separation properties of ethylene/ethane and H_2/C_2 in ZIF-8 membranes as a function of temperature and feed pressure in addition to the adsorption isotherms of these gases in ZIF-8 at different temperatures. These data will provide an improved understanding of gas diffusion in ZIF-8 as compared to other microporous materials and effects of intermolecular interaction on binary gas separation by ZIF-8 membranes.

4.2 Experimental

4.2.1 ZIF-8 Sorbent and Membrane Synthesis and Characterization

ZIF-8 membranes were prepared according to our previously reported protocol (James & Lin, 2017). Briefly, A-16 calcinated alumina powders (Almantis, Pennsylvania,

U.S.A.) were formed into 22 mm diameter green-body disks using a custom prepared mold/die set and a pressing apparatus (Carver Inc., Indiana, U.S.A.). Mechanically strengthened α-alumina substrates were formed by sintering the custom prepared green-body disks at 1150°C for 30 hours. The substrates were polished with 500, 800, 1200 and 2000 grit SiC polishing papers (Struers, Ohio, U.S.A.) then washed in deionized water and methanol under sonication.

ZIF-8 sorbent crystals were prepared by the method reported by Cravillion et al. (Cravillon et al., 2011) 0.734 g of zinc nitrate hexahydrate [$Zn(NO_3)_2 \bullet 6H_2O$] (98% Sigma Aldrich) and 0.811 g of 2-methylimidazole (99% Sigma Aldrich) were each dissolved separately in glass beakers each containing 25 mL of methanol (99% Sigma Aldrich) under stirring for 30 minutes. The 2-methylimidazole solution was poured dropwise into the zinc nitrate hexahydrate solution and kept stirring for 1 hour. After mixing, the ZIF-8 crystals were aged for 24 hours without stirring. A well separated, clear methanol supernatant and white crystal precipitant interface was formed after aging. The white precipitant crystals were washed and centrifuged in methanol then dried in a vacuum oven at 60 kPa and 25°C. 0.028 g of dried, ground ZIF-8 crystals were placed in a glass container containing 100 mL of methanol. A homogeneous 0.035 wt% colloidal ZIF-8 seeding solution was formed by sonicating the mixture for 15 minutes.

Slip-cast coating of the α-alumina supports with a ZIF-8 seed layer was performed by bringing the previously prepared α-alumina support in contact with the seeding solution for 10 seconds, the support was dried in ambient air for 10 minutes then the coating procedure was repeated a once more. The seeded supports were placed in a furnace which was ramped to 95°C at a rate of 0.3°C/min, held at constant temperature for 3 hours and

subsequently ramped down to room temperature at the same rate. For secondary growth, the seeded supports were placed in a Teflon holder, held vertically, and submerged into a growth solution containing 0.11 g of [$Zn(NO_3)_2 \bullet 6H_2O$] and 2.27 g of 2-methylimidazole in 40 mL of deionized water contained within a Teflon lined stainless steel autoclave and placed in an oven at 120°C for 7 hours. Secondary growth was repeated again to seal defects.

Visual analyses of ZIF-8 crystal and membrane surface morphology were performed using an XL30 Environmental FEG (FEI) scanning electron microscope with an accelerating voltage of 20 kV. ZIF-8 membrane crystallinity was analyzed using a X'Pert Pro PANalytical x-ray diffractometer at 45 kV, 40 mA with a scan speed of 2°/min for 2θ, using Cu Kα radiation (λ = 0.1543 nm).

4.2.2 Ethylene/Ethane Adsorption Analysis and Permeation/Separation Experiments

Equilibrium adsorption experiments for ethylene and ethane were carried out utilizing a Micromeritics ASAP 2020 volumetric adsorption device. Adsorption isotherms for each gas were collected at temperatures between 25-100°C using gas pressures up to 1 atm. A dewar with a circulating oil bath was utilized to maintain each isothermal temperature. Approximately 80 mg of ZIF-8 powder from the same batch of crystals synthesized for membrane seeding were used for each adsorption test. Initial sample degassing took placed at the degassing sample port of the ASAP 2020 for 12 hours at 150°C at a vacuum pressure of 500 μm Hg. Subsequent degassing between each isotherm experiment took place for 3 hours at 150°C at the same vacuum pressure. The free space of the system was determined using helium gas. Commercially pure grade (99.5%)

ethylene and Instrument grade (99.5%) ethane gasses from Air Liquide were utilized for all gas adsorption and permeation test. All hydrocarbons were used as received without any further purification.

In gas permeation tests, the α-alumina supported ZIF-8 membrane was sealed into a stainless steel permeation cell using VITON O-rings (O-rings West). The effective permeation area after sealing the membrane was 2.27 cm^2. The as-synthesized membrane probed with helium (He) and sulfur hexafluoride (SF_6) to assess the quality of ZIF-8 membranes. He or SF_6 was supplied directly to a single gas steady-state permeation apparatus (James & Lin, 2017) and maintained at 2.4 atm using a needle valve. The permeate side was maintained at atmospheric pressure and connected directly to a bubble flow meter without a sweep gas.

Subsequent ethylene, ethane, single gas/binary permeation/separation experiments were performed utilizing the Wicke-Kallenbach technique. A total feed flow rate of 100 mL/min (50 mL/min of each gas in binary experiments) and a nitrogen sweep gas flow rate of 50 mL/min was utilized in each experiment. Volumetric flow rates correspond to measurements collected at ambient temperatures ranging between 23.6-25°C and atmospheric pressure. All gas flow rates were maintained by mass flow controllers connected directly to the respective gas cylinders through non-combustive tubing. The feed pressure was modulated by a needle valve which was remained fully open for 1 atm feed pressure and incrementally closed to reach pressures up to for 4 atm. All temperature dependent tests were performed between 25-100°C at total feed pressure of 1 atm, a ramp rate of 1°C/minute was utilized to reach each 25°C temperature increment spanning the

interval. Each temperature or pressure was held typically for 2 hours or longer, until a steady state permeance was reached before collecting permeation readings.

The composition of the retentate and sweep sides of the membrane were analyzed using gas chromatography (Agilent 6890, Alltech Haysep DB 100/120 packed column with dimensions: 9.14 m, 0.3175 cm, 0.2159 cm). In each permeation experiment, triplicate runs were performed and the error bars represent the standard error of the mean for permeation and selectivity/separation factor measurements reflected in experimental plots.

4.3 Results and Discussion

4.3.1 Characteristics of ZIF-8 Crystals and Membranes

Figure 4.1 shows an XRD pattern and SEM micrograph top view and cross section of the as-synthesized ZIF-8 membrane utilized in this work. The ZIF-8 phase of the α-alumina supported membrane is confirmed through XRD spectral intensities and physical morphology in agreement with that of ZIF-8 crystalline powders from simulation (Lewis et al., 2009) and membranes from our previous work (James & Lin, 2017). The ZIF-8 membrane thickness is ~ 5 μm. Table 4.1 tabulates permeance and separation data for molecular probing of the ZIF-8 membrane. The data were measured at 1 atm, 25°C for the light olefin/paraffin pairs and at 2.4 atm, 25°C for He and SF_6. SF_6 permeance on the order of 10^{-10} mol/m^{2}sPa and an He/SF_6 ideal selectivity of 1000 (165 times greater than the Knudsen selectivity value of 6.0) are both indicative of a good quality ZIF-8 thin film layer.

The 50:50 binary propylene/propane permeances and separation factor of 36.0 are competitive with ZIF-8 membrane literature values tabulated by Kwon et al. (Kwon et al.,

2015) and further corroborates a ZIF-8 membrane with molecular sieving ability. The 50:50 binary ethylene/ethane separation factor of 2.0 is slightly lower than the value of 2.4 obtained by Caro and co-workers who performed binary experiments at a total feed pressure of 1.5 atm under similar conditions utilizing a 25 μm thick membrane formed from in-situ microwave growth (Bux, Chmelik, et al., 2011). However our binary separation factor is comparable to the ideal $C_{2=}/C_{2-}$ selectivity (2.1) calculated from the work of Lai and co-workers who also utilized seeded secondary growth (Pan & Lai, 2011). Differences in the $C_{2=}/C_{2-}$ separation factor could be due to slight differences in polycrystalline structures as a result of different synthesis protocols; a relatively thick ZIF-8 membrane likely possesses fewer or covered defects. The ethylene permeance of 7.8 x 10^{-8} mol/m^{2}sPa obtained in this work for a 5 μm ZIF-8 membrane is approximately half that obtained by the 2.5 μm thick membrane obtained by Lai and co-workers (15.0 x 10^{-8} mol/m^{2}sPa, 1 atm feed pressure) and is consistent with the difference in membrane thickness. From the comparison data we conclude that the ZIF-8 membrane utilized in this work likely possesses some sub-nano/nanosized intercrystalline defects but is of high integrity.

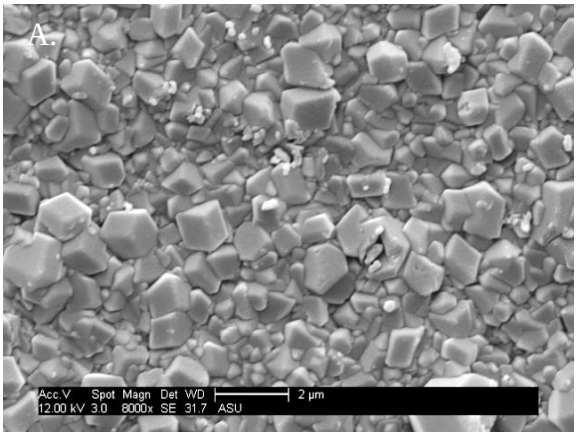

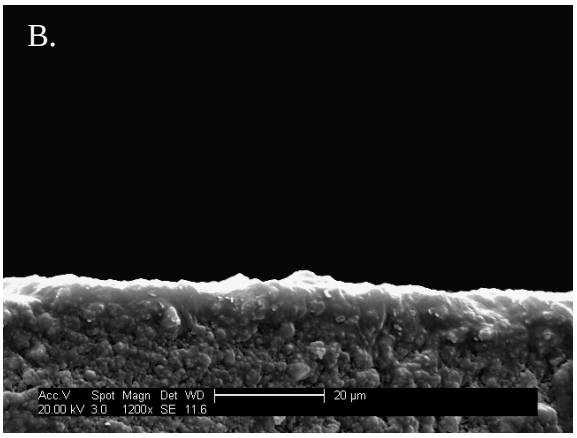

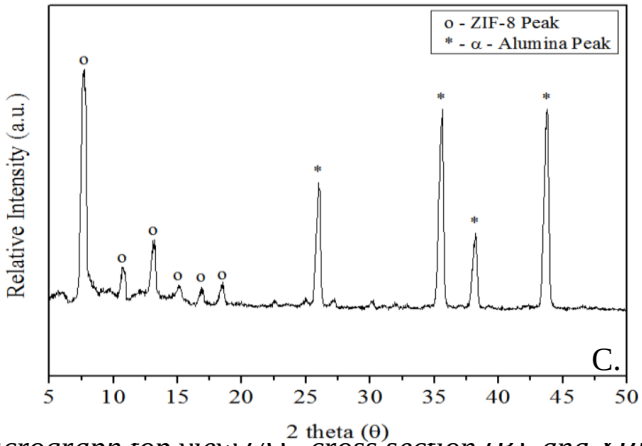

Figure 4.1 SEM micrograph top view (A), cross section (B) and XRD pattern (C) of the as-synthesized ZIF-8 Membrane

Table 4.1 Membrane Permeance (mol/m^{2}sPa) and Separation Factor (SF) for Molecular Probing of ZIF-8 Membrane with various gas pairs

Membrane	He Permeance	SF_6 Permeance	He/SF_6 Ideal SF	C_2H_4 Permeance	C_2H_6 Permeance	C_2H_4/C_2H_6 SF	C_3H_6 Permeance	C_3H_8 Permeance	C_3H_6/C_3H_8 SF
ZIF-8	3.1×10^{-7}	2.8×10^{-10}	**1100**	7.8×10^{-8}	3.9×10^{-8}	**2.0**	2.2×10^{-8}	6.1×10^{-10}	**36.0**

4.3.2 Ethylene/Ethane Permeation in Single Gas and Binary Mixtures

4.3.2.1 Ethylene/Ethane Permeation

Figure 4.2 presents ethylene and ethane single gas permeances and ideal selectivity as a function of temperature. Similar magnitude, monotonic permeance decreases for both ethylene and ethane (~ 30%) enables an approximately stable ideal $C_{2=}/C_{2-}$ selectivity of 2.3 over the temperature range studied. Figure 4.3 presents binary, equimolar ethylene/ethane permeance and separation factor under identical temperature and total feed pressure conditions as utilized in the single gas test. The permeances of ethylene and ethane in binary mixture present monotonic decreases of 31% and 34% respectively over the temperature range studied and selectivity increases from 2.0 to 2.1 at 100°C.

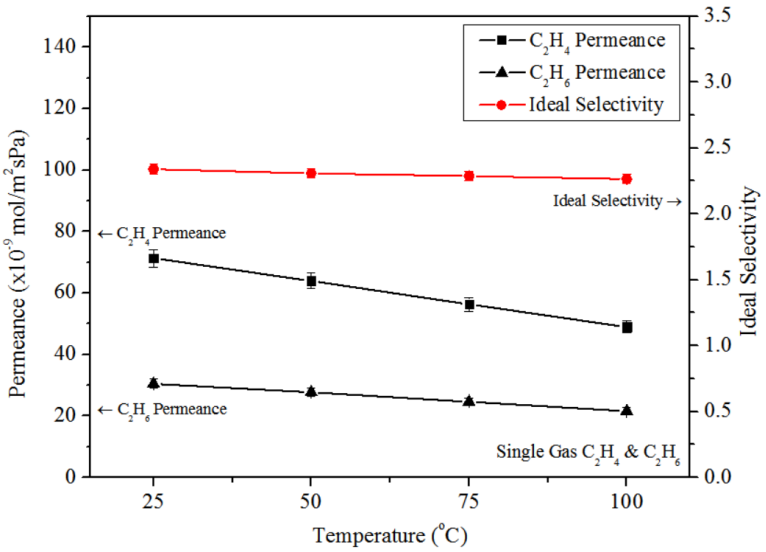

Figure 4.2 Single Gas ethylene and ethane permeances and ideal selectivity as a function of temperature (25-100°C) at 1 atm total feed pressure

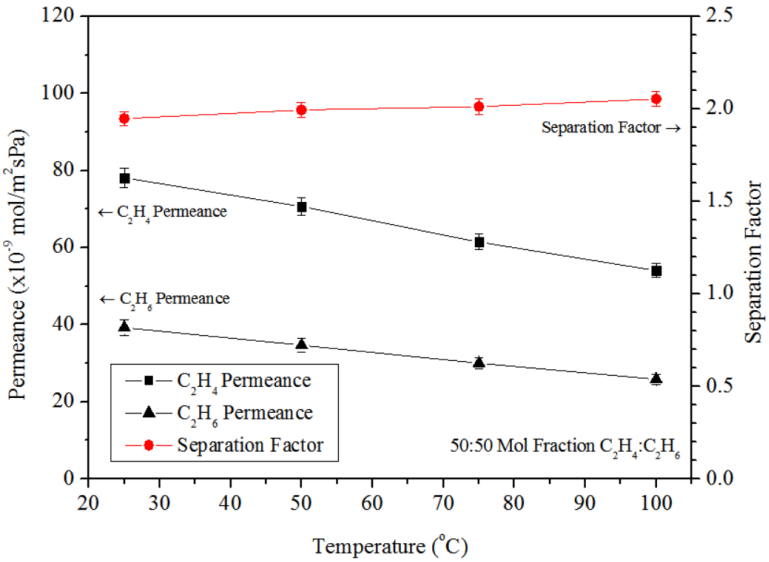

Figure 4.3 Binary equimolar ethylene/ethane permeances as a function of temperature (25-100°C) at 1 atm total feed pressure

It is noted that the binary separation factor is ~ 20% lower than the ideal separation factor. This phenomenon has not yet been linked to specific theory. The decrease in separation is likely a result of cooperative adsorption phenomena where lateral electrostatic interactions induce a preferentially parallel configuration between C_2 molecules as described in the theory by Do and Do (D. D. Do & Do, 2005), and presented in ZIF simulation studies by Wu et al. (Y. Wu, Chen, Liu, Qian, & Xi, 2014). At low pressures, the cooperative effect enhances ethane solubility in ZIF pores, however, the solubility enhancement is not mutual; the existence of ethane does not enhance the ethylene solubility (Y. Wu et al., 2014). In the binary C_2 mixture, enhanced ethane sorption decreases the C_2 selectivity as compared to the ideal case.

Figure 4.4 (A & B) shows the permeances and separation factors for single gas and binary ethylene and ethane separation tests with respect to total feed pressure. In both the gas and mixture separation tests, C_2 permeance increases between 1-2 atm. Beyond 2 atm,

slightly differing permeation trends and notable differences in selectivity profiles are observed. To provide a fundamental understanding the observed permeation behavior, Table 4.2 presents approximate C_2 diffusivities directly tabulated from the work of Caro and co-workers and solubilities calculated using the extended dual-site Langmuir parameters and IAST obtained from the same study (Bux, Chmelik, et al., 2011). It is important to note that ethylene and ethane intracrystalline diffusivities are independent of C_2 molar composition (Bux, Chmelik, et al., 2011; Mueller, Hariharan, Zhang, Lively, & Vasenkov, 2016). The estimated permeability/selectivity values are calculated as the product of diffusivity and single gas/binary solubility as outlined by solution-diffusion theory (Wijmans & Baker, 1995) and should be interpreted qualitatively in terms of increases/decreases rather than relative magnitudes due to the units provided.

As noted from Table 4.2, the increase in C_2 permeance for both the single and binary gas tests between 1-2 atm (Figure 4.4 A & B) is attributed to the increases in C_2 diffusivity which outpace decreases in C_2 solubility. C_2 diffusivity increases/diffusive selectivity decreases as a function of pressure for both C_2 molecules in ZIF-8 due to pressure induced rotational displacement of the imidazole ligand (Verploegh, Nair, & Sholl, 2015). Beyond 2 atm, the permeation trends are well predicted by calculated values from the solution-diffusion parameters generated from single crystal experiments. Large deviations from predicted behavior only occur for ethylene single gas permeance at 3/4 atm and ethylene binary permeance at 2 atm.

The single gas and binary C_2 selectivity profiles starkly contrast (Figure 4.4 A & B). C_2 diffusive selectivity is molar composition independent, therefore the differing trends observed are more strongly an effect of disparate single gas/binary $C_{2=}/C_2$ solubility

behavior. The solubility data in Table 4.2 show that single gas ideal ethylene sorptive selectivity in ZIF-8 increases as a function of pressure while binary $C_{2=}/C_{2-}$ sorptive selectivity is constant at 0.5 in favor of ethane due to cooperative adsorption effects as discussed above. The increasing $C_{2=}/C_{2-}$ permselectivity shown in Figure 4.4A is correlated with the pressure dependency of ideal sorptive selectivity, but deviates from solution-diffusion estimates (Table 4.2). The permeation data in Figure 4.4B agrees well qualitatively with the trends from the crystal experiments. The initial decrease in the binary $C_{2=}/C_2$ permeation separation factor (1-2 atm) followed by smaller decreases in selectivity beyond 2 atm are due to constant sorptive selectivity combined with the decreasing diffusive selectivity trend.

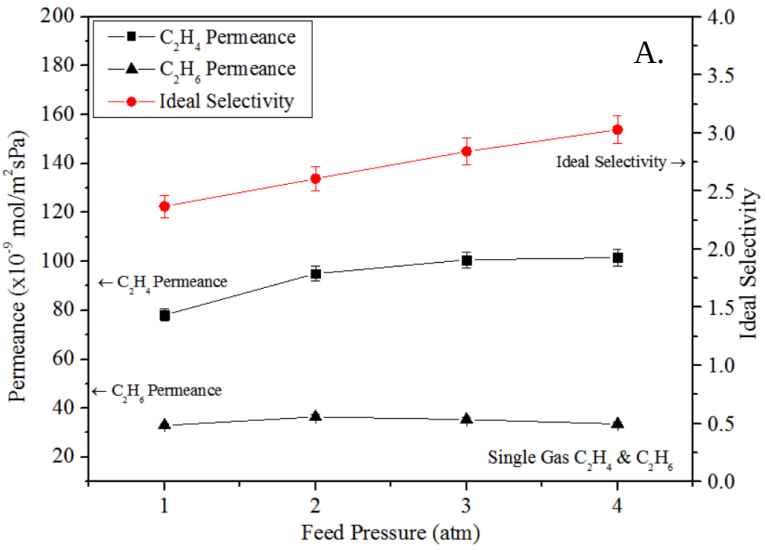

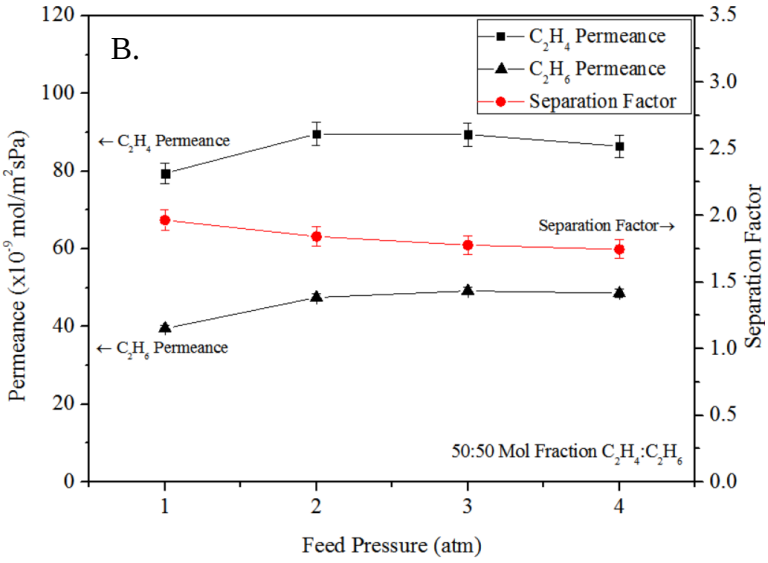

Figure 4.4 Ethylene and ethane single gas permeances/ideal selectivity (A) and binary equimolar permeances/separation factor (B) as a function of total feed pressure (1-4 atm, 25°C)

Table 4.2 Single Gas and Binary Ethylene/Ethane Solubilities, Diffusivities and Estimated Permeabilities in ZIF-8 as a Function of Pressure at 25°C

Total Pressure (mbar)	Diffusivity (x 10^{-11} m^2/s)			Single Gas Solubility (x 10^{-3} molecules/cage*mbar)			Binary (50:50) Solubility (x 10^{-3} molecules/cage*mbar)			Estimated Ideal Permeability			Estimated Binary Permeability		
	$C_{2=}$	C_{2-}	$C_{2=}/C_{2-}$	$C_{2=}$	C_{2-}	$C_{2=}/C_{2-}$	$C_{2=}$	C_{2-}	$C_{2=}/C_{2-}$	$C_{2=}$	C_{2-}	$C_{2=}/C_{2-}$	$C_{2=}$	C_{2-}	$C_{2=}/C_{2-}$
1000	5.0	1.0	5.0	2.0	2.3	0.9	1.6	3.0	0.5	10.0	2.3	4.3	8.0	3.0	2.7
2000	9.0	3.5	2.6	1.3	0.9	1.4	0.8	1.5	0.5	11.7	3.2	3.7	7.2	5.3	1.4
3000	10.5	7.0	1.5	0.8	0.5	1.6	0.4	0.8	0.5	8.4	3.5	2.4	4.2	5.6	0.8
4000	10.8	9.0	1.2	0.6	0.3	2.0	0.2	0.4	0.5	6.5	2.7	2.4	2.2	3.6	0.6

The deviations observed in membrane C_2 permeation/selectivity versus that predicted by IRM crystal studies likely are most related to diffusivity. The membrane data is collected using steady-state permeation while transient uptake experiments are used to measure diffusivity in single crystals. The transient process is more heavily influenced by heats of adsorption especially for thermally insulating MOF materials (B. L. Huang et al., 2007). The ZIF-8 membrane may experience slightly different relative changes in C_2 diffusivity as a function of pressure that may account for the deviations from values estimated from single crystal experiments.

4.3.2.2 Hydrogen/C_2 Permeation

Binary H_2/C_2 permeation studies were also conducted as a function of temperature to gain a better understanding of ZIF-8 membrane hydrogen/light hydrocarbon separation ability. Figure 4.5A and 4.5B present $H_2/C_{2=}$ and H_2/C_{2-} binary permeance as a function of temperature. In the H_2/ethylene system, the opposite permeation behavior of hydrogen and ethylene as a function of temperature enables the $H_2/C_{2=}$ separation factor to increase from 3.5 to 5.3. A similar trend in permeance and separation factor is noted for the H_2/Ethane system, enabling an increase in the H_2/C_{2-} separation factor from 7.3 to 11.6.

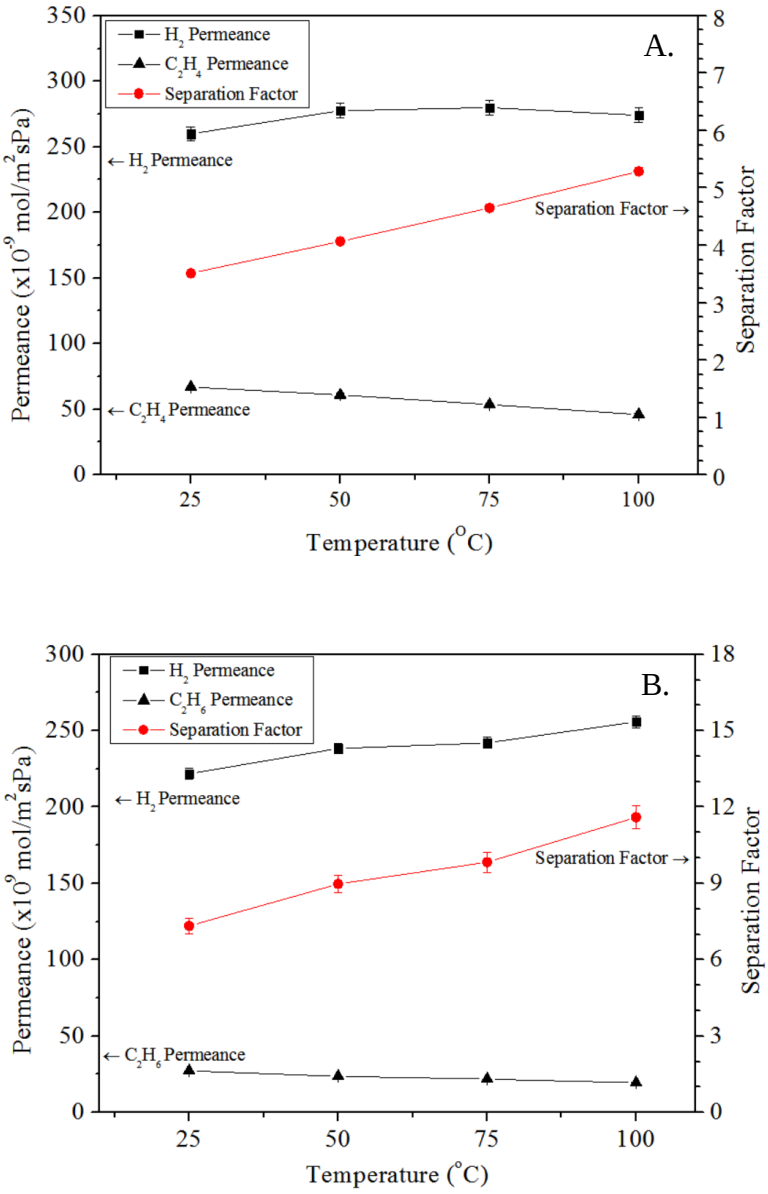

Figure 4.5 Binary equimolar H_2/ethylene (A) and H_2/ethane (B) permeances as a function of temperature (25-100°C) at 1 atm total feed pressure

It is noted that hydrogen permeation increases as a function of temperature in the presence of C_2 as shown in this work and C_3 mixtures reported by Nair and co-workers (Eum et al., 2016). The hydrogen permeation behavior contrasts that observed during single gas H_2 permeance and binary H_2/CO_2 permeance where hydrogen decreases as a function

of temperature (James & Lin, 2017; X. Zhang et al., 2014). Similar H_2 permeation behavior is noted in MFI zeolite membranes. At low temperatures in the presence of strongly adsorbing hydrocarbons (C_{2+}) (J. H. Dong, Lin, & Liu, 2000), hydrogen permeance increases as a function of temperature, but H_2 permeance is negatively correlated with temperature in the single gas (J. H. Dong et al., 2000)(M. Kanezashi & Lin, 2009) because the presence of strongly adsorbed hydrocarbons in mixture feeds have a large effect on the diffusivity of the more lightly adsorbed H_2. H_2 permeance is reduced at low temperatures while hydrocarbon solubility is enhanced. This work illustrates that the presence of C_2 molecules is also sufficient enough to reverse the temperature dependency of permeation for H_2 in ZIF-8 membranes.

4.3.3 Analysis of Ethylene/Ethane Adsorption and Diffusion

A fundamental study of C_2 transport in ZIF-8 can be developed through analyses of C_2 adsorption and diffusion as a function of temperature to better understand C_2 permeation characteristics. The transport behavior of both C_2 gasses in ZIF-8 are articulated well by the Maxwell-Stefan (M-S) solution-diffusion model explicit in terms of membrane physical properties (Bux, Chmelik, et al., 2011) and can provide further insight into the observed phenomena:

$$J = \frac{\rho}{L} * \frac{\varepsilon}{\tau} \int_{q_{feed}}^{q_{perm.}} D_c \frac{dlnP}{dlnq} dP \tag{4.1}$$

where ρ, L ε, and τ are membrane density (0.95 g/cm^3) (Tan, Bennett, & Cheetham, 2010), thickness (5μm), porosity (0.47) (Pan et al., 2015) and tortuosity (1.732, assuming diagonal transmission down the cubic lattice of the ZIF-8 structure) (D. Liu et al., 2014) respectively. P represents pressure. The M-S model which utilizes the thermodynamically corrected diffusion coefficient (D_c) is able to better predict diffusion in systems where adsorbent-adsorbate interactions are significant. Fickian diffusivity is highly loading dependent whereas, the Maxwell-Stefan treatment decouples drag effects from thermodynamic (sorption) effects and assumes that the mechanism of transport of molecules inside the micropores is by activated movement of adsorbed species along sorption sites (Krishna & van den Broeke, 1995). q is quantity adsorbed (mmol/g) derived from the Langmuir equation:

$$q = C_s \frac{bP}{1 + bP} \tag{4.2}$$

C_s is the capacity constant and b is the affinity constant. Upon integration of Equation 4.2, Equation 4.1 takes the form:

$$J = \frac{\rho}{L}\frac{\varepsilon}{\tau} C_s D_c \ln\left(\frac{1 + bP^{feed}}{1 + bP^{perm.}}\right) \tag{4.3}$$

Figure 4.6 (A & B) shows the adsorption isotherms for ethylene and ethane on ZIF-8 crystals from 25-100°C up to 1 atm for determination of the (thermodynamic) sorption

component of flux. The isotherms for both ethylene and ethane present linear Henry region behavior up to 1 atm. In the Henry pressure range where the product of the affinity constant and equilibrium pressure are negligible compared with unity, the Langmuir model can be reduced to Henry's Law and the product of C_s and b is Henry's constant (K). Equation 4.3 can be simplified to:

$$J = \frac{\rho}{L}\frac{\varepsilon}{\tau}D_c K(P^{feed} - P^{perm.}) \tag{4.4}$$

Table 4.3 presents Henry's constants for ethylene and ethane in ZIF-8 obtained from the isotherm slopes in Figures 4.6A and 4.6B. The Henry's constants obtained are comparable to those collected by Hartmann (Böhme et al., 2013) and Koros (C. Zhang et al., 2012). It is noted that ethane presents greater solubility in the ZIF-8 pores. Preferential adsorption of paraffin over olefin gasses is common in non-polar microporous materials where molecular polarizability is the main factor attributable to adsorption strength (Bux, Chmelik, et al., 2011; C. Zhang et al., 2012).

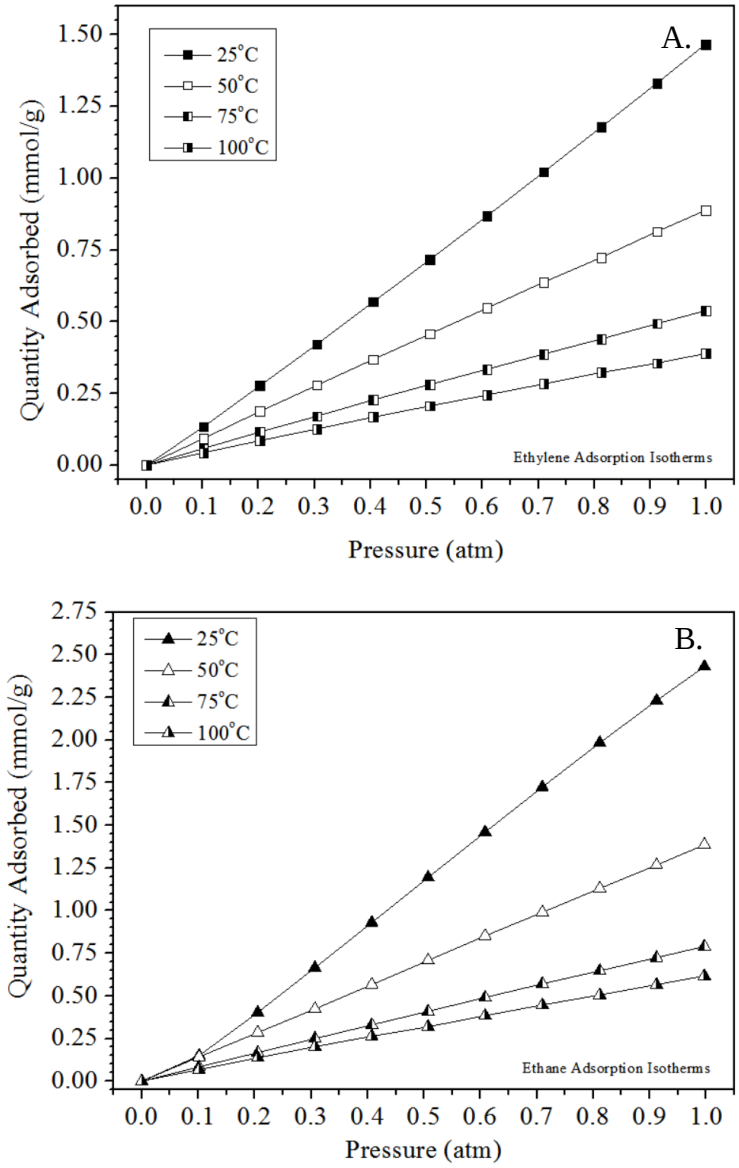

Figure 4.6 Ethylene (A) and ethane (B) isotherms at 25, 50, 75 and 100°C respectively

Table 4.3 Ethylene and ethane Henry's constants and transport diffusivities as a Function of Temperature

	Henry's Constant (mmol/g.bar)		Transport Diffusivity D_c (m^2/s)	
Temperature (ºC)	$C_{2=}$	C_{2-}	$C_{2=}$	C_{2-}
25	1.45	2.41	9.6×10^{-11}	2.5×10^{-11}
50	0.9	1.39	1.4×10^{-10}	4.0×10^{-11}
75	0.54	0.8	2.0×10^{-10}	6.2×10^{-11}
100	0.4	0.63	2.4×10^{-10}	7.0×10^{-11}

Although ethane presents greater solubility in the ZIF-8 framework, diffusivity is the dominating component that enables ethylene permselectivity in ZIF-8 (Chmelik et al., 2012). C_2 diffusivity values are calculated from the steady-state single gas experimental flux values in Figure 4.2 and parameters listed using Equation 4.4. Table 4.2 also tabulates the calculated diffusivity values as a function of temperature. Table 4.4 compares diffusivity values obtained in previous studies at 35°C to the interpolated value of D_c calculated from Equation 4.5 in this work. The thermodynamically corrected diffusivity values for ethylene (1.1×10^{-10} m^2/s) and ethane (3.1×10^{-11} m^2/s) calculated at 35°C in this work are in general agreement with the diffusivity values collected in literature (Bux, Chmelik, et al., 2011; Pan et al., 2015; C. Zhang et al., 2012).

Table 4.4 Calculated thermodynamically corrected diffusivities of ethylene and ethane in ZIF-8 at 35°C

	Transport Diffusivity (m^2/s)			
	Wicke-Kallenbach		Mixed-matrix membrane [6]	IR Microscopy [14]
	This work	Pan et al.[15]		
Ethylene	$1.1 \pm 0.6 \times 10^{-10}$	1.9×10^{-10}	$3.6 \pm 1.6 \times 10^{-11}$	5×10^{-11}
Ethane	$3.1 \pm 1.3 \times 10^{-11}$	2.4×10^{-11}	$8.8 \pm 2.7 \times 10^{-12}$	1×10^{-11}

The transport behavior of both C_2 components as a function of temperature can be elucidated through analysis of the temperature dependency of both diffusivity and solubility through the Arrhenius equation:

$$D_c = D_o e^{\frac{-E_d}{RT}} \tag{4.5}$$

and van't Hoff equation:

$$K = K_o e^{\frac{-\Delta H_s}{RT}} \tag{4.6}$$

respectively. D_0 and K_0 are pre-exponential factors for each equation, E_d is activation energy of diffusion and H_s is heat of adsorption. Arrhenius (Ln D_c vs 1000/T) and van't Hoff (Ln K vs 1000/T) plots are shown in Figure 4.7 (A & B) and the regression gives activation energy of diffusion values of 11.7 and 13.2 kJ/mol, and heat of adsorption values of 16.2 and 17.0 kJ/mol, respectively, for ethylene and ethane. For C_2 transport in ZIF-8,

the respective activation energies of diffusion are less than the heats of adsorption, meaning that the energy required to move a molecule from its equilibrium position at an initial adsorption site to a new adsorption site is less than the energy released upon adsorbing. Thus, C_2 permeance is greater function of exothermic adsorption interactions which well explains the negative correlation between permeance and temperature observed in Figures 4.2 & 4.3.

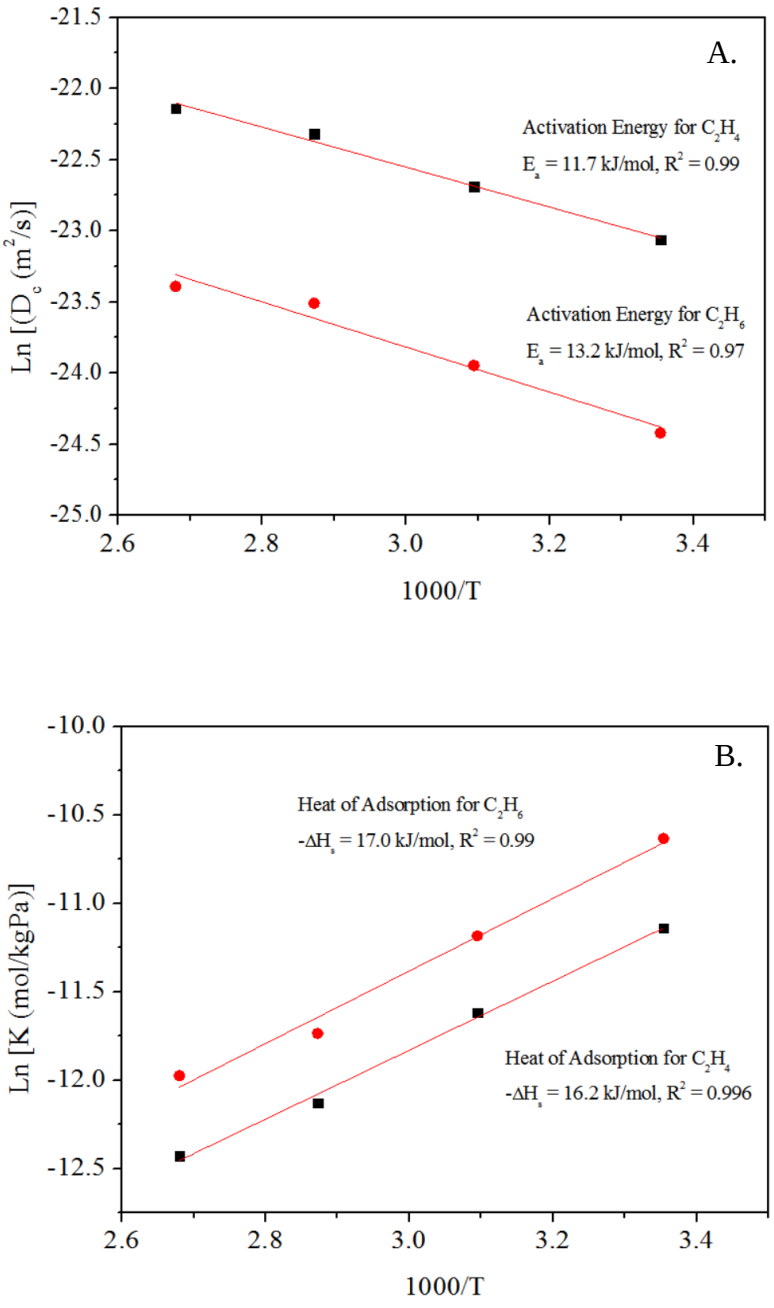

Figure 4.7 Arrhenius activation energy of diffusion (A) and van't Hoff plots (B) for ethylene and ethane

In terms of the C_2 ideal separation factor presented earlier in Figure 4.2, a stable ideal separation factor of 2.4 is maintained. The observed phenomenon is due to similar

decreases in ethane and ethylene permeances as a function of temperature. As temperature increases, similar magnitude (< 5% difference) increases in diffusivity and decreases in solubility occur for ethylene and ethane while permeating through the ZIF-8 framework which enables constant permselectivity.

Equation 4.5 models diffusivity in terms of a pre-exponential factor and an energetic (activation energy) component. The energetic contribution to diffusivity is a function of the ratio of permeating gas molecular diameter (van der Waals diameters: $C_{2=}$ = 0.359 nm, C_{2-} = 0.372 nm) to the pore aperture diameter ($\lambda = d_m/d_p$) and the pre-exponential term takes into consideration intracrystalline partitioning or the entropic contribution to diffusion. Larger, non-permanent gasses such as C_{2+} molecules experience reduced rotational, translational and vibrational degrees of freedom upon passage through interconnected ultramicropore (d_p < 0.5 nm) windows of adjacent cavities (D. M. Ruthven et al., 1973; Xiao & Wei, 1992). As a result of repulsive forces in addition to desorption energy, the passage of large molecules through ultramicropore windows can be considered a rate limiting process involving an activated transition state (D. M. Ruthven et al., 1973; D M Ruthven & Derrah, 1972). The pre-exponential factor for the specific case of intercrystalline partitioning in the ZIF-8 system can be modeled by:

$$D_o = e\gamma^2 \frac{kT}{h} e^{\frac{S_D}{R}} \tag{4.7}$$

where γ is the average diffusive jump length (approximately equal for C_2 molecules) (Rungta et al., 2012; A. Singh & Koros, 1996) , S_D is the activation of entropy, k is

Boltzmann's constant and h is Plank's constant. Ethylene/ethane diffusive selectivity or $D_{Ethylene}/D_{Ethane}$ can be expanded in terms of energetic and entropic contributions respectively:

$$\frac{D_{Ethene}}{D_{Ethane}} = e^{\frac{\Delta S_{D,Ethene/Ethane}}{R}} \cdot e^{-\frac{E_{a,Ethene-E_{a,}Ethane}}{RT}} \tag{4.8}$$

where the first term on the right of the equal sign is $D_{o,Ethene}/D_{o,Ethane}$ (entropic selectivity) or the ability of a molecular sieving material to exclude molecules based upon shape and the second term is the ratio of activation energies (energetic selectivity) which is based upon size exclusion.

Table 4.5 tabulates the energetic and entropic parameters for C_2 diffusive selectivity in ZIF-8 which contains a flexible sodalite structure and compares the parameters to those obtained for ultramicroporous molecular sieving Zeolite 4A (rigid sodalite structure) (Hayrettin Yucel- & Rutwen, 1980; Douglas M. Ruthven & Reyes, 2007) and a Matrimid® derived carbon molecular sieve (CMS) membrane (Rungta et al., 2012) (rigid slit-like pore structure) to elucidate the relationship between ultramicropore physical properties on the energetic and entropic effects on C_2 diffusive selectivity. Comparison of C_2 E_d values between materials shows that the energy required for C_2 diffusion is the lowest in ZIF-8. Although ZIF-8 posseses a smaller nominal crystallographic pore aperture than that of Zeolite 4A, the lower E_d for C_2 in ZIF-8 demonstrates that the effective pore aperture, derived from molecular sieving cut-off experiments, is most appropriate for determining the parameter λ in ZIFs. Temperature, pressure and adsorption induced disortion of the

flexible metal-ligand bonds and rotational displacement of methyl group on the imidazole moiety enables uptake and diffusion of molecules with larger diameters than the crystallographic ZIF-8 pore aperture (Peralta et al., 2013; Verploegh et al., 2015; K. Zhang et al., 2013). In contrast, relatively rigid Zeolite 4A and Matrimid derived CMS materials are less amenable to pore distortion and greater energy is required for diffusion.

Table 4.5 Ethane/Ethylene Diffusive Transport Parameter Comparison in Ultramicroporous Materials

		$\lambda = d_m/d_p$		E_d (kJ/mol)		Energetic Contribution to C_2 Diffusive Selectivity	D_0 (m^2/s)		Entropic Contribution to C_2 Diffusive Selectivity
Membrane	d_p (nm)	$C_{2=}$	C_{2-}	$C_{2=}$	C_{2-}	$e^{-\frac{E_{d,Ethene}-E_{d,Ethane}}{RT}}$	$C_{2=}$	C_{2-}	$D_{0,Ethylene}/D_{0,Ethane}$
ZIF-8	0.34 (Crystallographic)/ 0.42 (Effective)	1.06/0.85	1.09/0.89	11.7	13.2	1.8	1.1×10^{-8}	5.3×10^{-9}	2.1
Zeolite 4A	0.38	0.94	0.98	33.5	34.3	1.4	3.9×10^{-10}	2.3×10^{-10}	1.7
Matrimid® CMS	Bimodal (Ultramicropores, Micropores)	-	-	73.6	71.5	0.5	3.6×10^{-1}	2.2×10^{-2}	16.2

Comparison of the relative values of E_d for C_2 molecules shows that the energetic contribution to C_2 diffusive selectivity is most similar in ZIF-8 and Zeolite 4A as compared to the Matrimid derived CMS which shows an inverted energetic diffusive selectivity. Similar relative E_d values between ZIF-8 and Zeolite 4A is likely due to their similar pore structure (~ 11 Å pore cages interconnected by ultramicropore windows) and the similar size of the diffusing C_2 molecules. Both C_2 molecules present λ values < 1 for ZIF-8 and Zeolite A which prevents substantial energetic-based molecular sieving for C_2 in either material. Additionally, Zeolite 4A is assigned actual crystallographic pore dimensions of 0.38 x 0.42 nm due to non-idealities in the configuration of the 8-ring oxygen arrangement of the zeolitic pore window (Douglas M. Ruthven & Reyes, 2007). Thus, the averaged apertue size is slighlty larger than 0.38 nm and closer to the effective ZIF-8 aperture diameter.

The entropic selectivity for C_2 molecules in the Matrimid® derived CMS membrane is 16.2 and ~2.0 for the zeolitic materials. Due to its planar shape, ethylene is 16 times more likely than the bulkier ethane molecule to orient itself in a configuration such that it can diffuse through the rigid CMS slit-like pore. Ethylene's rotational, translational and vibrational degrees of freedom are less restricted upon diffusion into the CMS pore as compared to ethane which is more restricted and has a higher probability of rejection and thus higher resolution C_2 molecular sieving (Rungta et al., 2012). In the zeolitic structures this probability is decreased by a factor of 8 because the zeolitic pore apertures compared are not optimally shaped for efficient entropic discrimination of C_2 molecules.

4.4 Conclusions

Ethylene/ethane transport properties and separation characteristics were studied in single and binary gas mixtures as a function of temperature and pressure in a high quality ZIF-8 membrane. The activation energies of diffusion for ethylene and ethane (11.7 kJ/mol & 13.2 kJ/mol) are less than their respective heats of adsorption (16.2 & 17.1 kJ/mol). Pore flexibility enables low E_d values and λ values < 1 for both C_2 molecules limits energetic diffusive selectivity. The zeolitic pore shape of ZIF-8 limits entropic-based diffusive selectivity. Ethylene/ethane permeation selectivity is approximately 20% lower in the binary mixture as compared to ideal permselectivity due to cooperative adsorption effects which enhances ethane adsorption in the presence of ethylene. In binary mixtures with hydrogen, the presence of C_2 molecules decreases hydrogen permeability and inverts the temperature dependency of hydrogen permeation from adsorption to diffusion controlled. In pressure dependent single and binary C_2 permeation tests, rotational ligand displacement increases C_2 diffusivity/permeability and decreases ethylene diffusive selectivity. Ideal C_2 selectivity shows an increase with pressure while the binary C_2 separation factor decreases then stabilizes due to stark contrasts in single gas and binary C_2 adsorption isotherms.

CHAPTER 5
EX SITU TIME-BASED CHARACTERIZATION AND LIGHT HYDROCARBON GAS PERMEATION STUDY OF ZIF-8 MEMBRANES MODIFIED VIA MEMBRANE SURFACE LIGAND EXCHANGE

5.1 Introduction

Chapter 4 elucidated the ZIF-8 membrane transport characteristics of ethylene and ethane in single gas and binary mixtures. Although the nominal pore diameter of ZIF-8 is smaller than the van der Waals diameters of both molecules, pore flexibility limits C_2 diffusive selectivity and ethane is more soluble in the ZIF framework. Thus, C_2 permselectivity is limited in ZIF-8. Several opportunities exist to design, synthesize or even modify new or existing prototypical ZIFs to enhance light hydrocarbon separations as outlined in Chapter 1. The diverse number of linkers and metal nodes available for ZIF syntheses enables a myriad of structures that can be formed through de novo or postsynthetic routes. While reticular chemistry can be employed to form new structures designed for a specific application, there are many variables to control during the synthesis process which can lead to arduous, time consuming trial and error iterations to obtain the optimal structure for a specific application.

An attractive alternative to fully custom reticular synthesis for framework tuning is mixed linker syntheses to form hybrid ZIFs. Hybrid ZIFs incorporate the functionality of multiple ZIFs, often over a wide range of linker compositions by amalgamating the single linkers of two different ZIFs de novo followed by traditional solvothermal crystal growth. Hybrid ZIFs such as ZIF-7-8 (Thompson et al., 2012), ZIF-8-90 (Eum et al., 2015;

Thompson et al., 2012) and ZIF-7-90 (Rashidi, Blad, Jones, & Nair, 2016) have displayed chemical and physical properties that correspond to the relative amount of linker within the hybrid framework. The corresponding studies demonstrated the highly tunable nature of ZIF framework properties showing effective control the adsorption and/or diffusion properties of various molecules interacting with the framework.

As discussed in chapter 1, another quite facile approach to framework tuning and formation of mixed linker ZIFs is postsynthesis modification, specifically solvent assisted ligand exchange (SALE). SALE places a new linker in solution with already formed ZIF crystals that are composed of a different linker. The resulting daughter ZIF is topologically identical to the parent and contains a fraction of the new linker. This method overcomes some of the compositional control limitations of mixed linker syntheses because the effects of relative linker solubility in the synthesis solvent and metal site coordination competition experienced in de novo, mixed-linker syntheses are eliminated when utilizing SALE.

A number SALE studies have been performed to incorporate carboxylate or imidazole linkers with new functionalities within MOF crystals including MIL, highly stable UIO and ZIF structures (Karagiaridi et al., 2014; M. Kim, Cahill, Fei, et al., 2012; M. Kim, Cahill, Su, Prather, & Cohen, 2012). These studies have provided insight on the effects of SALE time (M. Kim, Cahill, Su, et al., 2012), temperature (Jayachandrababu et al., 2017; Karagiaridi, Bury, Sarjeant, Stern, Farha, & Hupp, 2012), linker concentration (Karagiaridi, Lalonde, et al., 2012), incoming linker functionality/size (Jiang et al., 2015; Karagiaridi, Bury, Sarjeant, Stern, Farha, & Hupp, 2012; Lalonde et al., 2015; C. Liu et al., 2016) and solvent (Karagiaridi, Lalonde, et al., 2012) on the resultant changes in

composition and physical properties of the exchanged ZIF crystals. Further studies have sought out to observe specifically enhance the properties of MOFs and ZIFs through SALE. Yang and co-workers enhanced the hydrothermalstability properties of ZIF-8 through incorporation of the more hydrophobic 5,6 dimethylbenzimidazole ligand for water/butanol separation (X. Liu et al., 2013), Zhang et al. demonstrated hydrostability enhancement of ZIF-8 membranes using the same linker through membrane surface ligand exchange (H. Zhang et al., 2017). In ZIF-8 crystal SALE experiments with Imca (ZIF-90 linker) exchange, Nair and co-workers noted that the SALE process is diffusion-limited and leads to formation of core-shell morphologies under moderate postsynthetic conditions via diffusion of 2-imidazolecarboxaldehyde (Imca) into the crystal lattice and counter-diffusion of the original 2-methylimidazole (2-MIm) out of the crystal structure (Jayachandrababu et al., 2017). The study provided a better mechanistic understanding of the SALE process and illustrated the enhancement of water uptake with respect to increased incorporation of the relatively hydrophilic Imca ligand. This is one of few mechanistic studies on the topic.

In terms of gas separation property enhancement, most studies highlight CO_2 adsorptive separations. Hu et al. demonstrated the ability to enhance the CO_2 working capacity and IAST CO_2/N_2 separation of UIO-66 through ligand exchange with metalated 1,2,4,5-benzenetetracarboxylic acid (Z. Hu et al., 2015) and Hong et al. enhanced CO_2/CH_4 adsorptive separation in UIO-66 through ligand exchange with alkanedioic acid (D. H. Hong & Suh, 2014).

The aforementioned studies have provided a better understanding of the SALE process and its potential to enhance the separation properties of MOFs, however there is still much room for further elucidation of the ligand exchange mechanism and there has yet to be a detailed fundamental study of its effects on ZIF membrane-based gas separations. An analysis of both physical property/structural changes and gas separation changes as a function of ligand exchange time has yet to be conducted, but can give further insight into the process and its efficacy for gas separation enhancement.

In this work we will perform a time-based ex-situ study of ZIF-8 membrane surface ligand exchange (MSLE) with 5,6 DMBIm as the exchanging ligand. The membrane surface ligand exchange reaction (MSLER) time and temperature will be controlled and changes in structure property-relationships will be examined through physical characterization analyses and light hydrocarbon gas separations. The larger 5,6 DMBIm ligand was chosen as the exchanging ligand to potentially enhance hydrogen/light hydrocarbon and/or light olefin/paraffin gas phase separations.

5.2 Experimental

5.2.1 ZIF-8 Membrane Synthesis and Modification

As-synthesized ZIF-8 membranes were prepared with modifications to our previously reported method, however α-alumina substrate fabrication and preparation was identical to our previous reports (James & Lin, 2017; James, Wang, Meng, & Lin, 2017). ZIF-8 crystals for membrane seeding were prepared according with modifications to the method of Lai and co-workers (Pan et al., 2012). All chemicals were purchased from Sigma

Aldrich (U.S.A) unless otherwise stated. 1.17 g of zinc nitrate hexahydrate [$Zn(NO_3)\cdot 6H_2O$] (98%) was dissolved in 8 mL of deionized water and 22.7 g of 2-methylimidazole (2-MIm) was dissolved separately in 80 mL of deionized water. The separate dissolved solutions were stirred for 10 minutes. The imidazole solution was poured into the zinc solution and stirred for 5 minutes. After mixing, the resultant white solution was centrifuged (10,000 rotational centrifugal force) and washed 1 time in 50% (v/v) water/methanol and 2 times in 99% methanol (BDH, U.S.A). The resulting white crystals were washed and centrifuged in methanol then dried under vacuum at room temperature at 60 kPa for 24 hours. 0.04 grams of dried, ground ZIF-8 crystals were placed in glass vial containing 100 mL of methanol to form a 0.05 wt% colloidal ZIF-8 seeding solution.

Slip-cast coating of the prepared α-alumina substrate was conducted by bringing the substrate into contact with the seeding solution for 20 seconds, the support was then dried in ambient air for 10 minutes and then the coating procedure was repeated once more. The seeded supports were placed in a furnace which was ramped to 95°C by 0.3°C/min, held at constant temperature for 3 hours and subsequently ramped down to room temperature at the same rate. Secondary growth was performed by placing the seeded support vertically in a Teflon holder with the seeded side slightly tilted face-up and submerged in a growth solution containing 0.11 g of [$Zn(NO_3)\cdot 6H_2O$] and 2.27 g of 2-methylimidazole in 40 mL of deionized water within a Teflon lined stainless steel autoclave and placed in an oven at 130°C for 8 hours, secondary growth was repeated as needed subsequently for 7.5 hours to seal defects. After synthesis the ZIF-8 membrane was

washed in methanol for 12 hours, then allowed to dry under ambient conditions for 24 hours. After drying the membrane is place in solution with 4.54 grams of 2-MIm in 40 mL of deionized water, sealed in an autoclave and heated to 130°C for 4 hours. After ligand treatment, the membrane was washed and dried as reported above.

Post-synthesis modification of ZIF-8 membranes with 5,6 dimethylbenzimidazole was conducted using the solvent assisted ligand exchange method utilized in the ZIF-8 crystal study by Yang and co-workers (X. Liu et al., 2013) and modified in our previous work for supported ZIF-8 membranes (H. Zhang et al., 2017). 0.1 g of 5,6 Dimethylbenzimidazole (5,6 DMBIm) was added to a glass beaker, dissolved in 20 mL of methanol then placed under stirring. After 5 minutes, 0.1 grams of triethylamine was added into the 5,6 DMBIm solution using a burette. The solution was allowed to stir for 5 minutes. A dried ZIF-8 membrane was placed in a Teflon holder and held vertically, the holder was then placed into the autoclave liner and submerged by the 5,6DMBIm solution. The liner was sealed in the stainless steel autoclave for reaction.

Time-dependent membrane surface ligand exchange (MSLER) experiments were performed by reacting a single ZIF-8 membrane in fresh 5,6DMBIm solutions for a total of 30 minutes, 5 hours, 10 hours and 15 hours respectively. A single membrane was utilized to avoid confounding effects. After each reaction, the membrane was washed in methanol for 2 hours and dried at room temperature for 24 hours. After drying, characterization then gas permeation were performed. After gas permeation, the membrane was placed under helium flow at 2 bar for 12 hours to remove adsorbed molecules, then washed in methanol for 12 hours to clean the surface, dried for 12 hours then placed in the 5,6 DMBIm solution

for the subsequent reaction time. Reactions were performed isothermally at 60°C or 75°C using separate membranes of similar quality.

5.2.2 Characterization

Membrane surface imaging of ZIF-8 crystal and membrane surface morphology were performed using an XL30 Environmental FEG (FEI) scanning electron microscope (SEM) with an accelerating voltage of 10 kV. ZIF-8 membrane crystallinity was analyzed using a SIEMENS D5000 x-ray diffractometer (XRD) at 30 kV, 30 mA with a scan speed of 2°/min for 2θ, using Cu Kα radiation (λ = 0.1543 nm). Samples underwent gold/palladium deposition prior to visual analyses to prevent surface charging.

Water contact angle analyses of as-synthesized and modified ZIF-8 membranes were conducted using a Kruss Easy Drop Contact Angle apparatus equipped with a CCD camera. Measurements were conducted at ambient pressure with temperatures ranging between 21-23°C. A 4μL water droplet was contacted with the surface of each modified membrane at 5 different points on the membrane surface, each drop was allowed to settle for 5 minutes before taking contact angle measurements. Drop Shape Analyzer software was used to measure the contact angle. The average of the 5 measurements and the error bars represent the standard deviation in the mean. Solution ^{1}HNMR experiments were performed using a Bruker 400 MHz spectrometer. As-synthesized and modified membrane layers were scraped from the support and fully digested in a 99% solution of d_4-acetic acid (CD_3CO_2D) with TMS standard. To determine the fraction of 5,6 DMBIm in the sample, the peak area of the methyl groups at the 5 and 6 position of 5,6 DMBIm peak was

normalized by the sum of the HMIm methyl peak area and the 5,6 DMBIm peak area, accounting for 2 methyl groups per 5,6 DMBIm ligand.

5.2.3 Gas Permeation

In gas permeation tests, the α-alumina supported ZIF-8 and modified ZIF-8 membranes were sealed into a custom-fabricated stainless steel permeation cell using VITON O-rings (O-rings West, U.S.A.). The effective membrane permeation area after sealing was 2.27 cm^2. All tests were conducted under binary (50:50) feed conditions at a total feed pressure of 2 atm at room temperature (23.6-25°C) using the Wicke-Kallenbach technique (James et al., 2017). Brooks mass flow controllers were utilized to control the total feed flow rate of 100 mL/min (50 mL/min of each gas). The nitrogen sweep flow rate was set to 50 mL/min for the H_2 and C_2 binary pairs and a sweep flow of 10mL/min was utilized for the $C_{3=}/C_{3-}$ binary pair. Volumetric flow rates correspond to measurements collected at ambient temperatures ranging between 23.6-25°C and atmospheric pressure. Each binary pair was allowed to permeate for 2 hours or longer (4 hours for $C_{3=}/C_{3-}$ (Pan et al., 2015)), until a steady state permeance was reached before collecting permeation readings.

The composition of the retentate and sweep sides of the membrane were analyzed using an Agilent 7890 A gas chromatograph (TCD detector) with an Alltech Haysep DB 100/120 packed column (dimensions: 9.14 m L, 3.2 mm O.D.) for the H_2 and C_2 binary pairs and a silica gel column (dimensions: 1.8 m L x 3.2 mm O.D.) when analyzing the $C_{3=}/C_{3-}$ binary permeation mixture. In each permeation experiment, triplicate runs were

performed and the error bars represent the standard error of the mean for permeation and selectivity/separation factor measurements reflected in experimental plots.

5.3 Results and Discussion

5.3.1 Time and Temperature Effects of MSLER on ZIF-8 Membrane Physical Properties

Figure 5.1 shows SEM micrograph of an as-synthesized ZIF-8 membrane approximately 5 μm in thickness (Figure 5.1 A&B) and membranes after MSLER modification with 5,6 DMBIm after 15 hours at 60°C (Figure 5.1 C) and 75°C (Figure 5.1 D) respectively. No distinguishable changes in the membrane crystals' size, outer morphology or orientation are apparent from SEM images after modification for 15 hours. Micrographs of membranes reacted at intermediate times are not shown to avoid redundancy. This finding is consistent with previous ZIF-8 crystal and membrane studies (X. Liu et al., 2013; H. Zhang et al., 2017) using 5,6 DMBIm under similar reaction conditions (60°C, 15 hours) and shows that reaction at 75°C also maintains the outer surface morphology/integrity and orientation of the crystals. This also denotes that significant framework dissolution did not occur during the ligand exchange.

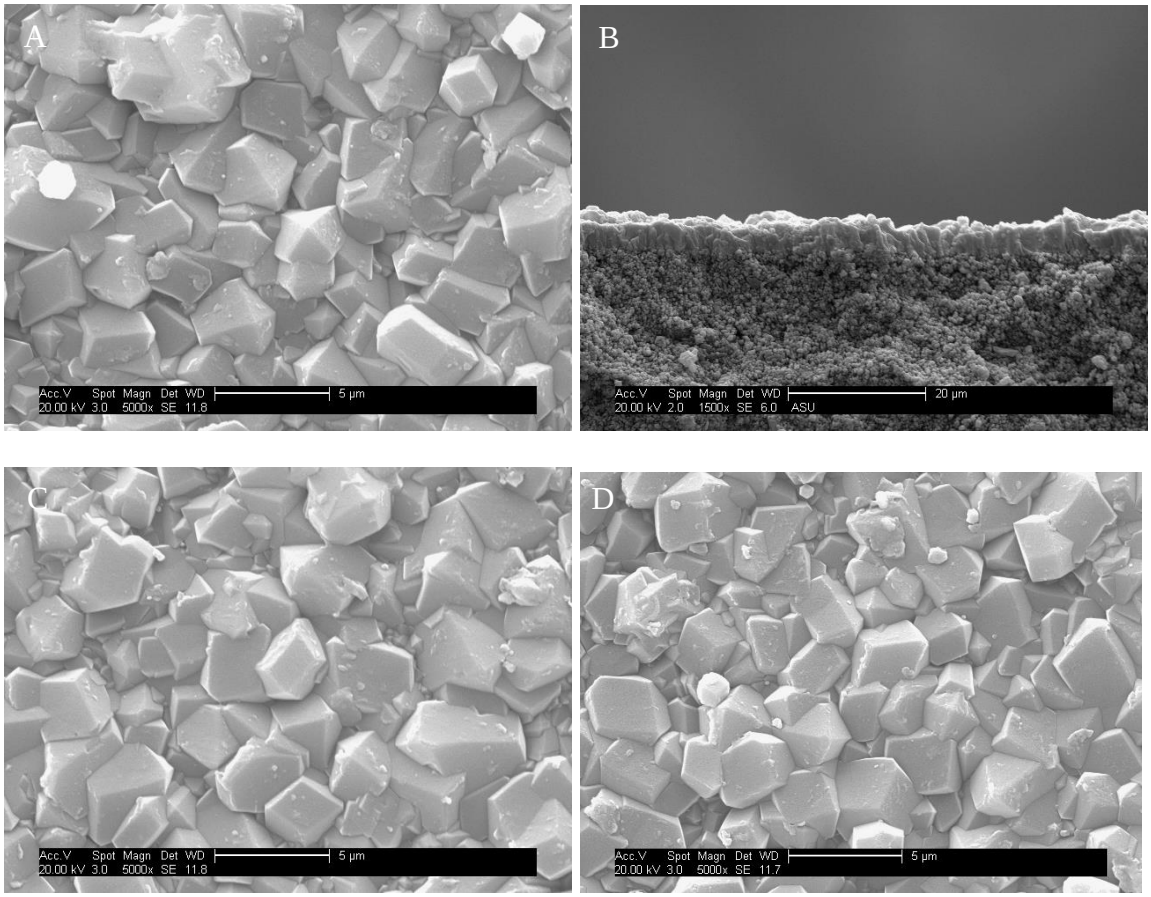

Figure 5.1 SEM micrograph of as-synthesized ZIF-8 membrane (A), as-synthesized membrane cross section (B) and membranes after 15 hours of MSLER at 60°C (C) and 75°C (D)

Evidence of membrane surface ligand exchange is presented in Figure 5.2 which shows static contact angles of as-synthesized and modified ZIF-8 membranes with respect to ligand exchange time and grouped by MSLER reaction temperature. As shown in Figure 5.2 and graphically illustrated in Figure 5.3, the rate of contact angle increase is greatest during the first 30 minutes of reaction then exhibits lesser extent increases thereafter. The increase in water contact angle is due to the more hydrophobic nature of the 5,6 DMBIm ligand as compared to HMIm. Furthermore, the contact angle trend shows that the surface

sites are heterogeneously covered with the new 5,6 DMBIm linker after short reaction time, then the density of new ligand coverage converges to a greater value at longer reaction times.

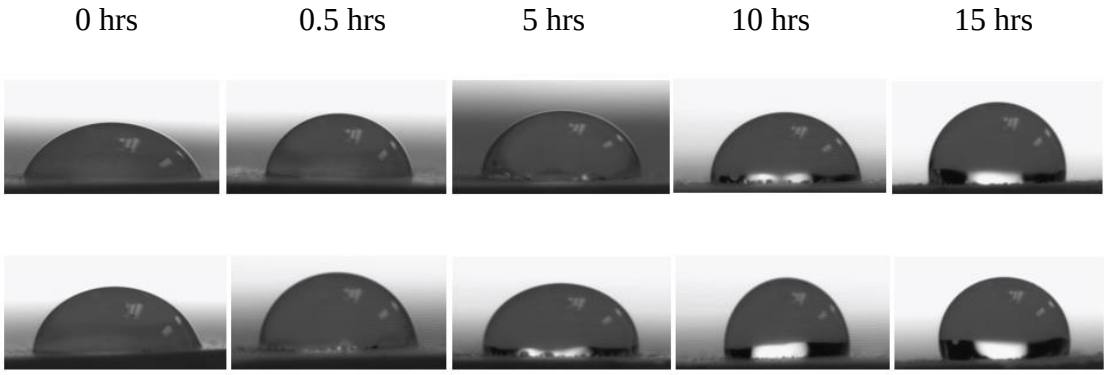

Figure 5.2 Static water surface contact angle micrographs of ZIF-8 membranes with respect to MSLER time at 60°C (top row) and 75°C (bottom row)

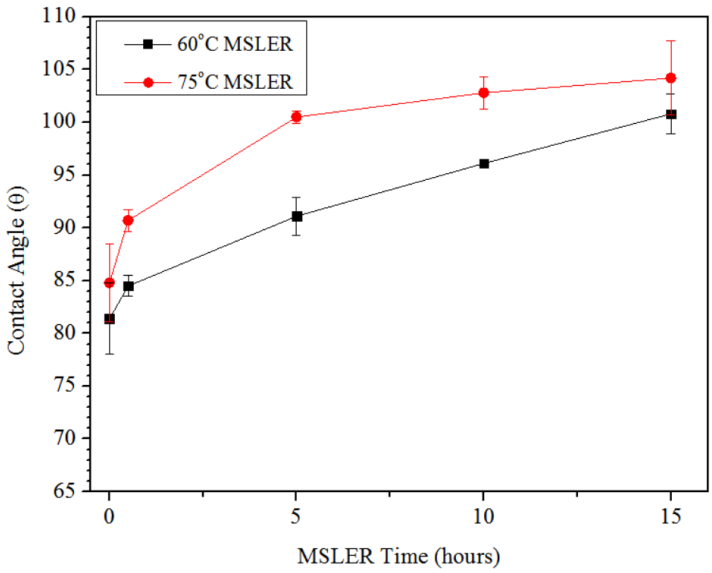

Figure 5.3 Plot of water contact angle with respect to MSLER time at 60°C and 75°C

To analyze internal microstructural changes occurring in the ZIF-8 membrane during the MSLER process, Figure 5.4 shows XRD patterns of ZIF-8 membranes before MSLER and as a function of MSLER time at 60°C (A) and 75°C (B) respectively. As the MSLER reaction proceeds, notable changes in the lowest angle ZIF-8 (011) peak intensity relative to that of alumina are presented at both temperatures which is indicative of microstructural change. All other ZIF peaks retained their intensities with respect to the alumina peaks Nair and co-workers also observed changes in the low angle peak intensities of ZIF-8 crystals exchanged with 2-imidazolecarboxaldehyde (ZIF-90 linker) during SALE experiments and noted that the observations were due to changes in the unit cell parameters while preserving the SOD structure (Jayachandrababu et al., 2017).

Figure 5.5 further illustrates/quantifies the changes in relative intensities shown in Figure 5.4 and plots the change in ZIF-8 XRD peak intensity relative to Al_2O_3 at time t and is normalized by the same ratio at time 0. The peak ratio reaches a minima after 5 hours then increases during the 60°C experiment and for the 70°C experiment, the peak intensity reaches a minima after 30 minutes of reaction then increases. The changes in x-ray intensity of the (011) peak is due to incorporation of the new 5,6 DMBIm linker within the internal framework surface along the corresponding plane. Changes only occurring at the outer membrane crystal surface likely would not be exhibited in the XRD patterns.

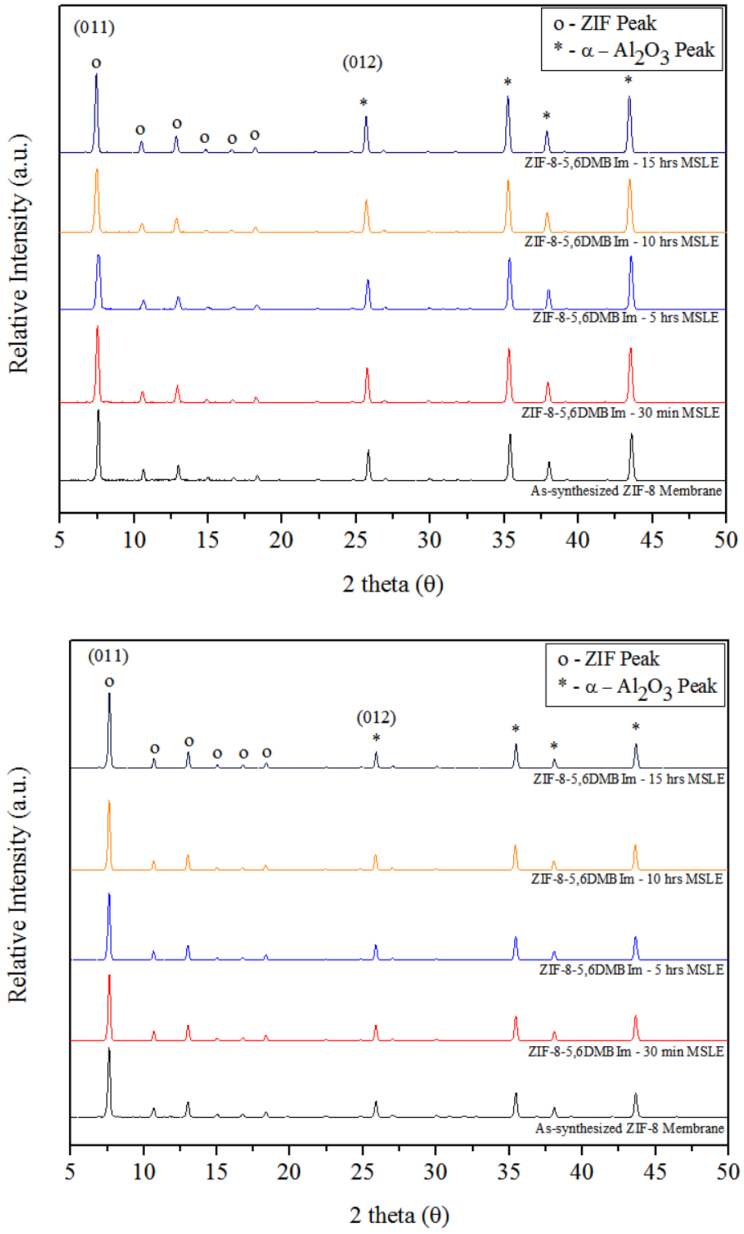

Figure 5.4 XRD patterns of as-synthesized ZIF-8 membranes and membranes after MSLER at 60°C (A) and 75°C (B) as a function of time

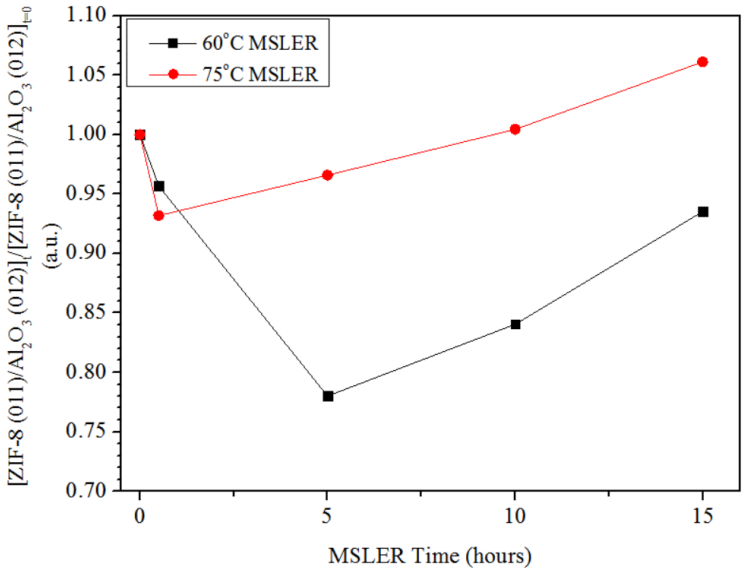

Figure 5.5 ZIF-8 (011)/Al_2O_3 (012) peak intensity ratio at time t normalized by the ratio at time 0 as a function of MSLER time for ZIF-8 membranes modified at 60 and 75°C respectively

During the initial period of x-ray intensity decline we postulate that the internal microstructure of the parent ZIF-8 structure loses periodicity upon incorporation of 5,6 DMBIm. After further reaction, the ZIF internal surface likely becomes more ordered with the new incoming ligand and reaction at higher temperature enables faster organization to a more ordered structure. In fact, after 10 hours of MSLER at 75°C, the (011) peak intensity is greater than the peak intensity of the as-synthesized membrane. This is due to incorporation of new ligand which carries a higher electron density benzene substituent. Farha and co-workers noticed an identical trend when functionalizing NU-1000 with perfluoroalkanes of varying lengths through solvent assisted linker incorporation; longer alkane chain lengths exhibited greater XRD peak intensity at low angles due to increased electron density along the corresponding plane (Deria et al., 2013).

The XRD phenomena observed in this work is partially analogous to the assembly-disassembly-organization-reassembly (ADOR) process studied in zeolites (Roth et al., 2013; Wheatley et al., 2014). Under specific reaction conditions time-dependent ADOR experiments show initial crystallinity reductions at short reaction times then a return in crystallinity after long reaction periods with a shift in the main XRD reflection (Wheatley et al., 2014). The ADOR process involves zeolite framework dissolution and leads to daughter zeolites with new topologies, while MSLE maintains the topology of the parent. Despite the noted differences, similar time-based XRD behavior between both processes may substantiate that ZIFs undergo some form of disassembly, organization and reassembly steps during the MSLER, but in a manner such that topology is conserved.

^{1}HNMR was performed to quantify the fraction of new linker incorporated in the ZIF structure and is graphically presented as a function of time in Figure 5.6. The exchange kinetics are greatest initially which is attributable to an initial exchange with surface ligands and is corroborated by the large initial increase in surface contact angle shown in Figure 5.1. The subsequent exchange kinetics are slower than initially but show acceleration between 5-15 hours of exchange. Exchange ratios of 1.3% and 1.6% were observed after 15 hours of reaction at 60°C and 75°C respectively. The MSLER exchange kinetics shown are much slower than that observed during ZIF-8 crystal ligand exchange with Imca which shows approximately 20% new linker incorporation after 16 hours of reaction (Jayachandrababu et al., 2017). The difference is due to faster diffusion of the smaller Imca linker into the ZIF-8 structure as compared to that of the bulkier 5,6 DMBIm. Additionally, the thin film studied in this work is a compact polycrystalline structure; not

all crystal facets are exposed to the reaction solution and thus also leads to slower surface exchange rates.

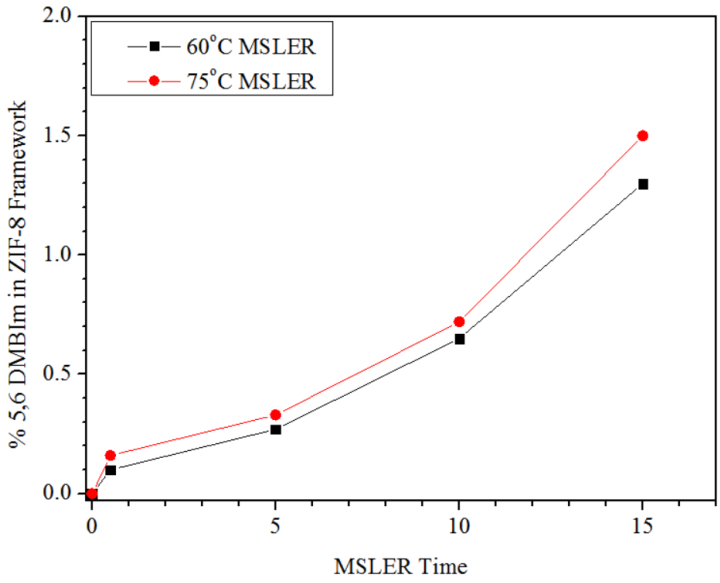

Figure 5.6 Composition analysis of modified ZIF-8 membrane with respect to MSLER time obtained by solution ^{1}HNMR

From the characterization data collected we propose a preliminary mechanism for further refinement. Upon initial contact with the highly concentrated 5,6 DMBIm ligand solution, ligand exchange occurs mainly at the membrane surface where hydrophobicity is increased. As time progresses, 5,6 DMBIm at the outer surface of the membrane breaks its initial bonding at the outer surface of the membrane crystals and proceeds inside the framework. Although 5,6 DMBIm is a large molecule, it can proceed into the large main cage of the ZIF-8 structure which is 11.6 Å in diameter, this is plausible as 1,2,4 Trimethylbenzene (7.6Å) has shown uptake in ZIF-8 due to the flexible nature of the framework (K. Zhang et al., 2013). The large ZIF-8 pore facilitates a large pathway for

diffusion of 5,6 DMBIm into the structure and counter-diffusion of HMIm out of the framework.

Significant changes in XRD intensity along the 011 plane (d-spacing of 11.6 Å) because it is the largest and most periodic plane in which the 5,6 DMBIm ligand can travel and exchange with original HMIm ligands. Initial exchange on the inner pore surface seemingly disrupts the periodicity of the 011 plane causing the decreases in relative XRD intensity shown in Figures 2 and 3. We postulate that after 5 hours of exchange at 60°C and 30 minutes of exchange at 75°C, the 011 plane becomes increasingly ordered with the new linker which leads to increases in 011 XRD peak intensity/periodicity. The difference in time to re-ordering is due to the faster diffusion and exchange occurring at higher temperatures.

Between 5-15 hours of reaction the acceleration in the ligand exchange rate exhibited in NMR suggests that there is a driving force for further incorporation of 5,6 DMBIm. SALE materials are often not well mixed (Jayachandrababu et al., 2017) and the observed phenomenon may suggest that the modified ZIF pore structure along the 011 plane exists in a high energy, unstable or metastable state that can attain lower free energy (stabilization) after the inner surface 5,6 DMBIm concentration is increased and/or the linker distribution is re-organized. The observation is directly correlated with the times in which Figures 5.4 & 5.5 present increases in XRD intensity and more strongly supports our postulation that the 011 plane becomes more ordered with an increasing amount of 5,6 DMBIm as MSLER time increases.

5.3.2 Effects of MSLER Time and Temperature on Light Hydrocarbon Gas Permeation

Figure 5.7 (A&B) shows binary ethylene/ethane permeance and separation factor as a function of time in membranes modified at 60 and 75°C respectively. After 30 minutes of modification, the ethylene and ethane permeances present notable declines. The permeation changes are concomitant with the initial exchange of ligand at the surface of the ZIF-8 membrane crystals and corresponds to the point at which the exchange kinetics are greatest. After 30 minutes of exchange, the relative changes in ethylene/ethane permeance enable an increase in separation factor from 2.1 to 2.2 after 30 minutes of MSLER at 60°C while the separation factor remains constant for the membrane reacted at 75°C. As the MSLER time proceeds, more monotonic decreases in permeance are observed for both membranes. The extent of C_2 separation factor increase and permeation decline corresponds to the extent of 5,6 DMBIm incorporation. After 15 hours of MSLER, the membrane reacted at 60°C gives a 68% decrease in ethylene permeance and the separation factor remains stable at 2.2. The membrane reacted at 75°C which contains a higher 5,6 DMBIm linker content shows an 82% decline in ethylene permeance and the separation factor increases from 2.2 to 2.4.

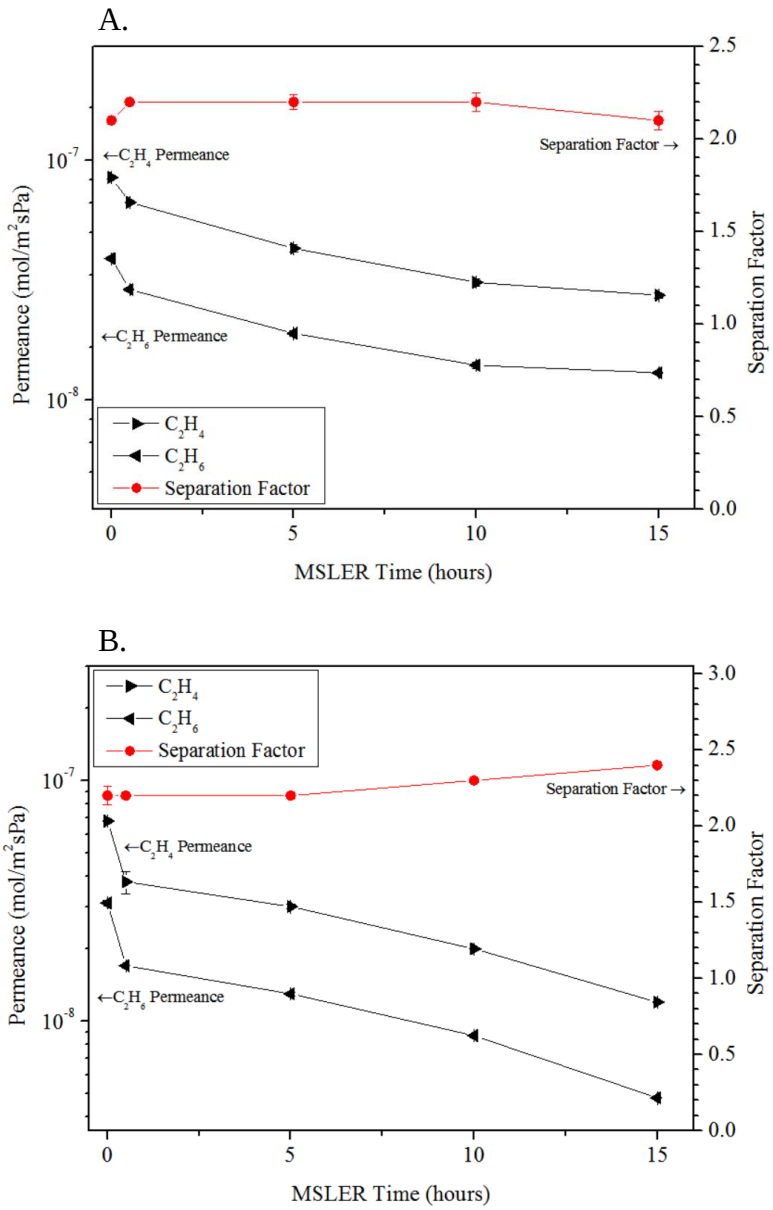

Figure 5.7 Ethylene/ethane permeance and separation factor as a function of MSLER time at 60°C (A) and 75°C (B)

From the current findings, incorporation 5,6 DMBIm into the ZIF-8 structure using the current synthesis parameters does not provide significant enhancement for C_2 olefin/paraffin separation. Permselectivity is a function the relative diffusivity and solubility of the permeating gasses. From the ZIF-7 work of Kapetijn and co-workers (Van

Den Bergh et al., 2011) we can deduce that ethylene and ethane solubility are similar in benzimidazole containing ZIF frameworks at the current feed pressure. It is reasonable to conclude that the current modification provides limited enhancement because the C_2 diffusivities are slowed to similar extents upon incorporation of the new bulkier linker.

Figure 5.8 (A&B) shows binary hydrogen/ethylene permeance and separation factor as a function of MSLER time. The ethylene permeation trend observed is similar to that of Figure 7, however, the extent of hydrogen permeation decline is not comparable to the ethylene molecule. The incremental addition of 5,6 DMBIm linker exhibits less of a slowing effect on the faster diffusing hydrogen molecule as compared to ethylene. This enables an $H_2/C_{2=}$ separation factor increase from 3.9 to 6.8 in the 60°C membrane and 3.6 to 11.3 in the 75°C membrane over the 15 hour MSLER reaction time.

Hydrogen/ethane permeation and separation factor is shown as a function of MSLER time in Figure 5.9 (A&B). The trend observed is almost identical to that of Figure 5.8 Hydrogen selectivity increases with increasing 5,6 DMBIm content. It is interesting to note that that step change increases in the H_2/ethane and H_2/ethylene separation factors are noted between 5-10 hours for the 60°C membrane and 5-10/10-15 hours for the 75°C membrane. These times correspond to the accelerated rate of 5,6 DMBIm increase as shown in the ^{1}HNMR data in Figure 5.6 and increases in crystallinity/electron density shown in Figures 5.4 & 5.5 and agrees well with the permeation phenomena observed.

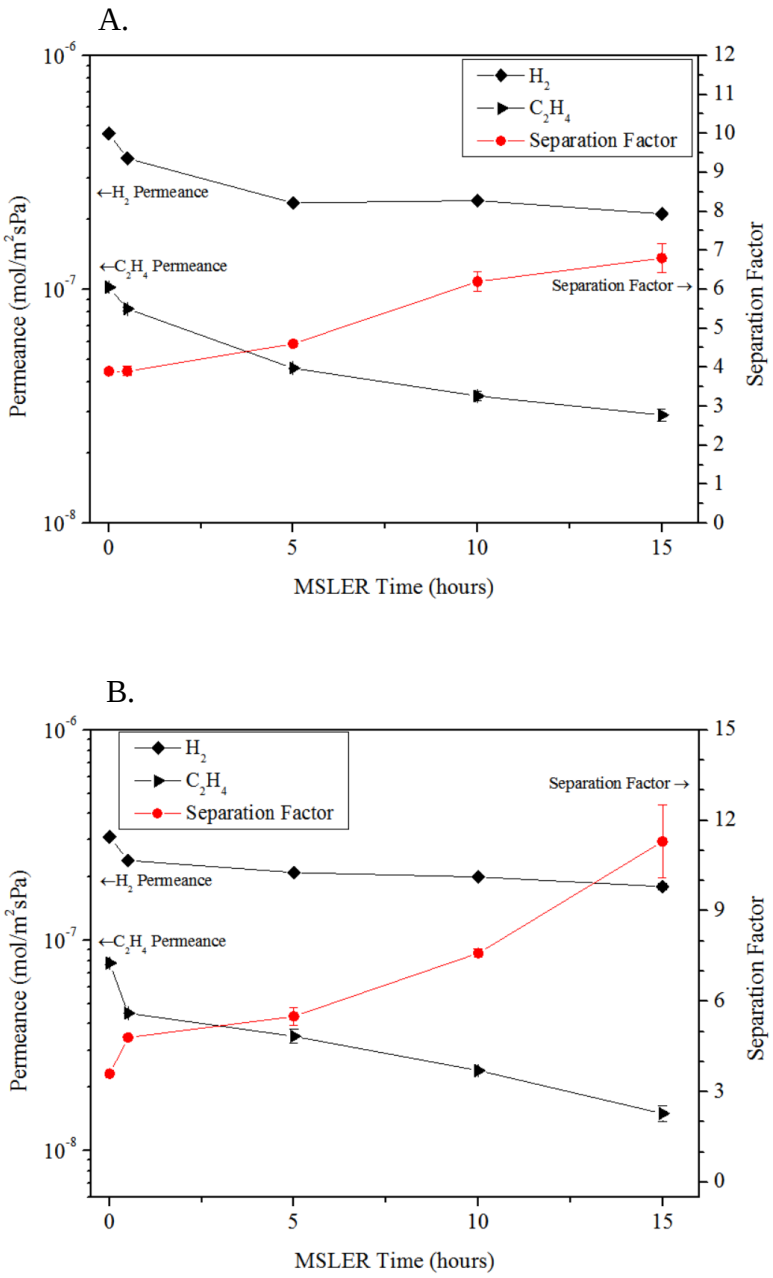

Figure 5.8 Hydrogen/ethylene permeance and separation factor as a function of MSLER time at 60°C (A) and 75°C (B)

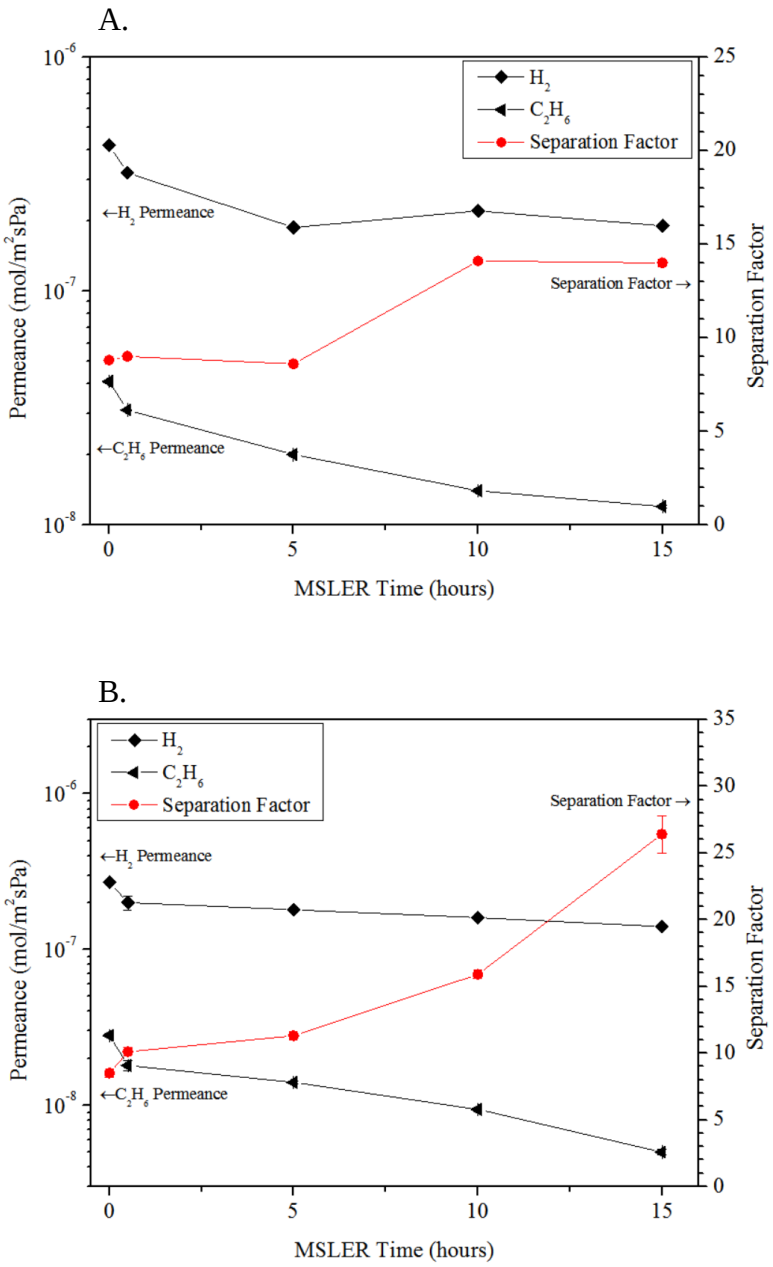

Figure 5.9 Hydrogen/ethane permeance and separation factor as a function of MSLER time at 60°C (A) and 75°C (B)

Figure 5.10 illustrates binary hydrogen/propylene permeance as a function of MSLER time. During $H_2/C_{3=}$ permeance in the 60°C membrane, hydrogen permeance

decreases to a similar extent as compared to C_3 between 0-5 hrs reaction time; this differs as compared to C_2. The larger propylene molecule more efficiently blocks H_2 during this time period and can more significantly slow H_2 as compared to C_2 molecules. Between 5-10 hrs propylene permeance increases, H_2 permeance does not and likely means that C_3 solubility is enhanced by the increased presence of the benzene-substituted linker. H_2/C_3 permeance and separation factor remains constant after 10 hours. The 75°C membrane presents similar phenomena but at shorter time, a small propylene permeance increase is shown after 30 minutes of MSLER followed by a relative flattening of the permeance and separation factor trends thereafter.

The $H_2/C_{3=}$ separation behavior seems to track or be correlated to the phenomena graphically illustrated in Figure 5.5. During the 60°C experiment, crystallinity decreases between 0-5 hours of exchange. During this time period relative changes in $H_2/C_{3=}$ permeances are similar. After 5 hours of exchange, Figure 5.5 shows an inflection point after which an increase in crystallinity/order or electron density along the 011 plane. At corresponding time of the inflection point in Figure 5.5, a decrease in the $H_2/C_{3=}$ separation factor is denoted which we ascribe to enhanced $C_{3=}$ solubility. In the case of reaction at 75°C, the inflection point in Figure 5.5 occurs just after 30 minutes of exchange and coincides with the $H_2/C_{3=}$ separation factor decrease. Between 30 minutes and 15 hours of exchange, the 011 peak intensity ratio increases and the $H_2/C_{3=}$ separation factor converges to a stable value. The relationship between the dynamic changes in crystallinity and $H_2/C_{3=}$ behavior suggest that $C_{3=}$ solubility is enhanced after the framework's crystallinity increases during incorporation of the new 5,6 DMBIm ligand.

A.

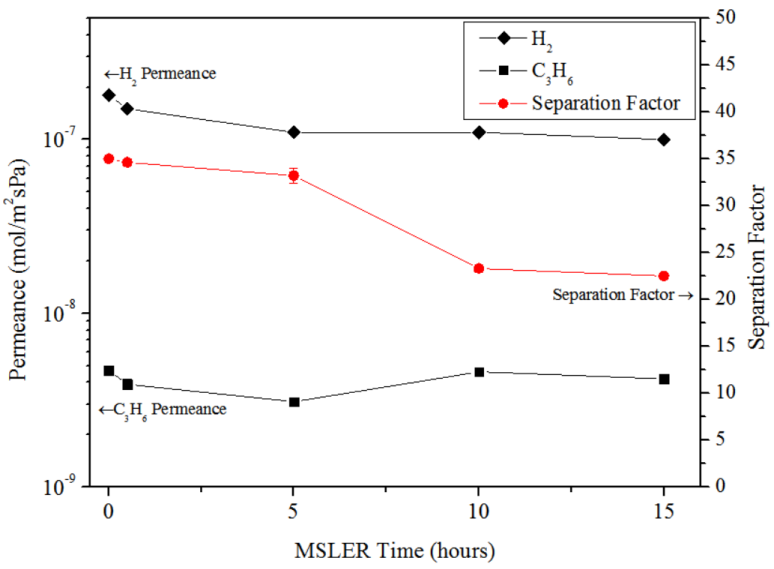

B.

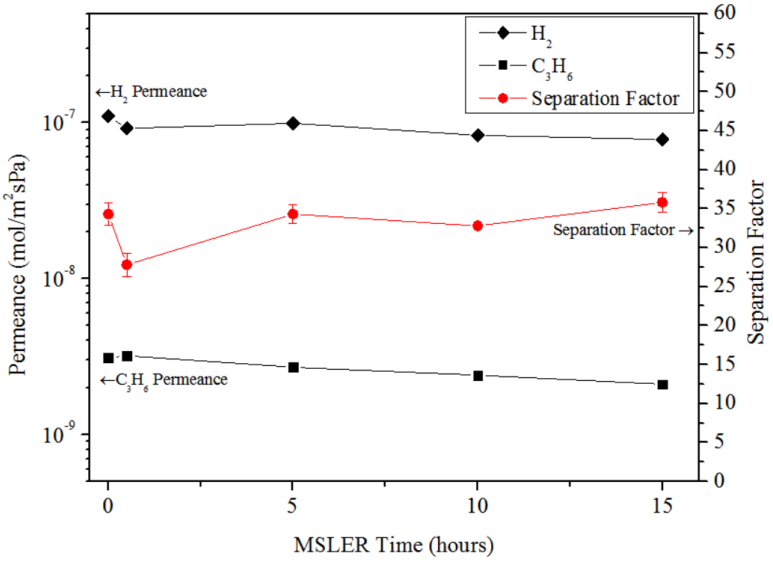

Figure 5.10 Hydrogen/propylene permeance and separation factor as a function of MSLER time at 60°C (A) and 75°C (B)

A.

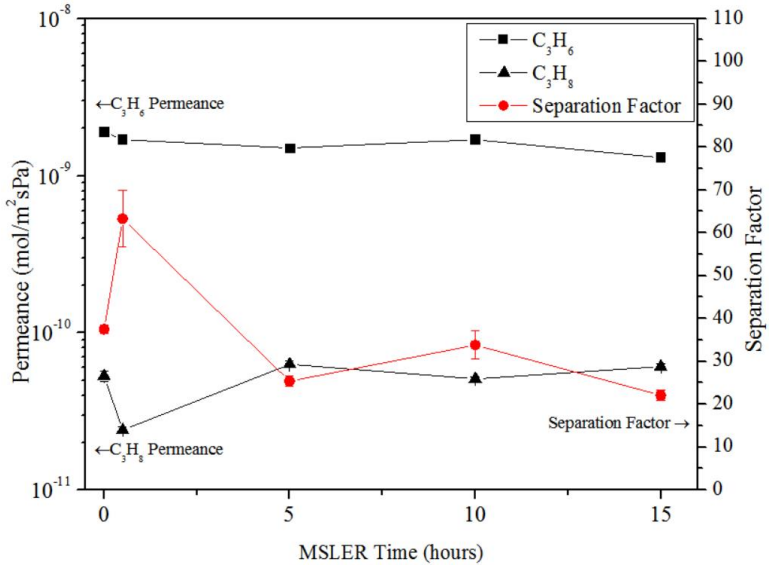

B.

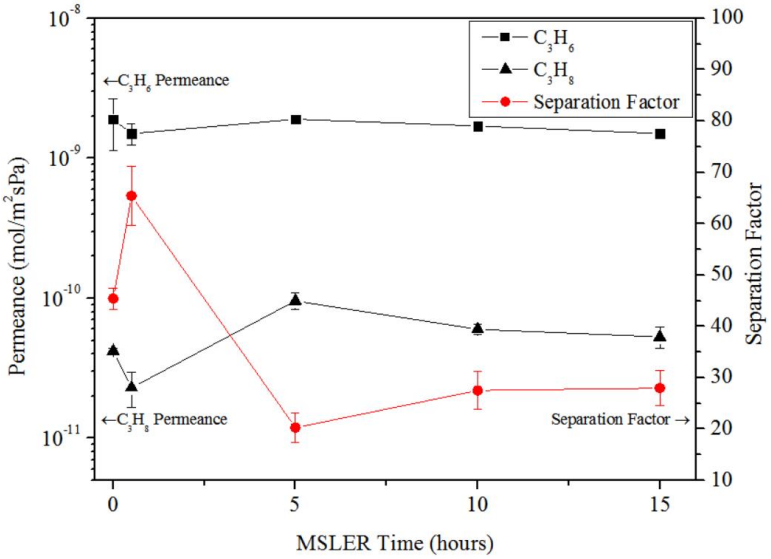

Figure 5.11 Propylene/propane permeance and separation factor as a function of MSLER time at 60°C (A) and 75°C (B)

Figure 5.11 presents propylene/propane permeance and separation factor as a function of MSLER time. Significant increases in C_3 selectivity and minimal propylene permeance losses occur after 30 minutes of reaction for both the 60°C membrane (70% SF

increase,~10% $C_{3=}$ permeance decrease) and the 75°C membrane (44% SF increase, ~20% decrease in $C_{3=}$ permeance). The finding implies that propane diffusivity is decreased more than propylene diffusivity after short-term modification. 30 minutes of exchange likely creates a decorated outer pore aperture containing a heterogeneous composition of both 2-MIm and 5,6 DMBIm linkers. Addition of the bulkier linker enhances the pre-existing $C_{3=}/C_{3-}$ diffusive selectivity exhibited in pure ZIF-8 while limiting propylene permeance loss. The short-time modification is more effective for C_3 molecules as compared to C_2 because of the molecular size difference the two groups.

Beyond 30 minutes of modification, propane permeance increases relative to propylene then stabilizes for both membranes and the separation factor decreases. The decreases in selectivity are also concomitant with the inflection points found in Figure 5.5 and the acceleration in 5,6 DMBIm exchange shown in Figure 5.6. We propose that the propane permeation enhancement is also an effect of increased solubility. Furthermore this effect may only be expressed for C_3 molecules because they are more polarizable than lower carbon molecules (C. Zhang et al., 2012) and may have more interaction with the benzene substituents of the imidazole ligands lining the ZIF pore undergo an adsorption/surface diffusion mechanism in the modified pore system.

5.4 Conclusions

ZIF-8 membranes were modified with 5,6 DMBIm through the membrane surface ligand exchange reaction technique. Changes in the modified ZIF's physical properties and resulting light hydrocarbon binary permeation/separation properties were analyzed ex-situ

as a function of MSLER time and temperature. Our findings suggest that MSLER with the bulky 5,6 DMBIm ligand proceeds quickly during the first 30 minutes of exchange mainly at the outer surface of the membrane crystals, then slows as the new ligand proceeds inside the framework, exchanges with the original linker and disrupts the original framework's crystallinity.

As the reaction time proceeds the exchange rate accelerates as crystallinity is increased with the new linker. The overall rate of exchange increases with MSLER temperature. MSLER with 5,6 DMBIm slows C_2 olefin/paraffin molecules to a similar extent and provides minimal separation enhancement. In H_2/C_2 separations, C_2 molecules are slowed to a greater extent than hydrogen which enables significant increases in H_2/C_2 the separation factor as a function of MSLER time and temperature. H_2/propylene separations are not enhanced by MSLER with the bulkier ligand and seems to be an effect of C_3 molecule blocking the smaller H_2 molecule and increased C_3 solubility as 5,6 DMBIm content increases in the inner pore surface. MSLER significantly enhances C_3 olefin/paraffin separation after short (30 min) modification time, but is decreased thereafter likely due to a relative solubility enhancement in propane over propylene.

CHAPTER 6

SUMMARY AND RECOMMENDATIONS

6. Summary and Recommendations

The studies presented in this dissertation were focused on providing a better fundamental understanding of the thermal stability of ZIF-8 crystals and thin films, the transport of light hydrocarbons in ZIF-8 membranes and the modification of ZIF-8 membranes though ligand exchange. The main goals of this work were to determine the feasibility of ZIF-8 to be utilized as high temperature membrane reactor material and study its potential as a template for surface modification to enhance light hydrocarbon and hydrogen separations.

6.1 ZIF-8 Thermal Stability Studies

6.1.1 ZIF-8 Crystal Thermal Stability Studies

To gain a better understanding of ZIF-8 crystal thermal stability, ZIF-8 crystalline powders were synthesized and subjected to temperatures of 200, 250 and 300°C in inert, oxidizing and reducing atmospheres for a duration of 20 hours during static TGA experiments. The study determined that ZIF-8 nanocrystals maintain their crystallinity up to temperatures of 200°C irrespective of environment. At 250°C and higher our findings support the postulation that ZIF-8 crystals undergo temperature induced decomposition through a set of thermolytic bond cleaving reactions to form an average structure composed of Imidazole-Zn-Azirine subunits. At 300°C the ZIF-8 decomposition rate in air is greatest

due to oxidative interactions likely at the methyl group of the 2-methylimidazole ligand. At lower temperatures, decomposition in air behaves more similarly to that of nitrogen. Decomposition in argon is greatest at lower temperatures because the decomposition environment is devoid of nitrogen as compared to air and N_2 gas which slow the driving force for nitrogen evolution from the framework. Decomposition in H_2/CO_2 environment is slowest at all temperatures. The findings from the crystal experiments enable the conclusion that ZIF-8 does not present static thermal stability at the temperatures normally utilized in applications such as propane dehydrogenation which occurs at temperatures > 300°C.

The preceding work was performed with ZIF-8 nanocrystals which are formed from synthesis protocols which enable fast nucleation and slow growth. Sometimes this method of crystal growth leads to structural defects and incomplete growth of crystal facets. The use of more mature, larger, faceted crystals may be a point of future study and can be employed in an analogous study to determine the differences in static thermal stability between ZIF-8 nanocrystals and microcrystals.

6.1.2 ZIF-8 Membrane Thermal Stability Studies

The findings in the ZIF-8 crystal decomposition experiments likely preclude ZIF-8 as a high temperature material for hydrocarbon dehydrogenation membrane reactor materials, however the observed preservation of crystallinity at 200°C necessitated a study of ZIF-8 thin film membrane stability and permeation characteristics at moderate to high temperatures for gas separations applications such as the low temperature water-gas shift

membrane reactor and dehydrogenation membrane assisted reactors which can run at temperatures of 180°C or higher.

Temperature dependent tests were conducted from room temperature to 300°C using hydrogen and carbon dioxide as permeation tests gasses. The permeance of both gasses behaved according to solution diffusion mechanism between 25-250°C, however as temperature was further increased, sudden increases in both gasses' permeance and H_2/CO_2 separation factor were observed. This departure from the solution diffusion mechanism was due the partial carbonization of the framework into amorphous ZIF-derived partially carbonized molecular sieve between 250-275°C. Further isothermal tests were performed at 50, 100, 150 and 300°C for 24 hours in separate, comparable membranes to de-convolute the time/temperature dependency of ZIF-8 thermal decomposition. The ZIF-8 membranes were determined to maintain crystallinity/bond integrity at temperatures below 150°C.

The differences in ZIF-8 membrane and ZIF-8 free crystal (stable up to 200°C) thermal stability is attributed to membrane thin film cracking that occurs during elevated temperature experiments. The observed cracking is likely an effect of thermomechanical instability due to the difference in the thermal expansion coefficients of the ZIF-8 membrane and the α-alumina support. We postulate that the thermomechanical stress creates incongruent strain in the framework in addition to thermal stresses and exacerbates the ZIF-8 bonding in the thin film membrane to a greater extent than what is experienced in free crystals. It is recommended that thermally and mechanically stable supports with thermal expansion coefficients more compatible with that of ZIF-8 be utilized in analogous

static thermal stability experiments to determine if the α-alumina support does in fact affect the stability of ZIF-8 thin films.

An interesting finding was discovered during the temperature dependent and 300°C transient experiments. The ZIF-8 membranes which were both partially carbonized on-line during the permeation tests still presented good H_2/CO_2 separation performance with higher H_2 and CO_2 permeances. The membrane carbonized during the temperature dependent experiment showed an increase in separation factor from 3.7 to 5.0 while the membrane partially carbonized during the 300°C experiment showed a stable H_2/CO_2 separation factor of 3.7 for 16 hours. The partially carbonized ZIF-8 membranes may be potential candidates for n-butane (n-C_4)/i-butane (i-C_4) isomer separations. In a ZIF-8 crystal transient uptake study by Koros and co-workers an n-C_4/i-C_4 diffusive selectivity of 2.5 x 10^6 was determined (C. Zhang & Koros, 2015). In the same study, the n-C_4/i-C_4 diffusive selectivity was increased 28 times with a 1 order of magnitude decrease in selectivity after partially carbonizing ZIF-8 crystals (C. Zhang & Koros, 2015). The increased n-butane diffusivity with still sizeable diffusive selectivity is highly attractive. It is recommended that further study of structure-property relationships of carbonized ZIF-8 crystalline powders and membranes be conducted. Variables such as decomposition atmosphere, temperature ramping rate, final temperature and temperature soak time can be modulated during on-line partial decomposition experiments and the resulting membranes' or powders' structural properties (composition, bonding, surface area, volume) can be characterized and correlated to their gas separation properties (adsorption, diffusion, permeability, selectivity).

6.2 ZIF-8 Membrane Transport and Modification Studies

6.2.1 ZIF-8 Membrane Ethylene/Ethane Transport Studies

According to the previous findings, ZIF-8 currently shows the most promise for separations which can be conducted at temperatures below 150°C. In subsequent experiments, the transport of light hydrocarbons, specifically ethane and ethylene in single gas and binary mixtures was studied in ZIF-8 membranes due to the lack of information on parameters which govern C_2 molecule permeation through the ZIF-8 framework. During single gas and binary ethylene and ethane experiments conducted from 25-100°C, the permeances of both molecules decreased monotonically with respect to temperature because the activation energies of diffusion for both molecules are less than their respective heats of adsorption as calculated from permeation and adsorption experiments.

Although the van der Waals diameters of ethylene and ethane are larger than the nominal pore aperture of ZIF-8, low activation energy of diffusion values and no appreciable energetic-based diffusive selectivity is exhibited for C_2 molecules in ZIF-8 due to the intrinsic pore flexibility of the framework. The similarly sized C_2 molecules are both smaller than the effective ZIF-8 pore aperture. Entropic selectivity for the C_2 molecules in ZIF-8 is limited by the zeolitic pore shape. Binary C_2 permeation selectivity is 20% lower than ideal selectivity due to cooperative adsorption which enhances ethane solubility in the presence of ethylene. Due to limited diffusive selectivity and preferential ethane adsorption in ZIF-8, C_2 binary selectivity in ZIF-8 is not much greater 2 in ZIF-8 membranes.

During H_2/C_2 separation experiments it was noted that the presence of strongly adsorbing C_2 molecules in mixture with hydrogen decreases H_2 permeability and inverts the H_2 temperature dependency of permeation from adsorption to diffusion controlled. Pressure dependent experiments illustrated that ideal and binary ethylene/ethane permeation behavior as a function of pressure starkly contrast due to differences in single gas and binary adsorption isotherms for the corresponding molecules.

6.2.2 ZIF-8 Membrane Modification Studies

A time based ex situ study of ZIF-8 membrane surface ligand exchange was conducted to determine the effects of ligand exchange time and temperature on the membrane structure and correlate the resulting structural changes to changes in light hydrocarbon gas permeation and separation behavior in the modified ZIF-8 framework. The bulky 5,6 dimethylbenzimidazole ligand was utilized for exchange with 2-methylimidazole with the goal providing enhanced large molecule resistance in olefin/paraffin and hydrogen/hydrocarbon gas separations.

According to the findings within the MSLER study, relatively fast exchange kinetics occur at the mainly at the outer surface of the ZIF-8 membrane between 0-30 minutes of exchange. Short time exchange enables significant increases in C_3 olefin/paraffin selectivity with minimal olefin permeance losses because mainly the outer ZIF-8 crystal surface is endowed with the new linker which provides enhanced propylene/propane selectivity while the inner surface maintains most of the original ZIF-8 linker which facilitates sizeable propylene permeability. The C_2 olefin/paraffin separation

factor does not show sizeable increases during MSLER because the permeances of both molecules are slowed to a similar extent upon incorporation of 5,6 DMBIm within the framework.

We postulate that as the reaction time proceeds, the ligand exchange rate slows as the 5,6 DMBIm linker proceeded into the ZIF-8 inner surface, exchanges with the original linker and disrupts the original framework's crystallinity. The majority of 5,6 DMBIm interpenetration occurs along the 011 plane as this plane contains the largest d-spacing suitable for diffusion of 5,6 DMBIm into the framework and counter-diffusion of the original linker out of the system. As the reaction time proceeds further, the exchange rate accelerates as crystallinity is increased with the new linker. The overall rate of exchange increases with increasing temperature. The H_2/C_2 separation factor shows increases with increasing 5,6 DMBIm content while H_2/C_3 and C_3 olefin paraffin binary selectivity decreased with respect to increasing MSLER time due to what seems to be an increase in the relative solubility of the larger molecule within each binary pair.

The MSLER study provided broad, new pathways for future study. From the current findings, modification for short durations can enhance olefin/paraffin separation. Potentially a ligand modification which only penetrates the very outermost crystals can provide a true gating effect in which enhanced sieving occurs at the outer membrane surface, then once inside, the fast molecule (hydrogen or olefin) can proceed efficiently through the uninterrupted ZIF-8 inner core.

To achieve outer surface only modification for enhanced olefin/paraffin separation, shorter MSLER times can be utilized while varying the ligand concentration and/or

reaction temperature. Additionally, the as synthesized ZIF-8 membrane can be placed in a flow cell apparatus in which two immiscible fluids such as butanol and water are flowed from opposite sides of the membrane and contact one another at the membrane surface to form an immiscible interface. The new exchanging linker likely solvated in alcohol can diffuse across the interface in a controlled manner to form a monolayer across the membrane surface.

New ligands of differing functionalities can also be utilized to modulate separation performance. Benzene substituted ligands with functionality at the two position of the ligand with or without the methyl groups at the 5 and 6 positions can be utilized. Also, modulation of the chemical functionality of the substituting linker may be a point for future study. Electron donating methyl groups were substituted on the benzimidazole ligands studied in this work. Electron withdrawing groups can be substituted on benzimidazole linkers to compare the effect chemical functionality on light hydrocarbon sieving.

Further work can also be performed to purposely decorate the inner pore surface of ZIF membranes. Hydrogen/hydrocarbon selectivity was significantly enhanced by incorporating the bulkier ligand within the ZIF framework. Further studies with new ligands may provide enhanced selectivity with minimal hydrogen permeability losses.

Lastly, ZIF-67 the Co analogue of ZIF-8 has already been proven as a superior propylene/propane molecular sieve over ZIF-8. The Co-N bond is stronger, shorter more ridged as compared Zn-N and facilitates a slightly smaller 3.0 Å pore aperture for higher resolution molecular sieving. C_3 selectivities of 200 with propylene permeabilities comparable to that of ZIF-8 have been reported by Jeong and co-workers (Kwon et al.,

2015). Further study of C_2 separation in ZIF-67 is suggested. Subsequent gating experiments may show improvement over analogous ZIF-8 studies because the gates (larger, exchanging linkers) may be tighter or more rigid.

REFERENCES

Agarwal, K., John, M., Pai, S., Newalkar, B. L., Bhargava, R., & Choudary, N. V. (2010). SAPO-34 assisted C3 separation: Modeling and simulation. *Microporous and Mesoporous Materials*, *132*(3), 311–318. http://doi.org/10.1016/j.micromeso.2010.02.024

Aguado, S., Daniel, C., Farrusseng, D., Recherches, I. De, Ircelyon, D. L., & Einstein, A. a. (2012). Absolute Molecular Sieve Separation of Ethylene / Ethane Mixtures. *J. Am. Chem. Soc.*, *134*, 14635–14637. http://doi.org/10.1021/ja305663k

Alshehri, A., & Lai, Z. (2015). Attainability and minimum energy of single-stage membrane and membrane/distillation hybrid processes. *Journal of Membrane Science*, *472*, 272–280. http://doi.org/10.1016/j.memsci.2014.08.056

Amrouche, H., Aguado, S., Javier, P., Siperstein, F., Farrusseng, D., Bats, N., & Nieto-draghi, C. (2011). Experimental and Computational Study of Functionality Impact on Sodalite À Zeolitic Imidazolate Frameworks for CO 2 Separation.

Angelini, P., Armstrong, T., Counce, R., Griffith, W., Klasson, T., Muralidharan, G., … Watson Disclaimer, J. (2005). Materials for Separation Technologies: Energy and Emission Reduction Opportunities and Vinod Sikka from ORNL, and the industrial experts working under subcontracts with ORNL.

Anniyappan, M., Sonawane, S. H., Pawar, S. J., & Sikder, A. K. (2015). Thermal decomposition and kinetics of 2,4-dinitroimidazole: An insensitive high explosive. *Thermochimica Acta*, *614*, 93–99. http://doi.org/10.1016/j.tca.2015.05.027

Aoki, K., Kusakabe, K., & Morooka, S. (1998). Gas permeation properties of A-type zeolite membrane formed on porous substrate by hydrothermal synthesis. *Journal of Membrane Science*, *141*(2), 197–205. http://doi.org/10.1016/S0376-7388(97)003001

Assfour, B., Leoni, S., & Seifert, G. (2010). Hydrogen adsorption sites in zeolite imidazolate frameworks ZIF-8 and ZIF-11. *Journal of Physical Chemistry C*, *114*, 13381–13384. http://doi.org/10.1021/jp101958p

Bai, F., Xia, Y., Chen, B., Su, H., & Zhu, Y. (2014). Preparation and carbon dioxide uptake capacity of N-doped porous carbon materials derived from direct carbonization of zeolitic imidazolate framework. *Carbon*, *79*, 213–226. http://doi.org/10.1016/j.carbon.2014.07.062

Baker, R. W. (2002). Future Directions of Membrane Gas Separation Technology. *Industrial & Engineering Chemistry Research*, *41*,1393–1411. http://doi.org/10.1021/ie0108088

Baker, R. W., & Lokhandwala, K. (2008). Natural Gas Processing with Membranes: An Overview. http://doi.org/10.1021/ie071083w

Bakker, W. J. W., Kapteijn, F., Poppe, J., & Moulijn, J. a. (1996). Permeation characteristics of a metal-supported silicalite-1 zeolite membrane. *Journal of Membrane Science*, *117*, 57–78. http://doi.org/10.1016/0376-7388(96)00035-X

Banerjee, R., Furukawa, H., Britt, D., Knobler, C., O'Keeffe, M., & Yaghi, O. M. (2009a). Control of pore size and functionality in isoreticular zeolitic imidazolate frameworks and their carbon dioxide selective capture properties. *Journal of the American Chemical Society*, *131*(11), 3875–3877. http://doi.org/10.1021/ja809459e

Banerjee, R., Furukawa, H., Britt, D., Knobler, C., O'Keeffe, M., & Yaghi, O. M. (2009b). Control of Pore Size and Functionality in Isoreticular Zeolitic Imidazolate Frameworks and their Carbon Dioxide Selective Capture Properties. *Journal of the American Chemical Society*, *131*(11), 3875–3877. http://doi.org/10.1021/ja809459e

Bao, Z., Alnemrat, S., Yu, L., Vasiliev, I., Ren, Q., Lu, X., & Deng, S. (2011). Adsorption of ethane, ethylene, propane, and propylene on a magnesium-based metal-organic framework. *Langmuir*, *27*(22), 13554–13562. http://doi.org/10.1021/la2030473

Barrer, R. M., & Rideal, E. K. (1939). Activated diffusion in membranes. *Transactions of the Faraday Society*, *35*(0), 644. http://doi.org/10.1039/tf9393500644

Barrer, R. M., & Skirrow, G. (1948). Transport and equilibrium phenomena in gas–elastomer systems. I. Kinetic phenomena. *Journal of Polymer Science*, *3*(4), 549–563. http://doi.org/10.1002/pol.1948.120030410

Beyond, M. ethylene/ethane separation: T. upper bound and, Rungta, M., Zhang, C., Koros, W. J., & Liren, X. (2013). Membrane-Based Ethylene/Ethane Separation: The Upper Bound and Beyond. *AIChE Journal*, *59*(9), 3475–3489. http://doi.org/10.1002/aic.14105

Bhange, D. S., Pandya, N. A., Jha, R. K., & Ramaswamy, V. (2008). Non-isothermal kinetic studies of the template decomposition from silicalite-1 framework-high temperature X-ray diffraction and thermogravimetric analysis. *Microporous and Mesoporous Materials*, *113*(1–3), 64–71. http://doi.org/10.1016/j.micromeso.2007.11.002

Bhattacharjee, S., Jang, M. S., Kwon, H. J., & Ahn, W. S. (2014). Zeolitic Imidazolate Frameworks: Synthesis, Functionalization, and Catalytic/Adsorption Applications. *Catalysis Surveys from Asia*, 101–127. http://doi.org/10.1007/s10563-014-9169-8

Bloch, E. D., Queen, W. L., Krishna, R., Zadrozny, J. M., Brown, C. M., & Long, J. R. (2012). Hydrocarbon Separations in a Metal-Organic Framework with Open Iron(II) Coordination Sites. *Science*, *335*(Ii), 1606–1610. http://doi.org/10.1126/science.1217544

Böhme, U., Barth, B., Paula, C., Kuhnt, A., Schwieger, W., Mundstock, A., … Hartmann, M. (2013). Ethene/Ethane and Propene/Propane Separation via the Olefin and Paraffin Selective Metal–Organic Framework Adsorbents CPO-27 and ZIF-8. *Langmuir*, *29*(27), 8592–8600. http://doi.org/10.1021/la401471g

Brown, A. J., Brunelli, N. A., Eum, K., Rashidi, F., Johnson, J. R., Koros, W. J., … Nair, S. (2014). Interfacial microfluidic processing of metal-organic framework hollow fiber membranes. *Science*, *345*(6192).

Brown, M. E. (1997). Steps in a minefield. Some kinetic aspects of thermal analysis. *Journal of Thermal Analysis*, *49*, 17–32.

Bryden, K. (2002). Nanostructured palladium–iron membranes for hydrogen separation and membrane hydrogenation reactions. *Journal of Membrane Science*, *203*(1–2), 29–42. http://doi.org/10.1016/S0376-7388(01)00736-0

Burns, R. L., & Koros, W. J. (2003). Defining the challenges for C3H6/C3H8 separation using polymeric membranes. *Journal of Membrane Science*, *211*(2), 299–309. http://doi.org/10.1016/S0376-7388(02)00430-1

Bux, H., Chmelik, C., Krishna, R., & Caro, J. (2011). Ethene/ethane separation by the MOF membrane ZIF-8: Molecular correlation of permeation, adsorption, diffusion. *Journal of Membrane Science*, *369*(1), 284–289. http://doi.org/10.1016/j.memsci.2010.12.001

Bux, H., Feldhoff, A., Cravillon, J., Wiebcke, M., Li, Y. S., & Caro, J. (2011). Oriented zeolitic imidazolate framework-8 membrane with sharp H 2/C3H8 molecular sieve separation. *Chemistry of Materials*, *23*, 2262–2269. http://doi.org/10.1021/cm200555s

Cadiau, A., Adil, K., Bhatt, P. M., Belmabkhout, Y., & Eddaoudi, M. (2016). A metal-organic framework-based splitter for separating propylene from propane. *Science*, *353*(6295), 137–140. http://doi.org/10.1126/science.aaf6323

Chaikittisilp, W., Hu, M., Wang, H., Huang, H.-S., Fujita, T., Wu, K. C.-W., … Ariga, K. (2012). Nanoporous carbons through direct carbonization of a zeolitic imidazolate framework for supercapacitor electrodes. *Chemical Communications*, *48*, 7259. http://doi.org/10.1039/c2cc33433j

Champagnie, A. M., Tsotsis, T. T., Minet, R. G., & Wagner, E. (1992). The study of ethane dehydrogenation in a catalytic membrane reactor. *Journal of Catalysis*, *134*(2), 713–730. http://doi.org/10.1016/0021-9517(92)90355-L

Chen, B., Yang, Z., Zhu, Y., & Xia, Y. (2014). Zeolitic imidazolate framework materials : recent progress in synthesis and applications. *Journal of Materials Chemistry A: Materials for Energy and Sustainability*, *2*, 16811–16831. http://doi.org/10.1039/C4TA02984D

Chmelik, C., Freude, D., Bux, H., & Haase, J. (2012). Ethene/ethane mixture diffusion in the MOF sieve ZIF-8 studied by MAS PFG NMR diffusometry. *Microporous and Mesoporous Materials*, *147*(1), 135–141. http://doi.org/10.1016/j.micromeso.2011.06.009

Choi, S.-W., Jones, C. W., Nair, S., Sholl, D. S., Moore, J. S., Liu, Y., … Pendergast, J. G. (2015). Material properties and operating configurations of membrane reactors for propane dehydrogenation. *AIChE Journal*, *61*(3), 922–935. http://doi.org/10.1002/aic.14700

Cohen, S. M. (2017). The Postsynthetic Renaissance in Porous Solids. *Journal of the American Chemical Society*, *139*(8), 2855–2863. http://doi.org/10.1021/jacs.6b11259

Cooms, D. (2016). *Propylene: The "Other" Olefin*. PowerPoint Presentation at the Goldman Sachs Chemical Intensity Conference, Houston Texas

Comyns, A. E. (2001). Chemical process technology. J.A. Moulijn, M. Makkee and A. van Diepen. John Wiley and Sons Ltd, Chichester, 2001. (paperback). *Applied Organometallic Chemistry*, *15*(12), 956–956. http://doi.org/10.1002/aoc.202

Cope, A. C., & Mehta, A. S. (1963). Mechanism of the Hofmann Elimination Reaction: An Ylide Intermediate in the Pyrolysis of a Highly Branched Quaternary Hydroxide. *Journal of the American Chemical Society*, *85*(13), 1949–1952. http://doi.org/10.1021/ja00896a012

Cravillon, J., Münzer, S., Lohmeier, S., Feldhoff, A., & Huber, K. (2009). Rapid Room-Temperature Synthesis and Characterization of Nanocrystals of a Prototypical Zeolitic Imidazolate Framework. *Chemistry of Materials*, *21*(8), 1–21. http://doi.org/10.1021/cm900166h

Cravillon, J., Nayuk, R., Springer, S., Feldhoff, A., Huber, K., & Wiebcke, M. (2011). Controlling zeolitic imidazolate framework nano- and microcrystal formation: Insight into crystal growth by time-resolved in situ static light scattering. *Chemistry of Materials*, *23*, 2130–2141. http://doi.org/10.1021/cm103571y

Da Silva, F. A., & Rodrigues, A. E. (1999). Adsorption Equilibria and Kinetics for Propylene and Propane over 13X and 4A Zeolite Pellets. *Industrial & Engineering Chemistry Research*, *38*(5), 2051–2057. http://doi.org/10.1021/ie980640z

DeCoste, J. B., Peterson, G. W., Schindler, B. J., Killops, K. L., Browe, M. a., & Mahle, J. J. (2013). The effect of water adsorption on the structure of the carboxylate containing metal–organic frameworks Cu-BTC, Mg-MOF-74, and UiO-66. *Journal of Materials Chemistry A*, *1*(1), 11922. http://doi.org/10.1039/c3ta12497e

Deria, P., Mondloch, J. E., Tylianakis, E., Ghosh, P., Bury, W., Snurr, R. Q., … Farha, O. K. (2013). Perfluoroalkane Functionalization of NU-1000 via Solvent-Assisted Ligand Incorporation: Synthesis and CO $_2$ Adsorption Studies. *Journal of the American Chemical Society*, *135*(45), 16801–16804. http://doi.org/10.1021/ja408959g

Do, D. D. (1998). *Adsorption Analysis: Equilibria and Kinetics* (Vol. 2). PUBLISHED BY IMPERIAL COLLEGE PRESS AND DISTRIBUTED BY WORLD SCIENTIFIC PUBLISHING CO. http://doi.org/10.1142/p111

Do, D. D., & Do, H. D. (2005). Cooperative and Competitive Adsorption of Ethylene, Ethane, Nitrogen and Argon on Graphitized Carbon Black and in Slit Pores. *Adsorption*, *11*(1), 35–50. http://doi.org/10.1007/s10450-005-1091-y

Dong, J. H., Lin, Y. S., & Liu, W. (2000). Multicomponent hydrogen/hydrocarbon separation by MFI-type zeolite membranes. *Aiche Journal*, *46*(10), 1957–1966. http://doi.org/10.1002/aic.690461008

Dong, J., Lin, Y. S., & Liu, W. (2000). Multicomponent hydrogen/hydrocarbon separation by MFI-type zeolite membranes. *AIChE Journal*, *46*(10), 1957–1966. http://doi.org/10.1002/aic.690461008

Drobek, M., Bechelany, M., Vallicari, C., Abou Chaaya, A., Charmette, C., Salvador-Levehang, C., … Julbe, A. (2015). An innovative approach for the preparation of confined ZIF-8 membranes by conversion of ZnO ALD layers. *Journal of Membrane Science*, *475*, 39–46. http://doi.org/10.1016/j.memsci.2014.10.011

Eldridge, R. B. (1993). Olefin/paraffin separation technology: a review. *Industrial & Engineering Chemistry Research*, *32*, 2208–2212. http://doi.org/10.1021/ie00022a002

Eriksen, O. I., Aksnes, E., & Dahl, I. M. (1993). Facilitated transport of ethene through Nafion membranes. Part I. Water swollen membranes. *Journal of Membrane Science*, *85*(1), 89–97. http://doi.org/10.1016/0376-7388(93)85009-L

Eum, K., Jayachandrababu, K. C., Rashidi, F., Zhang, K., Leisen, J., Graham, S., Nair, S. (2015). Highly Tunable Molecular Sieving and Adsorption Properties of Mixed-Linker Zeolitic Imidazolate Frameworks.

Eum, K., Ma, C., Rownaghi, A., Jones, C. W., & Nair, S. (2016). ZIF-8 Membranes via Interfacial Microfluidic Processing in Polymeric Hollow Fibers: Efficient Propylene Separation at Elevated Pressures. *ACS Applied Materials & Interfaces*, *8*(38), 25337–25342. http://doi.org/10.1021/acsami.6b08801

Faiz, R., & Li, K. (2012). Olefin/paraffin separation using membrane based facilitated transport/chemical absorption techniques. *Chemical Engineering Science*, *73*, 261–284. http://doi.org/10.1016/j.ces.2012.01.037

Fei, H., Cahill, J. F., Prather, K. A., & Cohen, S. M. (2013). Tandem postsynthetic metal ion and ligand exchange in zeolitic imidazolate frameworks. *Inorganic Chemistry*, *52*(7), 4011–4016. http://doi.org/10.1021/ic400048g

Fox, D. M., Gilman, J. W., De Long, H. C., & Trulove, P. C. (2005). TGA decomposition kinetics of 1-butyl-2,3-dimethylimidazolium tetrafluoroborate and the thermal effects of contaminants. *Journal of Chemical Thermodynamics*, *37*(9), 900–905. http://doi.org/10.1016/j.jct.2005.04.020

Freeman, B. D. (1999). Basis of Permeability/Selectivity Tradeoff Relations in Polymeric Gas Separation Membranes. http://doi.org/10.1021/MA9814548

Gadipelli, S., & Guo, Z. X. (2015). Tuning of ZIF-Derived Carbon with High Activity, Nitrogen Functionality, and Yield - A Case for Superior CO2 Capture. *ChemSusChem*. http://doi.org/10.1002/cssc.201403402

Gadipelli, S., Travis, W., Zhou, W., & Guo, Z. (2014). A thermally derived and optimized structure from ZIF-8 with giant enhancement in CO2 uptake. *Energy & Environmental Science*, *7*(7), 2232. http://doi.org/10.1039/c4ee01009d

Galiè, F. (2016). *Global Market Trends and Investments in Polyethylene and Polypropylene*. *ICIS*. Retrieved from: https://www.icis.com/globalassets/documents/forms/ppfpdf/global_trends_whitepaper_pp_pe.pdf

Gao, Y., Wu, J., Zhang, W., Tan, Y., Gao, J., Zhao, J., & Tang, B. (2014). The calcined zeolitic imidazolate framework-8 (ZIF-8) under different conditions as electrode for supercapacitor applications. *Journal of Solid State Electrochemistry*, *18*(11), 3203–3207. http://doi.org/10.1007/s10008-014-2578-9

Gardner, R. J., Crane, R. A., & Hannan, J. F. (1977). Hollow Fiber Permeater for Separating Gases. *Chemical Engineering Progress*, *73*(10), 76–78.

Ghanem, B. S., Swaidan, R., Litwiller, E., & Pinnau, I. (2014). Ultra-Microporous Triptycene-based Polyimide Membranes for High-Performance Gas Separation. *Advanced Materials*, *26*(22), 3688–3692. http://doi.org/10.1002/adma.201306229

Gobina, E., & Hughes, R. (1994). Ethane dehydrogenation using a high-temperature catalytic membrane reactor. *Journal of Membrane Science*, *90*(1–2), 11–19. http://doi.org/10.1016/0376-7388(94)80030-8

Gross, A. F., Sherman, E., Mahoney, S. L., & Vajo, J. J. (2013). Reversible ligand exchange in a metal-organic framework (MOF): Toward MOF-based dynamic combinatorial chemical systems. *Journal of Physical Chemistry A*, *117*(18), 3771–3776. http://doi.org/10.1021/jp401039k

Hadjiantoniou-Maroulis, C. P., Charalambopoulos, A. P., & Maroulis, A. J. (1998). Pyrolysis and photolysis of 1-aroylamino-4,5-diaryl-1,2,3-triazoles: Generation and thermal transformations of 4,5-diaryl-1,2,3-triazolyl radicals. *Journal of Heterocyclic Chemistry*, *35*(4), 891–894. http://doi.org/10.1002/jhet.5570350418

Haraya, K., Obata, K., Itoh, N., Shndo, Y., Hakuta, T., & Yoshitome, H. (1989). Gas permeation and separation by an asymmetric polyimide hollow fiber membrane. *Journal of Membrane Science*, *41*, 23–35. http://doi.org/10.1016/S0376-7388(00)82388-1

Hayashi, H., O E, A. P., Furukawa, H., & Yaghi, O. M. (2007). Zeolite A imidazolate frameworks. http://doi.org/10.1038/nmat1927

Hayrettin Yucel-, B., & Rutwen, D. M. (1980). Diffusion in 4A Zeolite Study of the Effect of Crystal Size, *76*, 60–70.

He, M., Yao, J., Liu, Q., Zhong, Z., Wang, H., Prestipino, C., … Laird, B. B. (2013). Toluene-assisted synthesis of RHO-type zeolitic imidazolate frameworks: synthesis and formation mechanism of ZIF-11 and ZIF-12. *Dalton Transactions*, *42*(47), 16608. http://doi.org/10.1039/c3dt52103f

Herm, Z. R., Bloch, E. D., & Long, R. (2014). Hydrocarbon Separations in Metal − Organic Frameworks. *Chemistry of Materials*, *26*, 323–338.

Hong, D. H., & Suh, M. P. (2014). Enhancing CO_2 Separation Ability of a Metal-Organic Framework by Post-Synthetic Ligand Exchange with Flexible Aliphatic Carboxylates. *Chemistry - A European Journal*, *20*(2), 426–434. http://doi.org/10.1002/chem.201303801

Hong, M., Li, S., Falconer, J. L., & Noble, R. D. (2008). Hydrogen purification using a SAPO-34 membrane. *Journal of Membrane Science*, *307*(2), 277–283. http://doi.org/10.1016/j.memsci.2007.09.031

Hou, X. J., & Li, H. (2010). Unraveling the high uptake and selectivity of CO2 in the zeolitic imidazolate frameworks ZIF-68 and ZIF-69. *Journal of Physical Chemistry C*, *114*, 13501–13508. http://doi.org/10.1021/jp103778j

Hu, Y., Kazemian, H., Rohani, S., Huang, Y., & Song, Y. (2011). In situ high pressure study of ZIF-8 by FTIR spectroscopy. *Chemical Communications*, *47*, 12694. http://doi.org/10.1039/c1cc15525c

Hu, Z., Faucher, S., Zhuo, Y., Sun, Y., Wang, S., & Zhao, D. (2015). Combination of Optimization and Metalated-Ligand Exchange: An Effective Approach to Functionalize UiO-66(Zr) MOFs for CO_2 Separation. *Chemistry - A European Journal*, *21*(48), 17246–17255. http://doi.org/10.1002/chem.201503078

Huang, A., Dou, W., & Caro, J. (2010). Steam-stable zeolitic imidazolate framework ZIF-90 membrane with hydrogen selectivity through covalent functionalization. *Journal of the American Chemical Society*, *132*, 15562–15564. http://doi.org/10.1021/ja108774v

Huang, A., Liang, F., Steinbach, F., Gesing, T. M., & Caro, J. (2010). Neutral and Cation-Free LTA-Type Aluminophosphate ($AlPO_4$) Molecular Sieve Membrane with High Hydrogen Permselectivity. *Journal of the American Chemical Society*, *132*(7), 2140–2141. http://doi.org/10.1021/ja100042x

Huang, A., Liu, Q., Wang, N., & Caro, J. (2014). Highly Hydrogen Permselective ZIF-8 Membranes Supported on Polydopamine Functionalized Macroporous Stainless-Steel-Nets. *Journal of Materials Chemistry A*. http://doi.org/10.1039/C4TA00299G

Huang, B. L., Ni, Z., Millward, A., McGaughey, A. J. H., Uher, C., Kaviany, M., & Yaghi, O. (2007). Thermal conductivity of a metal-organic framework (MOF-5): Part II. Measurement. *International Journal of Heat and Mass Transfer*, *50*(3), 405–411. http://doi.org/10.1016/j.ijheatmasstransfer.2006.10.001

Huang, X. C., Lin, Y. Y., Zhang, J. P., & Chen, X. M. (2006). Ligand-directed strategy for zeolite-type metal-organic frameworks: Zinc(II) imidazolates with unusual zeolitic topologies. *Angewandte Chemie - International Edition*, *45*(10), 1557–1559. http://doi.org/10.1002/anie.200503778

Huang, Y. H., Liapis, A. I., Xu, Y., Crosser, O. K., & Johnson, J. W. (1995). Binary adsorption and desorption rates of propylene-propane mixtures on 13 X molecular sieves. *Separations Technology*, *5*(1), 1–11. http://doi.org/10.1016/0956-9618(94)00102-X

Ioannis G. Giannakopoulos†, ‡ and, & Vladimiros Nikolakis*, †. (2004). Separation of Propylene/Propane Mixtures Using Faujasite-Type Zeolite Membranes. http://doi.org/10.1021/IE049508R

James, J. B., & Lin, J. Y. S. (2016). Kinetics of ZIF-8 Thermal Decomposition in Inert, Oxidizing and Reducing Environments. *The Journal of Physical Chemistry C*. http://doi.org/10.1021/acs.jpcc.6b01208

James, J. B., & Lin, Y. S. (2017). Thermal stability of ZIF-8 membranes for gas separations. *Journal of Membrane Science*, *532*(October 2016), 9–19. http://doi.org/10.1016/j.memsci.2017.02.017

James, J. B., Wang, J., Meng, L., & Lin, Y. S. (2017). ZIF-8 Membrane Ethylene/Ethane Transport Characteristics in Single and Binary Gas Mixtures. *Industrial & Engineering Chemistry Research*, *56*(26), 7567–7575. http://doi.org/10.1021/acs.iecr.7b01536

Jasinki, R. (1964). Kinetic Parameters from Thermal Gravimetric Data. *Nature*, *201*, 1212–1213.

Jayachandrababu, K. C., Sholl, D. S., & Nair, S. (2017). Structural and Mechanistic Differences in Mixed-Linker Zeolitic Imidazolate Framework Synthesis by Solvent Assisted Linker Exchange and *de Novo* Routes. *Journal of the American Chemical Society*, jacs.7b01660. http://doi.org/10.1021/jacs.7b01660

Jiang, J. Q., Yang, C. X., & Yan, X. P. (2015). Postsynthetic ligand exchange for the synthesis of benzotriazole-containing zeolitic imidazolate framework. *Chem Commun (Camb)*, *51*(30), 6540–6543. http://doi.org/10.1039/c5cc00366k

Jones, C. W., & Koros, W. J. (1994). Carbon molecular sieve gas separation membranes-II. Regeneration following organic exposure. *Carbon*, *32*(8), 1427–1432. http://doi.org/10.1016/0008-6223(94)90136-8

Jung, S. (2000). Effects of co-existing hydrocarbons on hydrogen permeation through a palladium membrane. *Journal of Membrane Science*, *170*(1), 53–60. http://doi.org/10.1016/S0376-7388(99)00357-9

Kaneti, Y. V., Dutta, S., Hossain, M. S. A., Shiddiky, M. J. A., Tung, K.-L., Shieh, F.-K., Yamauchi, Y. (2017). Strategies for Improving the Functionality of Zeolitic Imidazolate Frameworks: Tailoring Nanoarchitectures for Functional Applications. *Advanced Materials*, 1700213. http://doi.org/10.1002/adma.201700213

Kanezashi, M., & Lin, Y. S. (2009). Gas Permeation and Diffusion Characteristics of MFI-Type Zeolite Membranes at High Temperatures. *The Journal of Physical Chemistry C*, *113*(9), 3767–3774. http://doi.org/10.1021/jp804586q

Kanezashi, M., O'Brien-Abraham, J., Lin, Y. S., & Suzuki, K. (2008). Gas permeation through DDR-type zeolite membranes at high temperatures. *AIChE Journal*, *54*(6), 1478–1486. http://doi.org/10.1002/aic.11457

Karagiaridi, O., Bury, W., Mondloch, J. E., Hupp, J. T., & Farha, O. K. (2014). Solvent-assisted linker exchange: An alternative to the de novo synthesis of unattainable metal-organic frameworks. *Angewandte Chemie - International Edition*, *53*(18), 4530–4540. http://doi.org/10.1002/anie.201306923

Karagiaridi, O., Bury, W., Sarjeant, A. A., Stern, C. L., Farha, O. K., & Hupp, J. T. (2012). Synthesis and characterization of isostructural cadmium zeolitic imidazolate frameworks via solvent-assisted linker exchange. *Chemical Science*, *3*(11), 3256. http://doi.org/10.1039/c2sc20558k

Karagiaridi, O., Bury, W., Sarjeant, A. A., Stern, C. L., Farha, O. K., Hupp, J. T., … Nieto-Draghi, C. (2012). Synthesis and characterization of isostructural cadmium zeolitic imidazolate frameworks via solvent-assisted linker exchange. *Chemical Science*, *3*(11), 3256. http://doi.org/10.1039/c2sc20558k

Karagiaridi, O., Lalonde, M. B., Bury, W., Sarjeant, A. A., Farha, O. K., & Hupp, J. T. (2012). Opening ZIF-8: A Catalytically Active Zeolitic Imidazolate Framework of Sodalite Topology with Unsubstituted Linkers. *Journal of the American Chemical Society*, *134*(45), 18790–18796. http://doi.org/10.1021/ja308786r

Karwacki, L., & Weckhuysen, B. M. (2011). New insight in the template decomposition process of large zeolite ZSM-5 crystals: an in situ UV-Vis/fluorescence micro-spectroscopy study. *Physical Chemistry Chemical Physics : PCCP*, *13*(9), 3681–3685. http://doi.org/10.1039/c0cp02220a

Kim, J., & Lee, D. (2016). Marked inducing effects of metal oxide supports on the hydrothermal stability of zeolitic imidazolate framework (ZIF) membranes. *J. Mater. Chem. A*, *4*(14), 5205–5215. http://doi.org/10.1039/C5TA10190E

Kim, M., Cahill, J. F., Fei, H., Prather, K. A., & Cohen, S. M. (2012). Postsynthetic Ligand and Cation Exchange in Robust Metal–Organic Frameworks. *Journal of the American Chemical Society*, *134*(43), 18082–18088. http://doi.org/10.1021/ja3079219

Kim, M., Cahill, J. F., Su, Y., Prather, K. a., & Cohen, S. M. (2012). Postsynthetic ligand exchange as a route to functionalization of “inert” metal–organic frameworks. *Chemical Science*, *3*(1), 126. http://doi.org/10.1039/c1sc00394a

Kim, S.-J., Liu, Y., Moore, J. S., Dixit, R. S., Pendergast, J. G., Sholl, D., … Nair, S. (2016). Thin Hydrogen-Selective SAPO-34 Zeolite Membranes for Enhanced Conversion and Selectivity in Propane Dehydrogenation Membrane Reactors. *Chemistry of Materials*, *28*(12), 4397–4402. http://doi.org/10.1021/acs.chemmater.6b01458

Kiyono, M., Williams, P. J., & Koros, W. J. (2010). Effect of pyrolysis atmosphere on separation performance of carbon molecular sieve membranes. *Journal of Membrane Science*, *359*(1–2), 2–10. http://doi.org/10.1016/j.memsci.2009.10.019

Koros, W. J., & Fleming, G. K. (1993). Membrane-based gas separation. *Journal of Membrane Science*, *83*, 1–80. http://doi.org/10.1016/0376-7388(93)80013-N

Koros, W. J., & Lively, R. P. (2012). Water and beyond: Expanding the spectrum of large-scale energy efficient separation processes. *AIChE Journal*, *58*(9), 2624–2633. http://doi.org/10.1002/aic.13888

Koros, W. J., & Mahajan, R. (2001). Pushing the limits on possibilities for large scale gas separation: Which strategies? *Journal of Membrane Science*, *181*(1), 141. http://doi.org/10.1016/S0376-7388(00)00676-1

Krishna, R., Li, S., van Baten, J. M., Falconer, J. L., & Noble, R. D. (2008). Investigation of slowing-down and speeding-up effects in binary mixture permeation across SAPO-34 and MFI membranes. *Separation and Purification Technology*, *60*, 230–236. http://doi.org/10.1016/j.seppur.2007.08.012

Krishna, R., & Paschek, D. (2000). Separation of hydrocarbon mixtures using zeolite membranes: A modelling approach combining molecular simulations with the Maxwell-Stefan theory. *Separation and Purification Technology*, *21*(1–2), 111–136. http://doi.org/10.1016/S1383-5866(00)00196-9

Krishna, R., & van den Broeke, L. J. P. (1995). The Maxwell-Stefan description of mass transport across zeolite membranes. *The Chemical Engineering Journal and The Biochemical Engineering Journal*. http://doi.org/10.1016/0923-0467(94)02951-2

Kwon, H. T., Jeong, H.-K., Lee, A. S., An, H. S., & Lee, J. S. (2015a). Heteroepitaxially Grown Zeolitic Imidazolate Framework Membranes with Unprecedented Propylene/Propane Separation Performances. *Journal of the American Chemical Society*, *137*(38), 12304–12311. http://doi.org/10.1021/jacs.5b06730

Kwon, H. T., Jeong, H., Lee, A. S., An, H. S., & Lee, J. S. (2015b). Heteroepitaxially Grown Zeolitic Imidazolate Framework Membranes with Unprecedented Propylene/Propane Separation Performances. http://doi.org/10.1021/jacs.5b06730

Lai, T., Yin, H., & Lind, M. L. (2015). The hydrogen permeability of Cu–Zr binary amorphous metallic membranes and the importance of thermal stability. *Journal of Membrane Science*, *489*, 264–269. http://doi.org/10.1016/j.memsci.2015.03.098

Lalonde, M. B., Mondloch, J. E., Deria, P., Sarjeant, A. A., Al-Juaid, S. S., Osman, O. I., Hupp, J. T. (2015). Selective Solvent-Assisted Linker Exchange (SALE) in a Series of Zeolitic Imidazolate Frameworks. *Inorganic Chemistry*, *54*(15), 7142–7144. http://doi.org/10.1021/acs.inorgchem.5b01231

Lewis, D. W., Ruiz-Salvador, A. R., Gómez, A., Rodriguez-Albelo, L. M., Coudert, F.-X., Slater, B., … Haga, N. (2009). Zeolitic imidazole frameworks: structural and energetics trends compared with their zeolite analogues. *CrystEngComm*, *11*(11), 2272. http://doi.org/10.1039/b912997a

Li, J.-Z., Fan, X.-Z., Liu, X.-G., & Zheng, X.-D. (2008). Thermal Decomposition of 4-Nitroimidazole Catalyzed by Pb(NO3)2. *Chinese Journal of Chemistry*, *26*(1), 127–129. http://doi.org/10.1002/cjoc.200890005

Li, J., Zhu, Q.-L., & Xu, Q. (2015). Pd nanoparticles supported on hierarchically porous carbon derived from assembled nanoparticles of zeolitic imidazolate framework (ZIF-8) for methanol electrooxidation. *Chem. Commun.*, *51*, 10827–10830. http://doi.org/10.1039/C5CC03008K

Li, K., Olson, D. H., Seidel, J., Emge, T. J., Gong, H., Zeng, H., & Li, J. (2009). Zeolitic imidazolate frameworks for kinetic separation of propane and propene. *Journal of the American Chemical Society*, *131*, 10368–10369. http://doi.org/10.1021/ja9039983

Li, Y., Liang, F., Bux, H., Yang, W., & Caro, J. (2010). Zeolitic imidazolate framework ZIF-7 based molecular sieve membrane for hydrogen separation. *Journal of Membrane Science*, *354*, 48–54. http://doi.org/10.1016/j.memsci.2010.02.074

Lin, J. Y. S. (2016). Molecular sieves for gas separation. *Science*, *353*(6295), 121–122. http://doi.org/10.1126/science.aag2267

Lin, Y. S., & Burggraaf, A. J. (1993). Experimental studies on pore size change of porous ceramic membranes after modification. *Journal of Membrane Science*, *79*(1), 65–82. http://doi.org/10.1016/0376-7388(93)85018-R

Liu, C., Zeng, C., Luo, T.-Y., Merg, A. D., Jin, R., & Rosi, N. L. (2016). Establishing Porosity Gradients within Metal–Organic Frameworks Using Partial Postsynthetic Ligand Exchange. *Journal of the American Chemical Society*, *138*(37), 12045–12048. http://doi.org/10.1021/jacs.6b07445

Liu, D., Ma, X., Xi, H., & Lin, Y. S. (2014). Gas transport properties and propylene/propane separation characteristics of ZIF-8 membranes. *Journal of Membrane Science*, *451*, 85–93. http://doi.org/10.1016/j.memsci.2013.09.029

Liu, D., Wu, Y., Xia, Q., Li, Z., & Xi, H. (2013). Experimental and molecular simulation studies of CO2 adsorption on zeolitic imidazolate frameworks: ZIF-8 and amine-modified ZIF-8. *Adsorption*, *19*, 25–37. http://doi.org/10.1007/s10450-012-9407-1

Liu, Q., Wang, N., Caro, J., & Huang, A. (2013). Bio-inspired polydopamine: A versatile and powerful platform for covalent synthesis of molecular sieve membranes. *Journal of the American Chemical Society*, *135*, 17679–17682. http://doi.org/10.1021/ja4080562

Liu, X., Li, Y., Ban, Y., Peng, Y., Jin, H., Bux, H., … Yang, W. (2013). Improvement of hydrothermal stability of zeolitic imidazolate frameworks. *Chemical Communications (Cambridge, England)*, *49*, 9140–2. http://doi.org/10.1039/c3cc45308a

Ma, X., Lin, B. K., Wei, X., Kniep, J., & Lin, Y. S. (2013). Gamma-alumina supported carbon molecular sieve membrane for propylene/propane separation. *Industrial and Engineering Chemistry Research*, *52*, 4297–4305. http://doi.org/10.1021/ie303188c

Ma, X., Lin, Y. S., Wei, X., & Kniep, J. (2016). Ultrathin carbon molecular sieve membrane for propylene/propane separation. *AIChE Journal*, *62*(2), 491–499. http://doi.org/10.1002/aic.15005

McCool, B. A., & Lin, Y. S. (2001). Nanostructured thin palladium-silver membranes: Effects of grain size on gas permeation properties. *Journal of Materials Science*, *36*(13), 3221–3227. http://doi.org/10.1023/A:1017938403725

Min Wang, Q., Shen, D., Bulow, M., Ling Lau, M., Deng, S., Fitch, F. R., … Semanscin, J. (2002). Metallo-organic molecular sieve for gas separation and purification. *Microporous and Mesoporous Materials*, *55*(2), 217–230. http://doi.org/10.1016/S1387-1811(02)00405-5

Morisato, A., & Pinnau, I. (1996). Synthesis and gas permeation properties of poly(4-methyl-2-pentyne). *Journal of Membrane Science*, *121*(2), 243–250. http://doi.org/10.1016/S0376-7388(96)00183-4

Moura, L., Darwich, W., Santini, C. C., & Costa Gomes, M. F. (2015). Imidazolium-based ionic liquids with cyano groups for the selective absorption of ethane and ethylene. *Chemical Engineering Journal*, *280*, 755–762. http://doi.org/10.1016/j.cej.2015.06.034

Mueller, R., Hariharan, V., Zhang, C., Lively, R., & Vasenkov, S. (2016). Relationship between mixed and pure gas self-diffusion for ethane and ethene in ZIF-8/6FDA-DAM mixed-matrix membrane by pulsed field gradient NMR. *Journal of Membrane Science*, *499*, 12–19. http://doi.org/10.1016/j.memsci.2015.10.036

Myers, A. L., & Prausnitz, J. M. (1965). Thermodynamics of mixed-gas adsorption. *AIChE Journal*, *11*(1), 121–127. http://doi.org/10.1002/aic.690110125

Narasimhan Calamur, Mark P. Kaminsky, Vincent J. Kwasniewski, John A. Mahoney, Charles G. Scouten, R. A. W. (1999). Unsaturated hydrocarbon separation and recovery process. Retrieved from https://www.google.com/patents/EP0906256A1

Nikolakis, V., Xomeritakis, G., Abibi, A., Dickson, M., Tsapatsis, M., & Vlachos, D. G. (2001). Growth of a faujasite-type zeolite membrane and its application in the separation of saturated/unsaturated hydrocarbon mixtures. *Journal of Membrane Science*, *184*(2), 209–219. http://doi.org/10.1016/S0376-7388(00)00623-2

Nymeijer, K., Visser, T., Assen, R., & Wessling, M. (2004). Super selective membranes in gas–liquid membrane contactors for olefin/paraffin separation. *Journal of Membrane Science*, *232*(1–2), 107–114. http://doi.org/10.1016/j.memsci.2003.10.045

Ockwig, N. W., & Nenoff, T. M. (2007). Membranes for Hydrogen Separation. *Chemical Reviews*, *107*(10), 4078–4110. http://doi.org/10.1021/cr0501792

Ordoñez, M. J. C., Balkus, K. J., Ferraris, J. P., & Musselman, I. H. (2010). Molecular sieving realized with ZIF-8/Matrimid® mixed-matrix membranes. *Journal of Membrane Science*, *361*, 28–37. http://doi.org/10.1016/j.memsci.2010.06.017

Ozokwelu, D. (2005). Hybrid Separations/Distillation Technology: Research Opportunities for Energy and Emissions Reduction. Retrieved from https://energy.gov/sites/prod/files/2013/11/f4/hybrid_separation.pdf

Pan, Y., & Lai, Z. (2011). Sharp separation of C2/C3 hydrocarbon mixtures by zeolitic imidazolate framework-8 (ZIF-8) membranes synthesized in aqueous solutions. *Chemical Communications (Cambridge, England)*, *47*(d), 10275–10277. http://doi.org/10.1039/c1cc14051e

Pan, Y., Li, T., Lestari, G., & Lai, Z. (2012). Effective separation of propylene/propane binary mixtures by ZIF-8 membranes. *Journal of Membrane Science*, *390–391*, 93–98. http://doi.org/10.1016/j.memsci.2011.11.024

Pan, Y., Liu, W., Zhao, Y., Wang, C., & Lai, Z. (2015). Improved ZIF-8 membrane: Effect of activation procedure and determination of diffusivities of light hydrocarbons. *Journal of Membrane Science*, *493*, 88–96. http://doi.org/10.1016/j.memsci.2015.06.019

Pan, Y., Liu, Y., Zeng, G., Zhao, L., & Lai, Z. (2011). Rapid synthesis of zeolitic imidazolate framework-8 (ZIF-8) nanocrystals in an aqueous system. *Chemical Communications (Cambridge, England)*, *47*, 2071–2073. http://doi.org/10.1039/c0cc05002d

Park, K. S., Ni, Z., Côté, A. P., Choi, J. Y., Huang, R., Uribe-Romo, F. J., … Yaghi, O. M. (2006). Exceptional chemical and thermal stability of zeolitic imidazolate frameworks. *Proceedings of the National Academy of Sciences of the United States of America*, *103*, 10186–10191. http://doi.org/10.1073/pnas.0602439103

Peralta, D., Chaplais, G., Paillaud, J. L., Simon-Masseron, A., Barthelet, K., & Pirngruber, G. D. (2013). The separation of xylene isomers by ZIF-8: A demonstration of the extraordinary flexibility of the ZIF-8 framework. *Microporous and Mesoporous Materials*, *173*, 1–5. http://doi.org/10.1016/j.micromeso.2013.01.012

Pérez-Pellitero, J., Amrouche, H., Siperstein, F. R., Pirngruber, G., Nieto-Draghi, C., Chaplais, G., … Bats, N. (2010). Adsorption of CO2, CH4, and N2 on zeolitic imidazolate frameworks: Experiments and simulations. *Chemistry - A European Journal*, *16*, 1560–1571. http://doi.org/10.1002/chem.200902144

Perry, J. D., Nagai, K., & Koros, W. J. (2006). Polymer Membranes for Hydrogen Separations. *MRS Bulletin*, *31*(10), 745–749. http://doi.org/10.1557/mrs2006.187

Phan, A., Doonan, C. J., Uribe-Romo, F. J., Knobler, C. B., O'Keeffe, M., & Yaghi, O. M. (2010). Synthesis, Structure, and Carbon Dioxide Capture Properties of Zeolitic Imidazolate Frameworks. *Accounts of Chemical Research*, *43*(1), 58–67. http://doi.org/10.1021/ar900116g

Pimentel, B. R., & Lively, R. P. (2016). Enabling Kinetic Light Hydrocarbon Separation via Crystal Size Engineering of ZIF-8. *Industrial & Engineering Chemistry Research*, *55*(48), 12467–12476. http://doi.org/10.1021/acs.iecr.6b03199

Pimentel, B. R., Parulkar, A., Zhou, E., Brunelli, N. a., & Lively, R. P. (2014). Zeolitic Imidazolate Frameworks: Next-Generation Materials for Energy-Efficient Gas Separations. *ChemSusChem*, *7*(12), 3202–3240. http://doi.org/10.1002/cssc.201402647

Pinnau, I., Casillas, C. G., Morisato, A., & Freeman, B. D. (1996). Hydrocarbon/hydrogen mixed gas permeation in poly(1-trimethylsilyl-1-propyne) (PTMSP), poly(1-phenyl-1-propyne) (PPP), and PTMSP/PPP blends. *Journal of Polymer Science Part B: Polymer Physics*, *34*(15), 2613–2621. http://doi.org/10.1002/(SICI)1099-0488(19961115)34:15<2613::AID-POLB9>3.0.CO;2-T

Pinnau, I., & Toy, L. G. (2001). Solid polymer electrolyte composite membranes for olefin/paraffin separation. *Journal of Membrane Science*, *184*(1), 39–48. http://doi.org/10.1016/S0376-7388(00)00603-7

Plaza, M. G., Ribeiro, A. M., Ferreira, A., Santos, J. C., Lee, U. H., Chang, J. S., … Rodrigues, A. E. (2012). Propylene/propane separation by vacuum swing adsorption using Cu-BTC spheres. *Separation and Purification Technology*, *90*, 109–119. http://doi.org/10.1016/j.seppur.2012.02.023

Rashidi, F., Blad, C. R., Jones, C. W., & Nair, S. (2016). Synthesis, characterization, and tunable adsorption and diffusion properties of hybrid ZIF-7-90 frameworks. *AIChE Journal*, *62*(2), 525–537. http://doi.org/10.1002/aic.15102

Reine, T. A., & Eldridge, R. B. (2005). Absorption equilibrium and kinetics for ethylene-ethane separation with a novel solvent. *Industrial and Engineering Chemistry Research*, *44*(19), 7505–7510. http://doi.org/10.1021/ie0488546

Rezac, M. E., Koros, W. J., & Miller, S. J. (1994). Membrane-assisted dehydragenation of n-butane influence of membrane properties on system performance. *Journal of Membrane Science*, *93*(2), 193–201. http://doi.org/10.1016/0376-7388(94)80007-3

Robeson, L. M. (1991). Correlation of separation factor versus permeability for polymeric membranes. *Journal of Membrane Science*, *62*(2), 165–185. http://doi.org/10.1016/0376-7388(91)80060-J

Roth, W. J., Nachtigall, P., Morris, R. E., Wheatley, P. S., Seymour, V. R., Ashbrook, S. E., Čejka, J. (2013). A family of zeolites with controlled pore size prepared using a top-down method. *Nature Chemistry*, *5*(7), 628–633. http://doi.org/10.1038/nchem.1662

Rungta, M., Xu, L., & Koros, W. J. (2012). Carbon molecular sieve dense film membranes derived from Matrimid® for ethylene/ethane separation. *Carbon*, *50*(4), 1488–1502. http://doi.org/10.1016/j.carbon.2011.11.019

Rungta, M., Zhang, C., Koros, W. J., & Xu, L. (2013). Membrane-based ethylene/ethane separation: The upper bound and beyond. *AIChE Journal*, *59*(9), 3475–3489. http://doi.org/10.1002/aic.14105

Ruthven, D. M., & Derrah, R. I. (1972). Transition State Theory of Zeolitic Diffusion Diffusion of CH4 and CF4 in 5A Zeolite.

Ruthven, D. M., Derrah, R. I., & Loughlin, K. F. (1973). Diffusion of Light Hydrocarbons in 5A Zeolite. *Canadian Journal of Chemistry*, *51*(21), 3514–3519. http://doi.org/10.1139/v73-523

Ruthven, D. M., & Reyes, S. C. (2007). Adsorptive separation of light olefins from paraffins. *Microporous and Mesoporous Materials*, *104*(1), 59–66. http://doi.org/10.1016/j.micromeso.2007.01.005

Ryu, J. H., Lee, H., Kim, Y. J., Kang, Y. S., & Kim, H. S. (2001). Facilitated Olefin Transport by Reversible Olefin Coordination to Silver Ions in a Dry Cellulose Acetate Membrane. *Chemistry*, *7*(7), 1525–1529. http://doi.org/10.1002/1521-3765(20010401)7:7<1525::AID-CHEM1525>3.0.CO;2-U

Safarik, D. J., & Eldridge, R. B. (1998). Olefin/Paraffin Separations by Reactive Absorption: A Review. *Industrial & Engineering Chemistry Research*, *37*(7), 2571–2581. http://doi.org/10.1021/ie970897h

Salinas, O., Ma, X., Litwiller, E., & Pinnau, I. (2016). High-performance carbon molecular sieve membranes for ethylene/ethane separation derived from an intrinsically microporous polyimide. *Journal of Membrane Science*, *500*, 115–123. http://doi.org/10.1016/j.memsci.2015.11.013

Seader, J. D., & Henley, E. J. (2006). *Separation process principles*. Wiley.

Sholl, D. S., & Lively, R. P. (2016). Seven Chemical Separations to Change the world. *Nature*, *532*(7600), 435–437. http://doi.org/10.1038/532435a

Singh, A., & Koros, W. J. (1996). Significance of Entropic Selectivity for Advanced Gas Separation Membranes. *Industrial & Engineering Chemistry Research*, *35*(4), 1231–1234. http://doi.org/10.1021/ie950559l

Singh, R., & Koros, W. J. (2013). Carbon molecular sieve membrane performance tuning by dual temperature secondary oxygen doping (DTSOD). *Journal of Membrane Science*, *427*, 472–478. http://doi.org/10.1016/j.memsci.2012.10.004

Steel, K. M., & Koros, W. J. (2005). An investigation of the effects of pyrolysis parameters on gas separation properties of carbon materials. *Carbon*, *43*(9), 1843–1856. http://doi.org/10.1016/j.carbon.2005.02.028

Suda, H., & Haraya, K. (1997). Alkene / alkane permselectivities of a carbon molecular sieve membrane. *Chem. Commun.*, *3*, 93–94.

Tan, J., Bennett, T. D., & Cheetham, A. K. (2010). Chemical structure, network topology, and porosity effects on the mechanical properties of Zeolitic Imidazolate Frameworks. *Proceedings of the National Academy of Sciences of the United States of America*, *107*(22),9938–9943.http://doi.org/10.1073/pnas.1003205107/-/DCSupplemental.www.pnas.org/cgi/doi/10.1073/pnas.1003205107

Teramoto, M., Matsuyama, H., Yamashiro, T., & Katayama, Y. (1986). Separation of ethylene from ethane by supported liquid membranes containing silver nitrate as a carrier. *Journal of Chemical Engineering of Japan*, *19*(5), 419–424. http://doi.org/10.1252/jcej.19.419

Thompson, J. A., Blad, C. R., Brunelli, N. A., Lydon, M. E., Lively, R. P., Jones, C. W., & Nair, S. (2012). Hybrid Zeolitic Imidazolate Frameworks: Controlling Framework Porosity and Functionality by Mixed-Linker Synthesis. *Chemistry of Materials*, *24*(10), 1930–1936. http://doi.org/10.1021/cm3006953

Thompson, J. A., Blad, C. R., Brunelli, N., Lively, R. P., Lydon, M. E., Jones, W., & Nair, S. (2012). Hybrid Zeolitic Imidazolate Frameworks : Controlling Framework Functionality and Porosity in a Mixed-Ligand Synthesis. *Langmuir*, 1–8. http://doi.org/10.1021/cm3006953

Tian, Y. Q., Zhao, Y. M., Chen, Z. X., Zhang, G. N., Weng, L. H., & Zhao, D. Y. (2007). Design and generation of extended zeolitic metal-organic frameworks (ZMOFs): Synthesis and crystal structures of zinc(II) imidazolate polymers with zeolitic topologies. *Chemistry - A European Journal*, *13*(15), 4146–4154. http://doi.org/10.1002/chem.200700181

Tiscornia, I., Irusta, S., Téllez, C., Coronas, J., & Santamaría, J. (2008). Separation of propylene/propane mixtures by titanosilicate ETS-10 membranes prepared in one-step seeded hydrothermal synthesis. *Journal of Membrane Science*, *311*(1–2), 326–335. http://doi.org/10.1016/j.memsci.2007.12.028

Tranchemontagne, D. J., Mendoza-Cortés, J. L., O'Keeffe, M., & Yaghi, O. M. (2009). Secondary building units, nets and bonding in the chemistry of metal-organic frameworks. *Chemical Society Reviews*, *38*(5), 1257–1283. http://doi.org/10.1039/b817735j

US polyethylene inventories set to rise by 9bn pounds in 2016-2020. Retrieved September 23, 2017, from http://analysis.petchem-update.com/engineering-and-construction/us-polyethylene-inventories-set-rise-9bn-pounds-2016-2020

Van Amerongen, G. J. (1946). The permeability of different rubbers to gases and its relation to diffusivity and solubility. *Journal of Applied Physics*, *17*(11), 972–985. http://doi.org/10.1063/1.1707667

van de Graaf, J. M., Kapteijn, F., & Moulijn, J. a. (1999). Modeling permeation of binary mixtures through zeolite membranes. *AIChE Journal*, *45*(3), 497–511. http://doi.org/10.1002/aic.690450307

Van Den Bergh, J., Gücüyener, C., Pidko, E. a., Hensen, E. J. M., Gascon, J., & Kapteijn, F. (2011). Understanding the anomalous alkane selectivity of ZIF-7 in the separation of light alkane/alkene mixtures. *Chemistry - A European Journal*, *17*, 8832–8840. http://doi.org/10.1002/chem.201100958

van Krevelen, D. (1997). *Properties of Polymers* (3rd ed.). Amsterdam; The Netherlands: Elsevier Science.

Venkatesh, M., Ravi, P., & Tewari, S. P. (2013). Isoconversional kinetic analysis of decomposition of nitroimidazoles: Friedman method vs Flynn-Wall-Ozawa method. *Journal of Physical Chemistry A*, *117*(40), 10162–10169. http://doi.org/10.1021/jp407526r

Venna, S. R., Jasinski, J. B., & Carreon, M. a. (2010). Structural evolution of zeolitic imidazolate framework-8. *Journal of the American Chemical Society*, *132*, 18030–18033. http://doi.org/10.1021/ja109268m

Verploegh, R. J., Nair, S., & Sholl, D. S. (2015). Temperature and Loading-Dependent Diffusion of Light Hydrocarbons in ZIF-8 as Predicted Through Fully Flexible Molecular Simulations. *Journal of the American Chemical Society*, *137*(50), 15760–15771. http://doi.org/10.1021/jacs.5b08746

Wakai, F., Yoshida, M., Shinoda, Y., & Akatsu, T. (2005). Coarsening and grain growth in sintering of two particles of different sizes. *Acta Materialia*, *53*(5), 1361–1371. http://doi.org/10.1016/j.actamat.2004.11.029

Wang, H., & Lin, Y. S. (2012). Synthesis and modification of ZSM-5/silicalite bilayer membrane with improved hydrogen separation performance. *Journal of Membrane Science*, *396*, 128–137. http://doi.org/10.1016/j.memsci.2012.01.008

Ward, T. L., & Dao, T. (1999). Model of hydrogen permeation behavior in palladium membranes. *Journal of Membrane Science*, *153*(2), 211–231. http://doi.org/10.1016/S0376-7388(98)00256-7

Wheatley, P. S., Chlubná-Eliášová, P., Greer, H., Zhou, W., Seymour, V. R., Dawson, D. M., … Morris, R. E. (2014). Zeolites with continuously tuneable porosity. *Angewandte Chemie - International Edition*, *53*(48), 13210–13214. http://doi.org/10.1002/anie.201407676

Wijmans, J. G., & Baker, R. W. (1995). The solution-diffusion model: a review. *Journal of Membrane Science*, *107*(1–2), 1–21. http://doi.org/10.1016/0376-7388(95)00102-I

Wu, H., Qian, X., Zhu, H., Ma, S., Zhu, G., & Long, Y. (2016). Controlled synthesis of highly stable zeolitic imidazolate framework-67 dodecahedra and their use towards the templated formation of a hollow Co_3O_4 catalyst for CO oxidation. *RSC Adv.*, *6*(9), 6915–6920. http://doi.org/10.1039/C5RA18557B

Wu, H., Zhou, W., & Yildirim, T. (2007). Hydrogen Storage in a Prototypical Zeolitic Imidazolate Framework-8 Hydrogen Storage in a Prototypical Zeolitic Imidazolate Framework-8, *129*, 5314–5315. http://doi.org/10.1021/ja0691932

Wu, Y., Chen, H., Liu, D., Qian, Y., & Xi, H. (2014). Adsorption and separation of ethane/ethylene on ZIFs with various topologies: Combining GCMC simulation with the ideal adsorbed solution theory (IAST). *Chemical Engineering Science*, *124*, 144–153. http://doi.org/10.1016/j.ces.2014.07.019

Xiao, J., & Wei, J. (1992). Diffusion mechanism of hydrocarbons in zeolites—I. Theory. *Chemical Engineering Science*, *47*(5), 1123–1141. http://doi.org/10.1016/0009-2509(92)80236-6

Xu, G., Yao, J., Wang, K., He, L., Webley, P. a., Chen, C. S., & Wang, H. (2011). Preparation of ZIF-8 membranes supported on ceramic hollow fibers from a concentrated synthesis gel. *Journal of Membrane Science*, *385–386*, 187–193. http://doi.org/10.1016/j.memsci.2011.09.040

Xu, L., Rungta, M., Hessler, J., Qiu, W., Brayden, M., Martinez, M., … Koros, W. J. (2014). Physical aging in carbon molecular sieve membranes. *Carbon*, *80*, 155–166. http://doi.org/10.1016/j.carbon.2014.08.051

Xu, L., Rungta, M., & Koros, W. J. (2011). Matrimid ® derived carbon molecular sieve hollow fiber membranes for ethylene/ethane separation. *Journal of Membrane Science*, *380*, 138–147. http://doi.org/10.1016/j.memsci.2011.06.037

Yang, T., & Chung, T.-S. (2013). High performance ZIF-8/PBI nano-composite membranes for high temperature hydrogen separation consisting of carbon monoxide and water vapor. *International Journal of Hydrogen Energy*, *38*(1), 229–239. http://doi.org/10.1016/j.ijhydene.2012.10.045

Yildirim, Y., Gobina, E., & Hughes, R. (1997). An experimental evaluation of high-temperature composite membrane systems for propane dehydrogenation. *Journal of Membrane Science*, *135*(1), 107–115. http://doi.org/10.1016/S0376-7388(97)00133-6

Yin, H., Kim, H., Choi, J., & Yip, A. C. K. (2014). Thermal stability of ZIF-8 under oxidative and inert environments: A practical perspective on using ZIF-8 as a catalyst support. *Chemical Engineering Journal*. http://doi.org/10.1016/j.cej.2014.08.075

Yoshida, S., & Ishida, H. (1995). An investigation of the thermal stability of undecylimidazole on copper by IT-IR reflection-absorption spectroscopy, *89*(216), 39–47.

Zeise, W. C. (1831). Von der Wirkung zwischen Platinchlorid und Alkohol, und von den dabei entstehenden neuen Substanzen. *Annalen Der Physik Und Chemie*, *97*(4), 497–541. http://doi.org/10.1002/andp.18310970402

Zhang, C., & Koros, W. J. (2015). Tailoring the Transport Properties of Zeolitic Imidazolate Frameworks by Post-synthetic Thermal Modification. *ACS Applied Materials & Interfaces*, 151013120133002. http://doi.org/10.1021/acsami.5b07769

Zhang, C., Lively, R. P., Zhang, K., Johnson, J. R., Karvan, O., & Koros, W. J. (2012). Unexpected Molecular Sieving Properties of Zeolitic Imidazolate Framework-8. *The Journal of Physical Chemistry Letters*, *3*(16), 2130–2134. http://doi.org/10.1021/jz300855a

Zhang, H., James, J., Zhao, M., Yao, Y., Zhang, Y., Zhang, B., & Lin, Y. S. (2017). Improving hydrostability of ZIF-8 membranes via surface ligand exchange. *Journal of Membrane Science*, *532*, 1–8. http://doi.org/10.1016/j.memsci.2017.01.065

Zhang, H., Liu, D., Yao, Y., Zhang, B., & Lin, Y. S. (2015). Stability of ZIF-8 membranes and crystalline powders in water at room temperature. *Journal of Membrane Science*, *485*, 103–111. http://doi.org/10.1016/j.memsci.2015.03.023

Zhang, K., Lively, R. P., Zhang, C., Chance, R. R., Koros, W. J., Sholl, D. S., & Nair, S. (2013). Exploring the Framework Hydrophobicity and Flexibility of ZIF-8: From Biofuel Recovery to Hydrocarbon Separations. *The Journal of Physical Chemistry Letters*, *4*(21), 3618–3622. http://doi.org/10.1021/jz402019d

Zhang, L., Su, Z., Jiang, F., Yang, L., Qian, J., Zhou, Y., … Hong, M. (2014). Highly graphitized nitrogen-doped porous carbon nanopolyhedra derived from ZIF-8 nanocrystals as efficient electrocatalysts for oxygen reduction reactions. *Nanoscale*, *6*, 6590–602. http://doi.org/10.1039/c4nr00348a

Zhang, L., Wu, G., & Jiang, J. (2014). Adsorption and Diffusion of CO 2 and CH 4 in Zeolitic Imidazolate Framework-8: Effect of Structural Flexibility. *The Journal of Physical Chemistry C*, 140411102121001. http://doi.org/10.1021/jp500796e

Zhang, X., Liu, Y., Li, S., Kong, L., Liu, H., Li, Y., … Qiu, J. (2014). New membrane architecture with high performance : ZIF-8 membrane supported on vertically-aligned ZnO nanorods for gas permeation and separation New membrane architecture with high performance : ZIF-8 membrane supported on vertically-aligned ZnO nanorods f. *Chemistry of Materials*, *26*, 1975–1981. http://doi.org/10.1021/cm500269e

Zhang, Y., Wu, Z., Hong, Z., Gu, X., & Xu, N. (2012). Hydrogen-selective zeolite membrane reactor for low temperature water gas shift reaction. *Chemical Engineering Journal*, *197*, 314–321. http://doi.org/10.1016/j.cej.2012.05.064

Ziaka, Z. D., Minet, R. G., & Tsotsis, T. T. (1993). A high temperature catalytic membrane reactor for propane dehydrogenation. *Journal of Membrane Science*, *77*(2–3), 221–232. http://doi.org/10.1016/0376-7388(93)85071-4

APPENDIX A

LIST OF PUBLICATIONS

The preceding chapters are modified versions of papers published or to be submitted for publication:

Chapter 2

James, J. B., & Lin, Y. S. (2016). Kinetics of ZIF-8 thermal decomposition in inert, oxidizing, and reducing environments. *The Journal of Physical Chemistry C*, *120*(26), 14015-14026.

Chapter 3

James, J. B., & Lin, Y. S. (2017). Thermal stability of ZIF-8 membranes for gas separations. *Journal of Membrane Science*, *532*, 9-19.

Chapter 4

James, J. B., Wang, J., Meng, L., & Lin, Y. S. (2017). ZIF-8 membrane ethylene/ethane transport characteristics in single and binary gas mixtures. *Industrial & Engineering Chemistry Research*, *56*(26), 7567-7575.

Chapter 5

James, J.B., & Lin, Y.S. (2017) Ex situ time-based characterization and light hydrocarbon permeation study of ZIF-8 membranes modified via surface ligand exchange. In progress.

APPENDIX B

PROCEDURE FOR PREPARATION OF ALPHA ALUMINA SUPPORTS

Table B.1 Materials for Alpha Alumina Substrate Preparation

Chemicals	Molecular Formula	Purity	MW (g/mol)	Supplier
A-16 Alumina Powder	Al_2O_3	≥ 99.9%	101.96	Almatis
Deionized Water	H_2O	-	18.02	-
Ethanol	C_2H_5OH	99%	32.04	Koptek

The following protocol yields approximately 20, 2 mm thick alpha alumina substrates:

1. Measure 42 g of A16 alumina powder place in mortar bowl

2. Add between add between 4.2 – 5.08 g of deionized water to the alumina powder this yields a 1-1.12:10 ratio by weight, water to alumina powder mixture. The ratio of water added depends on the relative humidity of the laboratory. Below 15% relative humidity add larger amount of water.

3. Mix the water and powder thoroughly with a pestle; the powder will flatten and conform to the bottom of the mortar; gently scrape loose with a spatula and repeat 2 times more; the wet powder mixture should be free of large aggregates

4. Measure 2.1 g of the wet powder mixture and place into the 22 mm stainless steel mold

5. Insert the die assembly piece into the mold, and with the Carver Press, apply a load of 20,000 lbs. for 1.5 minutes

6. Remove from mold

7. Remaining powder within the mortar will dry over time, use clean spray bottle containing deionized water to moisten the powder (spray remaining powder modestly after pressing 5 or so supports)

8. The green bodies should be dried at 40°C at a relative humidity of 60% in the humidity chamber for 2 days

9. Sinter the green bodies according to Table B.2

Table B.2 Furnace Temperature Program for Alumna Substrate Preparation

STEP	RATE (°C/hr)	T_{SP} (°C)	t_{HOLD} (hrs)
1	60	600	0.1
2	96	1260	0.1
3	96	200	0.1
4	60	1150	30
5	60	200	0.1
6	60	50	1

10. The sintered supports are then polished with 500, 800, 1200 and 2000 grit sandpaper

11. After polishing immerse place supports in a 250 mL beaker and immerse in 50 mL of deionized water

12. Sonicate supports for 5 minutes, stop sonication, pour off water containing alumina powder precipitates, add fresh deionized water, then sonicate for 5 more minutes

13. After water sonication, pour off water, add 50 mL of 200 proof ethanol to the beaker containing the alumina substrates, sonicate for 10 minutes

14. Dry supports for 2 hours at 200°C before further processing for membrane synthesis

APPENDIX C

PROCEDURE FOR ZIF-8 MEMBRANE SYNTHESIS VIA SEEDED SECONDARY GROWTH

Table C.1 Materials for ZIF-8 Membrane Preparation Via Seeded Secondary Growth

Chemicals	Molecular Formula	Purity	MW (g/mol)	Supplier
Zinc Nitrate Hexahydrate	$Zn(NO_3)\cdot 6H_2O$	98%	297.49	Sigma Aldrich
2-Methylimidazole	$C_4H_6N_2$	99%	82.1	Sigma Aldrich
Methanol	CH_3OH	99.8 % (Anhydrous)	32.04	Sigma Aldrich
Deionized Water	H_2O	-	18.02	-

All chemicals utilized in this work were purchased from the following suppliers and used without further purification. The synthesis occurs in three separate stages: ZIF-8 seed formation, support seeding and secondary growth.

C.1 ZIF-8 Crystal Synthesis Procedure

1. Measure out 1.17 g of zinc nitrate hexahydrate into to a glass beaker, add 8 mL of deionized water to the zinc nitrate and stir at room temperature
2. In a separate beaker add 22.7 g of 2-methylimidazole (2-HMIm) to 80 mL of deionized water and stir vigorously at room temperature
3. Add the zinc solution to the 2-HMIm solution; vigorously mix the two solutions at room temperature for 7 minutes
4. After mixing, wash and centrifuge the crystals 1 time in a 50% water/methanol (v/v) solution followed by 2 times in pure methanol
5. Dry wet crystals under vacuum (60 kPa) for 24 hours at room temperature

5. Add 0.04 g of dried ground ZIF-8 crystals to 100 mL of methanol to form a 0.05 wt.% seeding solution

6. Sonicate seeding solution for 20 minutes and allow larger crystals to settle at the bottom of the solution for 12 hours

C.2 Procedure for Seeding Alpha Alumina Supports

7. Place approximately 15 mL of the seed solution into a weighing boat using a disposable pipette

8. Bring the polished support surface in contact with the seed solution for 20 seconds

9. Allow the excess solution to run off

10. Allow the seeded support to dry in ambient air for 10 minutes

11. Repeat steps 8-10 once more

12. Place the seeded support in a glass covered petri dish, place dish in a furnace, ramp temperature to 95°C by 0.3°C/min and hold at constant temperature for 3 hours

13. Ramp temperature down to 50°C by 0.3°C/min

C.3 Procedure for Secondary Growth:

14. Place the seeded support in a Teflon lined autoclave with the seeded side facing slightly up

15. Add 10 mL of deionized water to 0.11 g of zinc nitrate hexahydrate and stir

16. Add 30 mL of deionized water to 2.27 g of 2-MIm and stir

17. Add the zinc solution to the stirring 2-MIm solution dropwise to form the ZIF-8 secondary growth solution

18. Pour the secondary growth solution slowly into the 50 mL Teflon liner which contains the seeded support secured vertically in a Teflon holder, seal the liner within a stainless steel autoclave

19. Place the autoclave into an oven at 130°C for 8 hours

20. After 8 hours remove the stainless steel autoclave from the furnace allow and allow to cool

21. Remove membrane, rinse under water, then place in a bath of approximately 35 mL methanol for 12 hours

22. Remove membrane from methanol and allow to dry under ambient conditions for 1 day

APPENDIX D

PROCEDURE FOR ZIF-8 CRYSTAL AND MEMBRANE LIGAND EXCHANGE

Table D.1 Materials for ZIF-8 Crystal and Membrane Ligand Exchange

Chemicals	Molecular Formula	Purity	MW (g/mol)	Supplier
5,6 Dimethylbenzimidazole (5,6 DMBIm)	$C_9H_{10}N_2$	99%	146.19	Sigma Aldrich
Triethylamine (TEA)	$(C_2H_5)_3N$	99%	101.19	Sigma Aldrich
Methanol (MeOH)	CH_3OH	99.8 % (Anhydrous)	32.04	Sigma Aldrich

D.1 Standard Procedure for ZIF-8 Crystal Ligand Exchange

1. Measure 0.1 g of ZIF-8 crystals and place in Teflon liner

2. Measure 0.1 g of 5,6 DMBIm linker and place in a beaker

3. Add 20 mL of methanol to the 5,6 DMBIm linker solution and stir for 5 minutes

4. While stirring, add 0.1 g of triethylamine to the 5,6 DMBIm linker solution and stir for 5 minutes; standard syntheses utilize a 1:1:1:160 ZIF-8:5,6 DMBIm:TEA:MeOH weight ratio

5. Add the linker solution to the Teflon liner containing the ZIF-8 powder allow the stir bar to fall into the liner

6. Place the liner on the stir plate and mix the entire solution containing ZIF-8 crystals, 5,6 DMBIm linker, TEA and methanol for 5 minutes then remove stir bar from liner

    a. If ZIF crystals are stirred in the beaker, the crystals will fall to the bottom of the solution and will be need to be rinsed out with excess methanol upon pouring into the autoclave

7. Place Teflon liner into a stainless steel autoclave

8. Heat autoclave to 60°C for 15 hours

9. After 15 hours remove autoclave and allow to cool naturally

10. Wash and centrifuge crystals 3 times in methanol

11. Dry crystals at 60°C under ambient pressure

D.2 Standard Procedure for ZIF-8 Membrane Ligand Exchange

1. Measure 0.1 g of 5,6 DMBIm linker and place in a beaker

2. Add 20 mL of methanol to the 5,6 DMBIm linker solution and stir for 5 minutes

3. While stirring, add 0.1 g of triethylamine to the 5,6 DMBIm linker solution and stir for

4. minutes

5. Secure as-synthesized ZIF-8 Membrane vertically in a Teflon holder and place in a Teflon liner

6. Add the linker solution to the Teflon liner containing the as-synthesized ZIF-8 membrane and seal in a stainless steel autoclave

7. Heat autoclave to 60°C for 15 hours

9. After 15 hours remove autoclave and allow to cool naturally

10. Place modified ZIF-8 membrane in a beaker containing 35 mL of methanol for 12 hours

11. Remove modified ZIF-8 membrane from methanol and allow to dry under ambient conditions for 1 day

APPENDIX E

PROCEDURE FOR ZIF LIGAND AND MEMBRANE PREPARATION FOR ^{1}HNMR ANALYSIS

Table E.1 Materials for ZIF-8 Membrane Ligand Exchange ^{1}HNMR Analysis

Chemicals	Molecular Formula	Purity	MW (g/mol)	Supplier
Acetic Acid – d_4	CD_3COOD	≥ 99.5 Atom %D 0.03% (v/v) w/TMS Standard	101.96	Sigma Aldrich
2-Methylimidazole	$C_4H_6N_2$	99%	82.1	Sigma Aldrich
5,6 Dimethylbenzimidazole (5,6 DMBIm)	$C_9H_{10}N_2$	99%	146.19	Sigma Aldrich

Ligand Preparation:

1A. Measure 1 to 2 mg of ligand (either 2-MIm or 5,6 DMBIm) and add to a 5 mL glass vial

Membrane Preparation:

1B. For membrane analysis, use an X-Acto knife to gently scrape the membrane material grown on top of the alpha alumina support onto weighing paper; it is best to hold the membrane vertically against the weight paper and scrape the contents down onto the paper; be sure to obtain the entire membrane sample which weighs between 1-2 mg; carefully pour contents into 5 mL glass vial

Further Steps for Ligand and Membrane Preparation:

2. Use a Pasteur pipet to add approximately 0.6-1 mL of d_4 acetic acid to the glass vial containing either ligand or membrane contents

3. Fully dissolve the sample in the deuterated acetic acid by agitating the sample (shaking, vortexer or ~1 minute of sonication); sample should be clear not cloudy for accurate ^{1}H NMR measurement

4. Use Pasteur pipette to add the solution from the glass vial to an NMR tube (Norell 5 mm width, High Throughput 178 length Secure Series NMR Tube)

5. Use Bruker 400 MHz NMR spectrometer with ^{1}HNMR using 512 scans

APPENDIX F

PROCEDURE FOR ^{1}HNMR ANALYSIS AND QUANITIFICATION OF LIGAND EXCHANGE IN ZIF-8 MEMBRANES

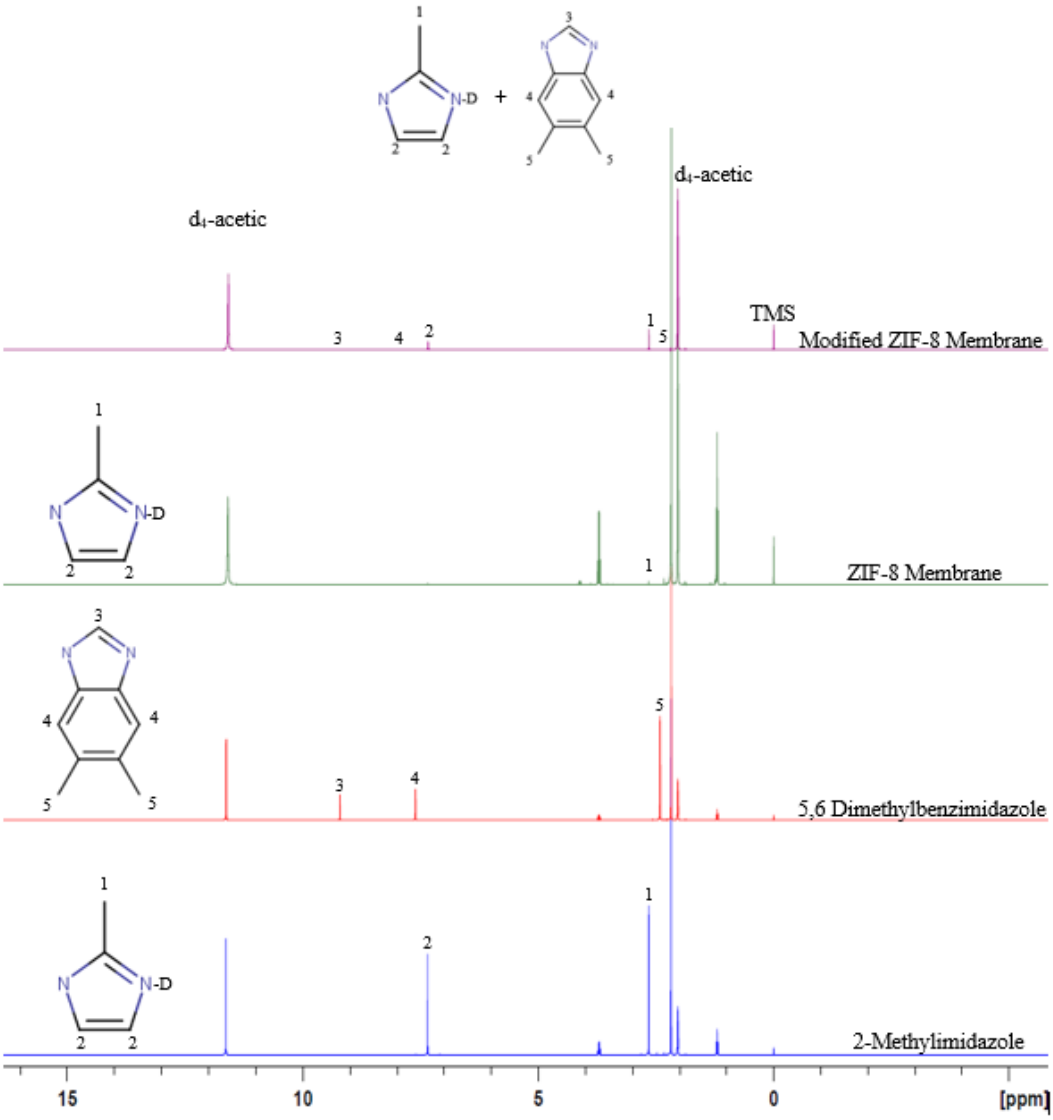

Figure F.1 [1]HNMR spectra of 2-methylimidazole, 5,6 dimethylimidazole, an as-synthesized ZIF-8 membrane and a ZIF-8 membrane modified with 5,6 dimethylbenzimidazole at 60°C for 30 minutes

^{1}HNMR peak shift assignment according to Figure E.1 using standard notation:

2-Methylimidazole ^{1}HNMR (400 MHz, d_4-Acetic) δ (ppm): 7.35 (1H, s), 2.66 (1.57H, s).

5,6 Dimethylbenzimidazole ^{1}HNMR (400 MHz, d_4-Acetic) δ (ppm): 9.21 (1H, s), 7.61 (2H, s), 2.41 (6H, s), 2.18.

The numbers next to the protons of each molecule correspond to the peak shifts in the ^{1}HNMR spectra. The numbers in the above peak shift assignments are the relative integration areas which correspond to the relative number of protons at each position of the respective 2-methylimidazole and 5,6 dimethylbenzimidazole ligands.

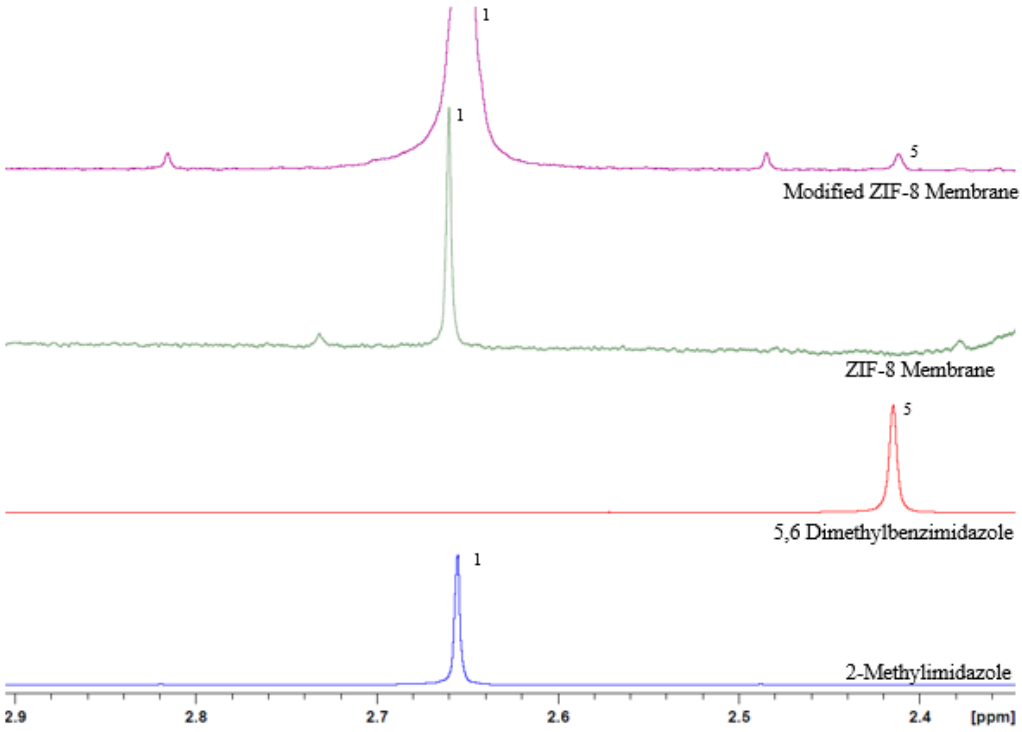

Figure F.2 Scaled view of ^{1}HNMR spectra: 2-methylimidazole, 5,6 dimethylimidazole, an as-synthesized ZIF-8 membrane and a ZIF-8 membrane modified with 5,6 dimethylbenzimidazole at 60°C for 30 minutes

The relative ratio of 2-methylimidazole and 5,6 dimethylimidazole content or molar ligand exchange ratio for the modified ZIF-8 membrane can be calculated after integration of the peak areas found for the modified ZIF-8 membrane ^{1}HNMR spectrum (purple) using the following equation:

$$\frac{M_{5,6\ DMBIm}}{M_{5,6\ DMBIm} + M_{2Mim}} \qquad (F.1)$$

In this work, the methyl groups of the 5,6 dimethylbenzimidazole molecule (peak labled 5) give the strongest signal for calculation of the ligand exchange molar ratio. The molar ligand exchange ratio can be calculated using the relative peak areas of peak 1 (methyl group of 2-MIm) and peak 5 (2 methyl groups of 5,6 DMBIm):

$$0.5 \cdot \frac{Peak\ 5\ Area}{Peak\ 5\ Area + Peak\ 1\ Area} \qquad (F.2)$$

The 0.5 accounts for the two methyl groups (dimethyl group) of the 5,6 DMBIm ligand which correspond to only one 5,6 DMBIm molecule.

APPENDIX G

X-RAY DIFFRACTION AND SCANNING ELECTRON MICROSCOPY

G.1 X-ray Diffraction

1. X-ray diffraction (XRD) is performed (Bruker AXS-D8 Focus, Cu Kα radiation) to characterize the crystal structure of ZIF-8 membranes and sorbent powders

2. Place the alumina disk supported membrane in the designated plastic, zero background sample holder in the XRD machine

3. Set 2θ in the range of 5-40° with a scan rate of 2°/min

G.2 Scanning Electron Microscopy

1. Scanning electron microscopy (SEM) is performed using a Phillips FEI XL-30 SEM to observe the morphology, crystallinity and intergrowth of alumna supports, sorbent crystals and membranes

2. If needed us a mechanical device such as pliers to break the membrane sample into smaller pieces for top surface and/or cross-section analyses and use clean, dry compressed air to remove debris from the sample

3. Place conductive carbon adhesive tape on a sample stage, place the membrane sample on the conducting tape

4. For ZIF membrane samples place carbon conductive tape directly on top of the supported membrane to allow a drain for electron flow to prevent surface charging and eventual burning of the sample

5. Coat the sample with Ag (best) or Ag/Pd or carbon for at least 4 minutes

6. Place the sample in to the SEM apparatus, choose the appropriate voltage (often 20 kV) choose a spot size of 2 for measurements

APPENDIX H

LIGHT HYDROCARBON MIXTURE MEMBRANE SEPARATION MEASUREMENTS

H.1 Binary Gas Separation Measurement

1. Light hydrocarbon binary gas separation measurements were measured using the Wicke-Kallenbach technique as shown in Figure H.1.

2. Load the membrane into the stainless steel permeation apparatus. Use Viton o-ring to seal the membrane

3. Using mass flow controllers connected to primary gas cylinders, feed the propylene/propane or ethylene/ethane mixture to the membrane side. Typically the total feed flow rate is controlled to 100 mL/min (measured at atmospheric pressure and temperature) with the binary substituent gasses usually in 50:50 mixture with flow rates of 50 mL/min each

4. On the retentate side use the needle valve to control the feed pressure. The pressure is measured by an Omega pressure transducer with a digital pressure readout

5. Feed nitrogen sweep gas flow at a rate of 50 mL/min for C_2 mixtures; utilize 10 mL/min for C_3 mixtures (propane flux is low, a smaller sweep flow will concentrate the permeate for higher resolution gas chromatograph peaks)

6. Use a bubble flow meter to measure the permeate flow rate

H.2 Gas Chromatography (GC) Measurements

1. Use gas chromatography (GC) (Agilent 6890 with Thermal Conductivity Detector) to measure the nitrogen and light hydrocarbon concentrations on both the retentate and permeate sides of the membrane

2. An Alltech Haysep DB 100/120 column with dimensions: 9.1 m L x 3.2 mm O.D. with argon carrier gas (28.9 mL/min) and an oven temperature of 130°C and detector temperature of 200°C is utilized for C_2 separation experiments

3. A silica gel column with dimensions: 1.8 m L x 3.2 mm O.D. with argon carrier gas (5 mL/min) was utilized for C_3 separation experiments with an oven temperature of 150°C and a detector temperature of 200°C

4. The GC calibration curves for ethylene and ethane gasses in the Haysep column are shown in Figure H.2. The nitrogen calibration constant is detailed in the Membrane and Energy Laboratory standard calibration chart

5. The GC calibration curves for nitrogen, propylene and propane using the silica gel column are shown in Figure H.3

6. Table H.1 shows the calibration constants and approximate retention times for each of the light hydrocarbon gasses in their respective columns

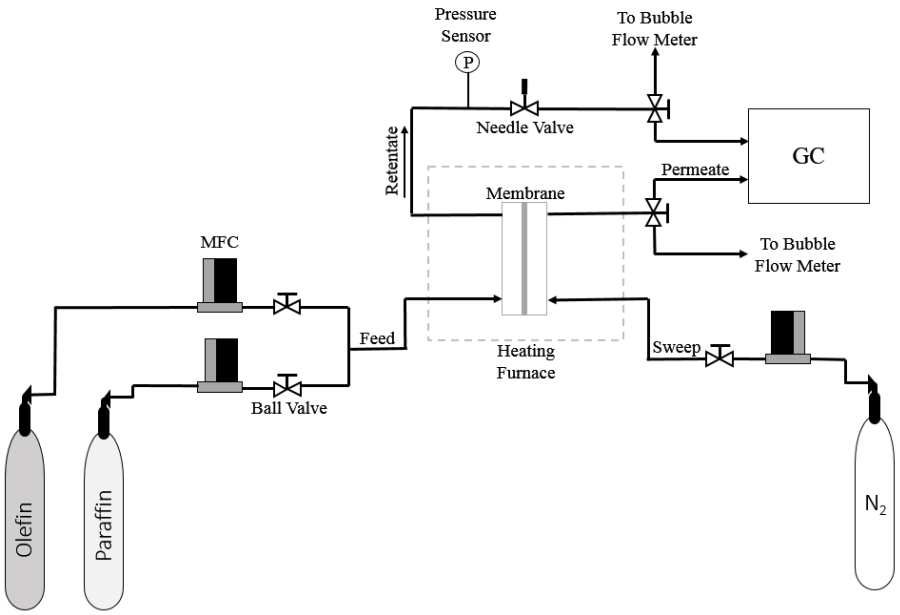

Figure H.1 Light hydrocarbon binary gas permeance apparatus and configuration

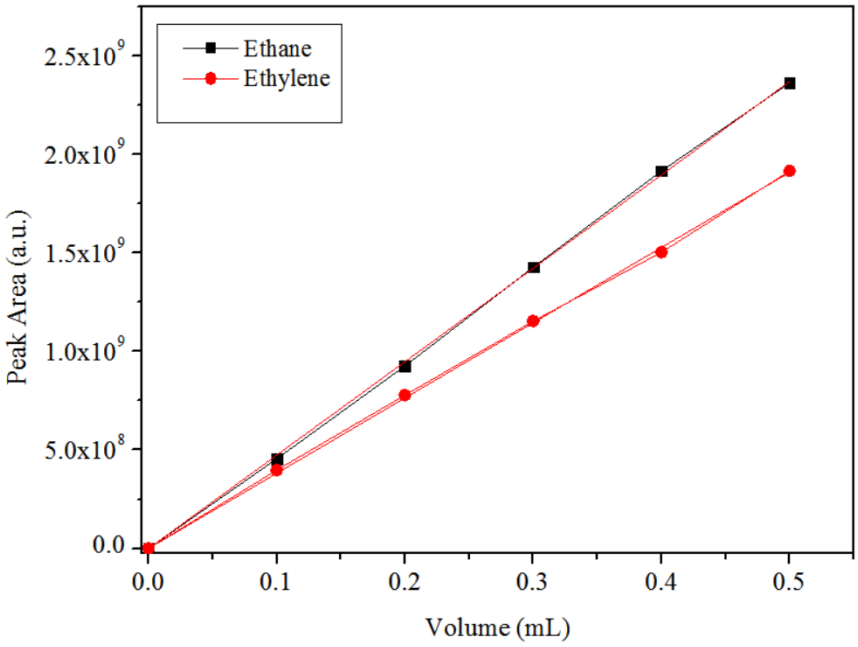

Figure H.2 GC calibration curve for ethylene and ethane gasses

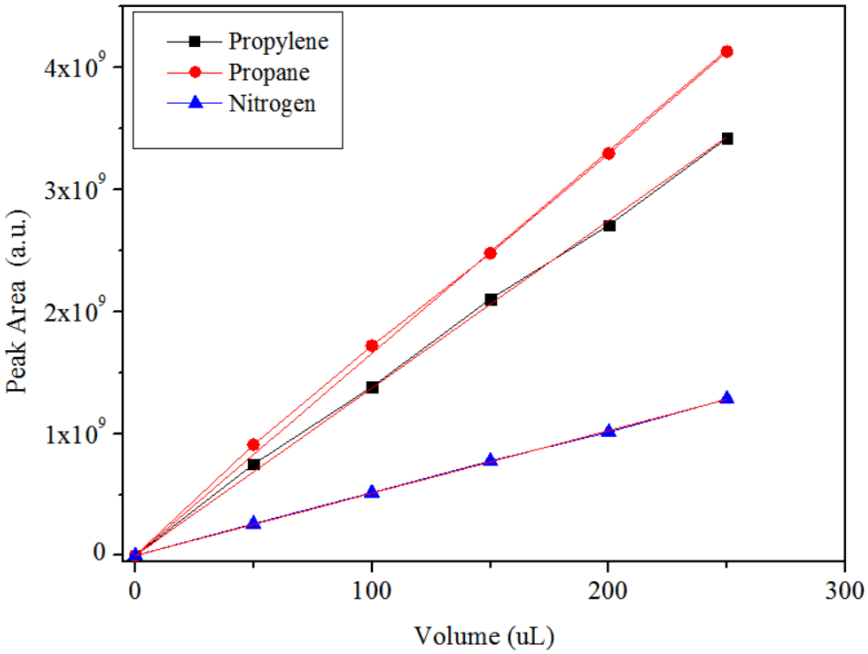

Figure H.3 GC calibration curve for nitrogen, propylene and propane gasses

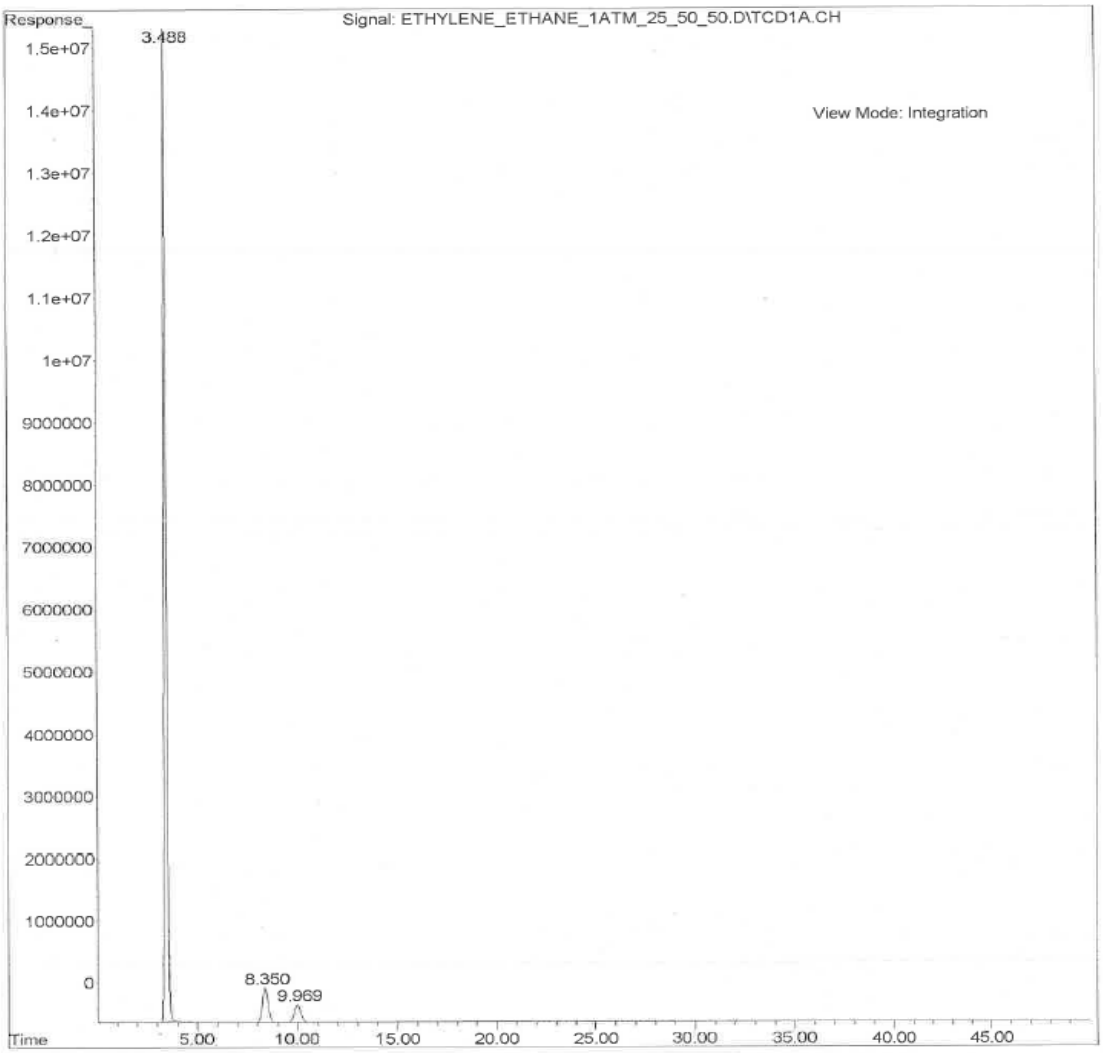

Figure H.4 Representative chromatogram of permeate for ethylene/ethane separation with nitrogen sweep gas

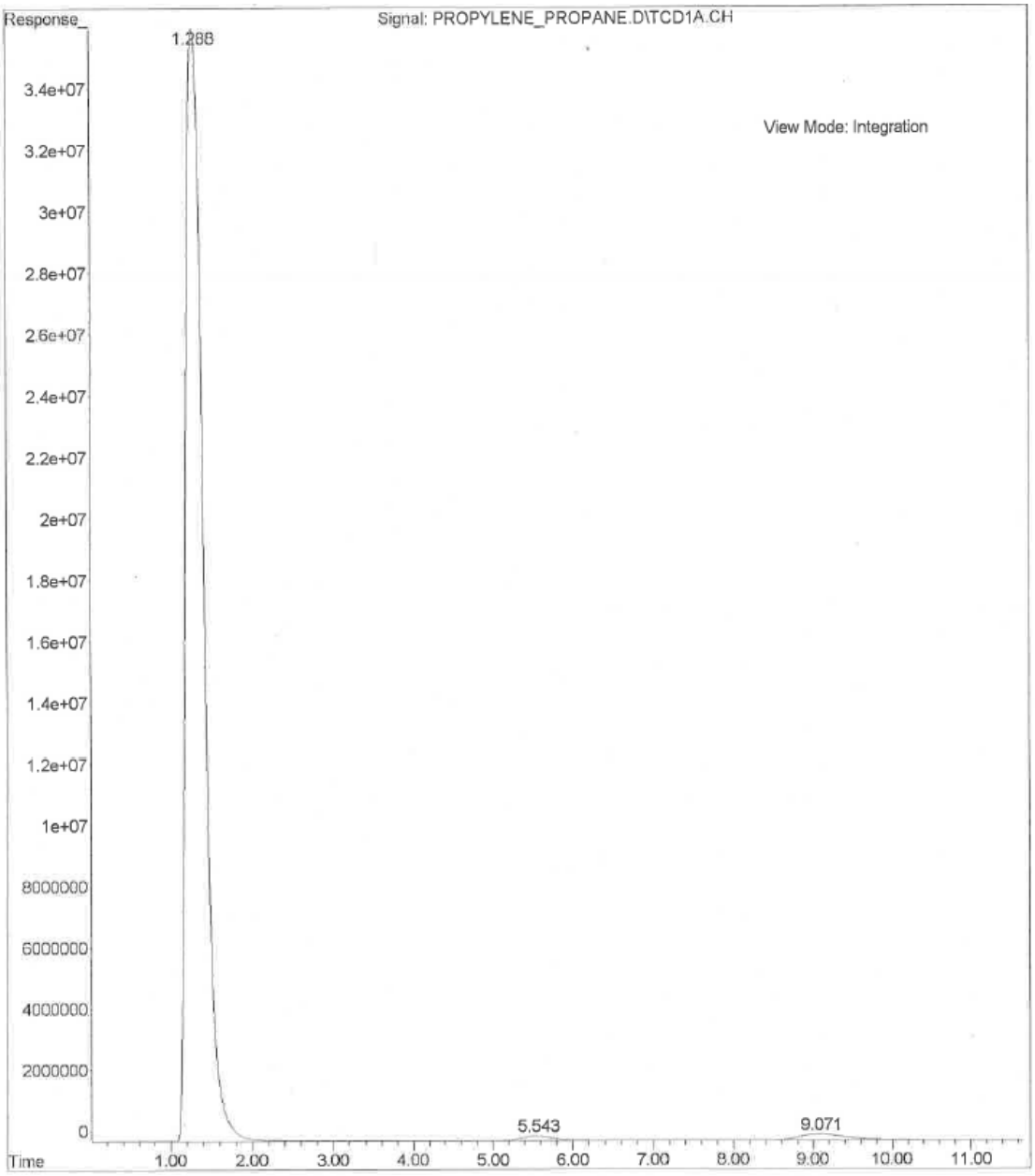

Figure H.5 Representative chromatogram of permeate for propylene/propane separation with nitrogen sweep gas

Table H.1 Calibration Constants and Retention Times for Light Hydrocarbon Gasses

	Haysep DB Column			Silica Gel Column		
	Nitrogen	Ethylene	Ethane	Nitrogen	Propylene	Propane
Retention Time (mins)	3.49	8.35	9.96	1.29	9.07	5.54
GC Constant	1.56×10^9	3.82×10^9	4.74×10^9	5.12×10^9	1.37×10^{10}	1.66×10^{10}